LANCASTER UNIVERSITY

Dusk-Dawn Convection Asymmetries in the Earth's Magnetotail: The Influence of IMF B_y and Transient Dynamics

by

James H. Lane

This thesis is submitted in partial fulfilment of the requirements
for the degree of Doctor of Philosophy

in the
Faculty of Science and Technology
Department of Physics

March 2022

Declaration of Authorship

I, James H. Lane, declare that this thesis titled 'Dusk-Dawn Convection Asymmetries in the Earth's Magnetotail: The Influence of IMF B_y and Transient Dynamics' and the work presented in it are my own. I confirm that:

- This work was done wholly or mainly while in candidature for a research degree at this University.
- Where any part of this thesis has previously been submitted for a degree or any other qualification at this University or any other institution, this has been clearly stated.
- Where I have consulted the published work of others, this is always clearly attributed.
- Where I have quoted from the work of others, the source is always given. With the exception of such quotations, this thesis is entirely my own work.
- I have acknowledged all main sources of help.
- Where the thesis is based on work done by myself jointly with others, I have made clear exactly what was done by others and what I have contributed myself.

Signed: ____

Date: ____

Abstract

When a significant B_y (dusk-dawn) component exists in the Interplanetary Magnetic Field (IMF), magnetic reconnection with the terrestrial field introduces asymmetries into the Earth's magnetosphere on a global scale, resulting in a 'twisting' of the magnetotail. The fast earthward convective flows which subsequently 'untwist' the tail are expected to have a dusk-dawn component which is inherently dependent on the sign of IMF B_y, giving rise to the 'untwisting hypothesis'. This expected dependence is, however, only observed around $\sim$70% of the time. In this thesis, data is used from magnetospheric spacecraft missions, such as Cluster, and the radar system SuperDARN, to attempt to understand why the remaining $\sim$30% of flows do not exhibit this expected direction and to refine our understanding of the drivers of dusk-dawn asymmetry in the Earth's magnetosphere.

In Chapter 4, we derive a statistical dataset of magnetotail fast flow 'detections' and investigate a number of parameters associated with only those flows which explicitly demonstrate a dusk-dawn asymmetry. An overview of our 1639 asymmetric flows suggests differences between flows which *agree* and *disagree* with the expected dusk-dawn asymmetry. In Chapters 5 and 6, we present case studies containing instances of 'disagree' flow where the expected asymmetry is not always observed. We find that transient, dynamic phenomena, including a localised 'flapping' of the magnetotail current sheet (Chapter 5) and strong dipolarisation (Chapter 6) appear to be associated with flows which are independent of the large-scale asymmetry in the convection. In Chapter 7, we present further statistics intended to elucidate the $\sim$30% of disagree flows. We find that the expected IMF B_y-control of the dusk-dawn flow is strongest ($\geq$ 90%) when the possibility that any transient, dynamic phenomena (including current sheet flapping and strong dipolarisation) are less likely to be occurring.

Collectively, this thesis presents evidence to suggest that transient, localised dynamics can override or prevent the expected IMF B_y-control of convective dusk-dawn magnetotail flows, notably when |IMF B_y| is weak, explaining at least two thirds (i.e. 20%) of the $\sim$30% disagreement.

Acknowledgements

I firstly have to thank my Mum and Dad, who have always been there for me. They have supported me in all my endeavours and always encouraged me to do my best. I also have to thank my close family, particularly my Grandma and Grandad, my Uncle Paul, and my Uncle Matt. I would also like to thank my girlfriend, Maddie, for her unwavering support as she has always believed in me and reassured me after stressful days. I'm very grateful that she didn't grow tired of listening to my continuous space physics commentary!

Next, I have to say a huge thanks to my PhD supervisor, Professor Adrian Grocott, for giving me the opportunity to undertake this PhD - I honestly couldn't have asked for a better supervisor. Through his continual support, I have learnt an unbelievable amount about magnetospheric and ionospheric physics, how to present and discuss my research effectively, and greatly improved my coding ability, amongst other things. I also wish to extend my thanks to Nathan and Maria, who I have really enjoyed working closely with throughout my PhD and learnt a lot from (particularly in relation to IDL!), and for that I am grateful. Despite not being in the office for a while due to the COVID-19 pandemic, I also want to thank Joe for putting up with me sitting next to him and constantly going on about football - it was a great laugh, and really kept me going. I have to admit, I did not think back when I was battling my way through A-Level Physics that I would be where I am today, so I want to thank all my close friends and everyone who has played a part in that journey, both directly and indirectly.

I am also very grateful for the hard work of all of the PI's and teams involved in the Cluster, THEMIS and Geotail missions, the Space Physics Data Facility OMNIWeb service, and the SuperDARN radar network; all without which, the research I have conducted would not be possible. Finally, I must thank the Faculty of Science and Technology at Lancaster University for providing me with the funding for this research.

Contents

List of Figures

List of Tables

Abbreviations

ACE - Advanced Composition Explorer

BBF - Bursty Bulk Flow

CIS - Cluster Ion Spectrometry

CODIF - Composition and Distribution Function analyser

ECPC - Expanding-Contracting Polar Cap

ESA - Electrostatic Analyser

FAC - Field-Aligned Current

FGM - Fluxgate Magnetometer

GEO - Geographic (coordinates)

GSE - Geocentric Solar Ecliptic

GSM - Geocentric Solar Magnetospheric

HF - High Frequency

HIA - Hot Ion Analyser

IGRF - International Geomagnetic Reference Field

IMF - Interplanetary Magnetic Field

IMP 8 - International Monitoring Platform 8

LEP - Low Energy Particle experiment

LOS - Line-Of-Sight

MAG - Geomagnetic (coordinates)

MGF - Magnetic Field experiment

M-I - Magnetosphere-Ionosphere

MLAT - Magnetic Latitude

MLON - Magnetic Longitude

MLT - Magnetic Local Time

MHD - Magnetohydrodynamics

MVA - Minimum Variance Analysis

NH - Northern Hemisphere

OCB - Open-Closed (field line) Boundary

RG96 - Ruohoniemi and Greenwald (1996) Statistical Convection Model

RST - Radar Software Toolkit

SEA - Superposed Epoch Analysis

SH - Southern Hemisphere

SMC - Steady Magnetospheric Convection

SPDF - Space Physics Data Facility

SST - Solid State Telescope

SuperDARN - Super Dual Auroral Radar Network

TA15 - Tsyganenko and Andreeva (2015) Magnetic Field Model

TS18 - Thomas and Shepherd (2018) Statistical Convection Model

THEMIS - Time History of Events and Macroscale Interactions during Substorms

UT - Universal Time

VDF - Velocity Distribution Function

Chapter 1

Theoretical Background

1.1 Introduction and Motivation

It is relatively well known that our Sun, the bright ball of mainly hydrogen gas at the centre of our solar system 1 AU ($\sim$1.496 $\times 10^{11}$ m) from the Earth with a mass of around 1.989 $\times 10^{30}$ kg, is a key driver of geomagnetic activity [*Pulkkinen* (2007)]. One of the the most important breakthroughs in linking our Sun to geomagnetic activity came in 1859. This was the year of the great *Carrington* storm [*Carrington* (1859)]. Carrington had been studying sunspots when he suddenly observed a great white-light flare during an extreme *geomagnetic storm*, a product of *space weather* [*Gonzalez et al.* (1994)], on the 1st of September in 1859. This coincided with disturbed magnetic field measurements at the Kew Observatory in London.

Chapman and Ferraro (1931) suggested that geomagnetic storms were somehow related to a 'stream' of charged particles which flowed radially outwards from the Sun and interacted with the Earth's magnetic field, resulting in electric currents flowing in near-Earth geospace. Electric currents in geospace can create measurable magnetic field disturbances on the ground, similar to those observed by Carrington [e.g. *Milan et al.* (2017)]. It was later that *Parker* (1958) coined this stream as being the *solar wind* - a continual outflow of hot plasma (ions and electrons). 'Frozen-in' to this flow is the Sun's magnetic field, carried as the *Interplanetary Magnetic Field* (IMF). When the solar wind and IMF interact with the Earth, a magnetic 'bubble' containing the Earth's magnetic field is formed. This was indeed hinted at by *Chapman and Ferraro* (1931), but only later termed as a *magnetosphere* by *Gold* (1959). The dayside (sunward facing) of the magnetosphere is compressed due to the solar wind pressure, whereas the nightside (anti-sunward facing) magnetosphere extends away from the Earth as a long magnetic tail, known as a *magnetotail* [*Dungey* (1965)]. The exact formation of the magnetotail is related to a process called *magnetic reconnection*; under the right conditions, the IMF and Earth's magnetic field can 'reconnect' to one-another, resulting in a reconfiguration of the field and an energisation of particles. This drives a large-scale circulation of magnetic field lines within the magnetosphere known as the *Dungey Cycle*, after *Dungey* (1961).

The IMF can be thought of as a typical 3-dimensional vector. When a significant east-west component (also known as dusk-dawn, or B_y component) exists in the IMF, the reconnection process introduces asymmetries into the Earth's magnetosphere, 'twisting' the magnetotail [*Cowley* (1981)]. Plasma flowing within the magnetotail, as part of the Dungey Cycle, subsequently acquires a dusk-dawn direction which is inherently dependent on IMF B_y [*Grocott et al.* (2007)]. This has been observed to occur ~70% of the time [*Pitkänen et al.* (2013, 2017)]. The aim of the research presented in this thesis is to understand why the remaining ~30% of plasma flows do not have this expected IMF B_y-dependence. We find evidence to suggest that localised, dynamical and transient processes in the magnetotail can prevent or override the plasma flow direction expected from IMF B_y.

The fundamental physics that governs these observations is electromagnetism - that is, the action of electric and magnetic forces on charged particles. We begin in the current chapter by introducing the mathematics describing these interactions, and expanding on a number of the terms introduced above, including the solar wind, IMF, magnetosphere and magnetotail, and explain how these are all linked to one-another. In Chapter 2, we build on the theory presented in Chapter 1 by discussing convection in the magnetosphere-ionosphere system, and provide a review of the literature concerning our research topic, including how the B_y component of the IMF introduces large-scale asymmetries into the Earth's magnetosphere-ionosphere system. In Chapter 3, we discuss the instrumentation used in the research presented in this thesis, before presenting this research in Chapters 4-7.

1.2 Charged Particle Motion

A *plasma* is a highly conductive, hot ionised gas consisting of positively and negatively charged particles (ions and electrons). Plasmas are generally *quasi-neutral* on length scales greater than the *Debye length* [*Baumjohann and Treumann* (1997)], meaning that within a given volume, there is approximately zero net charge, requiring equal number densities of ions and electrons ($n_i \approx n_e$). However, due to the abundance of charged particles, the particles that make up the plasma will both create, and be acted upon by, electromagnetic fields [*Baumjohann and Treumann* (1997); *Russell et al.* (2016)].

A charged particle with charge q_0 will produce an electric field $\mathbf{E}$ which exerts a *Coulomb force* $\mathbf{F}$ on a nearby charge q:

$$\mathbf{F} = q\mathbf{E} \tag{1.1}$$

Whether the force is attractive or repulsive depends on the signs of the charges, as charge q will of course produce its own electric field, resulting in an equal and opposite Coulomb force on q_0. If q_0 is moving it will generate a magnetic field $\mathbf{B}$. Differential motion of positively and negatively charged particles will constitute a current - a net flow of charge from one region to another [*Ganushkina et al.* (2018)], driven by a potential difference. A charged particle q moving at velocity $\mathbf{v}$ in a magnetic field $\mathbf{B}$ experiences a *Lorentz force*:

$$\mathbf{F} = q(\mathbf{v} \times \mathbf{B}) \tag{1.2}$$

For a moving charged particle under the action of both forces, superposition of forces dictates that this becomes the *Complete Lorentz force equation.* By *Newton's Second Law of Motion*, we therefore have:

$$\mathbf{F} = m\mathbf{a} = m\frac{d\mathbf{v}}{dt} = q(\mathbf{E} + \mathbf{v} \times \mathbf{B}) \tag{1.3}$$

where m is the mass of the charged particle.

Initially, let us assume we have a uniform magnetic field $\mathbf{B}$, with no electric field or other forces present. In the case that $\mathbf{v} = (v_x, v_y, v_z)$ and $\mathbf{B} = (0, 0, B_z)$ in a standard cartesian (x, y, z) coordinate system, from the cross-product in equation 1.2, we get:

$$\frac{dv_x}{dt} = \frac{qB_z v_y}{m} \tag{1.4}$$

$$\frac{dv_y}{dt} = -\frac{qB_z v_x}{m} \tag{1.5}$$

$$\frac{dv_z}{dt} = 0 \tag{1.6}$$

Equations 1.4 and 1.5 show that a charged particle is accelerated perpendicular to the magnetic field (in the x-y plane). Equation 1.6 shows that motion parallel to the magnetic field is constant ($|\mathbf{v}_{\|}| = v_{\|} = v_z$). By taking the derivatives of equations 1.4 and 1.5 with respect to time, and substituting equations 1.4 and 1.5 back into the result, we obtain:

$$\frac{d^2 v_x}{dt^2} = -\frac{q^2 B_z^2}{m^2} v_x \tag{1.7}$$

$$\frac{d^2 v_y}{dt^2} = -\frac{q^2 B_z^2}{m^2} v_y \tag{1.8}$$

This is simply the equation for a simple harmonic oscillator, with the oscillation frequency, or *gyrofrequency*:

$$\omega = \frac{qB_z}{m} \tag{1.9}$$

Thus, equations 1.7 and 1.8 show that motion in the x-y plane (perpendicular to the magnetic field) is variable and forms a system of coupled harmonic oscillators. The radius of this motion is commonly known as the *gyroradius*, or *Larmor radius*, given as:

$$r_L = \frac{v_\perp}{\omega} = \frac{mv_\perp}{B_z q} \tag{1.10}$$

where in this case:

$$v_\perp = |\mathbf{v}_\perp| = \sqrt{v_x^2 + v_y^2} \tag{1.11}$$

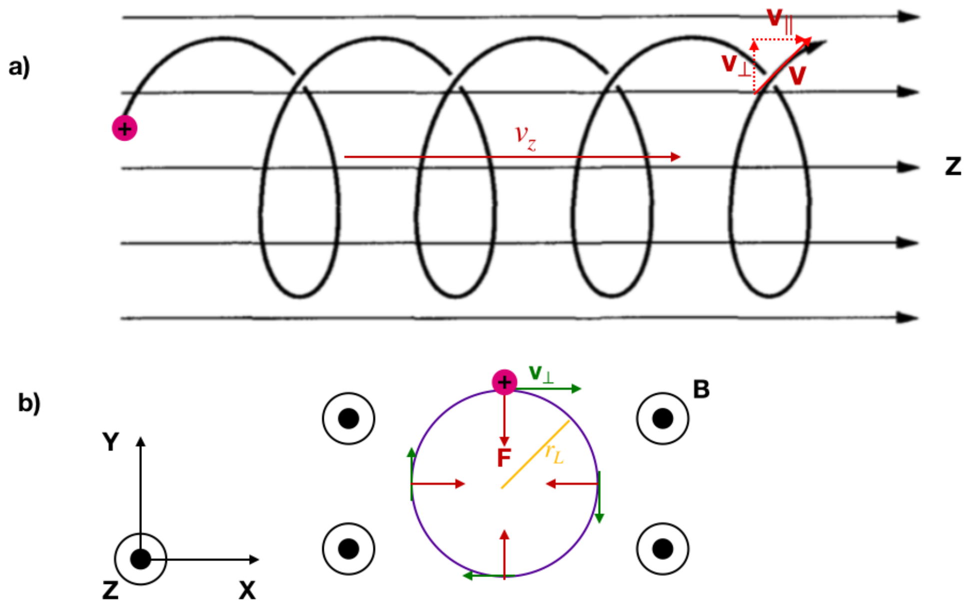

FIGURE 1.1: a) An illustration of the helicoidal orbit of a positively charged particle along a magnetic field, moving parallel to (drifting along) the field at constant velocity v_z whilst gyrating around the field. A velocity vector $\mathbf{v}$ and its components parallel ($\mathbf{v}_{\parallel}$) and perpendicular ($\mathbf{v}_{\perp}$) to the magnetic field at one instant are indicated. Adapted from *Baumjohann and Treumann* (1997). b) A 2D projection of the particle motion into the X-Y plane, showing the particle gyrating (purple outline). The magnetic field is directed vertically out of the page. The direction of the Lorentz force and velocity vector at four instances are indicated by the red and green arrows, respectively. The Larmor radius r_L of the particle is also shown by the yellow line.

It can be seen from equation 1.10 that heavier particles would have a larger Larmor radius, and that particles of positive (negative) charge would gyrate in a clockwise (anti-clockwise) direction. The centre of the gyration is known as the particle's *guiding centre*. The Lorentz force thus acts perpendicular to the magnetic field and velocity vector and forces particles into circular gyrations, providing a centripetal force. Meanwhile, the particle moves parallel to the field at a constant velocity as there is no net force acting on it along the field. The resultant helicoidal motion from the above discussion is depicted in Figure 1.1.

1.2.1 Electric Field Drift

In the case that a uniform electric field $\mathbf{E}$ is present *in addition* to a uniform magnetic field, our change in velocity with respect to time is just the complete Lorentz force (eq. 1.3). The particle velocity $\mathbf{v}$ may be decomposed into its respective vector components parallel

($\mathbf{v}_{\parallel}$) and perpendicular ($\mathbf{v}_{\perp}$) to the magnetic field:

$$\mathbf{v} = \mathbf{v}_{\perp} + \mathbf{v}_{\parallel} \rightarrow |\mathbf{v}| = \sqrt{v_{\perp}^2 + v_{\parallel}^2} \tag{1.12}$$

Firstly, considering motion parallel ($\mathbf{v}_{\parallel}$) to the magnetic field, we have:

$$\frac{d\mathbf{v}_{\parallel}}{dt} = \frac{q}{m}\mathbf{E}_{\parallel} \tag{1.13}$$

since $\mathbf{v}_{\parallel} \times \mathbf{B} = 0$. Equation 1.13 illustrates that particles will be accelerated parallel to (along) the magnetic field by the parallel component of the electric field, with positively and negatively charged particles moving in opposite directions. Generally, in most geophysical plasmas, the electrons are extremely mobile along magnetic field lines, and as such any electric fields parallel to the magnetic field are usually quickly cancelled out by the electrons re-arranging themselves [*Baumjohann and Treumann* (1997); *Russell et al.* (2016)].

Next, considering motion perpendicular ($\mathbf{v}_{\perp}$) to the magnetic field, we have:

$$\frac{d\mathbf{v}_{\perp}}{dt} = \frac{q}{m}(\mathbf{E} + \mathbf{v}_{\perp} \times \mathbf{B}) \tag{1.14}$$

If we assume that $\mathbf{E}$ and $\mathbf{B}$ are uniform and constant, take the time derivative of the above equation and then substitute equation 1.14 back in to this time derivative, we arrive at an expression:

$$\frac{d^2\mathbf{v}_{\perp}}{dt^2} = \frac{q^2}{m^2}(\mathbf{E} \times \mathbf{B} - \mathbf{v}_{\perp}|\mathbf{B}|^2) \tag{1.15}$$

The time-independent solution to equation 1.15 (LHS $= 0$, $\mathbf{v}_{\perp}(t) = \mathbf{v}_E = const$) [*Russell et al.* (2016)], reveals that the electric field exerts a drift:

$$\mathbf{v}_E = \frac{\mathbf{E} \times \mathbf{B}}{|\mathbf{B}|^2} \tag{1.16}$$

This is known as the $\mathbf{E} \times \mathbf{B}$ drift, and states that in the presence of uniform electric and magnetic fields, *all* particles, regardless of mass or charge, will drift with velocity $\mathbf{v}_E$ in a direction perpendicular to $\mathbf{E}$ and $\mathbf{B}$ (i.e. the direction of $\mathbf{E} \times \mathbf{B}$), with gyroradius r_L and gyrofrequency ω. Shown on Figure 1.2, is a diagram illustrating the $\mathbf{E} \times \mathbf{B}$ drift.

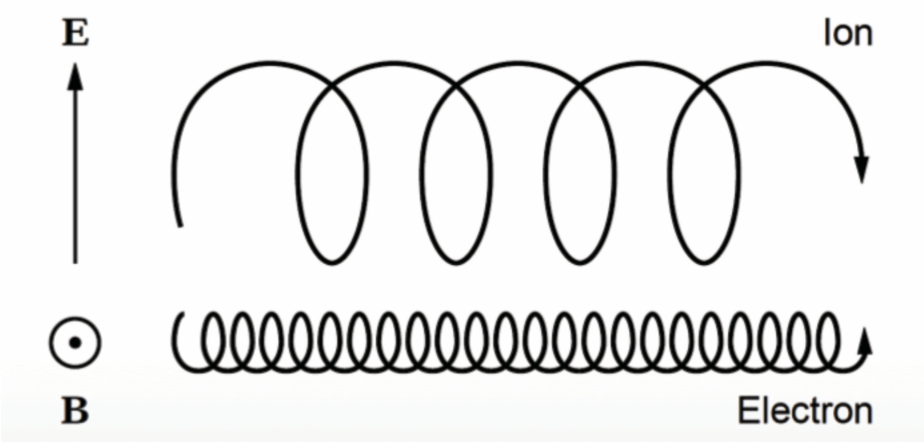

FIGURE 1.2: An illustration of the $\mathbf{E} \times \mathbf{B}$ drift for both ions (positive) and electrons (negative). The electric field is directed vertically upward, and the magnetic field is directed out of the page [*Baumjohann and Treumann* (1997)].

Ions are accelerated in the direction of the electric field, increasing the gyroradius. They are then decelerated during the second half of the gyratory orbit, which decreases the gyroradius. The difference in gyroradii resultantly shifts the ions guiding centre into the $\mathbf{E}\times\mathbf{B}$ direction. The same (but opposite) effect occurs for the electrons, and the result is the net drift motion depicted on Figure 1.2, with the guiding centres moving in the same direction.

In a perfectly $\mathbf{E}\times\mathbf{B}$ drifting quasi-neutral plasma consisting of just protons and electrons, all particles drift at the $\mathbf{E}\times\mathbf{B}$ velocity meaning no net current density $\mathbf{J}$ is produced. This can be shown by considering the equation for the total current density [e.g. *Paschmann and Daly* (1998)]:

$$\mathbf{J} = n_i \mathbf{v}_i q_i + n_e \mathbf{v}_e q_e = ne(\mathbf{v}_i - \mathbf{v}_e) = ne(\mathbf{v}_E - \mathbf{v}_E) = 0 \tag{1.17}$$

where n_i (n_e) is the ion (electron) number density, e is the electron charge ($q_i = e, q_e = -e$), and the ion (electron) drift velocities $\mathbf{v}_i$ ($\mathbf{v}_e$), are both equal to $\mathbf{v}_E$.

Finally, we note that if we replace $\mathbf{E}$ in equation 1.16 with our expression for the Coulomb force (eq. 1.1), we can derive an expression for a generalised force drift velocity [*Russell* *et al.* (2016)]:

$$\mathbf{v}_d = \frac{\mathbf{F} \times \mathbf{B}}{q|\mathbf{B}|^2} \tag{1.18}$$

the direction of which is always perpendicular to **F** and **B**. Any substitution for a force **F** which does not remove q from the expression for $\mathbf{v}_d$ will result in some current-inducing drift due to differential motion of positive and negative charge (owing to equation 1.17). For further reading on the different types of particle drifts, I direct the reader to Chapter 2 of *Baumjohann and Treumann* (1997).

1.3 Magnetohydrodynamics

1.3.1 The Momentum Equation

Magnetohydrodynamics (MHD) is the approach of treating a plasma as a single collective fluid [see e.g. *Priest* (2012); *Freidberg* (2014)], which is particularly useful when the plasma is highly ionised and the ions and electrons are forced to act in unison, such as in the solar wind (introduced in Section 1.4). Beginning with eq. 1.3, a simplified *momentum equation* (i.e. equation of motion) of a unit volume of fluid for a quasi-neutral collisionless plasma consisting of just protons and electrons may be derived [see e.g. *Paschmann et al.* (1998)]:

$$\rho_m \frac{d\mathbf{v}}{dt} = \mathbf{J} \times \mathbf{B} - \nabla P \tag{1.19}$$

where ρ_m is the mass density, **v** is the bulk (average) flow velocity, **J** is the current density, **B** is the magnetic field and ∇P is a thermal plasma pressure gradient. This equation represents the ***force per unit volume*** acting on an element of plasma.

1.3.2 The J x B Force

The plasma velocity (eq. 1.19) would be constant (or zero) in the case of a current-free (or field-aligned current only) plasma with no thermal pressure gradients. This would also be true in the case that the force-balance condition:

$$\nabla P = \mathbf{J} \times \mathbf{B} \tag{1.20}$$

is met [e.g. *Wolf et al.* (2006)]. However, should this condition not be met, and if there is some current flowing non-parallel to the magnetic field (induced by the relative particle motions within the plasma), we can expect the plasma to feel a net force, and thus an acceleration. We can consider substituting for **J** using *Ampère's Law*:

$$\nabla \times \mathbf{B} = \mu_0 \mathbf{J} \tag{1.21}$$

where $\mu_0 = 4\pi \times 10^{-7}$ NA^{-2} is the vacuum permeability. This states that the curl of a magnetic field at any point is proportional to the current density which exists there [*Milan et al.* (2017)]. Substitution of **J** into equation 1.19 and expanding gives:

$$\rho_m \frac{d\mathbf{v}}{dt} = \frac{(\mathbf{B}.\nabla)\mathbf{B}}{\mu_0} - \nabla \frac{|\mathbf{B}|^2}{2\mu_0} - \nabla P \tag{1.22}$$

Equation 1.22 is our momentum equation formulated purely in terms of **B** and **v** [*Shiokawa et al.* (1997)]. To demonstrate the significance of this equation, suppose a plasma is 'threaded' by a magnetic field line (see Sections 1.3.3 and 1.4). The first term on the RHS of equation 1.22 corresponds to the *magnetic tension force*, which acts on the plasma in a direction which is radially inwards with respect to the curvature of a magnetic field line, analagous to the restoring force on an elastic band. The second term is the *magnetic pressure force*, which indicates that where there are gradients in the magnetic field strength perpendicular to **B**, the plasma will experience a force perpendicular to **B** toward regions of weaker magnetic field [*Baumjohann and Treumann* (1997); *Russell et al.* (2016)]. The relevance of magnetic tension and pressure forces is discussed in Chapter 2.

1.3.3 The Frozen-In Theorem and Ohm's Law

One of the most fundamental concepts applied in space physics is the *frozen-in theorem*. First put forward by *Alfvén* (1942), the frozen-in theorem states that for a fluid with infinitely high electrical conductivity, a magnetic field embedded in the fluid is 'frozen'

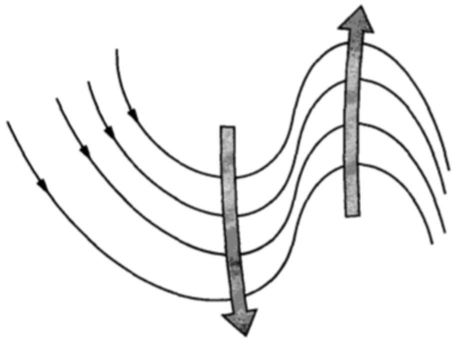

FIGURE 1.3: A schematic illustrating the concept of a frozen-in magnetic field. The magnetic field lines are the thin black lines, which are deformed by the bulk motion of the plasma (direction shown by the thicker, grey lines) [*Baumjohann and Treumann* (1997)].

into the fluid and must move along with it. The mathematical form of *Alfvén's theorem* is:

$$F_B = \int\int_S \mathbf{B} \cdot d\mathbf{S} = const \tag{1.23}$$

which simply means that the magnetic flux (i.e. the surface integral of the magnetic field $\mathbf{B}$ passing through a surface with infinitesimal vector area $d\mathbf{S}$) moving along with the fluid is conserved [e.g. *Wilmot-Smith et al.* (2005)]. Thus, as a consequence of the frozen-in theorem, any magnetic field lines (flux) which thread a moving plasma will be forced to travel with the plasma, or similarly, the plasma will be bound to the magnetic field lines, and plasmas on separate field lines should not mix. This concept is depicted in Figure 1.3.

A direct consequence of the frozen-in theorem can be examined by considering *Ohm's law*, which relates current density $\mathbf{J}$ to an applied electric field $\mathbf{E}$. A *Generalised Ohm's Law* may be derived specifically in the case of an MHD plasma:

$$\mathbf{E} = -\mathbf{v} \times \mathbf{B} + \frac{\mathbf{J}}{\sigma} + \frac{1}{ne}(\mathbf{J} \times \mathbf{B}) - (\frac{1}{ne})\nabla \cdot \mathbf{P}_e + (\frac{m_e}{ne^2})\frac{d\mathbf{J}}{dt} \tag{1.24}$$

The derivation is non-trivial, but may be found in Chapter 7.3 of *Baumjohann and Treumann* (1997). In eq. 1.24, the first term on the right corresponds to the electric field produced by a moving plasma. The two latter terms on the RHS, which contribute to $\mathbf{E}$ consist of anisotropic electron pressure and electron inertia, respectively, and are typically small on length and time scales greater than the electron gyroradius and gyroperiod.

In addition to this, the $\mathbf{J} \times \mathbf{B}$ term is negligible on length and time scales larger than the ion gyroradius and gyroperiod [e.g. *Stawarz et al.* (2021)]. In ideal MHD, infinite conductivity ($\sigma \to \infty$) - the 'frozen-in approximation', is also assumed, so eq. 1.24 becomes:

$$\mathbf{E} = -\mathbf{v} \times \mathbf{B} \tag{1.25}$$

which is the equation for *frozen-in flow.* This equation states that, in the rest frame of a stationary observer (i.e. in the frame of the rotating Earth), a 'convection' electric field is produced from the cross product of the bulk plasma velocity and magnetic field [see e.g. *Stern* (1977); *Song et al.* (2001)]. The $\mathbf{E} \times \mathbf{B}$ drift equation (eq. 1.16), which may be obtained by taking the cross product of eq. 1.25 with $\mathbf{B}$, tells us the magnitude and direction of the field-perpendicular component of that flow which we associate with the *transport of frozen-in flux*, or *convection* [*Paschmann and Daly* (1998)]. Thus, $\mathbf{E} \times \mathbf{B}$ drift is a *convective* plasma flow.

The frozen-in approximation is valid for space plasmas in collisionless regimes and where magnetic field gradients and associated timescales only vary slowly relative to the ion gyroradii and gyrofrequencies. When gradients in the magnetic field are comparable to the ion gyroradii, or characteristic timescales are similar to the ion gyrofrequency, then ideal MHD and thus the frozen-in theorem may break down [*Freidberg* (2014)]. Other processes, such as *diffusion*, can then begin to dominate over the convection. This is discussed further in the following section.

1.3.4 The Magnetic Induction Equation

The concept of frozen-in flow can be envisaged through the *magnetic induction equation.* Deriving this equation requires two of the famous *Maxwell's Equations.* These are Ampère's Law (eq. 1.21) and *Faraday's Law*:

$$\nabla \times \mathbf{E} = -\frac{\partial \mathbf{B}}{\partial t} \tag{1.26}$$

which states that a non-conservative electric field is always accompanied by a time varying magnetic field [*Baumjohann and Treumann* (1997)]. If we consider eq. 1.24, where only the first and second terms on the RHS are non-zero (finite conductivity) and take the curl of this equation, we get:

$$\nabla \times \mathbf{E} = -\frac{\partial \mathbf{B}}{\partial t} = \nabla \times \left(\frac{\mathbf{J}}{\sigma} - \mathbf{v} \times \mathbf{B} \right) \tag{1.27}$$

If we then substitute for $\mathbf{J}$ from eq. 1.21, then by expanding the RHS, and also using the fact that $\nabla \cdot \mathbf{B} = 0$ (absence of magnetic monopoles), we obtain the *magnetic induction equation*:

$$\frac{\partial \mathbf{B}}{\partial t} = \nabla \times (\mathbf{v} \times \mathbf{B}) + \frac{\nabla^2 \mathbf{B}}{\mu_0 \sigma} \tag{1.28}$$

The first term on the RHS of eq. 1.28 is the 'convective' (frozen-in flow) term, whereas the second term on the RHS is the 'diffusion' term. This equation generally means that the magnetic field at a given point can be changed by convective motion of plasma and due to diffusion [*Wilmot-Smith et al.* (2005)]. In an infinitely conducting (ideal MHD) plasma, the diffusive term disappears from eq. 1.28, thus meaning that any changes in the magnetic field lines are as if the field was constrained to move with the plasma (frozen-in) [*Baumjohann and Treumann* (1997)].

If we divide the convective term by the diffusive term, noting that $[\nabla] = 1/Length$, we acquire a quantity known as the *Magnetic Reynolds Number*:

$$R_m = vL\mu_0\sigma \tag{1.29}$$

where v is the average plasma speed perpendicular to the magnetic field, and L is some characteristic length over which the magnetic field varies. R_m is essentially a measure of deciding whether a plasma is convection or diffusion dominated. $R_m >> 1$ corresponds to a large conductivity and large length scales (much longer than the ion or electron gyroradii) with large velocities, meaning the magnetic fields are 'frozen-in' to the plasma flow, and convection dominates. The solar wind (introduced below in Section 1.4), for example, has $R_m \approx 7 \times 10^{16}$ [*Baumjohann and Treumann* (1997)]. In this instance, the second term on the RHS of eq. 1.28 disappears. Should $R_m \leq 1$, diffusion becomes important, and the magnetic field may begin to slip across different plasma regimes, or equivalently, plasma on different field lines may mix. We shall discuss the significance of this when we discuss the process of *magnetic reconnection* in Section 1.8.

1.4 The Solar Wind and Interplanetary Magnetic Field

The solar corona is the outermost layer of the Sun's atmosphere - it is a highly ionised plasma consisting mainly of protons and electrons. Temperatures here are of the order of 10^6 K with number densities of order of 10^{17} cm^{-3} [*Baumjohann and Treumann* (1997)]. The intense gas pressure at the base of the corona cannot be contained by the Sun's gravity, so it escapes the solar corona as the *solar wind* - a collisionless plasma with extremely high conductivity which flows radially outwards across interplanetary space at speeds of around 400 km s^{-1} before terminating at the heliopause. The solution to this, after *Parker* (1958), can be derived from considering the momentum equation in terms of a steadily expanding wind, previously assumed to be in hydrostatic equilibrium [*Parker* (1965)]. In reality, the solar wind is not a steady outflow, but is highly dynamic and subject to variations in number density, temperature and velocity [*Pizzo* (1978)].

The Sun produces its own intrinsic magnetic field. At the base of the corona, this may be of the order of 10^{-2} nT [*Baumjohann and Treumann* (1997)]. When this field is 'closed', meaning both ends of the field line (footpoints) are on the Sun, the solar wind cannot expand radially outward but is trapped by the magnetic field. However, the field lines originating from 'coronal holes' (regions of colder, less dense plasma than the surrounding corona, commonly found in the polar regions) are 'open', meaning they don't return to the Sun's surface. As a result of this, as the solar wind flows outwards, it carries, or 'convects' the Sun's open magnetic field with it across interplanetary space (as a consequence of the frozen-in theorem) to form the *Interplanetary Magnetic Field* (IMF). This strength of this field generally falls off with radial distance as r^{-2} [*Russell et al.* (2016)].

We can consider the state of the solar wind 'magnetisation' by looking at a parameter known as the *plasma beta*. This is the ratio of plasma thermal pressure to magnetic

Property	**Value**
Speed	400 km s^{-1}
Proton number density	10^6 m^{-3}
Temperature	10^5 K
Average IMF Strength	5 nT
Plasma Beta	$1 < \beta < 30$

TABLE 1.1: Some typical solar wind and IMF properties at 1 AU [*Kivelson and Russell* (1995)].

pressure, given as:

$$\beta = \frac{P_{plasma}}{P_{magnetic}} = \frac{nk_bT}{\frac{B^2}{2\mu_0}} \tag{1.30}$$

If $\beta \geq 1$, then the plasma dominates and is considered 'hot'. If $\beta \ll 1$, then the magnetic field dominates and the plasma is 'cold'.

As the Sun rotates (period of approx. 27 days), due to the frozen-in foot point still being embedded in the Sun, the radially outflowing solar wind winds the IMF into an 'archimedian spiral' configuration, known as the Parker spiral [*Parker* (1958)]. This is depicted in Figure 1.4. Consequently, the exact direction and strength of the IMF at Earth (1 AU) can vary, but it generally makes an angle of about 45° to the Earth-Sun line [*Baumjohann and Treumann* (1997)]. Some typical solar wind and IMF properties at 1 AU are detailed in Table 1.1.

1.5 The Earth's Magnetic Field

The continual flow of liquid iron within the Earth's outer core, driven through rotation and thermal convection associated with temperature gradients creates electrical currents [*Pallé* (2010)]. These currents create magnetic fields, and this continual cycle results in the creation of the Earth's magnetic field, that is, the Earth's magnetic field is essentially a self-regulating hydromagnetic dynamo [*Levy* (1976)].

In the absence of any external interference, such as no solar wind or IMF, the Earth's magnetic field would be approximately 'dipolar'. This is a field which has a minimum at

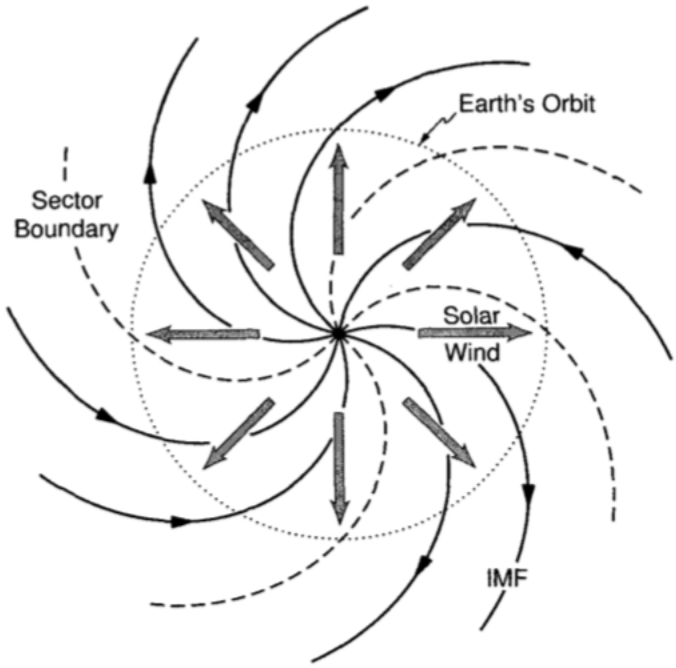

FIGURE 1.4: A schematic showing how the (anti-clockwise) rotation of the Sun coupled with the expanding solar wind causes the interplanetary magnetic field lines to be wound into a spiral configuration. The schematic is shown as though looking down onto the Sun from above. The 'sector boundaries', shown by the dashed lines, are depicting crossings of the heliospheric current sheet [*Thomas and Smith* (1981)] as it separates oppositely directed magnetic field lines [*Baumjohann and Treumann* (1997)].

the equator, field lines which converge towards the magnetic poles in both hemispheres, and a magnitude which falls with radial distance as r^{-3} [*Baumjohann and Treumann* (1997)]. The concept of dipolar field lines is conveyed in Figure 1.5. A more accurate description of the Earth's magnetic field is given by the International Geomagnetic Reference Field (IGRF) - a 13th generation model, which represents the magnetic field as the gradient of a spherical harmonic expansion of a magnetic scalar potential [e.g. *Wardinski et al.* (2020)]. The strength of the Earth's magnetic field on the Earth's surface is generally of the order of ∼25,000 nT at the equator, and ∼60,000 nT near the poles [e.g. *Thébault et al.* (2015)]. The line through the Earth joining the northern and southern magnetic poles is known as the magnetic dipole axis (discussed below).

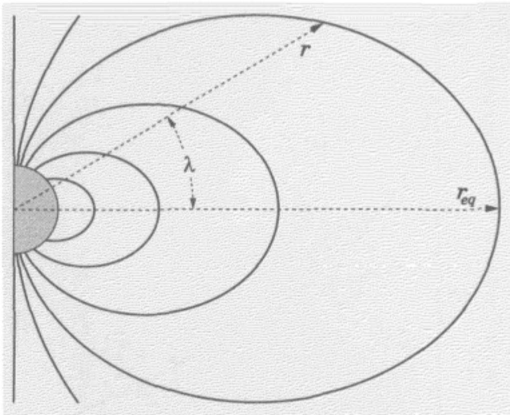

FIGURE 1.5: A schematic illustrating the dipolar magnetic field lines of the Earth. λ represents the angle between the magnetic equator and some radial vector [*Baumjohann and Treumann* (1997)].

1.5.1 Coordinate Systems

It is now that we choose to introduce the various coordinate systems which are often utilised when dealing with phenomena in near-Earth space, as these will be required in the coming chapter(s). Two of the mostly commonly used coordinate systems are geocentric, meaning the Earth lies at the centre. These are listed, and described as follows [*Hapgood* (1992); *Laundal and Richmond* (2017)]:

- *Geocentric Solar Ecliptic* (GSE) - X is directed towards the Sun, Y is in the ecliptic plane, opposite to the direction the Earth is travelling, and Z is perpendicular to the ecliptic plane.
- *Geocentric Solar Magnetospheric* (GSM) - X is the same as in GSE, however Y is perpendicular to both the magnetic dipole axis and the Earth-Sun line (positive towards dusk), such that Z is aligned with the projection of the Earth's magnetic dipole (positive North) in the plane perpendicular to the X-axis. The X-Z plane thus contains the dipole axis.

As the Earth rotates, the magnetic dipole (offset from the rotation axis by $\sim 11°$) will rotate with Earth, and thus, viewed along the X-axis, the Y-Z GSM axes can appear to 'rock' back and forth. This effect, along with the GSM coordinate system is depicted in

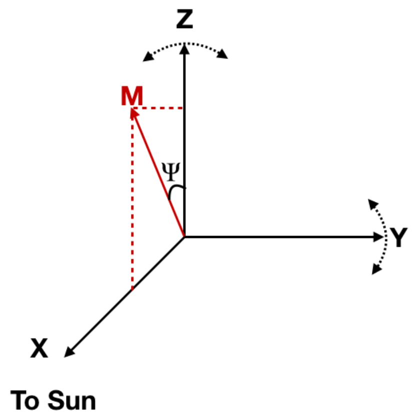

FIGURE 1.6: The GSM coordinate system. M is the dipole axis, and Ψ is the dipole tilt angle, which depends on time and season [see Fig. 1 of *Cnossen et al.* (2012)]. The 'rocking' of the Y-Z GSM axes as the Earth rotates is also indicated by the dashed curved arrows. Adapted from Fig. 1 of *Hones Jr et al.* (1986).

Figure 1.6. Both systems are therefore based on the Earth-Sun line, with the difference between the two frames simply being a rotation about the X-axis. In the instance that the projection of the dipole is perpendicular to the ecliptic plane, the GSE and GSM systems would thus be equal. The GSM coordinate system is particularly useful to use when working with magnetospheric spacecraft, as it is more useful to know their position and measurements with respect to the Earth's magnetic frame.

The above coordinate systems are often useful when describing phenomena in near-Earth space. However, to describe ground or atmospheric-based observations we can use further coordinate systems:

- *Geographic* (GEO) - Z is parallel to the Earth's rotation axis, the X-axis points towards the intersection of the equator and the Greenwich Meridian and the Y-axis makes up the right hand set.
- *Geomagnetic* (MAG) - Z is aligned with the magnetic dipole axis, and the Y-axis is perpendicular to the plane containing the dipole axis and the rotation axis (Z-GEO) of the Earth with the X-axis making up the right-hand set.

These coordinate systems are typically described by convention of *latitude* (θ) and *longitude* (ψ) following a spherical coordinate transformation $(x, y, z) \rightarrow (r, \theta, \psi)$, ranging from

($-90° < \theta < 90°$) and ($0° < \psi < 360°$) respectively [*Laundal and Richmond* (2017)]. In the case of MAG coordinates, 90° magnetic latitude (MLAT) would be the northern magnetic pole. Magnetic longitude (MLON) is often expressed in terms of magnetic local time (MLT), defined in hours where 1 hour = 15° MLON, ranging from 0 to 24 hours. MLT is defined such that 12 MLT is known as 'noon', and is always sunward (dayside) facing, whereas 00 MLT is known as 'midnight', and is anti-sunward (nightside) facing.

Any coordinate transforms required as part of the research presented in this thesis have been done using the IDL Geopack DLM software provided by Haje Korth [`http://ampere.jhuapl.edu/code/idl_geopack.html`].

1.6 Formation of the Earth's Magnetosphere

The approximation that the Earth's magnetic field is dipolar is only accurate at very close radial distances; the Earth's magnetic field is actually distorted, due to the presence of the solar wind and the IMF. When the solar wind (carrying the IMF) senses the 'obstacle' of the Earth's magnetic field (which contains its own frozen-in plasma regimes), due to it moving at supersonic speeds and encountering a much more stationary medium, a bow shock is produced, slowing and heating the solar wind [e.g. *Russell* (1972); *Ganushkina et al.* (2018)], in a region known as the *magnetosheath*. The solar wind resultantly cannot actually penetrate the Earth's magnetic field (as a consequence of the frozen-in theorem), so flows around it, and a cavity is formed known as the Earth's *magnetosphere* [*Gold* (1959)], which contains the Earth's magnetic field. This idea was first argued by *Chapman and Ferraro* (1931).

A standoff of pressure balances between the Earth's magnetic field and the solar wind dynamic pressure occurs, at a boundary known as the *magnetopause* ($\sim$10 R_E). Along the magnetopause, *Chapman-Ferraro* currents flow [*Chapman and Ferraro* (1931)] (see Fig. 1.8b in the following section). Their generation can be understood by considering the trajectory of ions and electrons in the solar wind. As these encounter the Earth's magnetic field (much stronger than the IMF), the action of the Lorentz force means they undergo gyrations in opposite directions and are forced to return to the magnetosheath after only half a gyration [*Ganushkina et al.* (2018)]. A flux of these ions and electrons therefore results in a current flowing from dawn to dusk at equatorial latitudes, and from dusk to dawn at higher latitudes, with the change in direction resulting from the change in direction of the field. The thickness of the magnetopause current sheet is resultantly of the order of a few ion gyroradii - between 400 and 1000 km [e.g. *Sonnerup and Ledley* (1979); *Berchem and Russell* (1982)].

Whilst the dayside magnetic field is compressed, the nightside magnetic field is free from intense solar wind pressures and expands away from the Earth as a long magnetic tail, known as a *magnetotail* [see e.g. *Dungey* (1965); *Ness* (1965)]. The magnetic field lines which make up this magnetotail are generally 'open', meaning they are only connected to the Earth at one end. Conversely, field lines which converge on the planetary surface at both ends are 'closed' (see Fig. 1.8a in the following section). The formation of 'open' magnetotail field lines is a result of the process of *magnetic reconnection*, which drives a large-scale circulation of magnetic flux known as the *Dungey Cycle*, and we discuss this in much greater detail in Sections 1.8 and 2.1. Due to the orbital motion of the Earth around the Sun, the magnetotail is typically deflected from the Earth-Sun line by an angle of around $\sim 4°$ about the Z_{GSM} axis [e.g. *Hones Jr et al.* (1986)]. To account for this, an 'aberrated' GSM (AGSM) coordinate system has been occasionally utilised in studies of the magnetotail [e.g. *Kiehas et al.* (2018)]. *Hones Jr et al.* (1986) suggested that at $\sim$220 R_E downtail, a change in the solar wind direction of $10°$ could deflect the tail by up to 35-40 R_E. However, as the work presented in this thesis is concentrated on observations only up to 31 R_E downtail, the aberration effect will not be considered in this research.

In Figure 1.7, we present a schematic illustrating the Earth's magnetosphere, labelled with some of the key features discussed so far. Any labels not addressed thus far may be disregarded for now as these will be introduced in the coming sections.

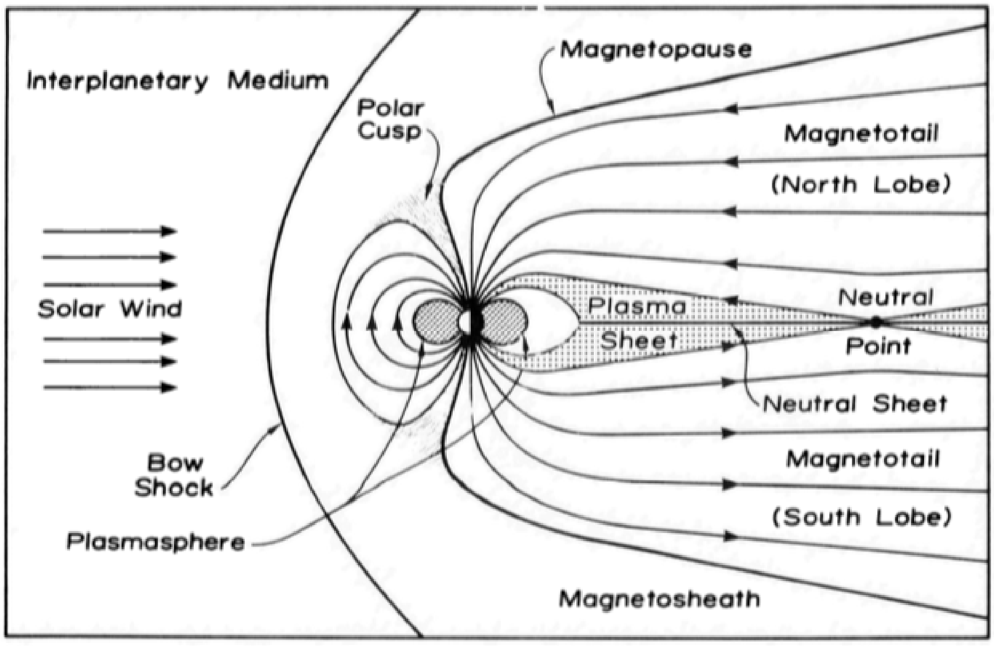

FIGURE 1.7: An illustration of the Earth's magnetosphere taken as a 'slice' in the noon-night meridian, labelled with all the key features [*Russell* (1972)].

1.6.1 Magnetospheric Current Systems

Owing to Ampère's Law (eq. 1.21), anywhere that the Earth's magnetic field is not approximately dipolar, some external current must exist which is producing some perturbation to the internally generated dipolar field [*Stern* (1994); *Milan et al.* (2017)]. As a consequence of the solar wind-magnetosphere interaction (discussed further in Section 2.1), many of the charged particles within the Earth's magnetosphere are of solar wind origin, and time-dependent dynamics result in these particles creating and contributing to the formation of many different current systems. The main current systems flowing within the Earth's magnetosphere are shown in Figure 1.8.

As briefly discussed in Section 1.6, on the nightside of the Earth, the magnetic field is distorted into a long 'magnetotail' (see Fig. 1.7). At the centre of this magnetotail, bound by 'closed' field lines is a hot *plasma sheet*, consisting of trapped high energy ($\sim$1 keV), hot (10^7 K), low density (0.3 cm^{-3}), $\beta \geq 0.1$ plasma [e.g. *Baumjohann et al.* (1989)], most of which originates from the solar wind [e.g. *Hill* (1974); *Russell et al.* (2016)]. In the middle of the $\sim$5 R_E thick plasma sheet [*Bame et al.* (1967)] is a *cross-tail current sheet*, or

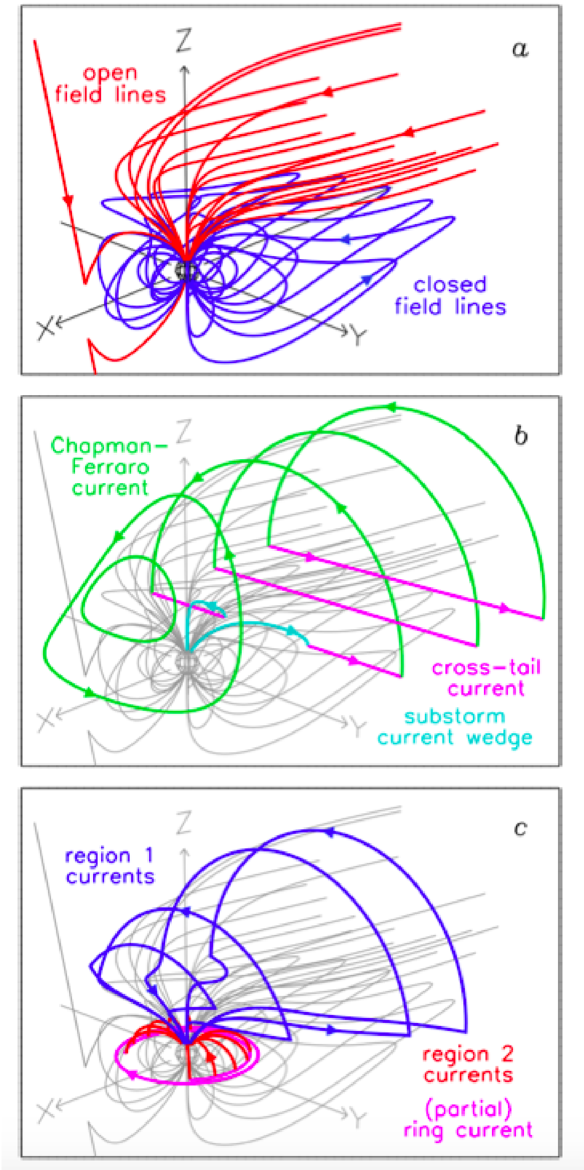

FIGURE 1.8: An illustration of a) ‘open’ and ‘closed’ magnetospheric field lines, and b, c) the Earth’s main current systems (discussed in-text). The direction of each of the current systems is indicated by the arrows [*Milan et al.* (2017)].

neutral sheet. This current flows from dawn to dusk (i.e. out of the page in Fig. 1.7) and, by definition, separates the oppositely directed earthward ($B_x > 0$) and tailward ($B_x < 0$) facing tail field lines [*Ness* (1965); *Russell and Brody* (1967)]. Due to the change in direction of the field across the sheet and the plasma sheet pressure gradients [*Artemyev et al.* (2021)], ions (electrons) close to the sheet will overall drift diamagnetically towards dusk (dawn) [*Speiser* (1965)] in a serpentine motion [see Fig. 2c of *Kistler et al.* (2005)], giving rise to the current. This current sheet also satisfies Ampère's Law; the sudden earthward to tailward reversal of the magnetic field implies a large curl in the magnetic field (spatial gradients), requiring a current to exist. This current closes along the tail magnetopause (Chapman-Ferraro) current as illustrated in Fig. 1.8b.

In the closed inner magnetosphere, a westward (clockwise) flowing *ring current* flows [*Chapman and Ferraro* (1941)] which forms as a result of the gradient and curvature drifts of ions and electrons trapped within the near-Earth region [see Chapter 2 of *Baumjohann and Treumann* (1997)]. It generally flows at distances between 2 and 9 R_E and inflates the inner magnetosphere away from the generally dipolar configuration [*Milan et al.* (2017)].

As a consequence of the solar wind-magnetosphere interaction, *field-aligned currents* (FACs), also known as *Birkeland currents* [*Birkeland* (1908); *Stern* (1983)] flow, which enable both the Chapman-Ferraro (magnetopause) current and an enhanced part of the ring current, known as the *partial ring current*, to close in the ionised layer of the Earth's atmosphere known as the *ionosphere.* This occurs through Region 1 and Region 2 currents (Fig. 1.8c), respectively [*Iijima and Potemra* (1976)], and is discussed further in Section 1.7.1.

Finally, the *substorm current wedge* is a current system which acts to divert the cross-tail current into the ionosphere [*McPherron et al.* (1973)] as a consequence of dynamic near-Earth processes, which we discuss in Section 2.2. This current wedge flows into the ionosphere in the post-midnight ($-Y_{GSM}$) sector and out of the ionosphere in the pre-midnight ($+Y_{GSM}$) sector and closes along a current known as the westward substorm electrojet [*Milan et al.* (2017)].

1.7 Formation of the Earth's Ionosphere

The *ionosphere* is the lower boundary (base) of the magnetosphere and marks the transition region of the fully, upper-ionised atmosphere to the neutral atmosphere. The plasma in the ionosphere is coupled with the neutral *thermosphere*, and in contrast to the outer magnetosphere and solar wind, is generally a 'collisional' regime, specifically referring to plasma collisions with neutrals [e.g. *Song et al.* (2001); *Ridley et al.* (2006)].

The ionosphere is produced through two main mechanisms. The first is ionisation from solar radiation, known as *photoionisation.* This occurs when photons strike neutral atmospheric gas molecules, resulting in the ejection of an electron which turns the neutral atom into an ion. The second mechanism is ionisation through *energetic particle collisions.* For example, precipitating electrons accelerated along magnetic field lines from the magnetosphere towards the ionosphere can collide with neutrals. This results in a reduction in energy of the electron and ionisation of the neutral atom, causing an increase in the ion density. This specific process is known as *electron impact.* Excitations of ions or neutrals may also produce auroral emissions when they relax [*Kivelson and Russell* (1995)].

The ionosphere can be split into 3 distinct layers: 'D', 'E', and 'F'. The D region has a peak free electron density of 10^8 m^{-3} at 90 km. It is dominated by neutral gas dynamics, and therefore isn't really considered as a plasma. Above the D region lie the E and F regions. The E region has a peak free electron density of around 10^{11} m^{-3} at 110 km, and in this region collisions are highly important and significant currents flow, which we examine in Section 1.7.1. The F region, however, has a peak free electron density of around 10^{12} m^{-3} at an altitude of around 300 km, and is generally collisionless [*Baumjohann and Treumann* (1997)].

1.7.1 Ionospheric Current Systems

Owing to the abundance of charged particles in the ionosphere, just like in the magnetosphere, a number of currents flow. Winds in the upper atmosphere can result in the movement of ionospheric medium [*Hargreaves* (1979)]. In the F-region ionosphere, collisions between charged particles and atmospheric neutrals are very rare, and so the plasma can be approximated as $\mathbf{E} \times \mathbf{B}$ drifting. In the E-region ionosphere, ions are occasionally brought to rest (and exchange momentum) through collisions with neutrals [*Ridley et al.* (2004)], giving the ions an additional drift in the direction of an ionospheric electric field $\mathbf{E}$, whereas electrons continue to $\mathbf{E} \times \mathbf{B}$ drift at all ionospheric heights [*Cowley* (2000)]. From equation 1.17, even for a quasi-neutral plasma this differential drift motion will induce a current - there are, in fact, two field-perpendicular currents created by the diverted ion motion. There is, firstly, the *Hall* ($\mathbf{J}_h$) current, and secondly, the *Pedersen* ($\mathbf{J}_p$) current, both of which are carried by the electrons [*Ridley et al.* (2004)]. The Hall current has components in the $-(\mathbf{E} \times \mathbf{B})$ direction (opposite to the plasma flow), and the Pedersen current flows in the same direction as the electric field, $+\mathbf{E}$. At auroral latitudes, the Hall current flows as the eastward and westward auroral electrojets. At these high latitudes, shears in plasma convection between 'open' and 'closed' magnetic field lines result in Region 1 FACs flowing to connect the Pedersen current to the magnetopause current, and Region 2 currents flow out of the ionosphere at lower latitudes at the equatorward edge of 'return-flow convection', which connect the Pedersen current to the partial ring current [e.g. *Anderson and Vondrak* (1975); *Stern* (1983); *Milan et al.* (2017)], and ensure current continuity ($\nabla \cdot \mathbf{J} = 0$). This is illustrated schematically in Fig. 1.9.

As a consequence of Ohm's Law, the overall strength of the ionospheric currents depend on the ionospheric conductance (highly dependent on the number density of electrons), as well as the electric and magnetic fields [*Cowley* (2000)]. One may envisage the total ionospheric electric field $\mathbf{E}$ as being produced through a combination of currents and convection [e.g. *Stern* (1977); *Hargreaves* (1979)]. The nature of this convection is driven through magnetosphere-ionosphere (M-I) coupling [e.g. *Friis-Christensen et al.* (1985); *Watanbe et al.* (1998)], which we discuss in Chapter 2.

1.8 Magnetic Reconnection at Earth

The magnetopause boundary is a good example of where the frozen-in theorem begins to break down and diffusion becomes important ($R_m \approx 1$), due to the fact that there are sharp gradients in the magnetic field on a spatial length scale comparable to the ion gyroradii, which effectively defines the magnetopause thickness. Here, diffusion of magnetic field lines through the current sheet enables *magnetic reconnection* to occur, whereby oppositely directed magnetic field lines which were previously separate can merge together to join as one, resulting in a reconfiguration of the magnetic field. The energy stored in the magnetic field is converted to plasma thermal and kinetic energy, and plasma is

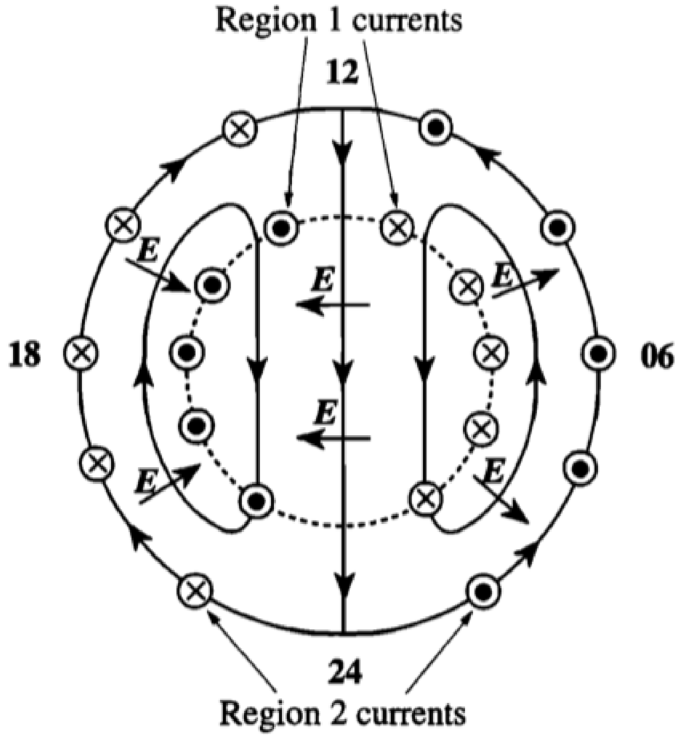

FIGURE 1.9: A schematic of the high-latitude ionospheric 'twin-cell' convective plasma flow (discussed in Chapter 2) and associated currents. The plasma flow streamlines are shown by the solid arrows; plasma flows anti-sunward across the polar cap at high latitudes and then sunward via dusk or dawn at lower latitudes. The plasma flow shear boundary is marked by the dashed line. Pedersen currents flow in the direction of the electric field **E**, and the Hall currents flow as the eastward and westward electrojet currents opposite to the direction of the plasma flow. FACs flow where the Pedersen currents (and **E**) diverge; region 1 FACs flow at the plasma flow shear between open and closed flux (between sunward and anti-sunward moving plasma), and region 2 currents flow at the equatorward edge of the return convection where the electric field disappears, known as the Heppner-Maynard boundary [see *Heppner and Maynard* (1987)]. Magnetic local times are labelled. Schematic taken from [*Cowley* (2000)].

accelerated away from the reconnection site by the $\mathbf{J} \times \mathbf{B}$ force. The previously separate magnetospheric and solar wind plasma regimes are permitted to mix. The concept of this process was first proposed by Sweet and Parker [*Parker* (1957)], and is illustrated in a 2D case for a reconnection 'X-line' in Figure 1.10.

Magnetic reconnection is the main solar wind-magnetosphere coupling mechanism at Earth [e.g. *Cowley* (1982); *Frey et al.* (2003); *Chisham et al.* (2008a)]. Given that the potential difference between two points a and b can be expressed as the integral of the electric field

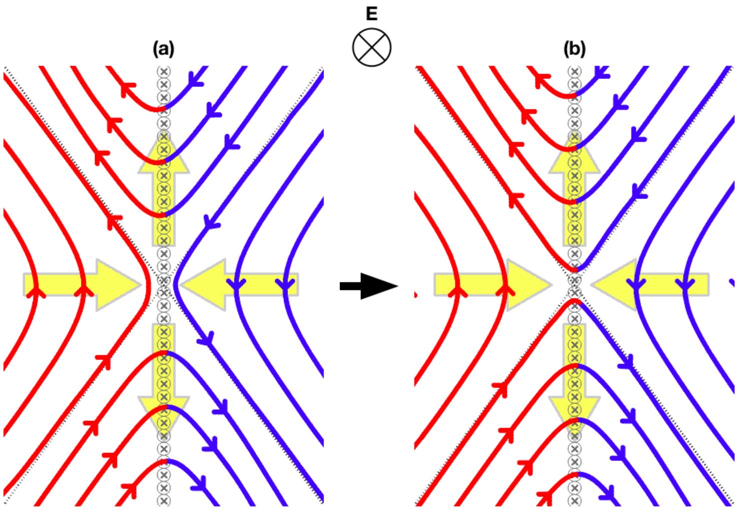

FIGURE 1.10: An illustration of magnetic reconnection. Red and blue magnetic field lines are initially separate and oppositely directed, until they reconnect with one-another at the current sheet (directed into the page), shown in (a)-(b). The yellow arrows indicate the motion of plasma towards (left-right) and away (up-down) from the diffusion region, prior to and following reconnection, respectively. The direction of the electric field (into the page) is also shown. [Public domain image from *https://commons.wikimedia.org/wiki/File:Reconnection.gif*].

along some path $\mathbf{l}$ between those points:

$$\Delta\Phi = -\int_a^b \mathbf{E} \cdot d\mathbf{l} \tag{1.31}$$

then using $\mathbf{E} = -\mathbf{v} \times \mathbf{B}$, a 'reconnection voltage', Φ_{rec}, describing the 'efficiency' of magnetic reconnection may be defined:

$$\Phi_{rec} = v_{sw} B_{\perp} L sin^2\left(\frac{\theta_c}{2}\right) \tag{1.32}$$

where v_{sw} is the solar wind bulk flow velocity (assumed to be mostly in the negative X-direction, i.e. earthward), $B_{\perp} = \sqrt{B_y^2 + B_z^2}$ is the magnitude of the IMF perpendicular to the solar wind flow in the Y_{GSM}-Z_{GSM} plane, L is some effective length which reconnection occurs over, and θ_c is known as the *clock angle* [*Kan and Lee* (1979); *Fedder et al.* (1991)]. The clock angle is defined as:

$$\theta_c = tan^{-1}\left(\frac{B_y}{B_z}\right) \tag{1.33}$$

and is always measured clockwise beginning at the Z_{GSM} axis (northward), and ranges from $-180° < \theta_c < 180°$, with $\theta_c < 0°$ for $B_y < 0$.

Typical values for Φ_{rec} at the Earth's magnetopause are of the order of a few tens of kV [e.g. *Milan et al.* (2007, 2012); *Newell et al.* (2007)]. From *Faraday's Law of Magnetic Induction*, Φ_{rec} can be written as the rate of change of magnetic flux (F_B) at the dayside magnetopause:

$$\Phi_{rec} = \frac{dF_B}{dt} \tag{1.34}$$

Therefore, eq. 1.32 governs the rate of transport of magnetic flux, or more specifically, the rate at which flux is 'opened'. We discuss the consequences of the opening of magnetic flux at the Earth's magnetopause in Chapter 2.

Magnetic reconnection is also a generator of *Alfvén waves* [e.g. *Chaston et al.* (2005)]. These are a type of transient MHD wave manifested by travelling oscillations of ions and the magnetic field, which propagate along the magnetic field lines [e.g. *Keiling* (2009)]. The waves travel at an *Alfvén speed*, v_A, defined as:

$$v_A = \frac{|\mathbf{B}|}{\sqrt{\mu_0 \rho_m}} \tag{1.35}$$

This governs the maximum speed at which plasma may be accelerated away from the reconnection site as a consequence of the $\mathbf{J} \times \mathbf{B}$ force, and is essentially the speed at which information regarding the diffusion region may be transferred to the outflowing plasma [*Eriksson* (2001); *Keiling* (2009)]. As a result, convective plasma flows, such as the ones explored in this thesis, have a speed which is fundamentally limited by the Alfvén speed.

Chapter 2

Convection in the Magnetosphere-Ionosphere System

2.1 The Dungey Cycle

The process of magnetic reconnection at Earth drives a large-scale circulation of magnetic flux known as the Dungey Cycle, after *Dungey* (1961). This is most easily envisaged, and most efficient, when the IMF is purely southward ($B_z < 0$, $\theta \approx 180°$) [e.g. *Fairfield* (1967)], and is illustrated in Figure 2.1. In this scenario, reconnection between the IMF and dayside terrestrial magnetic field usually occurs at the low-latitude dayside magnetopause as this is where the field lines are oppositely directed (1) - (1'). This reconnection produces 'open' field lines, where one end is frozen into the solar wind-magnetosheath flow and the other end attached to the Earth. The solar wind ends are 'convected' downstream over the Earth in both hemispheres (2 - 3 - 4; 2' - 3' - 4'), forming a long *magnetotail* (approximately 1000 R_E in length) [*Dungey* (1965)], with an associated northern and southern magnetotail lobe (5 - 5'). Reconnection occurs again on the nightside, as the addition of open field lines to the lobes forces the oppositely directed lobe tail field lines to diffuse and reconnect at the centre of the magnetotail at the neutral sheet, closing the field lines (6 - 6'). The newly closed field lines which are earthward of the reconnection site are accelerated earthward by the release of magnetic tension (7). As they are convected by earthward-moving plasma 'flows', they dipolarise (8) and return to the dayside via dusk or dawn (9). The cycle can then repeat; continually driven by reconnection and the effect of magnetic tension and pressure gradients on the plasma [see Fig. 1 of *Artemyev et al.* (2021)]. As a consequence of the Dungey Cycle, a majority of the plasma within the Earth's magnetosphere is of solar wind origin [e.g. *Borovsky et al.* (1997)].

During the Dungey Cycle, in the high-latitude ionosphere, 'twin-cell' plasma convection cells develop [e.g. *Lockwood et al.* (1990); *Cowley and Lockwood* (1992)]. The magnetic field line footpoints are convected anti-sunward across the centre of the polar cap and returned to the dayside at lower latitudes via dusk and dawn. This is also shown and labelled accordingly in Fig. 2.1 in terms of a snippet of the dusk-cell ionospheric projection of the magnetic field lines. The polar cap forms a highly dynamic and variable region bound by the open-closed field line boundary (OCB, see the dashed line in Fig. 1.9). Whether a given magnetic field line returns via dusk or dawn depends on which cell the footpoint is frozen-in to. Regions of open field lines map to high ionospheric latitudes, poleward of the OCB, with regions of closed field lines mapping to lower latitudes, equatorward of the OCB. The ionospheric convection is thus indicative of the large-scale nature of the magnetospheric convection (i.e. geomagnetic field-line mapping from the ionosphere to the magnetosphere encompasses both open and closed flux across several Earth radii). It is perhaps not so intuitive as to why the Dungey Cycle process would set up a pattern of ionospheric convection, however. This is explored further, in Section 2.1.1.

2.1.1 Magnetosphere-Ionosphere (M-I) Coupling

The Dungey Cycle was once envisaged to be a *steady state* process, where the rates of dayside and nightside reconnection were equivalent [*Milan et al.* (2007)]. Under these conditions, the amount of open magnetic flux within the polar cap would be roughly constant and we have what is known as steady magnetospheric convection (SMC) [e.g. *Sergeev et al.* (1996a); *Milan et al.* (2003); *Kissinger et al.* (2012)], so the total change in open magnetic flux would be zero:

$$\frac{dF_B}{dt} = \Phi_D - \Phi_N = 0 \tag{2.1}$$

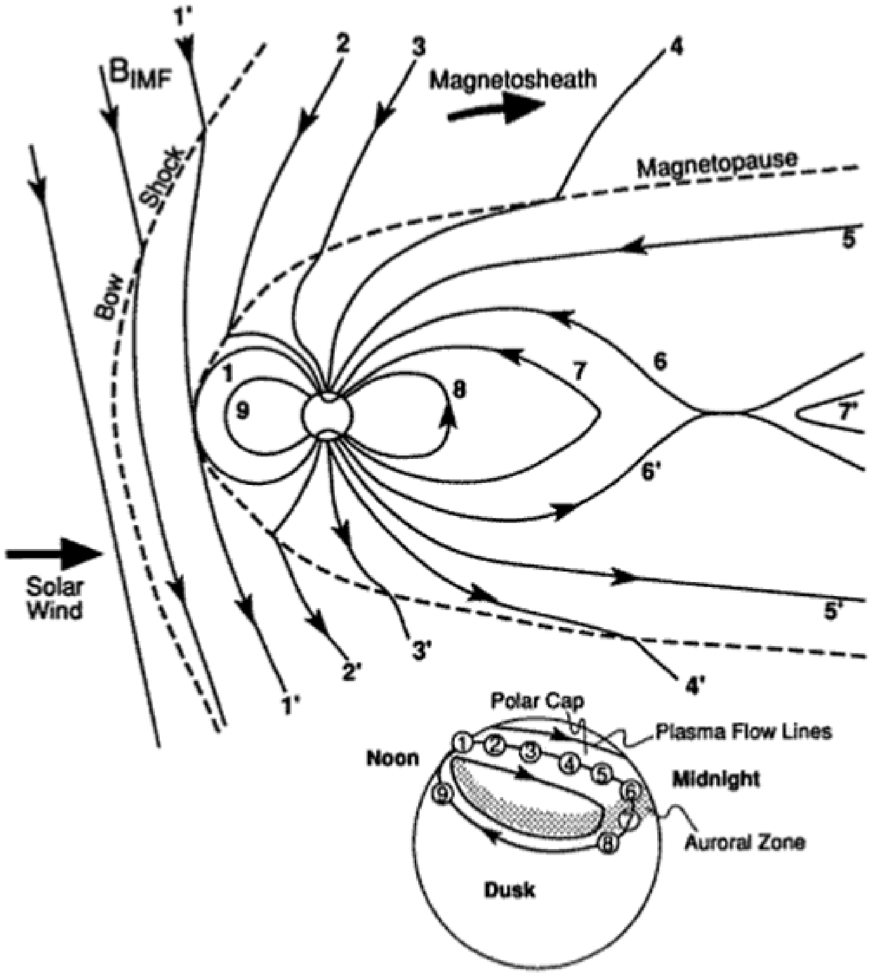

FIGURE 2.1: An illustration of the Dungey Cycle, including a snippet of the dusk-side polar cap ionospheric projection of the field lines (discussed in-text) [*Russell et al.* (2016)].

where $\Phi_{D(N)}$ is the dayside (nightside) reconnection voltage. In this time-independent 'steady state' scenario [see '**E, J**' paradigm in *Milan et al.* (2017)], it was assumed that the curl-free convection electric field associated with the anti-sunward solar wind flow could be 'mapped' along the approximately vertical open magnetic field lines into the ionosphere where it drives an $\mathbf{E} \times \mathbf{B}$ flow [e.g. *Stern* (1977); *Lockwood* (1991); *Parker* (1996)], such that:

$$\mathbf{E} = -\nabla\Phi \tag{2.2}$$

where Φ is the distribution of electrostatic potential, and hence:

$$\mathbf{v}_E = \frac{-\nabla\Phi \times \mathbf{B}}{|\mathbf{B}|^2} \tag{2.3}$$

which indicates that ionospheric convective plasma flow is perpendicular to $\mathbf{B}$, but also perpendicular to the gradient of the electrostatic potential. This means that equipotentials of Φ are not only the magnetic field lines, but also streamlines of the plasma flow. The ionospheric electric field is directed from dawn to dusk (in the same sense as the solar wind electric field), illustrated in Fig. 1.9 [see also, Fig. 8 of *Cowley* (2000)]. The dawn cell therefore has a positive electric potential, with the dusk cell having a negative potential - the difference between these is known as the *cross-polar cap potential*, Φ_{PC}, and in the steady state we have $\Phi_D \approx \Phi_N \approx \Phi_{PC}$ [*Milan et al.* (2007)]. Of course, it is this direction of dawn to dusk that the Pedersen current flows across the polar cap [e.g. *Cowley* (2000)]. FACs resultantly flow at the OCB due to the shear plasma flow in the convection pattern and thus electric field (and current) divergence, imposing a requirement on current continuity.

In reality, the two reconnection rates are not identical; the dayside reconnection rate is modulated heavily by the IMF strength, orientation, and the solar wind conditions (eq. 1.32). Conditions in the tail will then depend on e.g. the amount of open flux being loaded, and the time taken for the open field lines to convect into (and reconnect in) the tail, which *Milan et al.* (2007) suggest takes 70 minutes on average. If dayside reconnection exceeds nightside reconnection ($\Phi_D > \Phi_N$), the area of the polar cap (i.e. the OCB) containing open field lines expands to accomodate more open flux. Similarly, nightside reconnection exceeding dayside reconnection ($\Phi_N > \Phi_D$) would result in a contraction of the boundary. This idea of an expanding and contracting polar cap is known as the *Expanding-Contracting Polar Cap* (ECPC Paradigm), first considered by *Siscoe and Huang* (1985) [see Fig. 3 in *Cowley and Lockwood* (1992)]. Such imbalances in dayside and nightside reconnection rates can lead to the phenomenon of a *substorm* [e.g. *Akasofu* (1964); *McPherron* (1979); *Milan et al.* (2003); *Angelopoulos et al.* (2008)], with three phases: *growth* ($\Phi_D >> \Phi_N$), *expansion* ($\Phi_N >> \Phi_D$) and *recovery* ($\Phi_D \approx \Phi_N$). Notably, the expansion phase, where persistant, bursty-like tail reconnection occurs [e.g. *Baumjohann* (2002); *McPherron et al.* (2008)], is a driver of high speed convective flows which play a major role in the transport of mass, energy, and magnetic flux in the magnetotail [e.g. *Sergeev et al.* (1996b)], which we discuss the properties of in Section 2.2. Auroral emissions are often enhanced as particles are accelerated along field lines and current systems disrupted, including the formation of a substorm current wedge and the associated ionospheric substorm electrojet current [e.g. *McPherron et al.* (1973); *Fukunishi* (1975)].

In this non-steady state scenario, dynamical effects, such as variable reconnection rates, acceleration and deceleration of plasma, collisions and induced electric and parallel electric fields due to variability in the currents and magnetic field mean that electrostatics (time-independence) won't always be satisfied ($\frac{\partial}{\partial t} \neq 0$), and thus field lines are not always equipotentials [see e.g. *Hesse et al.* (1997)]. Inherently, one might rightly ask how ionospheric convection still proceeds, if we can not simply 'map' the solar wind electric field to drive the coincident plasma flow in the ionosphere. The answer to this conundrum requires closer consideration about the implications of ionospheric collisions in terms of the frozen-in theorem.

Let us consider the simple case that an open field line is being convected downstream in the solar wind flow. Any coincident plasma flow in the E-region ionosphere will undergo collisions with neutrals, resulting in a 'drag' effect on the plasma [*Cowley* (2000)]. If we assume that the plasma and magnetic field lines are a frozen-in regime, the ionospheric end of the field line will begin to 'lag' behind the solar wind end. The field line is therefore perturbed by an amount $\delta\mathbf{B}$ due to the stretching of the field in the upstream direction, with 'kinks' at the magnetopause and ionosphere. These kinks are associated with the magnetic field perturbations caused by the respective field-perpendicular currents in the ionosphere (Pedersen currents) and at the magnetopause (Chapman-Ferraro currents) [*Strangeway et al.* (2000); *Milan et al.* (2017)]. These currents thus provide a $\mathbf{J} \times \mathbf{B}$ force; the $\mathbf{J} \times \mathbf{B}$ force acting on the plasma associated with the solar wind end acts to decelerate the plasma, whereas the $\mathbf{J} \times \mathbf{B}$ force in the ionosphere acts to accelerate the plasma to counter the drag, in order to 'straighten' the field line out and keep the ionospheric end of

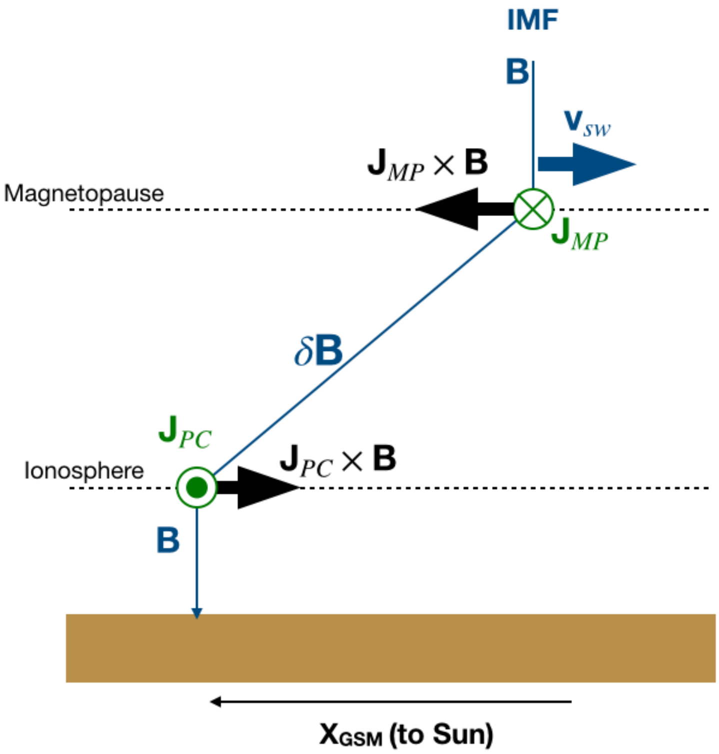

FIGURE 2.2: An illustration of the high latitude M-I coupling over the polar cap, far from the reconnection site, taken as a vertical 'slab' looking dawnward. The open magnetic field line (blue) is perturbed by an amount $\delta\mathbf{B}$ in the upstream direction, with kinks at the magnetopause and ionosphere. The kinks are associated with magnetopause current ($\mathbf{J}_{MP}$) and Pedersen current ($\mathbf{J}_{PC}$), shown in green. The direction of the respective $\mathbf{J} \times \mathbf{B}$ forces are shown by the black arrows.

the field line moving with the solar wind end. These dynamics are encapsulated schematically in Fig. 2.2, which illustrates the high-latitude M-I coupling over the polar cap, far from the reconnection site.

In a more physical sense, it is simply the magnetic tension and pressure forces (eq. 1.22) accelerating (or decelerating) plasma in a direction which will remove the kinks from the field line, transferring momentum between the solar wind, magnetospheric and ionospheric plasma along field lines, and this is also true in the case of return-flow convection. Thus, any deformation of the frozen-in magnetic field in the magnetosphere or ionosphere will result in magnetic tension and pressure forces acting on the plasma in order to balance the mechanical stress acting on the field lines. This fundamentally drives the coincident M-I convection.

2.2 Convective Magnetotail Fast Flows

Convective magnetotail plasma flows within Earth's plasma sheet have been studied extensively for many years [e.g. *Angelopoulos et al.* (1992); *Chen and Wolf* (1993); *Sergeev et al.* (1996b); *Petrukovich et al.* (2001); *Raj et al.* (2002); *Cao et al.* (2006); *McPherron et al.* (2011); *Juusola et al.* (2011); *Kissinger et al.* (2012); *Frühauff and Glassmeier* (2016); *Kiehas et al.* (2018)] using a suite of magnetospheric spacecraft (Section 3.1.2). Most commonly, the ion population, as opposed to the electron population has been studied [see e.g. *Kletzing et al.* (2003) and references therein], owing to the fact that their greater mass means they contribute more to momentum transport. In this section, we outline and review numerous known properties and characteristics of these flows.

2.2.1 Generation and Termination of Fast Flow

Generally, fast flow in the plasma sheet is regarded to be a manifestation of reconnection in the magnetotail [*Sergeev et al.* (1992); *Chen and Wolf* (1993)] - a key process in driving the Dungey Cycle - and the flows are thus often bursty in nature [*Baumjohann et al.* (1990)]. Following magnetotail reconnection, plasma earthward of the reconnection site (usually where $B_{z[GSM]} > 0$ [*Nishida and Russell* (1978)]), is accelerated earthward by magnetic tension [*Li et al.* (2011); *Karlsson et al.* (2015)]. As magnetic flux is transported earthward, dipolarisation occurs, turning the field from being strongly X-oriented, parallel to the current sheet, to Z-oriented, perpendicular to the current sheet and thus more dipole-like [e.g. *Hesse and Birn* (1991); *Ohtani et al.* (2004); *Snekvik et al.* (2007); *Miyashita et al.* (2009); *Schmid et al.* (2011)]. As a fast plasma flow approaches the Earth, at between 10 and 15 R_E it is decelerated, undergoing 'flow braking' and diverted duskward or dawnward (azimuthally) by plasma pressure gradients as well as the magnetic pressure gradient associated with encountering the more dipolar field of the Earth [*Shiokawa et al.* (1997); *Kissinger et al.* (2012)]. During a substorm expansion, continual fast flow braking may lead to a flux 'pile-up'. Consequently, the magnetic field twisting due to azimuthal flow diversion and variable pressure gradients can disrupt the cross-tail current, resulting in the substorm current wedge forming (Section 1.6.1) [*McPherron et al.* (1973); *Birn et al.* (1999); *Baumjohann* (2002)].

2.2.2 What is Considered to be a 'Fast' Flow?

Collectively, studies have attributed a flow as being 'fast' if its flow speed reaches of the order of a couple-hundred (> 200 km s^{-1}) up to over 1000 km s^{-1} [e.g. *Baumjohann et al.* (1990); *Angelopoulos et al.* (1992); *Ohtani et al.* (2004); *Pitkänen et al.* (2013); *Kiehas et al.* (2018)], well above what is considered to be the average, dominant 'background' plasma sheet flow speed of < 100 km s^{-1} [e.g. *Juusola et al.* (2011)].

2.2.3 Where do the Flows Occur?

Studies such as *Baumjohann et al.* (1990) have shown that the largest fast flow occurrence rates are close to midnight ($\mathrm{Y}_{GSM} = 0$) with this dropping significantly towards the dusk-dawn flanks of the plasma sheet. *Nagai et al.* (1998) discovered that during substorm expansions, fast earthward flow was only observed within $X_{GSM} \approx -30$ R$_E$, with tailward flows mostly observed beyond $X_{GSM} \approx -20$ R$_E$. Studies such as *Schödel et al.* (2001) and *Kiehas et al.* (2018) have shown that earthward fast flows can still occur at up to 50-60 R$_E$ downtail, suggesting that distant reconnection in the tail also generates fast flows.

2.2.4 What are the Temporal and Spatial Extents of the Flow?

Studies such as *Baumjohann et al.* (1990) have suggested that the absolute fastest of plasma sheet flows may only last for around 1 minute. However, studies such as *Angelopoulos et al.* (1992, 1994) and *Sergeev et al.* (1996b) have suggested that periods of continual, enhanced bursty flow may last for a few minutes up to $\sim$10 minutes (discussed below), with these periods of enhanced bursty flows consisting of minute-scale flow 'burst' enhancements. A more recent Superposed Epoch Analysis by *Frühauff and Glassmeier* (2016) indeed suggested that fast flows have a typical timescale of around 1-2 minutes. Spatially, it has been demonstrated that the flows have a cross-tail scale size of up to around 3 R$_E$ [*Nakamura et al.* (2004); *Frühauff and Glassmeier* (2016)]. A particularly well-defined special category of flow is the Bursty Bulk Flow (BBF), which are segments of highly convective earthward ion flow continually above 100 km s^{-1}, exceeding $v_x > 400$ km s^{-1}

at least once across some interval, usually on the timescale of a few minutes, up to ∼10-min [*Angelopoulos et al.* (1992, 1994)].

2.2.5 What is the Typical Direction of the Flows?

Juusola et al. (2011) suggested that the fastest of earthward plasma sheet flows appear almost exclusively earthward, with a minimal dusk-dawn component. It has also been suggested that earthward fast flows during periods of steady magnetospheric convection (SMC) are highly symmetric about midnight (i.e. dawnward in the post-midnight sector and duskward in the pre-midnight sector) [e.g. *Hori et al.* (2000), see Fig. 4 of *Kissinger et al.* (2012)]. Although a key characteristic of convective magnetotail flows is their earthward nature, they will invariably exhibit a dusk-dawn (azimuthal) component in their bulk flow as well [e.g. *Angelopoulos et al.* (1994); *Petrukovich et al.* (2001); *Grocott et al.* (2004c); *Walsh et al.* (2014)], which has a known dependence on the IMF B_y component [*Pitkänen et al.* (2013)]. We discuss the significance of this further in Sections 2.3.2 and 4.1.1.

2.3 IMF B_y Influence on the Earth's Magnetosphere

2.3.1 The Twisting of the Magnetotail

Owing to the nature of the Parker spiral (see Section 1.4), the IMF embedded in the solar wind will, on average, always contain a significant dusk-dawn (B_y) component. It has been widely reported by e.g. *Cowley* (1981), *Khurana et al.* (1996), *Grocott et al.* (2007) and *Pitkänen et al.* (2013) that the IMF B_y component can have a profound impact on the symmetry of the solar wind-magnetosphere coupling and associated plasma flows. When the IMF reconnects with the dayside terrestrial magnetic field, a non-zero IMF B_y component results in the site of anti-parallel dayside reconnection moving from the subsolar point toward the high-latitude flanks [e.g. *Crooker* (1979); *Park et al.* (2006); *Eriksson et al.* (2017); *Grocott* (2017); *Case et al.* (2018)]. This is illustrated in Figure 2.3.

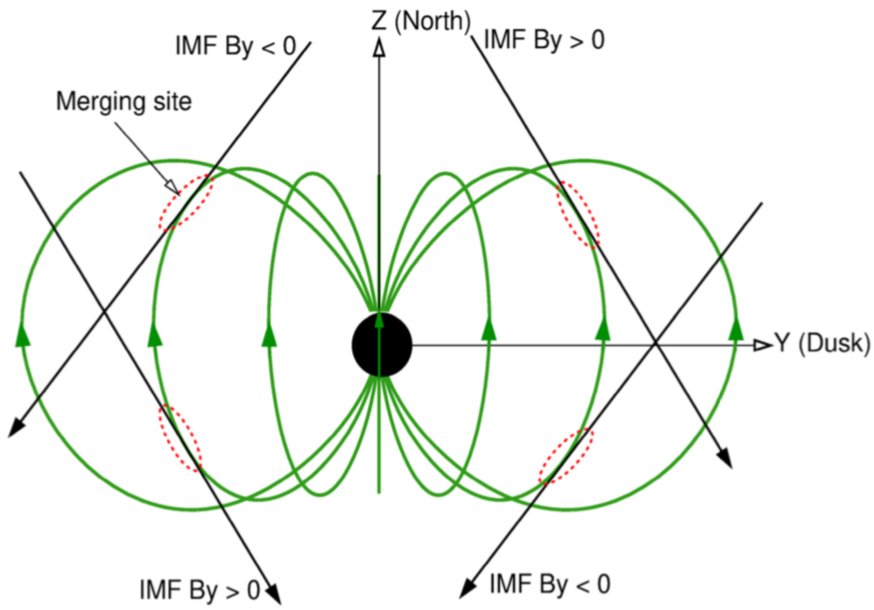

FIGURE 2.3: A diagram showing the reconnection regions (merging sites) of a non-zero IMF B_y component (black lines) with the Earth's dayside magnetic field (green lines) for both positive and negative IMF B_y, in the case of an IMF which is also southward. The Earth is shown by the solid black circle at the centre. The view is shown as though looking earthward from the Sun [*Liou and Mitchell* (2019)].

Let us consider the case where we have dayside reconnection with a positive IMF B_y component (IMF $B_y > 0$). In this situation, newly reconnected field lines experience a magnetic tension force that tends to load open flux into the lobes towards dawn in the northern hemisphere and towards dusk in the southern hemisphere [*Khurana et al.* (1996); *Grocott et al.* (2007); *Tenfjord et al.* (2018); *Ohma et al.* (2018)], creating a dusk-dawn imbalance of magnetic pressures (this dusk-dawn shift is opposite for negative IMF B_y). This is illustrated schematically in Fig. 2.4a.

The magnetic pressure imbalance created as a result of asymmetric flux loading into the lobes exerts a torque on the magnetotail, resulting in a tilting/rotation of the neutral sheet around the tail axis [*Cowley* (1981); *Tenfjord et al.* (2017)]. This ultimately propagates to the inner magnetosphere, leading to a 'twisted' magnetotail configuration, whereby a B_y component in the same sense as the IMF B_y is superimposed onto the tail field (though this is not the only 'source' of B_y in the tail - see Chapters 4 and 5), twisting the magnetotail from the north-south symmetry about the midnight meridian. The exact process which causes this to occur has been debated, but one of two mechanisms are thought to be responsible:

The first mechanism, hereafter referred to as the *Dungey Cycle mechanism*, is based on the idea presented by *Cowley* (1981) and supported by e.g. *Østgaard et al.* (2004), *Pitkänen et al.* (2016) and *Browett et al.* (2017), that newly reconnected dayside field lines retain the sense of IMF B_y which is convected into the magnetotail. Reconnection of these B_y-oriented open field lines in the tail transfers the B_y asymmetry onto newly closed field lines, which subsequently convect into the inner magnetosphere. The timeframe of the appearence of the tail B_y is thus dependent on the speed of the convection in the tail, and has been suggested to be the order of 2-4 hours [e.g. *Fear and Milan* (2012); *Browett et al.* (2017)], dependent on the solar wind speed. This mechanism therefore suggests that the Dungey Cycle is responsible for transferring the B_y component onto closed field lines.

The second mechanism, hereafter referred to as the *Tenfjord mechanism*, proposed originally by *Khurana et al.* (1996) and supported further by *Tenfjord et al.* (2015, 2017, 2018) and *Case et al.* (2018), suggests that the asymmetric magnetic pressure created in the lobes is relieved by the excitation of dusk-dawn directed convective shear flows. These are driven both in the lobes and inner magnetosphere, resulting in a twisting/rotation of the inner magnetotail field, inducing a B_y component in the same sign as the prevailing IMF B_y. A key factor in this proposed mechanism is that it acts promptly on the inner magnetosphere within 40 minutes [e.g. *Tenfjord et al.* (2015)] and *does not* require the occurrence of magnetotail reconnection, unlike the Dungey Cycle mechanism. A schematic illustrating the Tenfjord mechanism is presented in Fig. 2.4b.

A point worth considering is that regardless of which mechanism introduces the twist, the open B_y-oriented field lines with still ultimately reconnect in the tail, which therefore may act to introduce or reduce any asymmetry dependent on which mechanism is responsible. In particular, it has recently been suggested that tail reconnection during substorms may act to reduce the asymmetric state of the magnetosphere [*Reistad et al.* (2018); *Ohma et al.* (2019)].

Owing to the coupled nature of the M-I system (Section 2.1.1), the IMF B_y coupling

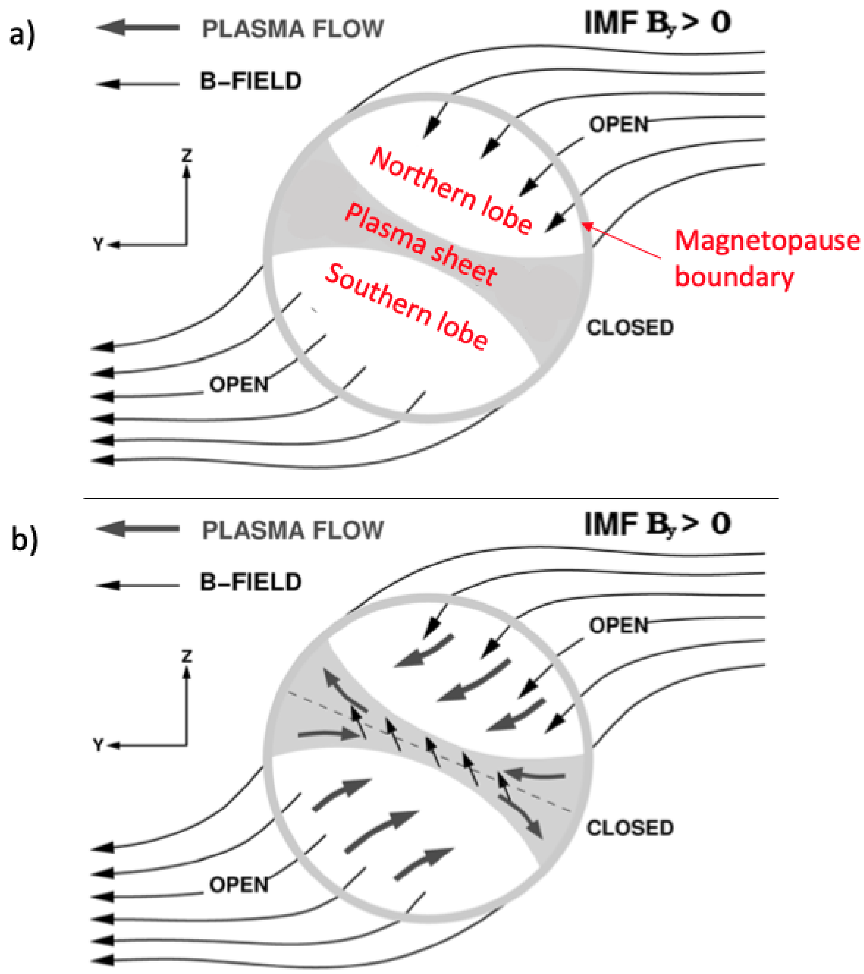

FIGURE 2.4: a) A schematic illustrating the loading of open flux in the lobes towards dawn (dusk) in the northern (southern) hemisphere as a consequence of the IMF $B_y > 0$ coupling. The view is shown from the Y_{GSM}-Z_{GSM} plane looking earthward from downtail. b) As in a), but now illustrating the pressure driven Y-directed shear convective plasma flows and induction of a B_y on closed tail magnetic field lines in the same sign as the IMF B_y. The dashed line marks the tilted neutral sheet. Adapted from *Liou and Newell* (2010).

has implications for the ionospheric convection pattern too, which readily responds to changes in the IMF within a few tens of minutes [*Grocott and Milan* (2014); *Case et al.* (2020)]. In the ionosphere, prolonged exposure to a non-zero IMF B_y dayside reconnection introduces asymmetries into the ionospheric flow patterns [*Cowley et al.* (1991)] as a result of eastward or westward directed (azimuthal) magnetic tension forces exerted on plasma at the footpoints of the newly reconnected field lines [*Tenfjord et al.* (2015); *Grocott* (2017); *Ohma et al.* (2018)]. In the case of IMF $B_y > 0$, this results in an azimuthal displacement of the frozen-in ionospheric footpoints at the nightside reconnection site along the OCB to

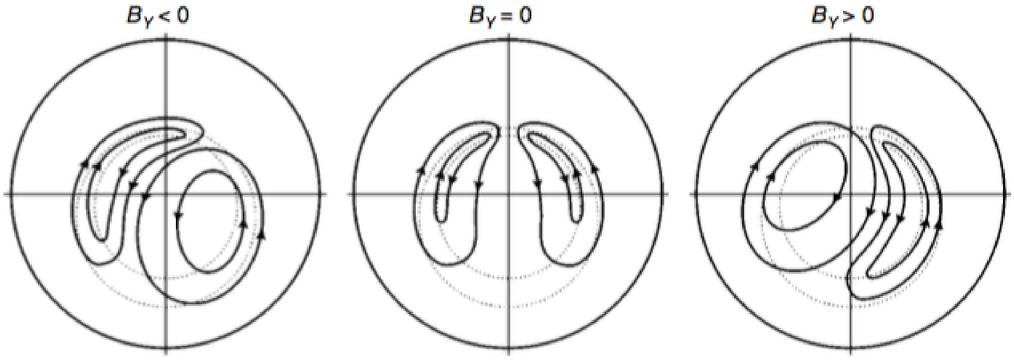

FIGURE 2.5: A schematic of the ionospheric convection patterns in the northern hemisphere for IMF $B_y < 0$, IMF $B_y = 0$ and IMF $B_y > 0$, from left to right respectively [*Grocott* (2017), after *Lockwood* (1991) and *Cowley and Lockwood* (1992)]. Noon is to the top, midnight to the bottom, dusk to the left and dawn to the right of each schematic.

pre- (post-) midnight in the northern (southern) hemispheres [e.g. *Grocott et al.* (2005); *Reistad et al.* (2016); *Ohma et al.* (2018)]. The traditional symmetric twin-cell pattern is overall distorted, with the convection cell on the duskside becoming more rounded, and the cell on the dawnside taking the shape of a crescent [see Fig. 8 of *Grocott et al.* (2004a)], with the opposite pattern in the southern hemisphere. The effect is opposite for the case of IMF $B_y < 0$ [see also, *Ruohoniemi and Greenwald* (1996); *Grocott et al.* (2008)]. This is shown in Figure 2.5.

2.3.2 The Untwisting of the Magnetotail

Regardless of the mechanism which may be involved in the magnetotail twisting, the result is to introduce field lines with azimuthally displaced footpoints which straddle the midnight sector in the northern and southern hemispheres [e.g. *Grocott et al.* (2005)]. The field lines are twisted from their north-south symmetry, and a B_y component of the same sign as the IMF B_y is superimposed onto the tail field.

The tail '*untwisting hypothesis*' put forward by *Grocott et al.* (2007) discusses how exposure to a non-zero IMF B_y for a sustained period of time results in the ionospheric footpoints of the newly reconnecting tail field lines being azimuthally displaced in each hemisphere [e.g. *Liou and Newell* (2010); *Østgaard et al.* (2011)] - and as a result, a given field line having a longer path back to the dayside in one hemisphere and thus convecting faster via dusk or dawn on its return to the dayside. This results in fast convective duskward or dawnward (azimuthal) ionospheric flow bursts at the footpoint of that field line on the nightside [*Grocott et al.* (2004a)] and coincident convective earthward fast flow in the magnetotail plasma sheet [*Grocott et al.* (2007)], with the faster flow burst being expected in the (dusk-dawn) direction (and magnetic hemisphere) where the field line has further to travel to return to the dayside [e.g. *Grocott et al.* (2005)], owing to the enhanced tension and pressure gradient forces [see Fig. 6 of *Tenfjord et al.* (2015)]. One should note the field line footpoint MLT displacement when comparing the northern and southern hemisphere counterparts of the same green or red field lines in Fig. 2.6, introduced below.

As the untwisting hypothesis implies, the convective earthward flows in the magnetotail are inherently expected to have a dusk-dawn direction which is highly dependent on, or 'controlled', by IMF B_y, and we discuss this further below and in Chapter 4. In order to be consistent with magnetotail untwisting, any convective flows associated with an individual tail field line should share the same dusk-dawn direction in both hemispheres. In Figure 2.6 we present a schematic illustrating the configuration of the magnetotail and associated untwisting flows in a simplified case where 'positive twisting' from IMF $B_y > 0$ penetration has occurred.

In-situ observations of the untwisting process have been presented previously by *Grocott et al.* (2007), by utilising multi-spacecraft observations from the Cluster mission (Section 3.1.2.1). Simultaneous measurements from above and below the neutral sheet near to midnight local time, with concurrent observations of the ionospheric flow using the SuperDARN radar system (Section 3.3.1), revealed a fast flow that was dawnward in the northern magnetic hemisphere (NH, $B_x > 0$) and duskward in the southern magnetic hemisphere (SH, $B_x < 0$). The ionospheric plasma observations had a convective azimuthal component which matched that of the magnetospheric fast flows. This was consistent with the suggestion made in their earlier work, *Grocott et al.* (2004a), where they postulated that the observed ionospheric flow bursts were associated with the reconfiguration of an asymmetric tail, but in that instance lacked the in-situ plasma sheet observations.

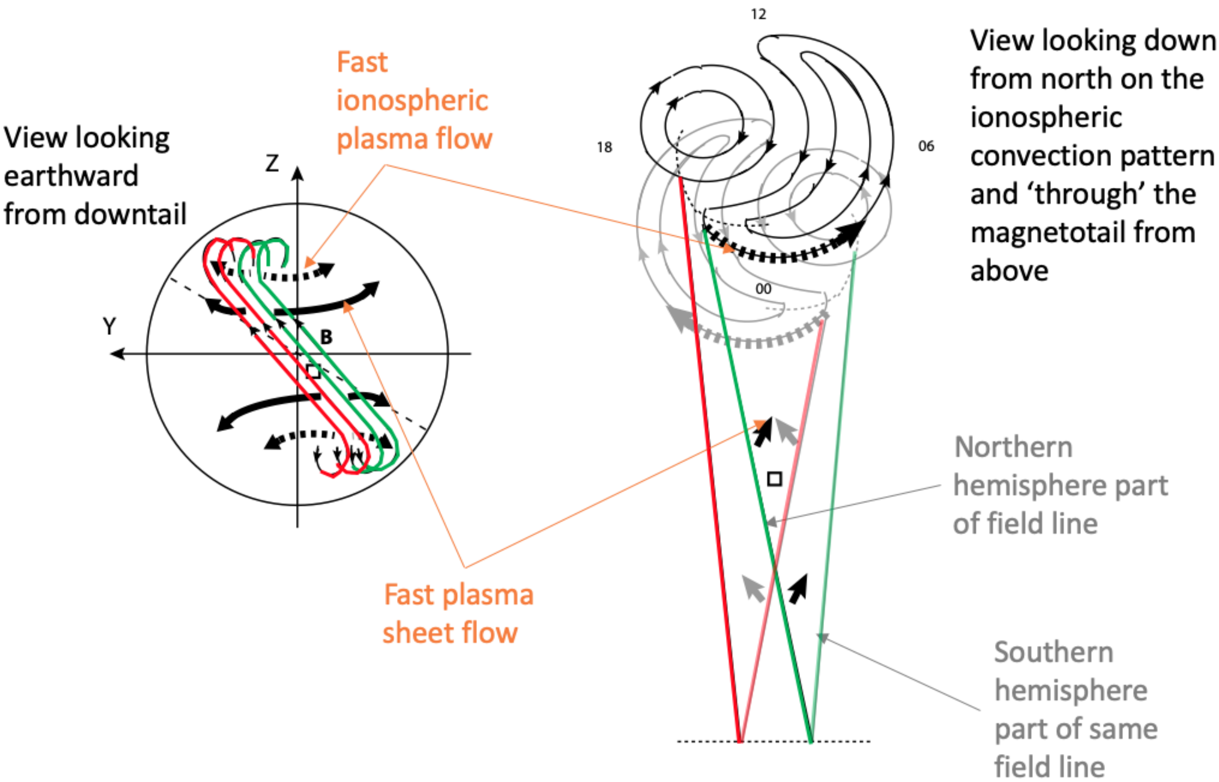

FIGURE 2.6: A simplified schematic illustrating the theoretical untwisting of twisted tail field lines, for positive twisting ($B_y > 0$). In each case, the white square depicts the location of an observing spacecraft. The fast convective flows associated with untwisting are labelled, and the red (green) lines are field lines associated with the dusk (dawn) ionospheric convection cells. **Left**: A view looking towards Earth from downtail. The thin coloured arrowed lines illustrate the closed magnetotail field lines with a positive B_y component present on them. The thicker arrows indicate plasma flow, with a longer arrow representing a faster flow. The dashed line marks the tilted neutral sheet. **Right**: A view looking downwards from north onto the ionospheric convection pattern and through the magnetotail. The black (faint) arrowed curves show the associated ionospheric plasma convection pattern for positive B_y in the northern (southern) hemisphere, and the short arrows indicate the expected fast plasma sheet convective flow. The dotted line marks a reconnection line. Adapted from *Grocott et al.* (2004a); *Pitkänen et al.* (2015).

The existence of an azimuthal flow shear close to the neutral sheet at midnight has also been supported by e.g. *Walsh et al.* (2009), and is in-fact is entirely consistent with the untwisting hypothesis. Of course, a given magnetic field line can only have its footpoints in the dusk *or* dawn cell, irrespective of hemisphere. This means that if one were to traverse the neutral sheet well away from midnight, and cross from e.g. field lines associated with the dawn cell in the NH to field lines associated with the dawn cell in the SH, the flow observed in the tail in both hemispheres should still be dawnward. However, close to midnight, one may be crossing into regimes of different field lines (see e.g. Fig. 6c of

Grocott et al. (2007) and the location of the white square in Fig. 2.6) - for example, from field lines associated with the northern ionospheric dawn cell to ones associated with the southern dusk cell. Thus the observed dusk-dawn flow reversal by *Grocott et al.* (2007) is completely consistent with untwisting.

Pitkänen et al. (2015) examined an almost identical case study to *Grocott et al.* (2007) and found an event which provided further observational evidence of the untwisting hypothesis. Like *Grocott et al.* (2007), observations from the Cluster spacecraft close to midnight revealed a change in the convective dusk-dawn flow direction from dawnward to duskward in association with the spacecraft constellation crossing from the NH to SH. Observations from the SuperDARN radar revealed a large scale IMF $B_y > 0$ asymmetry and fast dawnward flow at the Cluster footpoint in the NH.

The fast convective plasma sheet flow associated with magnetotail untwisting has also been studied statistically by *Pitkänen et al.* (2013, 2017). In agreement with the case studies of *Grocott et al.* (2007) and *Pitkänen et al.* (2015), they found that irrespective of the sign of IMF B_z, in the case of positive tail twisting (IMF $B_y > 0$), in the NH, it was favourable to get dawnward ($v_{\perp y} < 0$) fast flows, and that in the SH it was favourable to get duskward ($v_{\perp y} > 0$) fast flows (i.e. the situation depicted in Fig. 2.6). They also discovered that the flows exhibited an opposite dependence for IMF $B_y < 0$. This agreement with IMF B_y was found to be true approximately 70% of the time, with the remaining ~30% of flows having a dusk-dawn direction which was not in agreement with IMF B_y (i.e. not in agreement with the untwisting hypothesis). This key result forms the basis for the research presented in this thesis; that is, to address what is responsible for the remaining ~30%, and why they do not agree with IMF B_y. We begin our investigation by examining the study of *Pitkänen et al.* (2013) in more detail in Chapter 4. First, however, in Chapter 3, we introduce the various instrumentation and datasets which we will use to conduct this research.

Chapter 3

Instrumentation, Datasets and Models

3.1 Magnetospheric Observations

3.1.1 Instrumentation

3.1.1.1 The Fluxgate Magnetometer (FGM)

A *magnetometer* is a device used to measure both the strength, direction or change in a magnetic field at a given location [*Russell et al.* (2016)]. The simplest form of magnetometer is the *compass*, which uses a magnetic needle which points towards the Earth's north magnetic pole. Prior to the invention of modern magnetometers, traditional compasses had been used for centuries. A *fluxgate magnetometer* (FGM) is a special type of magnetometer extremely well suited to making magnetic field observations on the ground as well as in space due to the wide measurement range it can make (1-60,000 nT) as well as the low noise levels [*Primdahl* (1979)].

Traditionally, a fluxgate sensor is composed of a core of magnetic material (e.g. iron), wound by two conducting coils - one drive coil, and one sense coil. To the drive coil, an alternating current is fed. This creates a changing magnetic field in the iron core. On the sense coil, the changing magnetic field in the core generates an electromotive force (induced voltage) which is proportional to the changing magnetic field (see eq. 1.34, Fig. 3.1a) [*Musmann and Afanassiev* (2010)].

The current through the drive coil can be varied in a way that induces magnetic saturation in the core [*Primdahl* (1979)], where the magnetic field of the core is no longer able to increase. Since the induced voltage across the sense coil depends on the changing magnetic field in the core, which is now saturated, and thus not varying, the induced voltage across the sense coil will be lost.

If there is no external magnetic field present, the output voltage will be in-step with both half-cycles of the input current (Fig. 3.1a). If an external magnetic field (e.g. IMF) is present, the core will reach saturation quicker, and the output voltage will no longer be in-step with the input current (Fig. 3.1b). The size and phase of the voltage spikes enables us to acquire measurement of the magnitude of the magnetic field. In order to make a 3D vector measurement of the magnetic field, we are required to use a triaxial FGM, meaning we have three orthogonal coils [*Acuña* (2002)].

3.1.1.2 The Electrostatic Analyser (ESA)

Determining useful plasma quantities such as number density, velocity and temperature follows from measuring a plasma *velocity distribution function* (VDF) [e.g. *Fazakerley et al.* (1998)]. A traditional instrument for performing such a task is a 'Top hat' curved plate *electrostatic analyser* (ESA), which is able to distinguish particles based on their energy per unit charge (E/q). During one complete spin of a spacecraft, the full 4π field-of-view around the spacecraft is sampled in segments. Each segment is a fixed area of size $\Delta\theta \times \Delta\phi$, where $\Delta\theta$ ($\Delta\phi$) is a some polar (azimuthal) angle range. Only a particle with an appropriate trajectory can enter the analyser. A particle which enters is deflected through $\sim 90^\circ$ by pair of parallel, oppositely charged plates which have a potential difference and therefore an electric field between them. Equation 1.1 dictates that this electric field results in a Coulomb force (providing a centripetal force) acting on the particle. This electric field can then be varied (by changing the potential) to ensure that the particle's

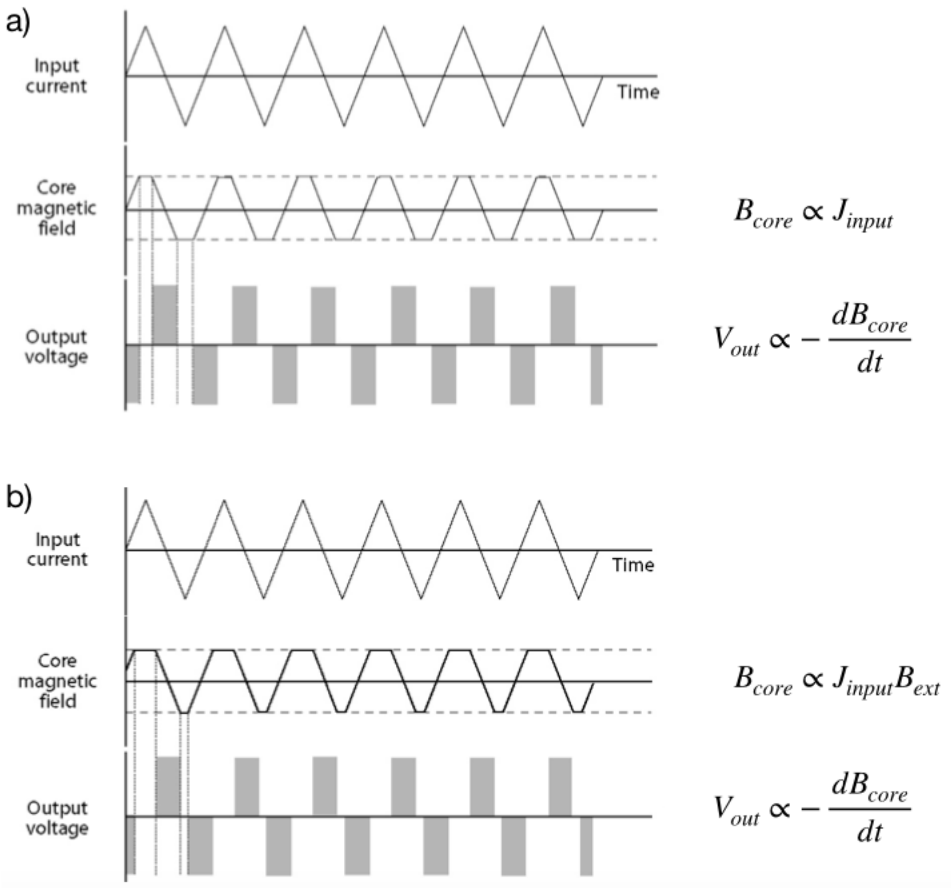

FIGURE 3.1: The principle workings of a fluxgate magnetometer for cases where a) No external magnetic field is present, and b) An external field (B_{ext}) is present. Adapted from *Wild* (2000); *Case* (2014)

trajectory (which depends on its mass, charge and velocity) is one which can reach the particle detector and be counted. The overall force which needs to be applied through the electric field allows inference of the particle's velocity and thus kinetic energy (E). Therefore, the overall 'acceptance volume', by which an incoming particle reaches the detector for a given segment is $\Delta\theta \times \Delta\phi \times \Delta E$. A simple schematic of the top hat analyser can be seen in Figure 3.2.

After making corrections for dead time effects [*Fazakerley et al.* (1998)], one obtains an expression for the number of counted particles $N_{ijk} = N(\theta_i, \phi_j, E_k)$, centred on each polar angle θ_i, azimuthal angle ϕ_j and energy E_k, with a particle count rate $C_{ijk} = N_{ijk}/t_{acc}$, where t_{acc} is some accumulation time interval. For example, an instrument which sampled 10 polar, 10 azimuthal and 10 energy ranges would acquire $10 \times 10 \times 10 = 1000$ samples

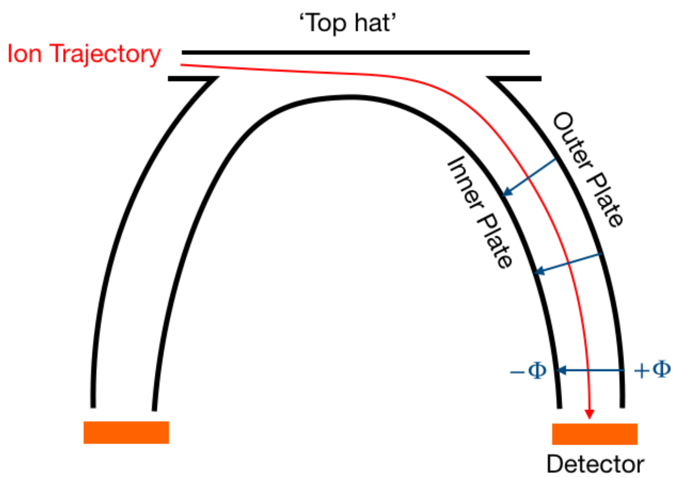

FIGURE 3.2: A schematic of a top hat electrostatic analyser. An ion which successfully enters the analyser is deflected (red line) by the difference in potential (Φ) between the inner and outer plates, before reaching the detector. The blue arrows show the direction of the associated electric field.

per spin, with each sample being the count rate [counts s^{-1}] at a specific angle and energy range. We can relate the *mean phase space density in the acceptance volume*, f_{ijk}, to C_{ijk} through:

$$f_{ijk} = \frac{C_{ijk}}{v_k^4 G_i} \tag{3.1}$$

where v_k is the velocity which corresponds to the 'centre energy' associated with the accumulation time interval, and G_i is a constant energy-independent geometry factor [*Fazakerley et al.* (1998)]. f_{ijk} represents the average value of a VDF, $f(\mathbf{v})$, in the solid angle and energy range assigned to coordinates ijk, with the mean velocity associated with the measurement being v_k.

We can use $f(\mathbf{v})$ to calculate meaningful physical quantities such as number density, velocity and temperature, and these are known as *moments*. The moments of the velocity distribution function for a given particle species are defined [*Paschmann et al.* (1998)] as:

$$M_n \equiv \int f(\mathbf{v})\mathbf{v}^n d^3v \tag{3.2}$$

The zeroth order moment, for example, is just the number density:

$$n = \int f(\mathbf{v}) d^3v \tag{3.3}$$

We can use eq. 3.1 and the fact that a velocity space volume element, $d^3v = v^2cos(\theta)dvd\theta d\phi$ to write:

$$n = \int\int\int \frac{C_{ijk}}{Gv^4} v^2 cos(\theta)dvd\theta d\phi \tag{3.4}$$

In practice, spacecraft data is discrete and so these integrals are replaced with summations [e.g. *Lavraud and Larson* (2016)], so eq. 3.4 becomes:

$$n = \frac{\Delta\theta\Delta\phi}{G} \sum_{v_k} \frac{\Delta v}{v^2} \sum_{\theta_i}\sum_{\phi_j} < cos(\theta) > C_{ijk} \tag{3.5}$$

A full table of moment summations, which may be calculated according to eq. 3.2, can be seen in *Paschmann et al.* (1998). Conveniently, spacecraft data moments are often calculated prior to the data being made available, meaning that the calculation of moments from the velocity distribution is not something which we are required to perform manually.

3.1.2 Spacecraft Missions

3.1.2.1 Cluster

The **Cluster** satellites (named C1-C4) are a four-spacecraft European Space Agency mission which launched in 2000, first providing data from 2001, and still partially active as of 2021, aimed at investigating the small scale plasma regions within the Earth's magnetosphere [*Escoubet et al.* (2001)]. These regions include the solar wind and bow shock, magnetopause, polar cusps, magnetotail and auroral zones. The Cluster satellites are flown in a highly elliptical polar orbit in a tetrahedron configuration [see Fig. 1 of *Escoubet et al.* (2001)], and can be separated by anywhere from 100 to 18,000 km. The choice to use a tetrahedron was considered to be the best configuration to allow the study of three dimensional plasma structures and deriving vectorial quantities. Over the course of a year, Cluster is designed to complete a full 360° sweep of the Earth's magnetosphere and spends four months per year (July to October) in the tail plasma regions [*Boakes et al.* (2014)].

Each of the Cluster spacecraft carries 11 specific instruments aimed at measuring numerous parameters, and these are listed in *Escoubet et al.* (2001). The Cluster data used in this thesis were made available and obtained through the Cluster Active Archive [*Laakso et al.* (2010)], at [`https://www.cosmos.esa.int/web/csa`]. This repository also includes documentation and up to date information on each individual instrument. Of particular importance to this research are data from the *Fluxgate Magnetometer* (FGM) experiment [*Balogh et al.* (2001)], used to measure the magnetic field vectors, provided at full resolution (22 Hz), 5 Hz, as well as spin resolution (∼4 s). The *Cluster Ion Spectroscopy* (CIS) experiment [*Rème et al.* (1997, 2001)] allows measurement of the composition, mass, and distribution of ions with energies ranging from 0 - 40 keV/q at spin resolution. The CIS package consists of two different instruments - the Hot Ion Analyser (HIA) and the COmposition and DIstribution Function (CODIF) analyser. The HIA selects and 'combines' ions based on their energy per unit charge (E/q) using a traditional top-hat analyser, at energies ranging from 5 - 32 keV/q. CODIF, however, is able to separate ions by species (such as H+, He+) by calculating the mass per charge (m/q) ratio of incoming ions and can cover the full 0 - 40 keV/q energy range. Moments for the HIA are calculated onboard, whereas CODIF moments are calculated on the ground. Ground moments are not provided for the HIA as similar anode calibrations required for CODIF mean the resolution of any HIA moments would be degraded. In our research, we use the 5 Hz FGM data, and CIS data only from the HIA, as this allows us to measure the bulk ion properties, which are more indicative of the overall plasma behaviour (and thus, convection) than individual ion species [e.g. *Paschmann et al.* (1998)]. The Cluster data that we use includes C1 (years 2001-2018 inclusive) and C3 (years 2001-2009, again inclusive). For the case studies presented in Chapters 5 and 6, we additionally include FGM data from C2 and C4.

3.1.2.2 THEMIS

The **Time History of Events and Macroscale Interactions during Substorms (THEMIS)** is another multi-spacecraft mission, launched in early 2007, and consists of five identical micro-satellite 'probes' (THA-THE) in elliptical, equatorial orbits in a 'string-of-pearls' configuration around the Earth [see Fig. 1 of *Angelopoulos* (2008)]. Specific details on the orbit of THEMIS can be read in *Frey et al.* (2008). The main objective of the THEMIS mission is to better understand the trigger and large-scale evolution of substorms. Consequently, THEMIS spends the majority of its time within the Earth's magnetotail [*Angelopoulos* (2008)]. Similar to Cluster, the THEMIS probes are also all equipped with a number of instruments which make measurements at varying resolution. This includes FGM's [*Auster et al.* (2008)] to take measurements of the magnetic field strength and orientation. This is provided at spin-res (∼3 s), low res (4 Hz) and high res (128 Hz). Instruments such as the Electrostatic Analyzer (ESA) [*McFadden et al.* (2008)] and Solid State Telescope (SST) [*Larson et al.* (2009)] provide particle measurements for THEMIS. The ESA can measure ions and electrons with energies ranging between 5 eV and 25 keV, with the SST's measurable energies ranging between 25 keV and $>$ 1 MeV [*Angelopoulos* (2008)]. These measurements are also provided at variable resolution, including 'FULL' (few min), 'REDUCED' (spin res) and 'BURST' (sporadic high res) modes. Data products from the THEMIS spacecraft, including the combined ESA and SST moments, may be obtained from the Space Science Laboratory at UC Berkeley [`http://themis.ssl.berkeley.edu/index.shtml`]. In our research, we use the low resolution (4 Hz) FGM data, and spin-res bulk ion velocity flow data calculated on the ground from the combined ESA and SST moments. The THEMIS data that we use includes THB, THC and THD and spans the years 2007-2019 inclusive.

3.1.2.3 Geotail

The **Geotail** satellite, launched in 1992, is a single spacecraft with the main goal of studying the structure and dynamics of the Earth's magnetotail [*Nishida* (1994)]. The equatorial Geotail orbit [see Fig. 2 of *Nishida* (1994)] was designed to cover a wide range of distances, ranging from 8 - 10 R_E (perigee) to 210 R_E (apogee). In order to study these regions, Geotail has utilised a variety of instruments. This includes the Magnetic Field Experiment (MGF) [*Kokubun et al.* (1994)] which provides 128 Hz measurements of the magnetic field, as well as a variety of particle measuring instruments such as the Low Energy Particle (LEP) Experiment [*Mukai et al.* (1994)]. The LEP can measure ion energies ranging from 60 eV to 40 keV. Data from Geotail is provided and maintained by The Data ARchive and Transmission System (DARTS) [`https://darts.isas.jaxa.jp/stp/geotail/`]. In this research, we use MGF data which are provided at spin res (∼3 s), and ground moments from the LEP at four-spin-res (∼12 s) by the Space Physics Data Facility (SPDF) at NASA [`https://spdf.gsfc.nasa.gov/pub/data/geotail/`]. We also apply the appropriate daily Geotail B_z MGF offset, as described in the caveat section of DARTS. The Geotail data that we use spans the years 1993-2006, inclusive.

3.2 Solar Wind and IMF Observations

The IMF and solar wind plasma data used in the following studies was taken from the OMNIWeb [*King and Papitashvili* (2005)], which provides open access to such data at both high (1-min, 5-min) and low (1-hour) resolution averages [`https://omniweb.gsfc.nasa.gov`]. The OMNIWeb uses data from spacecraft upstream of the Earth in the solar wind, such as the Advanced Composition Explorer (ACE) [*Chiu et al.* (1998)] and Wind [*Ogilvie et al.* (1995)] at the Lagrange 1 (L1) point, as well as International Monitoring Platform 8 (IMP 8) [*Paularena and King* (1999)] and Geotail. L1 is the region approximately 0.01 AU sunward of the Earth whereby a third body, such as a spacecraft, is able to orbit our Sun with the same period as Earth, providing a near-constant stream of IMF and solar wind data [e.g. *Domingo and Wyn-Roberts* (1984)]. This is as a consequence of the gravitational pull of the Earth acting on the spacecraft, modifying the required centripetal orbit about the Sun in such a way that L1 can be used as a 'hover' point.

The OMNI data are conveniently pre-processed in such a way that observations are propagated, or 'lagged', to the Earth's bow shock nose. Such a lag time is typically of the order of one hour. Solar wind measurements are generally assumed to arrive in 'phase fronts' (i.e. flat planes convecting at the solar wind velocity) and are then propagated to the Earth's bow shock nose using a time shifting technique, defined by the equation:

$$\Delta t = \frac{\hat{\mathbf{n}}.(\mathbf{R}_d - \mathbf{R}_o)}{\hat{\mathbf{n}}.\mathbf{v}} \tag{3.6}$$

where Δt is the lag time, $\hat{\mathbf{n}}$ is a phase front normal, $\mathbf{v}$ is the solar wind velocity, $\mathbf{R}_o$ is the location of the observing spacecraft, and $\mathbf{R}_d$ is the 'displaced' location, i.e. the bow shock [see Section 3 of `https://omniweb.gsfc.nasa.gov/html/omni_min_data.html`]. A method of calculating the phase front normals is based on the Minimum Variance Analysis (MVA) technique [*Sonnerup and Cahill Jr.* (1967); *Sonnerup and Scheible* (1998)],

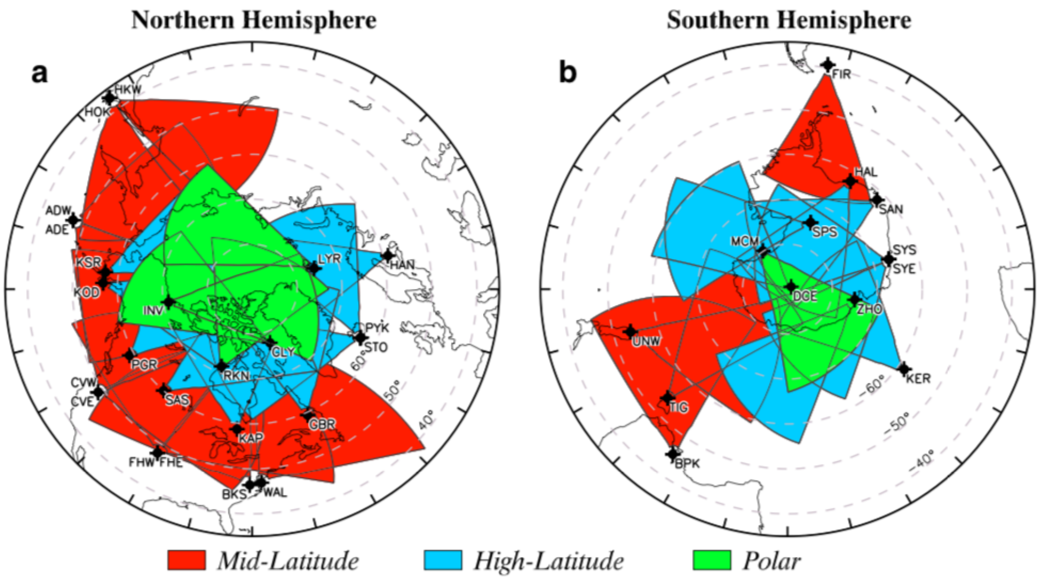

FIGURE 3.3: A schematic illustrating the fields of view of the different SuperDARN radars (names abbreviated) [*Nishitani et al.* (2019)].

which we discuss and apply to our Cluster data in Chapter 5. In our research, we exclusively use the 1-min OMNI dataset as our source of IMF and solar wind data, which spans the years 1993-2019 inclusive.

3.3 Ground-Based Observations

3.3.1 SuperDARN

The Super Dual Auroral Radar Network (SuperDARN) is an international collaboration of 36 high frequency (HF) radars aimed at monitoring the mid and high-latitude F-region convective horizontal plasma flows within the ionosphere. The full list of these is provided in *Nishitani et al.* (2019). Initially, SuperDARN was designed to only operate in the high-latitude regions (> 60° MLAT). However, over the last 15 years or so, the SuperDARN radars have been expanded to now be able to observe plasma at mid-latitudes (∼50° MLAT). A schematic showing the coverage (fields of view) of the different SuperDARN radars is presented in Figure 3.3.

3.3.1.1 Radar Operation

The SuperDARN radars work on the principle of coherent scatter, whereby a transmitted signal is returned (backscattered) to the radar. Backscattering occurs when HF beams come into contact with decametre field-aligned ionospheric electron density irregularities travelling at the $\mathbf{E} \times \mathbf{B}$ convection velocity [*Reid* (1968)] whilst propagating perpendicular to the (nearly vertical) geomagnetic field lines [e.g. *Ruohoniemi and Baker* (1998); *Chisham et al.* (2007, 2008b)].

The radars operate 24 hours, 365 days a year, and most provide 2-minute resolution scans beginning at 00:00 UT each day [*Ruohoniemi and Baker* (1998)]. Each 'scan' consists of electronically steering a HF (8 MHz to 20 MHz range - radio waves) radar beam through 16 successive azimuthal settings separated by 3.3° with an integration period (scanning time) per setting of 7 s. This means each radar beam covers approximately $3.3° \times 16 \approx 52.8°$ of azimuth in just under 2 minutes [*Ruohoniemi and Baker* (1998)], with the total range lying between 200 to 3,000 km [*Chisham et al.* (2007)] - this 'area' that the radar can observe is known as the 'field of view'. At each setting, backscatter returns are range-gated in steps of 45 km [*Ruohoniemi and Baker* (1998); *Ruohoniemi and Greenwald* (2005)] (corresponding to pulse times of around 300 μs [*Nishitani et al.* (2019)]), beginning at 180 km. The doppler shift in the backscattered signals provide an estimate for the line-of-sight (LOS) $\mathbf{E} \times \mathbf{B}$ velocity at F-region altitudes, for each beam and range gate [e.g. *Ruohoniemi and Greenwald* (1996); *Nishitani et al.* (2019)], and thus determination of whether plasma is moving towards or away from the radar.

3.3.1.2 Imaging the Large-Scale Convection

In order to image the large-scale convection, the LOS $\mathbf{E} \times \mathbf{B}$ velocity data (for each radar) for a given scan must first be geomagnetically mapped to a polar grid consisting of equi-area MLAT-MLON cells, with each cell measuring 1° in latitude. The data are also temporally and spatially averaged (by including data from the scan prior to and following the scan of interest and surrounding each target cell). The result is a median-averaged best estimate for the LOS velocity for each cell [see *Ruohoniemi and Baker* (1998)]. The mapping thus produces a set of N velocity values W_i and corresponding uncertainties σ_i, where i denotes a given grid cell [e.g. *Grocott et al.* (2012)]. It should be noted that where LOS data from different radars overlap, these are not cross-radar averaged and may both occupy the same cell. Traditionally, the mapping of scans is done for each 2-minute interval. This is related to the fact that most radar scans take ∼2 minutes, and thus a 2-minute-integrated map ensures maximal possible spatial coverage at the highest temporal resolution. Combining the data from multiple radars across the same 2-minute interval is also required if one wishes to image the large-scale convection, owing to the fact that each radar only has a finite field of view (Fig. 3.3).

To create maps of the ionospheric convection, a global 'best fit' for the LOS velocity data must be found. This is done by representing the global distribution of electrostatic potential, Φ, in terms of a spherical harmonic expansion [see details in e.g. *Weimer* (1995); *Ruohoniemi and Baker* (1998); *Grocott et al.* (2012)], and using equations 2.2 and 2.3 to obtain different 'fitted' velocity vectors $\mathbf{V}[i]$ at co-latitudes and longitudes (θ, ψ) corresponding to the grid cells i where LOS data were obtained. The best fit convection pattern is then the one which minimises the χ^2 quantity [*Ruohoniemi and Baker* (1998)].

The velocity data are also supplemented by additional velocity vectors from statistical models (not shown on the maps), which are added to the set of gridded LOS velocity measurements before performing the fitting. Arguably the most well known of these is the RG96 model, parameterised by the instantaneous IMF conditions [*Ruohoniemi and Greenwald* (1996)]. This statistical model helps to constrain the fitting solution where no SuperDARN data are available [*Shepherd and Ruohoniemi* (2000)]. For maps without much actual radar data coverage, a question must be asked of the reliability, since the convection pattern is constrained by model data and thus only somewhat provides a prediction of the convection based on IMF conditions, as opposed to real observations. Example SuperDARN convection maps, with both the LOS and fitted vectors plotted, are shown in Figure 3.4.

The SuperDARN data used in this thesis were acquired via the BAS data mirror [`http://bslsuperdarnc.nerc-bas.ac.uk:8093/docs/`], and processed into convection maps

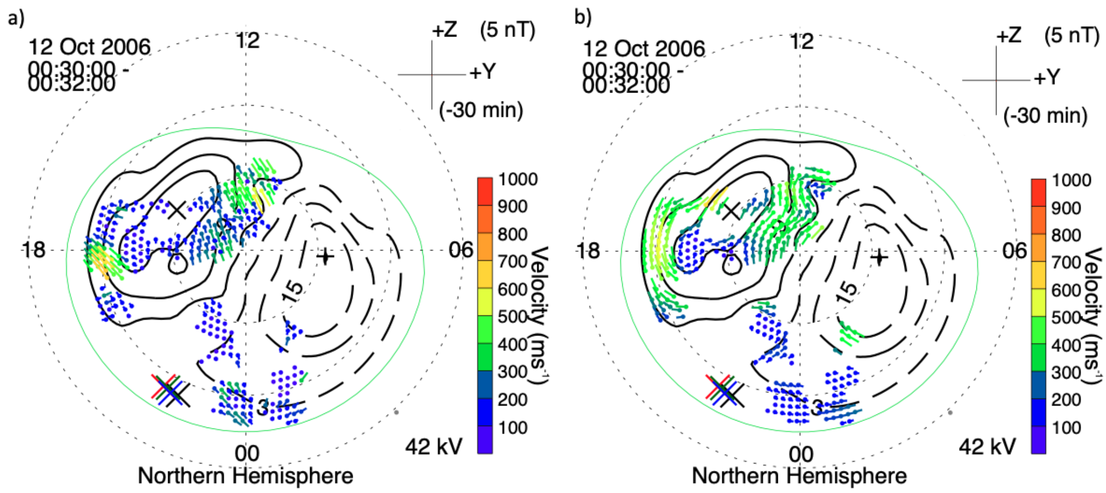

FIGURE 3.4: Maps of the ionospheric plasma convection derived from SuperDARN observations on 12 Oct 2006. Midnight is to the bottom of each map, noon to the top, dusk to the left and dawn to the right. The solid and dashed black lines represent the plasma streamlines and are the contours of the electrostatic potential. The green circle marks the Heppner-Maynard boundary [*Heppner and Maynard* (1987)]. In this instance, the statistical RG96 background model has been parameterised with IMF $(B_x, B_y, B_z) = (0, 0, -0.1)$ nT. Shown on each map by the small coloured points are a) LOS vectors, and b) fitted vectors (plotted at the locations where LOS data were obtained).

using a package of software known as the Radar Software Toolkit (RST) [*Thomas et al.* (2018)], allowing one to perform all of the steps described above.

3.3.2 Auroral Indices

Enhancements and variability in magnetospheric or ionospheric currents produce magnetic perturbations to the Earth's magnetic field which can be measured using ground-based magnetometers. North-south (horizontal) perturbations at auroral latitudes associated with the eastward and westward auroral electrojets (Hall currents) and substorm electrojet current systems, known as DP2 and DP1 perturbations, respectively, are measured by the Auroral Upper (AU) and Auroral Lower (AL) indices [see e.g. *Davis and Sugiura* (1966); *Milan et al.* (2017)]. These are determined from the upper and lower perturbation-envelopes measured by a network of 12 auroral-latitude magnetometers [*Weygand et al.* (2014)]. Subtracting these from one-another produces the Auroral Electrojet (AE) index:

$$AE = AU - AL \tag{3.7}$$

These indices are provided by the World Data Center for Geomagnetism in Kyoto and may be accessed via the OMNI dataset. A large (few 100 nT) AE index, as well as a significant (100 nT+) drop in the AL index (such that |AL| > AU), is an indicator for substorm activity [e.g. *Hsu and McPherron* (2012)]; a drop in AL is indicative of an enhanced westward electrojet, which would be expected if the substorm electrojet is present [see Fig. 2 of *Milan et al.* (2017)].

3.4 The Tsyganenko Magnetic Field Model

The Tsyganenko Magnetic Field Models [e.g. *Tsyganenko* (1996); *Tsyganenko and Andreeva* (2015)] are an empirical (data-driven) approach of modelling the external magnetic field of the Earth's magnetosphere. Firstly, the total *external* magnetic field is expressed as a sum of the contribution from all the major current systems within the Earth's magnetosphere:

$$\mathbf{B}_E = \mathbf{B}_{MP} + \mathbf{B}_{RC} + \mathbf{B}_{PRC} + \mathbf{B}_T + \mathbf{B}_{R1} + \kappa\mathbf{B}_{\perp IMF} \tag{3.8}$$

where the subscripts on the RHS for each term denote contributions to the field from the magnetopause current, ring current, partial ring current and R2 FAC, cross-tail current, R1 FAC, and some fraction of the transverse IMF component (penetration), respectively. Analytical expressions are derived for each term above using various approaches (approximations for current, use of scalar and vector potentials, harmonic expansions, fourier series), generating 23 model parameters in the case of *Tsyganenko and Andreeva* (2015), known as TA15. Data from spacecraft such as Cluster, THEMIS and Geotail are then used to find best-fit values of the model parameters using a least squares fitting.

In the case of TA15, the finished model is parameterised by four key parameters: 1) solar wind dynamic pressure (P_{dyn}), 2) IMF B_y, 3) IMF B_z, and 4) 'N-index', based on the solar wind coupling function of *Newell et al.* (2007). The N-index ranges from 0 (very quiet) to 2 (very active). Given a spacecraft GSM position (x, y, z) and a dipole tilt angle, the external model GSM field (B_x, B_y, B_z) at that location is then computed. Adding this to the *internal* field value gives the total magnetospheric field at a particular point in space.

In this research, we make use of the Tsyganenko magnetic field model routines provided in the IDL Geopack DLM.

Chapter 4

Dusk-Dawn Flow Asymmetry and The Local B_y Component

4.1 Introduction

4.1.1 IMF B_y Control of Magnetotail Fast Flows

As discussed in Section 2.3.2, a key factor that has been observed to influence the dusk-dawn direction of the magnetotail flow associated with magnetotail untwisting is the B_y component of the IMF. *Pitkänen et al.* (2013, 2017) investigated the statistical dependence of earthward plasma sheet magnetotail fast flows on the IMF B_y component using Cluster and THEMIS spacecraft data. They discovered that, regardless of the IMF B_z orientation, the fast flows demonstrated a strong statistical dependence on IMF B_y at $|Y_{GSM}|$ values up to 7 R_E. For positive tail twisting (IMF $B_y > 0$), they showed that above the neutral sheet ($B_x > 0$, i.e. NH), it was favourable to get dawnward convective ($v_{\perp y} < 0$) fast flows, and that below the neutral sheet ($B_x < 0$, i.e. SH) it was favourable to get duskward ($v_{\perp y} > 0$) convective fast flows, with an opposite correlation for IMF $B_y < 0$. The flows are thus directionally dependent on both hemisphere and IMF B_y, and this is expected both in the case of steadier, slower convection [*Pitkänen et al.* (2019)], and during more dynamic, transient BBF-like intervals [*Grocott et al.* (2007); *Pitkänen et al.* (2013)].

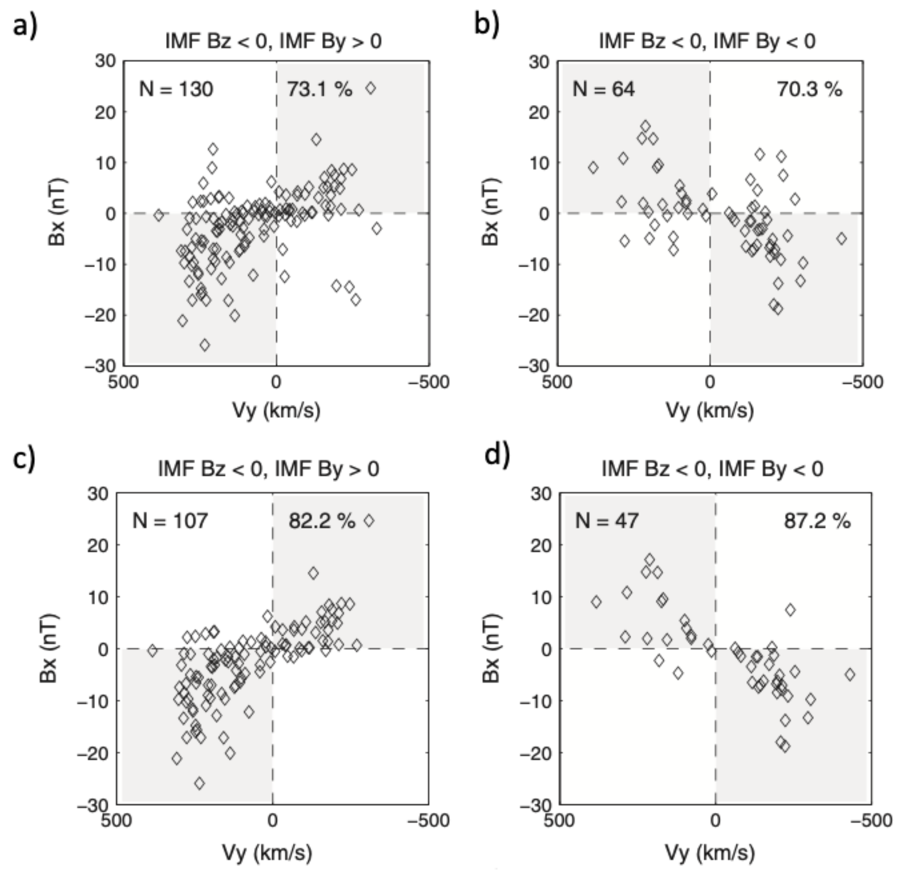

FIGURE 4.1: The in-situ convective dusk-dawn flow velocity (labelled here as V_y) plotted against the magnetic field B_x component for a) IMF $B_y > 0$, b) IMF $B_y < 0$, c) IMF $B_y > 0$ with local $B_y > 0$, and d) IMF $B_y < 0$ with local $B_y < 0$ conditions. N is the number of data in each plot, and the percentage shows the fraction of events lying in the 'expected' (shaded) quadrants. Adapted from *Pitkänen et al.* (2013).

To begin, we initially show some of the results of *Pitkänen et al.* (2013) in Figure 4.1, which indicate observations of 'fast flow events' made by the Cluster spacecraft. In each case, the dusk-dawn convective flow velocity has been plotted against the B_x component of the local magnetic field, subject to a constraint on the IMF B_y polarity, averaged over 130 minutes prior to each observation. Additionally, in panels c) and d), the local B_y component (i.e. the in-situ measured magnetotail B_y) is subjected to the same polarity checks as IMF B_y. The consequences of the choices made by *Pitkänen et al.* (2013) to use a 130-min IMF B_y averaging period and enforce a local B_y constraint are addressed below. Also highlighted on each plot is a pair of darker shaded quadrants. These indicate the hemisphere and direction where a fast flow is expected based on the untwisting hypothesis.

The overall agreement of around 70% in Figs. 4.1a and b does, as is perhaps to be expected, imply that IMF B_y overall has a clear effect on plasma sheet convection. However, this result also suggests that ~30% of the time, the observed dusk-dawn flow is independent of any IMF B_y-control (we return to this point at the end of this chapter). Following these preliminary results, in the analysis of *Pitkänen et al.* (2013), they further constrained the local B_y to be oriented in the same direction as the preceding 130-min averaged IMF B_y (Fig. 4.1c, d). Whilst *Pitkänen et al.* (2013) discovered that a 130-min IMF B_y average revealed the strongest dusk-dawn flow correlation, there is, inherently, uncertainty over whether the *Dungey Cycle* mechanism (acts within a couple of hours) or *Tenfjord* mechanism (acts within tens of minutes) is truly responsible for the superposition (penetration) of IMF B_y into the magnetotail. Therefore, even though a 130-min averaging period may not completely account for the possible timescales associated with both mechanisms, imposing that the local B_y have the expected twist effectively removes any IMF B_y penetration time uncertainty. As is evident from Fig. 4.1, this choice overall reduced the scattering in their results and improved the proportion of flows exhibiting the expected dusk-dawn asymmetry (now $> 80\%$). However, this constraint inadvertently introduced a locational bias into their analyses. This is because the local B_y component actually has a strong dependence on location in the Y_{GSM}-Z_{GSM} plane, in places stronger than the penetrated B_y (i.e. stronger than the B_y-perturbation introduced as a consequence of IMF B_y penetration). This is known as the *magnetotail flaring* effect, first put forward by *Fairfield* (1979).

4.1.2 Modelling the Magnetotail Background B_y Due to Flaring

Magnetotail flaring can be envisaged as the general 'curving' of the magnetic field away from midnight ($\mathrm{Y}_{GSM} = 0$), and can be readily demonstrated using any one of the Tsyganenko magnetic field models. Here, we use the TA15 model [*Tsyganenko and Andreeva* (2015)], and iterate through a range of Y_{GSM} and Z_{GSM} positions between 8 and -8 R_E, in steps of 0.1 R_E: firstly at $\mathrm{X}_{GSM} = -31$ R_E, and then at $\mathrm{X}_{GSM} = -14$ R_E, to obtain the modelled B_x and B_y values at each location. We then plot Y_{GSM} against model B_x, colour-coding each point based on the model B_y value, in Fig. 4.2. The choice to use B_x

instead of Z_{GSM} is due to the fact that B_x is a clearer indicator of magnetic hemisphere, which the untwisting hypothesis is generally discussed with respect to [e.g. *Pitkänen et al.* (2013)].

The model is paramaterised using the following arbitrary values: P_{dyn} = 3 nPa, IMF $B_z = -2$ nT, solar wind speed = 400 km s^{-1} (required to calculate the N-index). For the IMF B_y parameter, we firstly specify zero IMF B_y (Fig. 4.2a, b). In this way, we can inspect the expected magnetotail B_y component that is explicitly for the case of no IMF B_y penetration, and therefore purely due to flaring. Secondly, we specify IMF $B_y = +2$ nT (Fig. 4.2c, d), to allow us to examine the modelled effect on the local B_y of a *positive* IMF B_y penetrating into the magnetotail. Finally, we specify IMF $B_y = -2$ nT (Fig. 4.2e, f), to allow us to examine the modelled effect on the local B_y of a *negative* IMF B_y penetrating into the magnetotail. In each case, for simplicitly, we have enforced a zero dipole tilt (the local B_y too has a dependence on this, but we have removed this effect here [see *Petrukovich* (2011)]). Enforcing a zero tilt also positions the unperturbed neutral sheet at $Z_{GSM} \approx 0$ [*Xiao et al.* (2016)]. One should also note that the direction of Y_{GSM} has been reversed, going from positive to negative from left to right to be consistent with a view towards Earth from downtail.

Figs. 4.2a and b clearly demonstrate that away from the Earth-Sun line ($Y_{GSM} = 0$) and neutral sheet in a 'symmetric' magnetotail, the B_y component of the magnetotail field is expected to have a non-zero value; it is noticeable that $|B_y|$ increases towards the flanks and away from the neutral sheet, consistent with *Fairfield* (1979) and *Petrukovich* (2011). This effect appears to be more prominent closer to the Earth (in X_{GSM}), but is still readily apparent at 31 R_E downtail. In the case of a symmetric magnetotail (Fig. 4.2a, b), as one moves towards dawn ($-Y_{GSM}$) in the NH, the B_y value becomes positive, and towards dusk ($+Y_{GSM}$) it becomes negative. The effect is opposite in the SH. This 'background' B_y is present even in the case of no IMF B_y penetration.

Whilst it is true that e.g. a positive IMF B_y would be expected to introduce a localised B_y+ perturbation into the magnetotail field, this perturbation in itself may not be large enough to force the local B_y to change sign (thus, the topology of the field lines shown

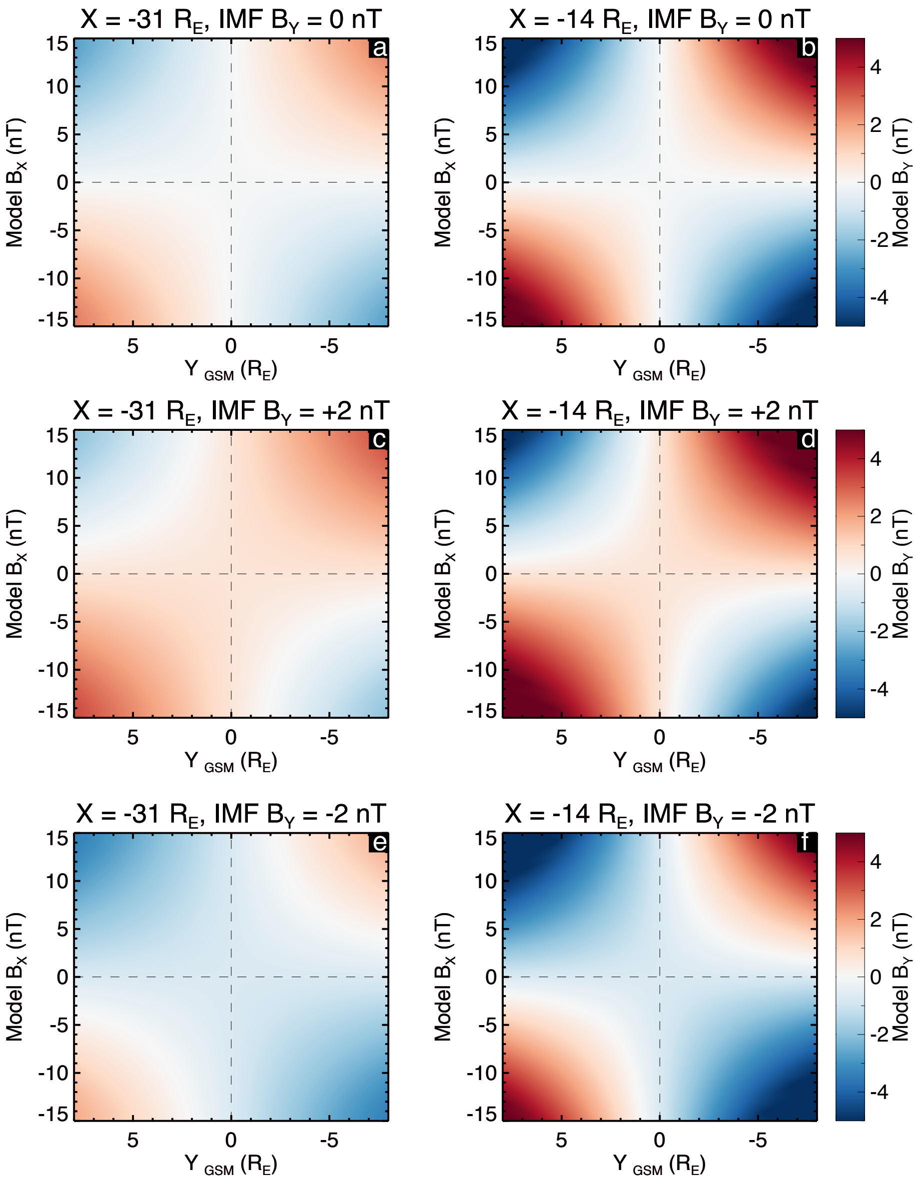

FIGURE 4.2: A plot of Y_{GSM} vs Model B_x showing the TA15 modelled distribution of B_y in the magnetotail at a) $X_{GSM} = -31$ R_E with IMF $B_y = 0$ nT, b) $X_{GSM} = -14$ R_E with IMF $B_y = 0$ nT, c) $X_{GSM} = -31$ R_E with IMF $B_y = +2$ nT, d) $X_{GSM} = -14$ R_E with IMF $B_y = +\,2$ nT, e) $X_{GSM} = -31$ R_E with IMF $B_y = -2$ nT and f) $X_{GSM} = -14$ R_E with IMF $B_y = -2$ nT. Red (blue) indicates regions of positive (negative) B_y.

in Fig. 2.6, for example, and later in Fig. 4.7b and c is grossly oversimplified). This is, in-fact, well represented by Fig. 2 of *Pitkänen et al.* (2019), which shows the average sense of the large-scale asymmetry as a consequence of clear IMF B_y penetration, but also shows that the B_y due to flaring dominates beyond $\sim \pm$ 4 R_E in Y_{GSM}. This argument is well reinforced by Figs. 4.2c and d, where the modelled effect of a positive IMF B_y 'penetrating' into the magnetotail is only apparent closer to midnight. Towards dusk (dawn) in the northern (southern) hemisphere, a negative local B_y is still observed. A similar effect is observed for negative IMF B_y penetration in Figs. 4.2e and f.

The upshot of filtering flows by local B_y as *Pitkänen et al.* (2013, 2017) did is that one is also in-effect filtering by the location of the observations. In the case of e.g. positive local B_y, then in the NH, one would be biasing the results towards dawn (post-midnight), in other words, favouring the removal of flows observed towards dusk (pre-midnight). In the SH, one would be biasing the results towards dusk, in other words favouring the removal of flows observed towards dawn. The opposite effect would also be true in the case of a negative local B_y. Owing to the fact that earthward plasma sheet flows are (on average) symmetric about midnight [*Hori et al.* (2000); *Kissinger et al.* (2012)], this single choice is likely to remove more of the flows which do not exhibit the expected dusk-dawn asymmetry, based largely on where they were observed.

In this chapter, we explore the above suggestions using our own dataset of fast flow 'detections', derived in the following section. Firstly, we demonstrate the problematic nature of using B_y as a criteria for filtering flow detections. We then discuss how this choice also leaves some ambiguity concerning the 'symmetry' of the observed flow, and what constitutes evidence of a flow asymmetry. Finally, we present an overview of our database of fast flows, which we explore further in the subsequent chapters of this thesis.

4.2 Derivation of the Fast Flow Dataset

To derive our database of magnetotail fast flows, we use all the data we have available from the Cluster, THEMIS and Geotail missions, detailed in Section 3.1.2. For this analysis, all data are firstly converted to GSM coordinates and then resampled to 1-min resolution via the use of a median boxcar average. Resampling of the data is required to allow us to synchronise the magnetic field and plasma data [*Harvey and Schwartz* (1998)]. The choice to use 1-minute data was based on three reasons: firstly, due to the typical 1-minute timescale of magnetotail flow 'bursts' [e.g. *Angelopoulos et al.* (1992); *Frühauff and Glassmeier* (2016)], secondly, so that our data is directly comparable and sychronised with the 1-min IMF data, and finally, due to the large volume of data that we were required to process. Indeed, other large statistical studies such as *Hori et al.* (2000) and *Case et al.* (2020) have used 1-min data. After resampling, we compute the plasma beta, β (eq. 1.30), and field-perpendicular velocity vector, $\mathbf{v}_\perp$ (a proxy for $\mathbf{E} \times \mathbf{B}$ frozen-in flow) using the equation:

$$\mathbf{v}_\perp = \mathbf{v} - \frac{(\mathbf{v} \cdot \mathbf{B})\mathbf{B}}{|\mathbf{B}|^2} = \mathbf{v} - (\mathbf{v} \cdot \hat{\mathbf{B}})\hat{\mathbf{B}} = \mathbf{v} - \mathbf{v}_\parallel \tag{4.1}$$

obtained from substituting eq. 1.25 into eq. 1.16, producing the vector $\mathbf{v}_\perp = (v_{\perp x},\ v_{\perp y},\ v_{\perp z})$. The data are then cleaned to remove 'bad' (unphysically large) data values.

Following the studies of *Pitkänen et al.* (2013, 2017), we then identify fast flow 'detections' as being any 1-minute data point where the following criteria are met:

- The ion plasma beta, $\beta > 0.5$.
- $-31 < \mathrm{X}_{GSM} < -14$ R_E and $|\mathrm{Y}_{GSM}| < 7$ R_E.
- The magnitude of the field-perpendicular (convective) flow in the X_{GSM}-Y_{GSM} plane, $v_{\perp xy} > 200$ km s^{-1}, where $v_{\perp xy} = \sqrt{v_{\perp x}^2 + v_{\perp y}^2}$ and $v_{\perp x} > 0$.

The resultant fast flow database consists of 5647 flow detections (C1: 625, C3: 396, THB: 591, THC: 663, THD: 37, Geotail: 3335). In Figure 4.3, we show the spatio-temporal distribution of our fast flows in the X_{GSM}-Y_{GSM} plane, in bins of 1×1 R_E. In each bin, for each spacecraft mission, we have divided the number of observed fast flow detections by the time each spacecraft spent in that region to produce a 'detection rate' (in detections/min).

Fig. 4.3 illustrates highly variable coverage when the data are split by spacecraft. The Cluster observations, for example, are restricted to $\mathrm{X}_{GSM} > -20$ R_E, and suggest a lower detection rate than Geotail, which observes a much greater detection rate in almost every 1×1 R_E bin. These differences undoubtedly arise due to the various orbits of the respective spacecraft (polar for Cluster, equatorial for Geotail, for example).

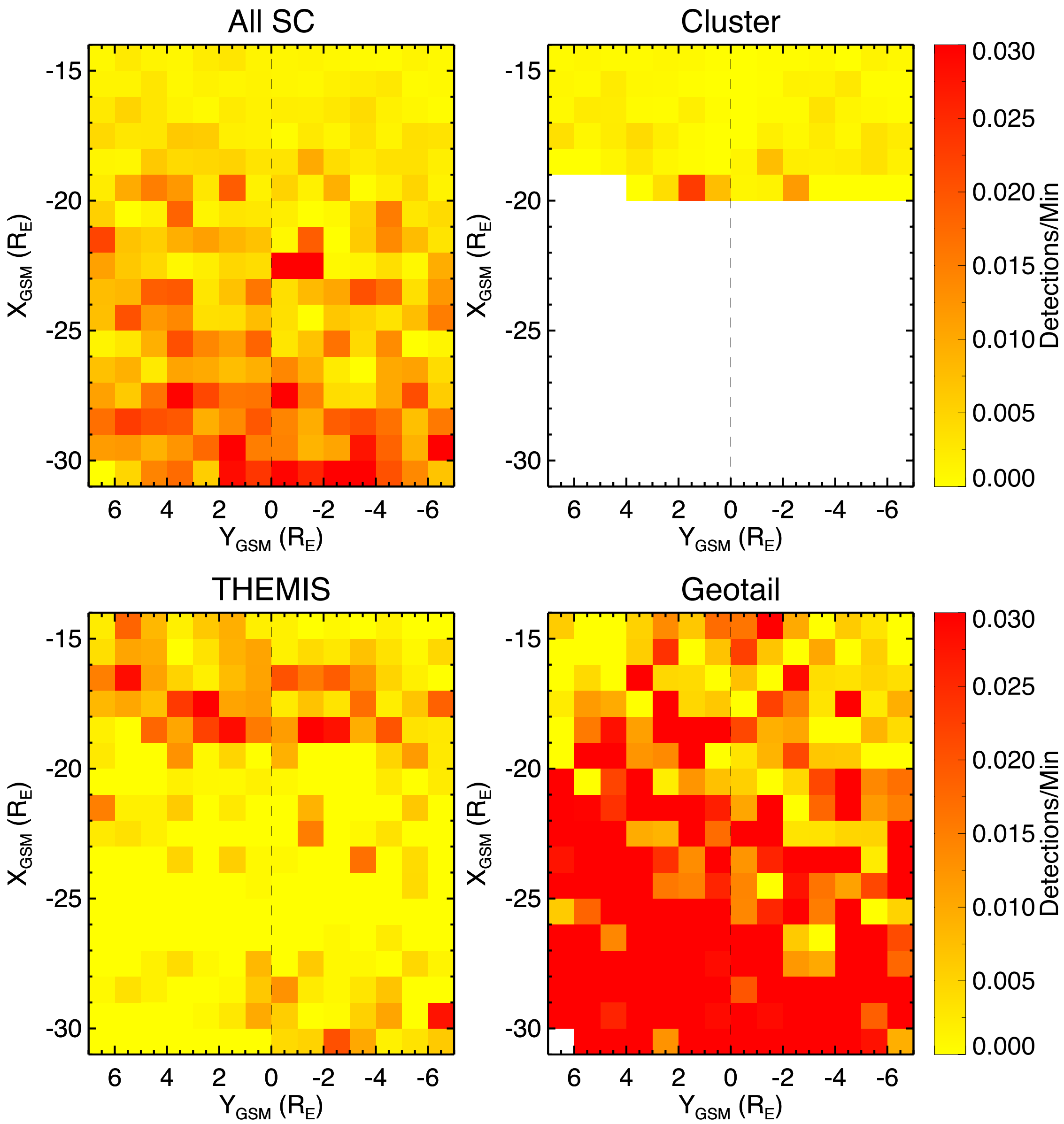

FIGURE 4.3: The detection rates of fast flows for the respective spacecraft missions (labelled) in the X_{GSM}-Y_{GSM} plane, in each 1×1 R_E region. Redder (yellower) regions indicate a greater (lower) detection rate. White regions indicate data gaps (i.e. where the spacecraft never sampled).

As additional checks, we required that there be continual spacecraft (plasma and magnetic field) data for ± 5 mins about each flow detection time, to ensure that we did not include any patchy data in our flow identifications. We also required there to be IMF data for at least 120 out of 130 mins prior to each flow to ensure that any IMF B_y averages were reliable. The 130 minute IMF B_y prior to each flow also had to have a coefficient of variation magnitude of less than 2, defined here as:

$$C_v = |\frac{\sigma}{\bar{x}}| \tag{4.2}$$

where σ is the standard deviation and $\bar{x}$ is the mean of IMF B_y. This choice was to ensure that only detections that occurred when the preceding IMF B_y conditions were fairly steady were included. We acknowledge that the above checks may seem somewhat arbitrary, but these criteria were reasonably selected after manual inspection of the data in order to leave 'reliable' detections, without also removing too many such that our statistics would be compromised. We do emphasise, however, that the results presented in the subsequent sections of this thesis are not sensitive to the exact arbitrary choices of these criteria. This is largely evidenced by the fact that the percentage of flows exhibiting the expected dusk-dawn asymmetry (~70%, see Fig. 4.8) remains relatively stable with changes in the number of detections.

We note that, on occasion, detections were made by two spacecraft at the exact same 1-minute timestamp (i.e. by C1 and C3). To decide whether to include both detections or just include one of them, we performed checks on the signs of Y_{GSM}, B_x, $v_{\perp y}$, and checked the radial distance between the spacecraft. If Y_{GSM}, B_x and $v_{\perp y}$ were of the same sign, and the spacecraft were < 3 R_E apart in the Y_{GSM}-Z_{GSM} plane (the typical spatial extent of fast flows, see *Nakamura et al.* (2004); *Frühauff and Glassmeier* (2016)), we included just one of the detections. Otherwise, we included them both. The choice to look at B_x and $v_{\perp y}$ was motivated by the definition of the untwisting hypothesis, whereas the choice to examine the sign of Y_{GSM} was motivated by a consideration related to flow asymmetry, discussed in the following section. Finally, we note that in our analysis, we treat each 1-min fast flow as a unique detection, despite them often occurring in succession (e.g. as part of a longer period of BBF-activity). We address this in Chapter 7, but we do note that other statistical studies of magnetotail flows such as *Frühauff and Glassmeier* (2016) have also used flow 'event' separations of 1-min. The reduced fast flow database consisted of 4053 fast flow detections.

4.3 Analysis and Discussion

4.3.1 The Effect of Imposing a Local B_y Threshold

In Section 4.1.2, we stated that earthward plasma sheet flows are expected to be symmetric about midnight ($Y_{GSM} = 0$) [e.g. *Kissinger et al.* (2012)]. Let us firstly reaffirm this idea using our dataset of fast flow detections. In Figure 4.4 we have plotted the Y_{GSM} position against the observed B_x for each detection and colour-coded these points based on the dusk-dawn sense of convective flow, $v_{\perp y}$. We also include a histogram of Y_{GSM}, to more clearly indicate the dusk-dawn distribution of the flows.

Fig. 4.4 illustrates that a majority (59.6%) of the 4053 fast flows observed were symmetric. These are flows which are either duskward directed in the pre-midnight sector, or dawnward directed in the post-midnight sector. This percentage therefore accounts for the combined sum of red points on the LHS and blue points on the RHS of Fig. 4.4, and this flow symmetry is also well indicated by the histogram, becoming more prominent beyond $\sim \pm 4$ R_E. We now consider breaking these flows up into four categories dependent on the preceding (130-min averaged) IMF B_y polarity prior to each flow, as well as the local B_y measured at the time of each flow, to attempt to indicate the locational bias introduced by imposing a local B_y criterion. The results of this are shown in Figure 4.5.

In Fig. 4.5a, there are 430, 486, 512 and 586 points in the top left, top right, bottom left, and bottom right quadrants, respectively. In Fig. 4.5c, imposing local $B_y > 0$ reduces this to 171, 404, 411 and 429 points. Overall, this choice has removed 259 (27 blue, 232 red), 82 (37 blue, 45 red), 101 (68 blue, 33 red) and 157 (126 blue, 31 red) points from the respective quadrants of Fig. 4.5c. The analysis presented in Fig. 4.5 therefore reveals two important features. Firstly, enforcing $B_y > 0$ has resulted in a majority of points being removed from pre-midnight ($+Y_{GSM}$) in the NH and post-midnight ($-Y_{GSM}$) in the SH, confirming the locational bias suggested from Fig. 4.2 (recall, these are locations where $B_y < 0$ is expected due to flaring). Second, this choice has overall resulted in the removal of 277 red and 64 blue points from the NH, and 64 red and 194 blue points from the SH. This has therefore removed mostly duskward (dawnward) flows in the northern (southern)

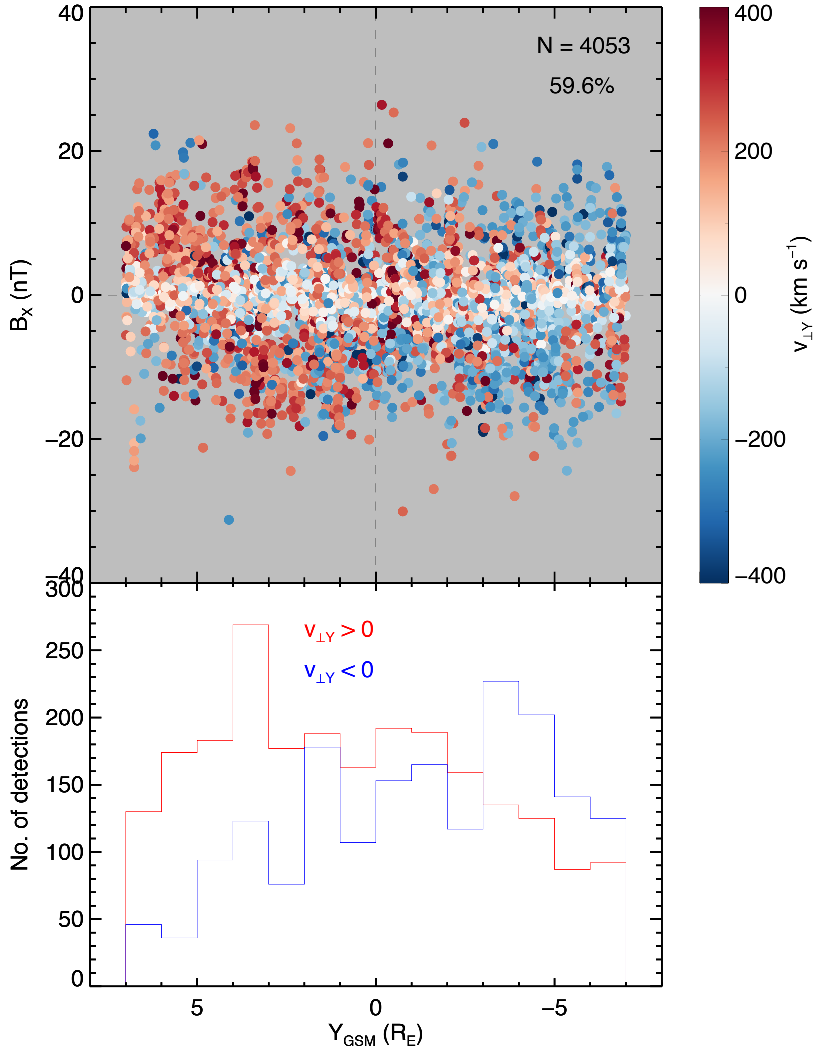

Figure 4.4: **Top:** The Y_{GSM} position of the observed fast flow detections plotted against the measured B_x value (circles), colour-coded in accordance with the measured $v_{\perp y}$. N is the total number of flows. The percentage indicates the proportion of 'symmetric' flows, such as flow which is duskward (red points) in a pre-midnight location ($+Y_{GSM}$) or flow which is dawnward (blue points) in a post-midnight location ($-Y_{GSM}$). **Bottom:** A histogram illustrating the Y_{GSM} distribution of the flows, split by observation of duskward ($v_{\perp y} > 0$, red) and dawnward ($v_{\perp y} < 0$, blue) flow.

hemispheres. Given that we expect dawnward (duskward) flow where $B_x > 0$ ($B_x < 0$) for IMF $B_y > 0$ conditions, this indicates how the percentage of flows having the 'expected' dusk-dawn flow would increase. A similar overall effect occurs in Fig. 4.5b and d when imposing local $B_y < 0$. Consequently, in the study of *Pitkänen et al.* (2013), using local B_y as a polarity filter would have 'artificially' increased the percentage of flows exhibiting the expected dusk-dawn asymmetry by removing a number of flows based largely on where

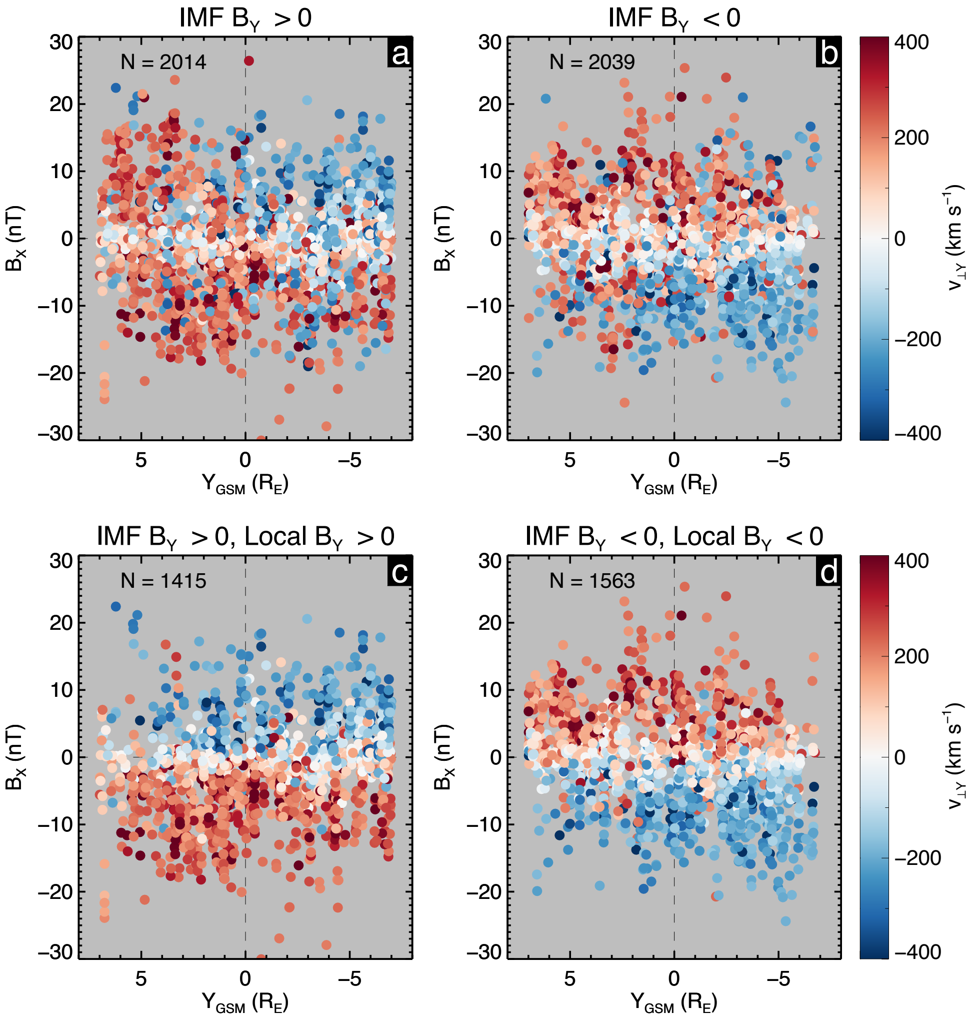

FIGURE 4.5: The Y$_{GSM}$ position of the observed fast flow detections plotted against the measured B_x value (circles), colour-coded in accordance with the measured $v_{\perp y}$. N is the total number of flows in each plot. The IMF B_y has been averaged over the 130 minutes prior to each flow, as done by *Pitkänen et al.* (2013). Shown in each panel are flows measured under a) IMF $B_y > 0$ conditions, b) IMF $B_y < 0$ conditions, c) IMF $B_y > 0$ with local $B_y > 0$, and d) IMF $B_y < 0$ with local $B_y < 0$.

they were observed.

To illustrate how this locational bias might manifest in an event study, we present in Figure 4.6 a time-series of data from a short interval consisting of a fast flow detection made by the Geotail spacecraft on 23 Feb 2003 at 13:22 UT, which illustrates this B_y issue.

As indicated in Fig. 4.6, this is an interval which occured during prolonged positive IMF B_y conditions. At the fast flow time (vertical black dashed line), Geotail detected a duskward

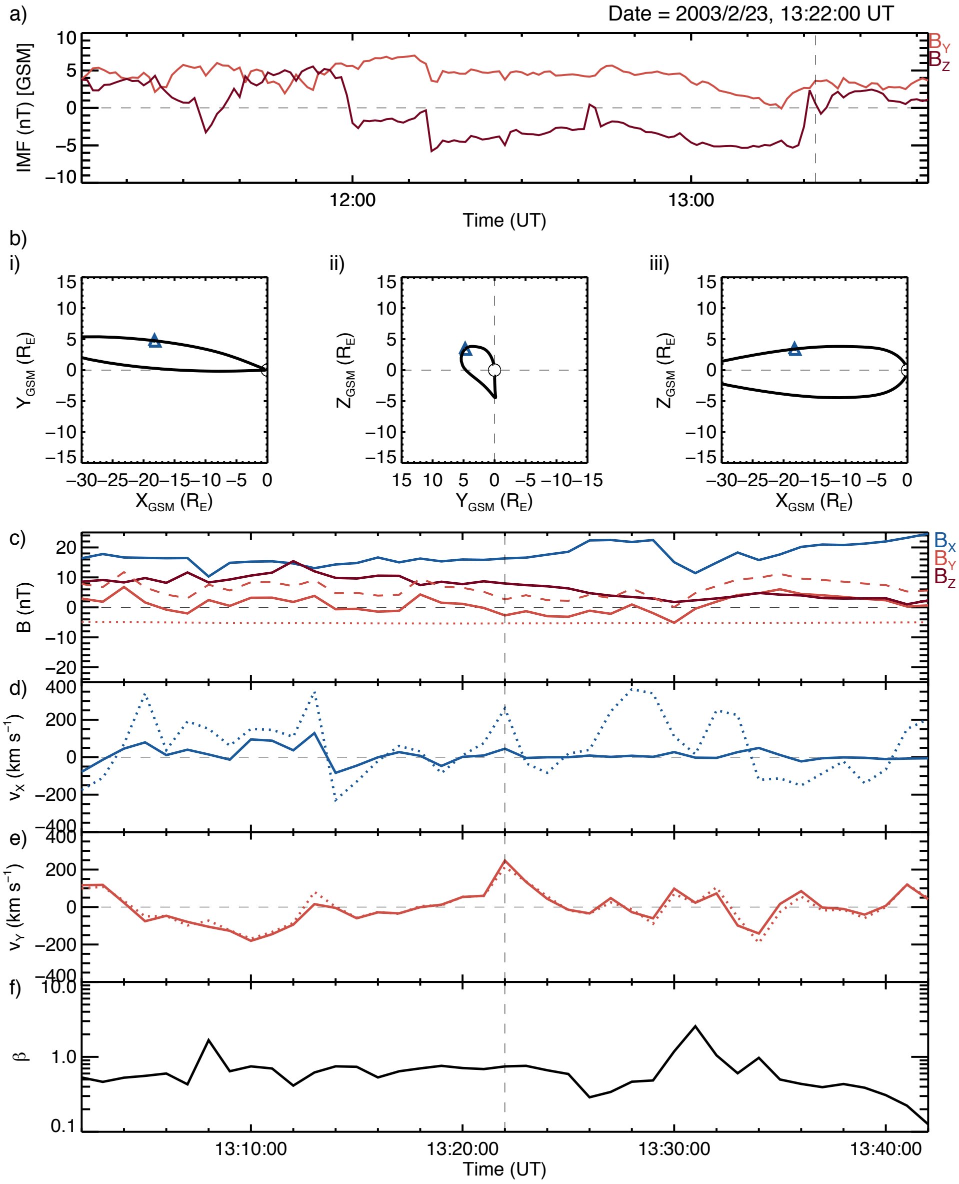

FIGURE 4.6: A fast flow detection observed by Geotail on 23 Feb 2003. Shown firstly is: a) the IMF B_y (B_z) data in orange (red) from 130-minutes prior to the fast flow time (dashed black line), and b) the location of Geotail at the fast flow time (blue triangle) in the i) X_{GSM}-Y_{GSM}, ii) Y_{GSM}-Z_{GSM}, and iii) X_{GSM}-Z_{GSM} planes. A TA15 modelled magnetic field line is also shown by the solid black line. In panel c) are the B_x, B_y and B_z components of the observed local magnetic field vector, in blue, orange, and red, respectively. The dotted orange line shows the TA15 modelled 'background' B_y, and the dashed orange line shows the 'penetrated B_y' (see text). In panel d) is the bulk earthward ion flow component, v_x, and in panel e) is the bulk ion dusk-dawn flow component, v_y (dotted lines). The field-perpendicular component of the flow in panels d) and e) is shown by the solid lines, indicative of the $\mathbf{E} \times \mathbf{B}$ convection. Finally, in panel f) is the ion plasma beta. The vertical black dashed line indicates the fast flow detection time.

($v_{\perp y} > 0$) flow (Fig. 4.6e) in the NH ($B_x > 0$) pre-midnight sector, which according to the study of *Pitkänen et al.* (2013) would be inconsistent with the untwisting hypothesis. This is a location, of course, where a 'background' $B_y < 0$ is expected (Fig. 4.2). Indeed, in Fig. 4.6c, this negative 'background' B_y, derived from TA15, is indicated by the dotted orange line. This represents the modelled B_y at the Geotail location, parameterised with a zero IMF B_y, 130-min averaged IMF B_z and appropriate solar wind dynamic pressure prior to each respective timestamp, and here taking into account the tailward dipole tilt of $\sim -3.8°$. The dashed orange line represents the 'penetrated' B_y ($B_{y,pen}$). This is calculated from subtracting the modelled B_y from the observed (local) B_y and provides an estimate for the 'amount' of penetration (i.e. excluding sources of B_y which are not due to IMF B_y penetration). At the fast flow time, $B_{y,pen}$ is positive, but B_y is briefly negative. In the study of *Pitkänen et al.* (2013), this duskward flow would have been excluded when the constraint of local $B_y > 0$ was imposed, with the suggestion that the flow itself may have been duskward due to a lack of the expected IMF B_y penetration, which would seem not to be the case, owing to $B_{y,pen} > 0$. Exclusion of a flow event such as this would have therefore contributed to increasing the percentage of flows exhibiting the expected dusk-dawn direction in their study, based on an incorrect assumption about the penetrated IMF B_y.

4.3.2 Asymmetry-Demonstrating Flow

In the situation presented in Fig. 4.6 (duskward flow in the pre-midnight sector), the extent to which this could be regarded as a flow which is 'inconsistent' with the untwisting hypothesis is, in-fact, questionable. The untwisting hypothesis, as considered by *Pitkänen et al.* (2013), relies on the assumption that the ionospheric convection cell to which the spacecraft is connected should be a factor of only hemisphere and the sense of IMF B_y. In the case of IMF $B_y > 0$, for example, the hypothesis dictates that a spacecraft in the NH would be located on the extended dawn cell (and observe dawnward flow), and a spacecraft in the SH would be located on the extended dusk cell (and observe duskward flow). This is true statistically, at least in the case that the spacecraft is close to midnight [*Grocott et al.* (2007); *Pitkänen et al.* (2013)]. In the above example, however, Geotail was located $\sim$5 R_E pre-midnight. If, therefore, Geotail was in a region which geomagnetically mapped to the

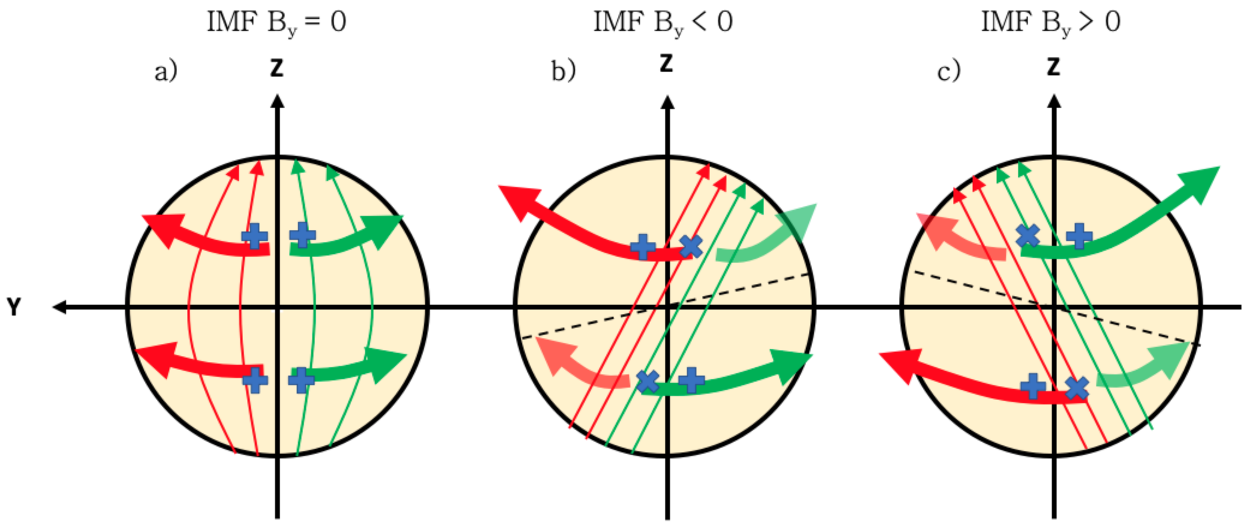

FIGURE 4.7: A schematic used to illustrate what is meant by an asymmetric flow. Three different magnetotail configurations for closed plasma sheet field lines are shown as though looking earthward in the Y$_{GSM}$-Z$_{GSM}$ plane from downtail, in simplified cases for a) IMF $B_y = 0$, b) IMF $B_y < 0$ and c) IMF $B_y > 0$ penetration. The thin lines are magnetic field lines, and the thick arrows indicate the direction of the convective plasma flows - a longer arrow indicates faster flow. Red (green) lines depict magnetic field lines and flow which are associated with the dusk (dawn) ionospheric convection cells. The blue X's represent the locations of flow observations which would be indicative of asymmetry, and the blue +'s represent flows which would demonstrate no asymmetry. The dashed line marks the neutral sheet. Adapted from *Grocott et al.* (2007).

NH dusk convection cell, rather than the extended dawn cell as the untwisting hypothesis presumes, then the observed duskward flow may have actually been perfectly consistent with the (IMF $B_y > 0$) larger-scale convection [e.g. *Pitkänen et al.* (2019)]. This concept is discussed and analysed further with respect to the case study presented in Chapter 5.

The above proposition highlights an important consideration regarding making statistical inferences about asymmetry and the tail untwisting process; that is, the location of any single point observations. A 'symmetric' flow, such as dawnward flow observed in the post-midnight sector, or duskward flow observed in the pre-midnight sector is, in itself, not explicitly indicative of magnetotail untwisting. To convey this point, in Figure 4.7, we present a schematic showing three magnetotail configurations in the case of IMF $B_y = 0$, IMF $B_y < 0$ and IMF $B_y > 0$ penetration. In each case, the topology of the field lines and associated convective earthward and dusk-dawn flows are shown. In Figs. 4.7b and c, the field line topology has been exaggerated to emphasise the sense of the IMF B_y penetration.

Firstly, let us consider the X in the top left quadrant of Fig. 4.7c. At this NH pre-midnight location, the observed flow would be dawnward, indicative of the asymmetric sense of the nightside flows directed azimuthally across the midnight sector. If we then consider the + in the top right quadrant of Fig. 4.7c, the observed flow would also be dawnward. Whilst this would be consistent with the asymmetric flows depicted in this schematic, this flow by itself is not indicative of a dusk-dawn asymmetry. This is illustrated by considering the + in the top right quadrant of Fig. 4.7a. At this post-midnight location, the observed flow would also be dawnward as in Fig. 4.7c, but there is no large-scale dusk-dawn asymmetry in the flows in this case. Furthermore, if a spacecraft was located duskward of the X in the top left quadrant of Fig. 4.7c, such that it was now associated with the (red) field lines of the dusk convection cell, then the observation of duskward flow would still be consistent with an IMF $B_y > 0$ configuration (i.e. the possibility highlighted in relation to the Geotail example above).

Our solution to the above conundrum is a simple suggestion; we remove all ~60% of the 'symmetric' flows from our fast flow dataset, and instead focus only on those flows which explicitly demonstrate asymmetry (that is, dawnward flow in the pre-midnight sector or duskward flow in the post-midnight sector, in-effect constraining the spacecraft observations to only be associated with the asymmetric 'extended' convection cells in a large-scale context). This choice reduces the total number of fast flow observations to 1639. We provide an overview of a number of key parameters associated with these detections in the following section.

4.3.3 Statistical Overview of the Asymmetric Fast Flows

In this section, we provide a statistical overview of our 1639 'asymmetric' fast flow detections. To begin, in analogy to the study of *Pitkänen et al.* (2013), we plot the dusk-dawn convective component of our flows, $v_{\perp y}$, against the B_x component of the magnetic field, thresholded by the sign of the 130-min mean-averaged IMF B_y, in order to examine what proportion of these asymmetric flows appear to be exhibiting the expected dusk-dawn asymmetry. Our flows are colour-coded based on their Y_{GSM} position, in order to clearly

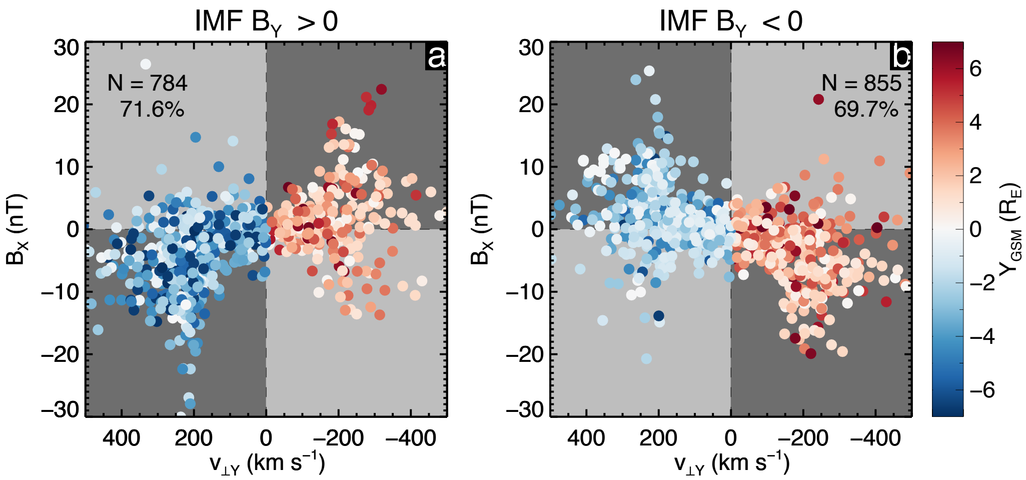

FIGURE 4.8: The dusk-dawn convective flow velocity, $v_{\perp y}$, plotted against B_x for each fast flow detection (circles), colour-coded according to the Y$_{GSM}$ position of the spacecraft, for a) IMF $B_y > 0$, and b) IMF $B_y < 0$. The darker-shaded regions indicate the expected $v_{\perp y}$ direction based on the prevailing IMF B_y conditions. N indicates the total number of detections on each plot, with the percentage illustrating the fraction of those in the darker-shaded (expected) regions.

indicate the asymmetric nature of the flows. The results of this analysis are shown in Figure 4.8.

Fig. 4.8 illustrates that 71.6% of the 784 fast flow detections for IMF $B_y > 0$, and 69.7% of the 855 fast flow detections for IMF $B_y < 0$, respectively, exhibit the expected dusk-dawn flow direction. These percentages are in good agreement with the (non-local B_y constrained) results of *Pitkänen et al.* (2013). Additionally, we show that this result holds for asymmetric flows, some of which occur as far away from midnight as $\pm$ 7 R$_E$. It is worth noting, however, that ~70% is not indicative of a strong correlation with IMF B_y; if completely uncorrelated we should still expect the flow direction to agree with the IMF B_y direction 50% of the time, purely by chance. Inherently, this result means that ~30% of flows do not have the expected dusk-dawn direction, with 'scattering' into the unexpected quadrants. In the remainder of this thesis, we therefore wish to answer the question: *what is responsible for this significant fraction of flows which do not exhibit the expected dusk-dawn sense*?

As a starting point for this investigation, we firstly choose to group our flows (separately) by *agree* (AG) and *disagree* (DAG). AG flows consist of flows which are dawnward (duskward) in the northern (southern) hemisphere for IMF $B_y > 0$, or duskward (dawnward) in the northern (southern) hemisphere for IMF $B_y < 0$. By contrast, DAG flows consist of flows which are duskward (dawnward) in the northern (southern) hemisphere for IMF $B_y > 0$ or dawnward (duskward) in the northern (southern) hemisphere for IMF $B_y < 0$. With our flows divided into these two categories, we then examine the distributions of a number of key parameters, the importance of which are discussed below. These parameters are: a) X_{GSM}, b) Y_{GSM}, c) |IMF B_y|, d) $|B_{y,pen}|$, e) $|B_x|$, f) B_z, g) $v_{\perp x}$ and h) $|v_{\perp y}|$. For each parameter, in Figure 4.9 we plot histograms of the AG and DAG distributions, normalised to the number of flow detections in each category. Here we provide an overview of the data; we provide more in-depth discussion of this in Chapters 6 and 7.

Fig. 4.9 overall reveals a number of interesting features when comparing the AG and DAG flow populations. Firstly, Figs. 4.9a and b reveal that in general, there is little difference between the locations at which the flow populations are observed in both X_{GSM} and Y_{GSM}; perhaps with the exception of $-2 \leq Y_{GSM} < -1$ R_E where over 20% of DAG flows are observed. A separate, manual inspection of the the flows at this Y-range suggested that there was a significant population of IMF $B_y < 0$ DAG flows being observed where $|B_x|$ was small, implying that they were observed close to the neutral sheet ($B_x = 0$). We address the potential issues associated with flow observations being made close to the neutral sheet below. In general, the largest proportion of flows are observed closer to midnight, with detections decreasing towards the dusk-dawn flanks, in agreement with *Baumjohann et al.* (1990).

Figs. 4.9c and d suggest that generally, AG (DAG) flows occur when |IMF B_y|, and in turn, our estimate of the 'penetrated' field, $|B_{y,pen}|$ (defined in Section 4.3.1) is stronger (weaker). Indeed, almost 35% of DAG flows were observed when $|B_{y,pen}|$ was less than 1 nT in magnitude, compared with around 16% of AG flows. The mean $|B_{y,pen}|$ is also around twice as large for the AG (~4 nT) than DAG (~2 nT) flows. As alluded to by *Pitkänen et al.* (2013), this suggests that 'weaker' IMF B_y penetration may be unable to sufficiently direct some dusk-dawn flows in a direction which agrees with the untwisting hypothesis. We expand on this discussion in Chapters 6 and 7.

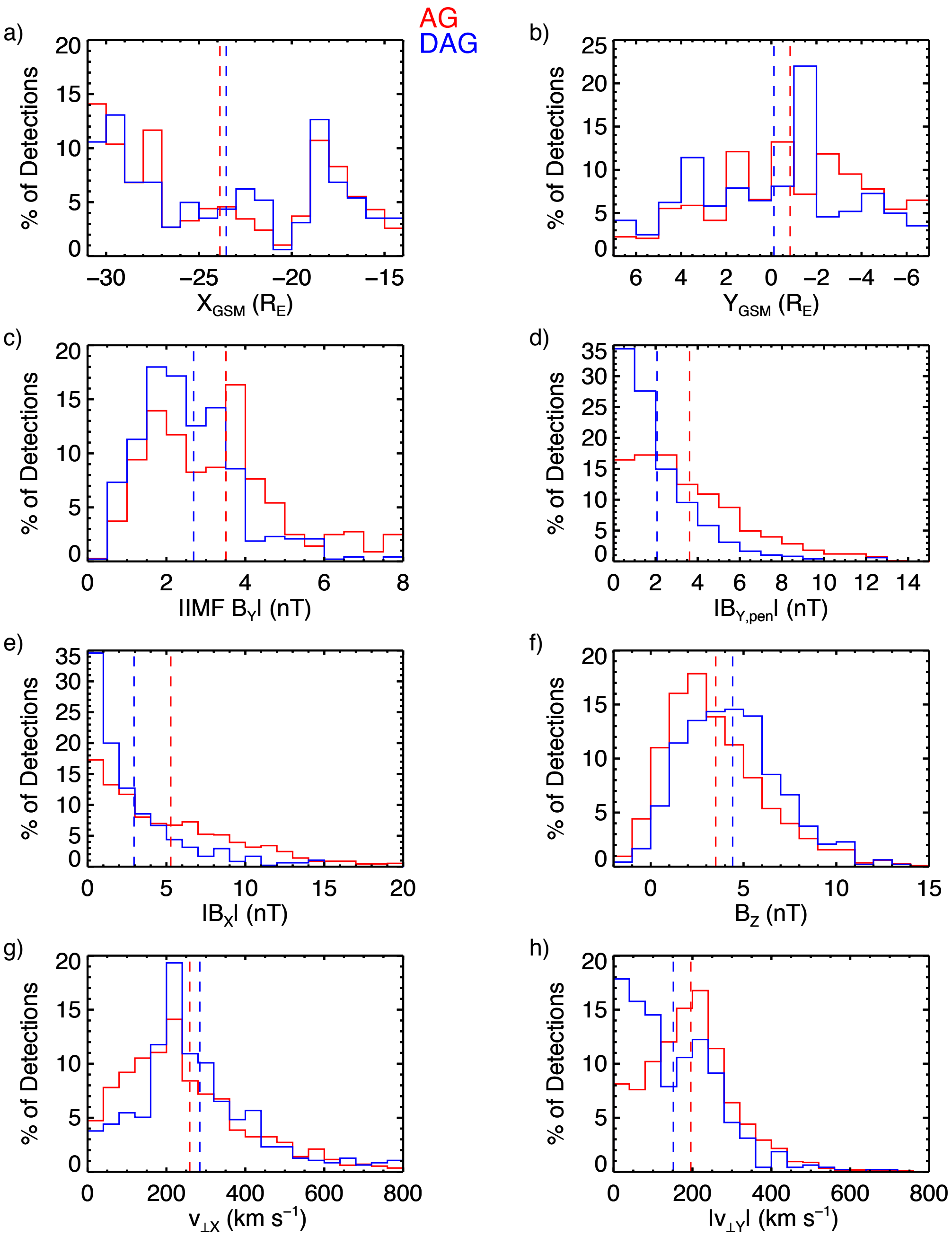

FIGURE 4.9: Normalised histograms of a number of key parameters, when the fast flow detections are split into their respective AG (red) and DAG (blue) categories (see text). The vertical dashed lines in each plot indicate the mean data value.

Fig. 4.9e shows that ~35% of DAG flows were detected when the measured $|B_x|$ was very small (< 1 nT), suggesting observation close to the neutral sheet, compared with just ~17% of AG flows. It is particularly noticeable how much steeper the distribution of $|B_x|$

is for the DAG flows, which have a mean $|B_x|$ of 3 nT; around 2 nT smaller than AG flows. It is perhaps intuitive that the highest percentages of fast flow detections, regardless of them being AG or DAG, would be observed closer to the neutral sheet, as this is where β and $v_{\perp x}$ (which help to define our fast flows) are expected to be larger [*Baumjohann et al.* (1989)], and this is also apparent from inspection of Fig. 4.8. As will be explored in Chapters 5 and 7, however, the neutral sheet is a dynamic region which can influence dusk-dawn flow [*Volwerk et al.* (2008); *Lane et al.* (2021)] and thus may be able to explain the high proportion of DAG flows observed there.

Fig. 4.9f illustrates the distribution of observed B_z. Increases in B_z are often observed during times of enhanced or transient magnetotail dynamics, when magnetic field lines dipolarise, turning perpendicular to the current sheet as they are convected earthward by bursty flows [e.g. *Ohtani et al.* (2004); *Schmid et al.* (2011)]. Fig. 4.9f suggests that AG flows, in particular, tend to be observed when the measured B_z is lower, which could be indicative of weaker dipolarisation. Conversely, the distribution of DAG flows has a much broader peak and a mean B_z ~1 nT larger than AG flows, which could be indicative of stronger dipolarisation. We note, however, that a proportion of AG flows are still observed in concert with larger (10+ nT) values of B_z. The link between B_z and our fast flow detections is discussed and analysed further in Chapters 6 and 7.

Finally, Figs. 4.9g and h show the distributions of $v_{\perp x}$ and $|v_{\perp y}|$, respectively. It is apparent how a larger proportion of AG flows tend to have a lower $v_{\perp x}$ and greater $|v_{\perp y}|$, whereas a higher proportion of DAG flows have a greater $v_{\perp x}$ and a lower $|v_{\perp y}|$. This is particularly evident around 200 km s^{-1}. Of course, our flows are defined based on a minimum 200 km s^{-1} threshold of $v_{\perp xy}$, and thus $v_{\perp x}$ and $v_{\perp y}$ are not independent (i.e. $v_{\perp x}$ $<<$ 200 km s^{-1} implies that $|v_{\perp y}| \approx 200$ km s^{-1}, and vice versa, for a flow detection to be met). Flows with enhanced $v_{\perp x}$ components (such as BBFs) are typical of more geomagnetically active periods [e.g. *Angelopoulos et al.* (1994)], when dusk-dawn asymmetry is known to be suppressed [e.g. *Ohma et al.* (2018)], which may explain the observed trends in $v_{\perp x}$ and $|v_{\perp y}|$. An inspection of the AE indices for the AG and DAG flow populations, however, suggested no apparent differences. Overall, Figs. 4.9g and h appear to suggest that flows with a more significant dusk-dawn direction (and perhaps a weaker earthward component) may have a greater probability of having the expected dusk-dawn direction.

Ultimately, the statistical overview presented in Fig. 4.9 has suggested that there are intrinsic differences between the populations of AG and DAG flows when inspecting key parameters related to the nature of the flows, despite there also being (perhaps expectedly) a significant degree of overlap and relative variability between the two distributions. This would make it difficult, based on the value of a single parameter, to suggest that a given flow detection would belong to the AG or DAG category without additional knowledge. To attempt to quantify this degree of overlap, we performed a simple two-sample Kolmogorov-Smirnov (K-S) test on each parameter, which finds the maximum distance between the cumulative distribution functions of the (unbinned) AG and DAG flow distributions [see Chapter 14 of *Press et al.* (1992)]. With the exception of Fig. 4.9a, the associated significance levels were all approximately 0, implying that the AG and DAG flows do not arise from the same underlying population.

4.4 Summary

In this chapter, we have used the TA15 magnetic field model to demonstrate the effect of magnetotail flaring on B_y in the Earth's magnetotail. We showed that using solely the local B_y as an inference for IMF B_y penetration is inappropriate (with the exception of observations extremely close to $\mathrm{Y}_{GSM} = 0$), due to the fact that the flaring appears to dominate further away from midnight and the neutral sheet (the apparent nature of this is highlighted further in the next chapter). We have also demonstrated the locational bias introduced by using the local B_y sign as a filter, as applied to our dataset of magnetotail fast flow 'detections', and discussed how this was not considered in the study of *Pitkänen et al.* (2013). In their study, use of the local B_y as a 'filter' likely increased the percentage of flows exhibiting the expected dusk-dawn asymmetry, by removing flows which didn't based largely on where they were observed. This also left issues regarding the symmetry of the observed flow. We argued that only flows which clearly demonstrate an asymmetry are appropriate to investigate in a study of dusk-dawn asymmetry associated with magnetotail untwisting. We hence presented a statistical overview of our asymmetric flow detections. Close inspection suggested that there were clear differences between flows which 'agreed' and 'disagreed' with the expected dusk-dawn asymmetry based on the untwisting hypothesis when inspecting a number of parameters related to the flows. Notably, a greater proportion of agree flows tended to occur when |IMF B_y|, $|B_{y,pen}|$ and $|v_{\perp y}|$ were larger than for disagree flows. Disagree flows, meanwhile, tended to be observed when $|B_x|$ was smaller than it was for agree flows, implying greater proximity to the neutral sheet ($B_x = 0$), and when B_z was larger, which could be indicative of more significant dipolarisation.

The aim of the research presented in this thesis is therefore to try and understand why the ~30% of 'disagree' asymmetric flows (Fig. 4.8) do not exhibit the expected dusk-dawn asymmetry. Our analysis in Fig. 4.9 revealed particularly interesting differences between the agree and disagree flow populations when examining $|B_x|$ and B_z. We therefore choose to consider these parameters in more detail, through examination of two case studies in the next two chapters.

In Chapter 5, we study Cluster observations of variable dusk-dawn flow containing instances of very small $|B_x|$ which occurred when C1 was repeatedly crossing the neutral sheet at $\mathrm{Y}_{GSM} \approx 6$ R_E. We discover that a localised 'flapping' motion of the neutral sheet appears to override (or prevent) the expected duskward convection in the SH.

In Chapter 6, we study Cluster observations of a strong dipolarisation (B_z increase) at $\mathrm{Y}_{GSM} \approx -5$ R_E in association with a duskward flow burst, which appears to be independent of the large-scale asymmetry in the convection. We attribute the flow to localised dynamics accompanied by transient changes in the local B_y and B_z. This event is also discussed with respect to a statistical superposed epoch analysis of our fast flow detections, which allows us to examine the average time variability of a number of parameters.

Finally, in Chapter 7, we return to the statistics of our fast flow detections, and attempt to examine the impact of dynamic phenomena such as flapping on the percentage of flows exhibiting the expected dusk-dawn asymmetry.

Chapter 5

Dynamics of Variable Dusk-Dawn Flow Associated with Magnetotail Current Sheet Flapping

The work presented in this chapter is formed from the published work of *Lane et al.* (2021).

5.1 Introduction

As discussed previously in Chapters 2 and 4, prolonged non-zero IMF B_y conditions are expected to introduce a twist into the magnetotail, and a subsequent dusk-dawn flow asymmetry associated with the 'untwisting' of newly reconnected closed field lines [*Grocott et al.* (2007); *Pitkänen et al.* (2013)]. These studies showed that for IMF $B_y > 0$ conditions, in the NH, the flows are expected to exhibit a dawnward component, and in the SH, a duskward component - with an opposite sense for IMF $B_y < 0$. In this chapter we present Cluster spacecraft observations of an interval of dynamic magnetotail behaviour from 12 October 2006 where this expected dusk-dawn flow dependence is not observed, and thus the event in question constitutes a fraction of the $\sim$30% of flows which do not appear to be IMF B_y-controlled and is therefore not in agreement with the untwisting hypothesis. In particular, we highlight the problematic nature of the observation of dawnward flow, in relation to the pre-midnight location of Cluster. We instead suggest that the flows are being driven by local perturbations due to a dynamic flapping of the neutral current sheet.

Flapping of the neutral sheet is best described as a sinusoidal-like variation in B_x of up to tens of nanoTesla, whereby an observing spacecraft would be expected to measure continual changes in the sign of B_x [*Runov et al.* (2009)], indicating crossings of the neutral sheet [see Fig. 1 of *Rong et al.* (2015)]. Characteristic times of such flapping can occur on a timescale of a few seconds, but more commonly several minutes [see e.g. *Sergeev et al.* (2006), Table 2 of *Wei et al.* (2019)]. Drivers of current sheet flapping have been investigated previously, with possible causes ranging from changes in solar wind or IMF conditions [*Runov et al.* (2009)] to periodical, bursty magnetotail reconnection [*Wei et al.* (2019)]. Notably, studies such as *Volwerk et al.* (2008) and *Kubyshkina et al.* (2014) have implied that current sheet flapping can occur in conjunction with variable dusk-dawn flow; potentially overriding the direction of the expected large-scale background flow and preventing any possible IMF B_y-control.

In this study, the B_y component of the concurrent upstream IMF had been largely positive for several hours prior to interval of Cluster observations. During this interval, C1 observed oscillations in the magnetic field B_x component, which we attribute to current sheet flapping, concurrent with a series of convective fast flows with significant and variable dusk-dawn components. Observations from C2, C3 and C4 indicated that the spacecraft were at a pre-midnight location where magnetotail flaring was dominating over IMF B_y-control of the flows, resulting in the expectation of (symmetrical) duskward return flows [*Pitkänen et al.* (2019)]. In the SH, such duskward flow was measured by C3, but not observed by C1, which instead measured flows with significant dawnward components. These dawnward flows were therefore inconsistent with any expectation that the flow was governed by flaring and, owing to evidence of a large-scale IMF $B_y > 0$ ionospheric convection pattern, could also not be explained by the magnetotail untwisting hypothesis (for which the observed dawnward flow would require IMF $B_y < 0$). We instead suggest that the current sheet flapping was exciting the variable dusk-dawn flow, overriding the expected large-scale net duskward convection at the location of C1.

5.2 Instrumentation and Data Sets

The magnetospheric observations presented in this case study were made by Cluster (see Section 3.1.2.1 and references therein). The FGM data have been 1 s median-averaged, and the HIA velocity data are shown at spin-res (∼4 s). Where we have combined these datasets to produce parameters such as the plasma beta and field-perpendicular velocity, we have resampled both the magnetic field and plasma data to 5 s res. All data are presented in GSM coordinates.

The interval of study presented in this chapter occurred between 00:00 - 00:55 UT on 12 Oct 2006. At 00:00 UT, the Cluster spacecraft were located pre-midnight in the magnetotail plasma sheet. C1 was located at ($X_{GSM} = -14.7$, $Y_{GSM} = 6.0$, $Z_{GSM} = -1.2$) R_E, C2 at ($X_{GSM} = -14.2$, $Y_{GSM} = 7.5$, $Z_{GSM} = -0.7$) R_E, C3 at ($X_{GSM} = -13.9$, $Y_{GSM} = 7.0$, $Z_{GSM} = -2.1$) R_E and C4 at ($X_{GSM} = -13.2$, $Y_{GSM} = 6.2$, $Z_{GSM} = -0.8$) R_E. This is depicted in Fig. 5.1a by the coloured triangles, including the spacecraft trajectories from 00:00 - 00:55 UT by the solid lines. In Fig. 5.1b we show a zoomed-out version of Fig. 5.1a, where the Earth and a traced magnetic field line achieved using TA15 (Section 3.4) are shown. TA15 was parameterised using mean-averaged P_{dyn}, IMF B_y and IMF B_z data from 1-hour prior to 00:28 UT (the beginning of our specific interval of interest, discussed in the following section). These values were P_{dyn} = 1.56 nPa, IMF B_y = +1.56 nT, IMF B_z = −2.17 nT. The calculated 'N-index' was ∼0.4, and there was also a tailward dipole tilt of $\sim -12°$.

The ionospheric observations in this study were provided by SuperDARN (see Section 3.3.1 and references therein). We use 2-min ionospheric convection maps created by fitting the LOS velocity data to an eighth order expansion of the electrostatic potential, implemented via RST. These data are supplemented with values derived from the statistical RG96 model, parameterised here with a nominal southward IMF and zero IMF B_y, to ensure that a background model with no pre-existing IMF B_y influence is used. This is to ensure that any IMF B_y-associated asymmetry in the maps is driven by the radar data from our interval of study, and not the background model. We also tested the fitting using

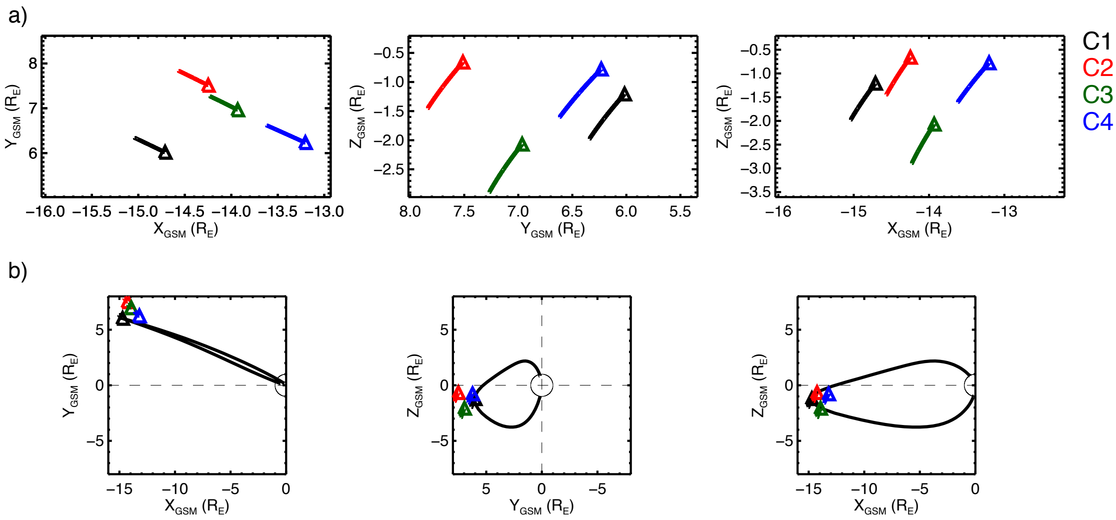

FIGURE 5.1: a) locations of Cluster in the X_{GSM}-Y_{GSM}, Y_{GSM}-Z_{GSM} and X_{GSM}-Z_{GSM} planes from left to right respectively, at 00:00 UT. The trajectories are shown by the solid lines, and colour coded according to the key on the right. b) As in a), zoomed-out and showing the Earth and a closed TA15 magnetic field line which passes through the location of C1.

the *Thomas and Shepherd* (2018) (TS18) model, and found that this had little impact on the maps and no impact on our conclusions.

5.3 Observations

5.3.1 IMF and Cluster Observations

Figure 5.2 presents an overview of the spacecraft observations. In Fig. 5.2a, we show IMF B_y and IMF B_z time-series data, from 20:00 UT on 11 Oct 2006 to 01:00 UT on 12 Oct 2006. These data show that IMF B_y was mostly positive for several hours before our interval of interest, with IMF B_z mostly negative. Of particular note, there were three small intervals of negative IMF B_y at ~21:35 UT, 23:00 UT and 23:40 UT, and we discuss the implications of this in Section 5.4.

In Fig. 5.2b, we show the Cluster magnetic field and plasma measurements from 00:00 - 00:55 UT. At ~00:06 UT, C1 crossed from the northern ($B_x > 0$) to southern ($B_x < 0$)

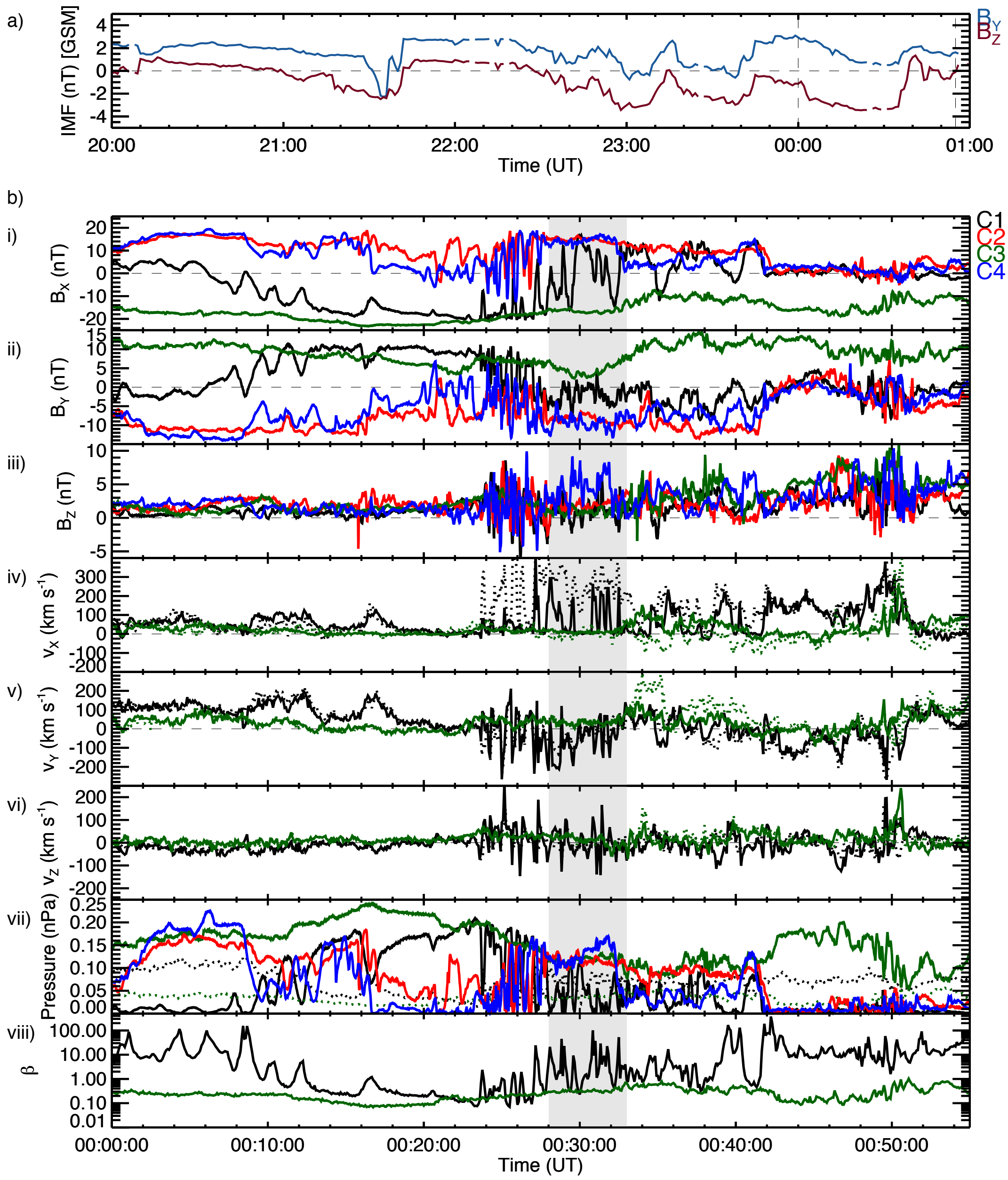

FIGURE 5.2: a) IMF time series data for B_y (blue) and B_z (red), from 20:00 UT on 11 Oct 2006 to 01:00 UT on 12 Oct 2006. The vertical dashed lines indicate the start (00:00 UT) and end (00:55 UT) of the Cluster data interval. b) The Cluster spacecraft measurements. Shown first is the local magnetic field data, i) B_x, ii) B_y, iii) B_z, followed by bulk ion velocity data, iv) v_x, v) v_y and vi) v_z (dotted lines). The field-perpendicular component of the flow (a proxy for $\mathbf{E} \times \mathbf{B}$ convection) is shown by the solid lines. The magnetic and ion thermal pressures are shown by the solid and dotted lines, respectively, in panel vii). The ion plasma beta, β, is shown in panel viii). Data are labelled according to the colour-coded key on the right. The grey shaded time-interval marks a time of interest (discussed in text).

hemisphere (Fig. 5.2b(i)), coincident with the observed B_y changing from negative to positive (Fig. 5.2b(ii)). Up until ~00:24 UT, C2 and C4 (NH) observed $B_y < 0$, and C1 and C3 (SH) observed $B_y > 0$. Such observations are consistent with the expected B_y due to magnetotail flaring [*Fairfield* (1979)]. Occasionally, a spacecraft encountered the neutral sheet ($B_x \approx 0$) and measured $B_y \approx 0$. We discuss the significance of this in Section 5.4. During this time, the bulk earthward flow (v_x) observed by C1 and C3 remained low in magnitude ≤ 100 km s^{-1} (Fig. 5.2b(iv)), the dusk-dawn (v_y) component of the flow (Fig. 5.2b(v)) remained weakly duskward ($v_y > 0$), and the north-south (v_z) component of the flow (Fig. 5.2b(vi)) remained close to 0.

After ~00:24 UT, C1 observed enhanced earthward flow ($v_x > 300$ km s^{-1}), variable v_y and v_z flow, coincident with variable B_x. These B_x fluctuations of several nT in magnitude were also observed by C2 and C4, but not C3, and were typical of current sheet flapping [e.g. *Runov et al.* (2009)]. Variations in both B_y and B_z seen by C1, C2 and C4 were also apparent. Again, C3 did not observe such signatures. Between 00:28 - 00:33 UT (grey shaded region), C1 started to repeatedly and rapidly cross the current sheet, as experienced just prior by C2 and C4, whilst measuring enhanced convective earthward ($v_{\perp x}$) and dusk-dawn ($v_{\perp y}$) flow. We focus on this interval of current sheet crossing and variable flow and present this in greater detail in Figure 5.3. We further note that across the entire interval, the ion plasma β (Fig. 5.2b(viii)) observed by C3 remained above ~0.1 and generally $\gg 0.1$ for C1 (up to ~100), indicating the presence of C1 at the centre of the current sheet, where β is larger as a consequence of larger thermal and smaller magnetic pressures [*Baumjohann et al.* (1989)].

Fig. 5.3(i) illustrates the extent of the large-amplitude B_x variations observed by C1, which varied between ~ -16 and 17 nT. The B_y component (Fig. 5.3(ii)) observed by C1 generally remained negative yet variable, with a number of negative enhancements (e.g. 00:29:30 UT), and a few small positive excursions. In particular, we note that C1 tended to observe $B_y < 0$ when below the neutral sheet ($B_x < 0$). Such an observation is inconsistent with what would be expected based on spacecraft location and any expectation that positive IMF B_y may have penetrated into the magnetotail, as will be discussed in Section 5.4.

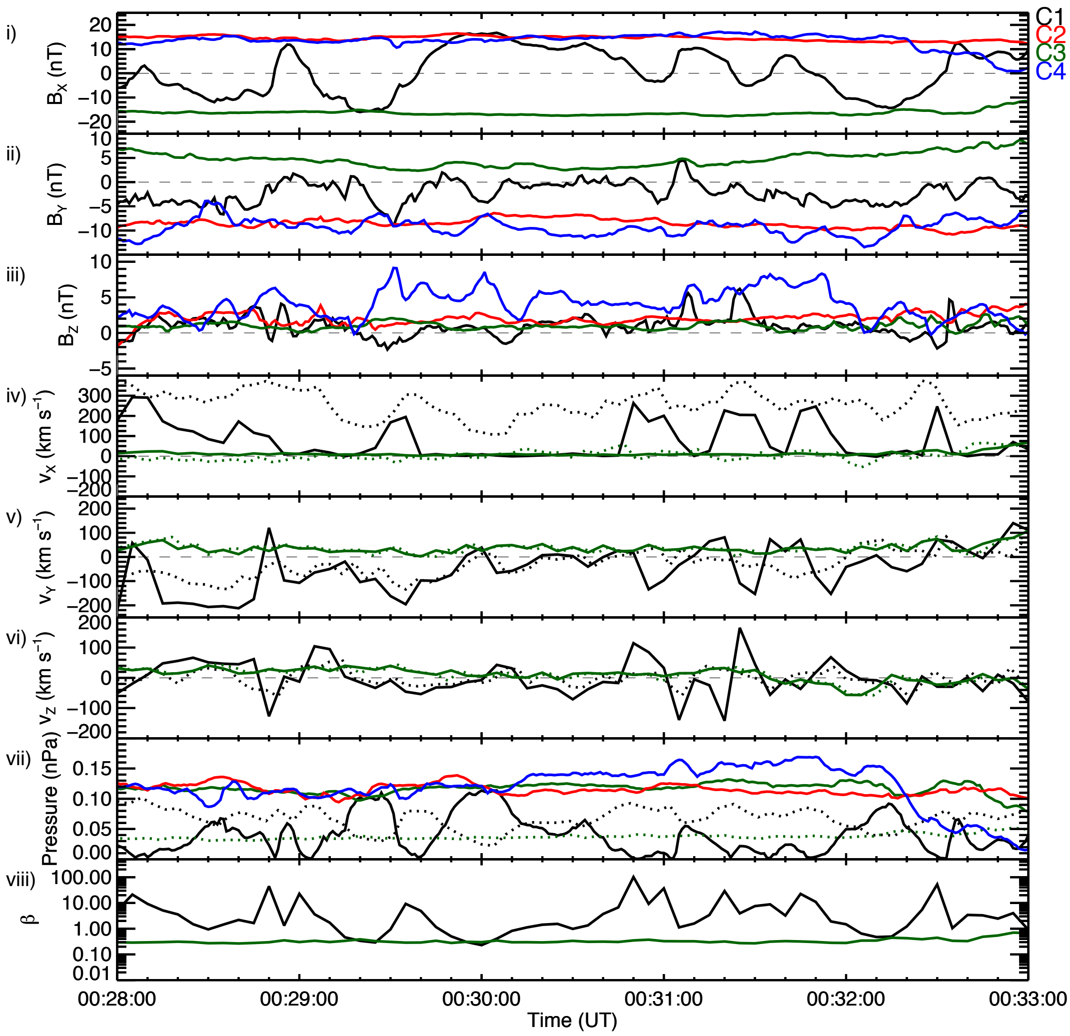

FIGURE 5.3: As in Fig. 5.2b, but for 00:28 - 00:33 UT.

Unlike C1, C2-C4 measured generally steady B_x during this five-minute interval; C2 and C4 measured positive B_x (and negative B_y), indicating that they resided above the neutral sheet, and C3 measured negative B_x (and positive B_y), indicated that it resided below the neutral sheet. These observations are consistent with the larger-scale B_y at the spacecraft location being dominated by magnetotail flaring. This C3 observation is in contrast to the C1 measurement of negative B_y below the neutral sheet. We suggest that these C1 B_y observations imply the existence of a localised 'kink' in the magnetic field, the ramifications of which are discussed in Section 5.4.

When below the neutral sheet ($B_x < 0$), C1 generally observed negative (dawnward)

$v_{\perp y}$ (Fig. 5.3(v)) with a magnitude varying between 100 and 200 km s^{-1}. When above the neutral sheet ($B_x > 0$), C1 mostly observed positive (duskward) $v_{\perp y}$. Irrespective of hemisphere, C1 also observed near continual $v_x > 200$ km s^{-1} flow, peaking close to 400 km s^{-1}, with coincident $v_{\perp x}$ peaks of over 200 km s^{-1}. By contrast, C3 only observed very weak (≤ 50 km s^{-1}) duskward flow and negligible earthward flow.

The implications of these observations in the context of the upstream IMF conditions and large-scale magnetospheric morphology are discussed in Section 5.4.

5.3.2 Ionospheric Convection Observations

To provide the large-scale context in which we can interpret the more localised observations from Cluster, we show ionospheric convection observations in Figure 5.4. In Fig. 5.4a we present a series of four 2-minute integration SuperDARN maps of the NH ionospheric convection pattern, beginning at 00:24 UT and ending at 00:34 UT, which encompasses our interval of Cluster data. In all maps, plasma is flowing anti-sunward across the polar cap at high latitudes, also with a noticeable duskward sense. The direction of the convection reverses in the pre-midnight sector before returning sunward at lower latitudes. The typical symmetrical twin-cell convection pattern has overall been rotated clockwise, with the dawn cell extending across into the pre-midnight sector, indicative of convection driven under a positive IMF B_y [e.g. *Reistad et al.* (2016, 2018)].

Fig. 5.4b shows two 2-minute integration SuperDARN maps of the SH ionospheric convection pattern, beginning at 00:30 UT and ending at 00:34 UT. Despite the coverage of radar data being much sparser than in the northern hemisphere, there are data in the pre- and post-midnight sectors which appear to be influencing the location of the flow reversal region at the nightside end of the dusk cell. Opposite to the NH case, it is the dusk cell in the SH which is extending towards, or just beyond, the midnight meridian, consistent with a large-scale positive IMF B_y influence [*Pettigrew et al.* (2010)].

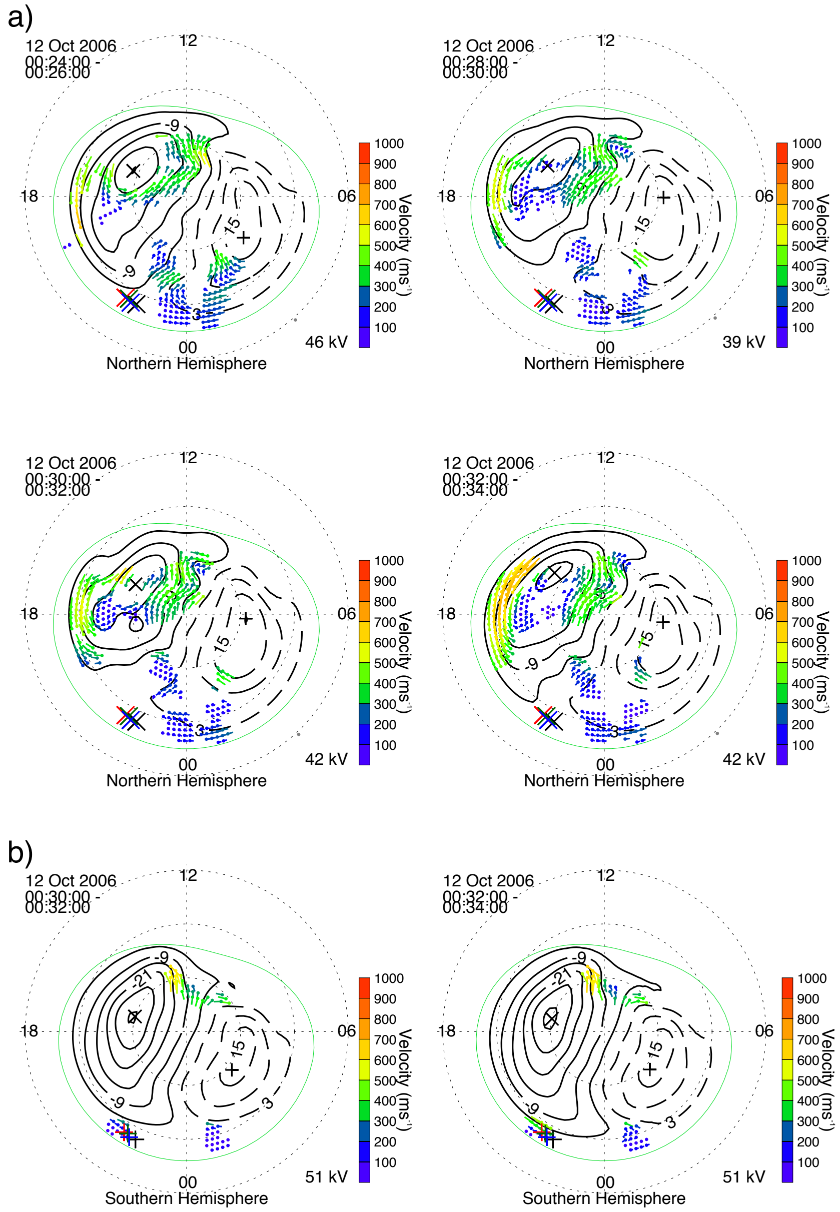

FIGURE 5.4: Maps of the ionospheric plasma convection derived from SuperDARN observations. Midnight is to the bottom of each map, noon to the top, dusk to the left and dawn to the right. The dashed black circles are marked for every 10° of magnetic latitude. The thicker solid and dashed black lines represent the plasma streamlines and are the contours of the electrostatic potential. Fitted vectors are plotted at the locations of LOS radar observations and colour-coded based on the magnitude of their velocity. a) Four 2-minute NH maps from 00:24 - 00:26, 00:28 - 00:30, 00:30 - 00:32 and 00:32 - 00:34 UT, respectively. b) Two 2-minute SH maps from 00:30 - 00:32 and 00:32 - 00:34 UT, respectively. On each northern (southern) hemisphere map, the footpoints of the Cluster spacecraft constellation are shown by the Xs (+s), mapped using TA15.

5.4 Analysis and Discussion

We have presented observations of a dynamic interval of plasma flows and magnetic field in the Earth's magnetotail. In this section we will discuss our reasoning for interpreting the flows as being inconsistent with the large-scale convection expected based on the spacecraft location and magnetotail untwisting considerations, and our alternative interpretation of their relationship to current sheet flapping.

5.4.1 Evidence for an Inconsistency with Large-Scale Magnetotail Untwisting

During the five-minute interval studied (00:28 - 00:33 UT), C1 measured a continually fluctuating B_x component (Fig. 5.3(i)), indicative of multiple crossings of the neutral sheet. C1 also measured a series of earthward convective magnetotail fast flows with variable dusk-dawn components. The data in Fig. 5.3(i) and Fig. 5.3(v) illustrate that when B_x was positive (negative), a duskward (dawnward) $v_{\perp y}$ was generally observed. The dawnward flow in the SH, in particular, is inconsistent with the expected symmetric duskward flow at the pre-midnight location of C1 which was, however, observed by C3. This suggests that the typical 'symmetrical' Dungey Cycle return flow [e.g. *Kissinger et al.* (2012)] cannot provide an explanation for the flow observations made by C1. We thus turn our attention to other possible explanations which we explore in detail, below.

The data in Fig. 5.3(ii) show that C1 tended to observe negative B_y. According to the magnetotail untwisting hypothesis [e.g. *Pitkänen et al.* (2015)], these flow and magnetic field observations are consistent with a negative IMF B_y penetration. Contrastingly, the IMF data presented in Fig. 5.2a revealed that IMF B_y was generally positive for several hours prior to fast flow interval (00:28 - 00:33 UT). Based on the IMF data alone, therefore, it would be reasonable to expect that a positive IMF B_y will have penetrated into the magnetosphere. In that case, the flows observed by C1 would have a dusk-dawn sense that is not explained by current theoretical models of magnetotail untwisting, meaning they are not IMF B_y-controlled [*Grocott et al.* (2007)]. Thus, in order to determine whether the observed flow is IMF B_y-controlled or not, it is therefore of vital importance to determine which sense of IMF B_y is governing the large-scale magnetospheric dynamics.

This issue is, firstly, made uncertain based on the fact that there were three small negative IMF B_y excursions prior to the interval of Cluster data. Uncertainties in IMF B_y propagation times [e.g. *Case and Wild* (2012)] have been cited as an explanation for observing an unexpected asymmetry [e.g. *Pitkänen et al.* (2013)]. Studies such as *Tenfjord et al.* (2015, 2017) and *Case et al.* (2018), for example, have suggested a reconfiguration time (to the prevailing IMF B_y conditions) for nightside closed field lines of around 40 minutes. At ~00:28 UT, IMF B_y had been positive for around 50 minutes. Based on the Tenfjord timescale, this would imply that our interval was wholly IMF $B_y > 0$ driven. Conversely, studies such as *Browett et al.* (2017) have shown that longer timescales of a few hours may be important. For these longer timescales to play a role, however, one would expect to have observed a relatively persistent IMF B_y component during that time. The integrated IMF B_y over the hours prior to our interval was convincingly B_y-positive, and it seems highly unlikely that a few minute-long fluctuations into the opposite IMF B_y polarity, 1 or 2 hours prior to the flows we observed, could have a significant influence.

The convincing argument that the IMF data alone imply a positive IMF B_y penetration is further reinforced by the NH SuperDARN data (Fig. 5.4a). These maps show that there were dozens of fitted vectors with a dawnward sense in the pre-midnight sector, which helps to confirm that the large-scale morphology of the ionospheric convection was consistent with a positive IMF B_y component; the pattern was rotated clockwise with the dawn cell having extended into the pre-midnight sector [*Lockwood* (1993); *Grocott* (2017)]. This is further supported by the fact that we parameterised RG96 with IMF $B_y = 0$ to ensure that the observed asymmetric convection patterns were data-driven, and not influenced by model data. Thus, all evidence points to a large scale IMF $B_y > 0$ asymmetry in the magnetosphere, implying that the flow observed by C1 cannot be IMF B_y-controlled, as this would require IMF $B_y < 0$.

A related issue concerns the certainty with which we can determine the location of the spacecraft with respect to the large-scale convection pattern. As discussed in Chapter 4, the untwisting hypothesis, as considered by *Pitkänen et al.* (2013, 2017), relies on the assumption that the convection cell to which the spacecraft is connected should be a factor of only hemisphere and sense of IMF B_y. This does not, however, account for the dusk-dawn location of Cluster, which here was $6 \leq \mathrm{Y}_{GSM} \leq 7$ R_E pre-midnight. If C1 was located on the dusk cell when above the neutral sheet, and on the dawn cell when below the neutral sheet, then the sense of the observed flows in the plasma sheet would in-fact be consistent with the large-scale convection.

To specify which cell C1 is located within, we mapped its location into the ionosphere using TA15 - shown by Xs (+s) on the northern (southern) hemisphere convection maps in Fig. 5.4a (Fig. 5.4b). For NH maps, there appears to be insufficient scatter to determine the exact division between the dusk and dawn convection cells, such that it is inconclusive as to which cell C1 maps to when above the neutral sheet. If C1 in-fact mapped to the dusk convection cell, however, then the observed duskward flows in the NH plasma sheet would actually be consistent with the large-scale convection pattern. Furthermore, given that the C2-C4 magnetic field observations are consistent with the local B_y being dominated by magnetotail flaring (as opposed to IMF B_y) at the pre-midnight location of Cluster, it is likely that we would expect the return sense of the convection to be dominated here by the symmetric (duskward) element both above and below the neutral sheet [see e.g. *Pitkänen et al.* (2019)].

By contrast, in the SH, the C1 footpoints are convincingly located on the dusk cell, meaning the dawnward flow observed by C1 in the SH plasma sheet is clearly inconsistent with the large-scale convection. Indeed, the dawnward flow at this SH pre-midnight location could only be interpreted in terms of the untwisting hypothesis for a situation with clear IMF $B_y < 0$ penetration (and associated extended dawn cell), which has already been ruled out. C3, meanwhile, continually observed duskward flow consistent with the large-scale convection. We thus conclude that the flow observed by C1 must be associated with more localised dynamics.

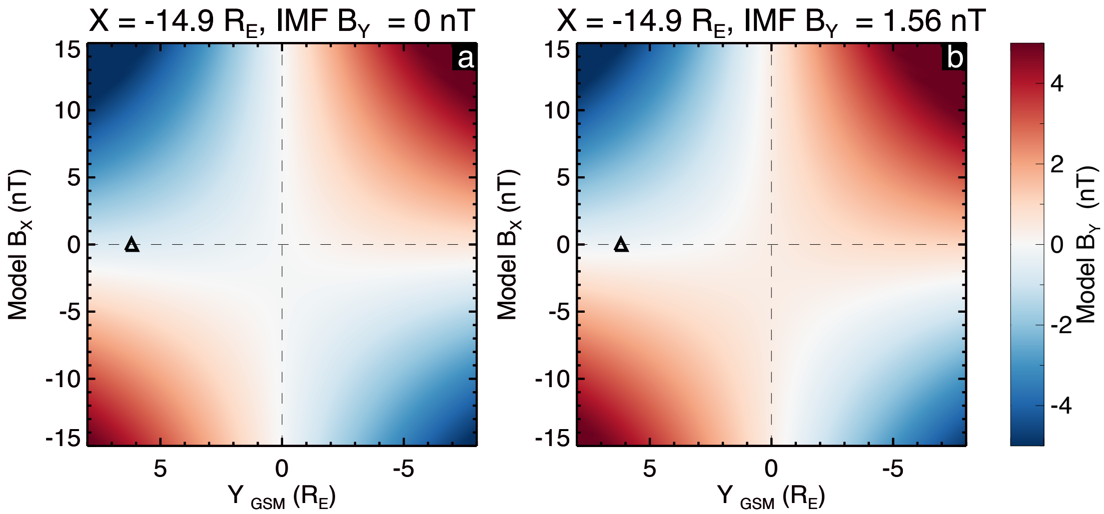

FIGURE 5.5: TA15 model magnetic field data. In each case, plotted is Y_{GSM} vs model B_x, with the TA15 modelled B_y value shown by the colour bar on the right. The black triangle shows the Y_{GSM}-location of C1 at $B_x = 0$. In a), we have imposed IMF $B_y = 0$, and in b) we have used the 1-hour mean-averaged IMF B_y (+1.56 nT) prior to 00:28 UT.

5.4.2 Evidence for a Local Perturbation in the Magnetotail

The lack of consistency of C1's observations with the large-scale convection leads us to another possibility - that there is a local perturbation in the tail, independent of any IMF B_y effects. This is in-fact supported by close examination of the local B_y observed by the Cluster spacecraft. Despite substantial evidence for IMF $B_y > 0$ penetration, C1, C2 and C4 all recorded mostly negative local B_y (Fig. 5.3(ii)); yet, this may be wholly consistent with a penetrated positive IMF B_y. This is largely as a consequence of the magnetotail flaring effect (Chapter 4), which dominates towards the dusk-dawn flanks. Dipole tilt effects and current sheet warping [*Petrukovich et al.* (2005); *Petrukovich* (2011)], may also be expected to influence the local B_y. To attempt to consider the possible effects of these phenomena on the magnetic field observations, in Figure 5.5 we present TA15 model magnetic field data. At $X_{GSM} = -14.9$ R$_E$, we plot Y_{GSM} against model B_x with each point colour-coded based on the modelled B_y value (analagous to Fig. 4.2).

In Fig. 5.5a, we show the field for the case that IMF $B_y = 0$, and in Fig. 5.5b the case that IMF $B_y = +1.56$ nT (the 1-hr mean-averaged value prior to 00:28 UT). Compared to Fig. 4.2, as well as flaring, the data in Fig. 5.5 additionally show the effect of the negative (tailward) dipole tilt (as appropriate to our study interval) and current sheet warping on the local (modelled) B_y. According to *Petrukovich* (2011), the current sheet warping (controlled by the dipole tilt) is expected to add a negative B_y component pre-midnight and a positive B_y component post-midnight, with the 'even tilt' effect adding a negative B_y component to both the pre- and post-midnight sectors for a negative tilt. As a result, the location of the B_y polarity change no longer occurs at the neutral sheet ($B_x \approx 0$), but now occurs in the SH (at $B_x \approx -3$ nT). Fig. 5.5b conveys the scenario relevant to our study, where we have (additionally) a global positive IMF B_y. This has the effect of moving the pre-midnight B_y polarity change back up towards the neutral sheet. This in-fact explains why the Cluster spacecraft observed coincident $B_x \approx 0, B_y \approx 0$ prior to 00:28 UT (Fig. 5.2). Fig. 5.5b also illustrates the dominance of the magnetotail flaring effect at this location, as e.g. C2 and C4 (located above the neutral sheet) are expected to (and did) observe $B_y < 0$, despite IMF $B_y > 0$ penetrating into the magnetotail. C3, meanwhile, was located below the neutral sheet and observed $B_y > 0$, again consistent with the expected B_y due to flaring. The local B_y observed by C1, however, remained mostly negative irrespective of hemisphere. This implies the presence of a B_y-negative 'kink' localised to the vicinity of C1. Our use of the term 'kink' is to highlight a deformation in the nearby field lines, resulting in the observed perturbations to the local B_y. In the following section, we examine this kink in relation to the observed current sheet flapping.

5.4.3 Evidence for Current Sheet Flapping as a Source of the Asymmetric Flows

If a localised magnetic field perturbation was associated with the lack of observation of the expected dusk-dawn flow for magnetotail untwisting, investigating its cause seems a worthwhile endeavour. A starting point for this investigation is the clear sinusoidal-like variation in B_x, which is evidence of current sheet flapping [e.g. *Runov et al.* (2009)]. The localised and/or low amplitude nature of this flapping is apparent; between 00:28 - 00:33 UT, only C1 observed the flapping. In order to better understand the behaviour of the flapping, we apply MVA to our data (briefly mentioned in Section 3.2). For each of the 11 current sheet crossings observed between 00:28 - 00:33 UT, we calculate the average

Centre Time (UT)	Δt (secs)	MVA Normal Vector [GSM] (n_x, n_y, n_z)	λ_2/λ_3	k
00:28:06	10	-0.202, -0.488, 0.849	1.6	-1
00:28:12	10	0.016, -0.659, -0.752	3.6	-1
00:28:52	10	-0.169, 0.927, 0.336	3.5	$+1$
00:29:04	10	-0.111, -0.026, -0.993	1.9	-1
00:29:39	10	-0.152, -0.004, 0.988	7.2	-1
00:30:52	10	0.128, -0.127, 0.984	2.2	$+1$
00:31:03	10	-0.507, 0.721, 0.473	15.7	$+1$
00:31:23	10	0.154, -0.804, 0.574	3.4	$+1$
00:31:35	10	-0.013, -0.442, -0.897	7.1	$+1$
00:31:49	10	-0.017, 0.022, 1.000	14.0	-1
00:32:32	10	0.170, 0.985, -0.025	14.5	-1

TABLE 5.1: The results of the MVA. In the leftmost column is the centre time (i.e. the time when C1 was crossing the current sheet, $B_x \approx 0$), followed by the time interval over which each iteration of MVA was performed (centred on the centre time), followed by the normal vector to the current sheet, the ratio of the intermediate to smallest eigenvalues (see text), and a k parameter (see text).

magnetic field vector, $<\mathbf{B}>$, defined as:

$$<\mathbf{B}>=\frac{1}{N}\sum_{n=1}^{N}\mathbf{B}_n \tag{5.1}$$

and $n = 1, 2, ...N$ is the number of measurements made during a crossing, and e.g.

$$<B_x>=\frac{1}{N}\sum_{n=1}^{N}B_{x,n} \tag{5.2}$$

to form the 3×3 symmetric magnetic variance matrix, M_{ij}^B:

$$M_{ij}^B =< B_iB_j > - < B_i >< B_j > \tag{5.3}$$

where $i, j = x, y, z$ are the cartesian components of the magnetic field vector $\mathbf{B}$ [*Dunlop et al.* (1995)]. The eigenvectors and eigenvalues of M_{ij}^B are then found; the normal vector to the current sheet is the eigenvector of M_{ij}^B which has the smallest eigenvalue, λ_3. The results of this analysis are shown in Table 5.1. The ratio of the intermediate to smallest eigenvalues, λ_2/λ_3, is generally used as a guide for how accurate a computed normal vector is, with the larger the ratio corresponding to a better vector [*Rong et al.* (2015)].

A technique was also developed by *Rong et al.* (2015) to determine the nature of the current sheet flapping, i.e. whether the flapping is a steady up-down oscillation or dusk-dawn propagating, and has been used by e.g. *Wu et al.* (2016). To determine this, the k parameter (Table 5.1) is used, defined as:

$$k = sign(n_y \times n_z) \times sign(\Delta B_x) \tag{5.4}$$

where n_y and n_z are the Y_{GSM} and Z_{GSM} components of the normal vector, and ΔB_x is the change in sign of B_x. If the spacecraft crosses from + to − B_x, then ΔB_x is negative, with the opposite for − to +. Up until 00:30:52 UT, k is negative for the first two crossings, then positive, then negative for a further two crossings. However, from 00:30:52 UT onwards, k remains consistently positive for the following 4 crossings across a ∼1-minute time window, suggesting that during this time, the flapping may be a kink-like wave propagating dawnward [*Rong et al.* (2015)]. k then switches sign to negative for the final two crossings, suggesting that any dawnward propagating may have ceased and that the flapping may now either be duskward propagating or steadily flapping in the Y_{GSM}-Z_{GSM} plane.

The physical processes which generate current sheet flapping have been discussed previously. One such mechanism is the occurrence of periodical, localised reconnection [*Wei et al.* (2019)]; a mechanism known to generate fast flows [e.g. *Angelopoulos et al.* (1994); *Zhang et al.* (2016)]. Indeed, our data in Fig. 5.3(iii) and Fig. 5.3(iv) show that C1 measured a generally positive B_z and continual fast ($v_x > 200$ km s^{-1}) earthward flow, peaking at over 370 km s^{-1}, with bursts of enhanced convective flow ($v_{\perp x} > 200$ km s^{-1}) also apparent. One possibility, therefore, is that C1 was located earthward of a localised reconnection site (owing to $B_z > 0$), where persistent, localised reconnection was exciting fast earthward flow. We suggest that reconnection may have been driving the current sheet flapping, inducing the localised kink, and ultimately controlling, or influencing, the dusk-dawn direction of the convective flow. To provide some scope to this suggestion, we attempted to find the direction of the $\mathbf{J} \times \mathbf{B}$ forces acting on the plasma. The current density vector, $\mathbf{J}$, is determined using an application of Ampère's Law (eq. 1.21) known as the *curlometer* [*Dunlop et al.* (1988, 2002, 2021)], which uses four spacecraft to estimate the average current density **J** flowing through the volume bound by the spacecraft tetrahedron (assumed to be constant, and thus a linear magnetic field variation between spacecraft) [*Robert et al.* (1998)]. The derivation provided in *Dunlop et al.* (1988) involves applying Stokes' theorem to Ampère's Law:

$$\mu_0 \int \mathbf{J} \cdot d\mathbf{S} = \int (\nabla \times \mathbf{B}) \cdot d\mathbf{S} = \oint \mathbf{B} \cdot d\mathbf{l} \tag{5.5}$$

and then finding a discrete expression for **J** in terms of the spacecraft position and magnetic field vectors:

$$\mu_0 \mathbf{J} \cdot (\Delta \mathbf{r}_i \times \Delta \mathbf{r}_j) = \Delta \mathbf{B}_i \cdot \Delta \mathbf{r}_j - \Delta \mathbf{B}_j \cdot \Delta \mathbf{r}_i \tag{5.6}$$

where $\Delta \mathbf{r}_i = \mathbf{r}_1 - \mathbf{r}_i$, $\Delta \mathbf{r}_j = \mathbf{r}_1 - \mathbf{r}_j$ etc; $\mathbf{r}_1$ ($\mathbf{B}_1$) is the position (magnetic field) vector of a reference spacecraft (e.g. C1), and $\mathbf{r}_{i(j)}$ ($\mathbf{B}_{i(j)}$) is the position (magnetic field) vector of another spacecraft $i(j)$. The LHS of eq. 5.6 describes a projection of **J** normal to the face of the tetrahedron defined by the positions of the spacecraft 1, i, j, whereas the RHS describes a traversal of the magnetic field around that face. Using C1 as our reference spacecraft and iterating (1, i, j) through (1, 2, 3), (1, 2, 4) and (1, 3, 4), where each number denotes the respective Cluster spacecraft, one obtains three equations for the three independent components of $\nabla \times \mathbf{B}$, which can be solved simultaneously to give values for $\mathbf{J} = (J_x, J_y, J_z)$.

After calculation of **J**, we then compute $\mathbf{J} \times \mathbf{B}$, firstly from taking the cross product of **J** with the average **B** ($\mathbf{B}_{AVG}$) from the four-spacecraft. We also calculate $\mathbf{J} \times \mathbf{B}$ using solely **B** from C1 ($\mathbf{B}_{C1}$), to provide a more local estimate of $\mathbf{J} \times \mathbf{B}$ at the location of C1. The results of this analysis are shown in Figure 5.6.

Shown in Fig. 5.6(i-iii) are the local magnetic field B_x, B_y and B_z components, as presented previously. The dashed black line represents the TA15 modelled magnetic field at the location of C1. In Fig. 5.6(iv) are the current density, J_x, J_y and J_z components determined from the curlometer. In Fig. 5.6(vi) is the dusk-dawn component of $\mathbf{J} \times \mathbf{B}_{AVG}$ and $\mathbf{J} \times \mathbf{B}_{C1}$. The dashed blue and black lines indicate $\mathbf{J} \times \mathbf{B}_{AVG}$ and $\mathbf{J} \times \mathbf{B}_{C1}$, where

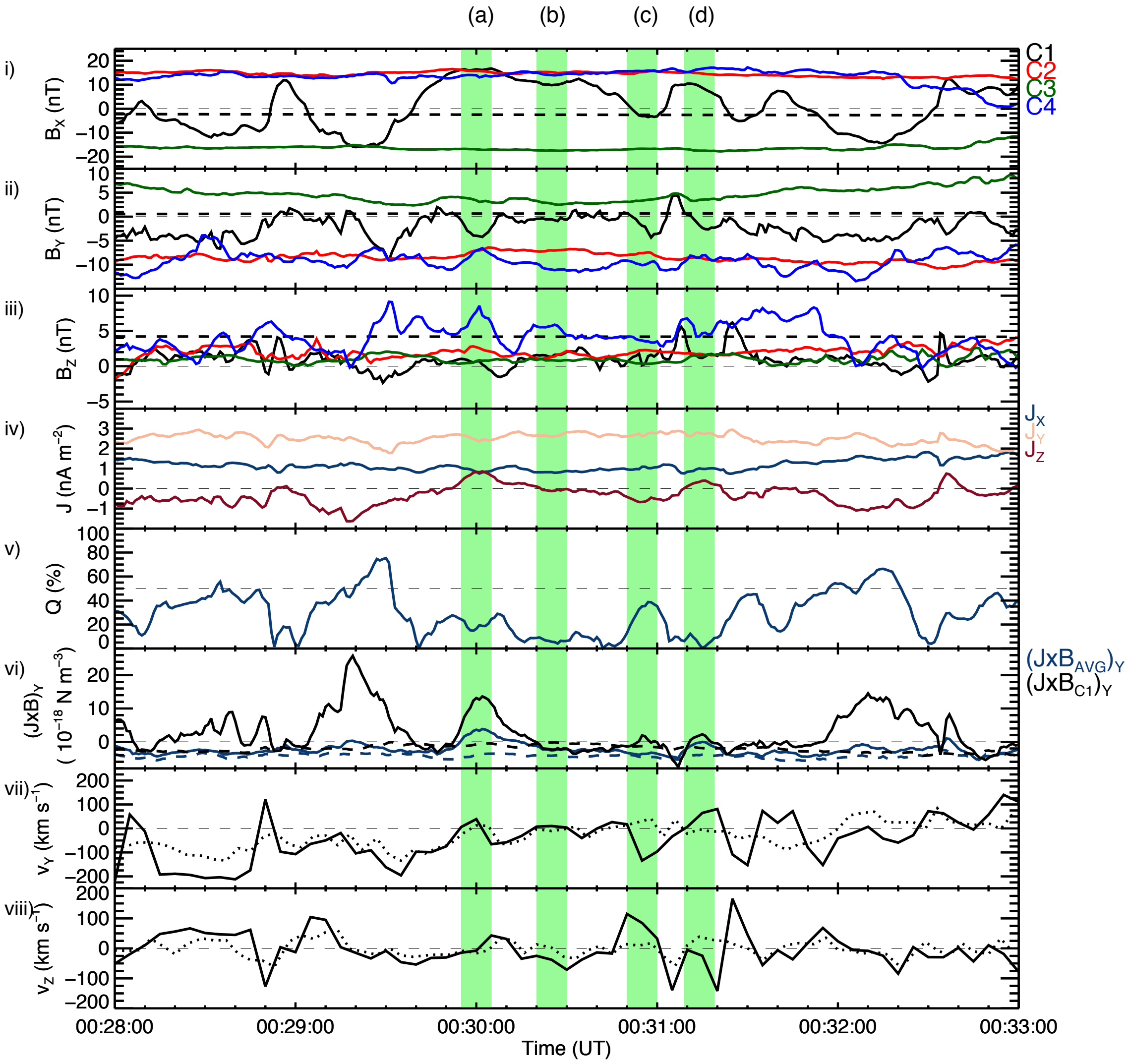

FIGURE 5.6: i - iii) The local magnetic field vector $\mathbf{B}$ (B_x, B_y, B_z) observed by C1-4, as shown previously (solid lines), and the TA15 modelled B vector for C1 (dashed black lines). iv) The components of the current density vector, $\mathbf{J}$ (J_x, J_y, J_z), v) Q (see text), vi) $(\mathbf{J} \times \mathbf{B}_{AVG})_y$ (solid blue line) and $(\mathbf{J} \times \mathbf{B}_{C1})_y$ (solid black line). The dashed blue and black lines indicate the equivalent calculation where the TA15 model $\mathbf{B}$ field of C1 has been used (see text). vii) v_y ($v_{\perp y}$ in solid lines), observed by C1 and v_z ($v_{\perp z}$ in solid lines), also observed by C1. The green highlighted regions labelled (a)-(d) correspond to four specific time-windows of interest (see text).

$\mathbf{J}$ and $\mathbf{J} \times \mathbf{B}$ have been computed using the TA15 model field at the location of C1 and the true magnetic fields measured by C2-C4. These 'model $(\mathbf{J} \times \mathbf{B})_y$ forces' have been computed to provide an illustration of the 'unperturbed' magnetic field at the location of C1 and the associated $(\mathbf{J} \times \mathbf{B})_y$ force, in absence of dynamical effects such as flapping or kinking. In both cases, the model $(\mathbf{J} \times \mathbf{B})_y$ forces are weakly dawnward, consistent with the 'background curvature' of the magnetic field at this pre-midnight location (see Fig. 5.7).

The Q parameter (Fig. 5.6(v)) is a proxy for the reliability of the curlometer estimate, calculated from:

$$Q = \frac{|\nabla \cdot \mathbf{B}|}{|\nabla \times \mathbf{B}|} \tag{5.7}$$

An expression for $\nabla \cdot \mathbf{B}$, which may be non-zero due to e.g. unoptimal spacecraft confirguation [*Grimald et al.* (2012)], can be calculated from applying the divergence theorem:

$$\int_V \nabla \cdot \mathbf{B} dV = \int_S \mathbf{B} \cdot d\mathbf{S} \tag{5.8}$$

and then finding a discrete expression [*Dunlop et al.* (2021)]:

$$|\nabla \cdot \mathbf{B}||\Delta \mathbf{r}_j \cdot \Delta \mathbf{r}_k \times \Delta \mathbf{r}_i| = |\sum_{cyclic} \Delta \mathbf{B}_i \cdot \Delta \mathbf{r}_j \times \Delta \mathbf{r}_k| \tag{5.9}$$

Fig. 5.6(v) suggests that the curlometer approach is generally appropriate due to Q mostly remaining $< 50\%$ (black dashed line). Unlike in previous studies which have used the curlometer at close inter-spacecraft separation of $\ll 1$ R$_E$ [e.g. *Dunlop et al.* (2002); *Runov et al.* (2003)], in our case the Cluster separation is large (≥ 1 R$_E$). Thus, the curlometer is likely to be underestimate of the true current at these scale sizes. Critically, however, the spacecraft configuration is such that the estimate of the direction of the currents should be stable. Therefore, while the volume enclosed by the spacecraft is greater than the scale sizes of the current sheet flapping and kink, a reliable estimate of the direction of the net $\mathbf{J} \times \mathbf{B}$ force within the enclosed volume may still be obtained.

Two key features of Fig. 5.6 are apparent. First, it seems as though the perturbations to $(\mathbf{J} \times \mathbf{B})_y$ are mostly associated with the magnetic field perturbations generally only observed by C1. In-fact, this is made apparent when comparing $\mathbf{J} \times \mathbf{B}_{AVG}$ and $\mathbf{J} \times \mathbf{B}_{C1}$, where the perturbations are much larger in magnitude for $\mathbf{J} \times \mathbf{B}_{C1}$. We also note that $\mathbf{J} \times \mathbf{B}_{AVG}$ and $\mathbf{J} \times \mathbf{B}_{C1}$ are almost always positive with respect to their model equivalents, although, $(\mathbf{J} \times \mathbf{B}_{AVG})_y$ is still mostly net negative, whereas $(\mathbf{J} \times \mathbf{B}_{C1})_y$ is net positive. This implies that using $\mathbf{B}_{C1}$ instead of $\mathbf{B}_{AVG}$ in calculation of $(\mathbf{J} \times \mathbf{B})_y$ has ultimately reduced any effects of the larger-scale background curvature of the magnetic field, which is incorporated when including the other spacecraft.

Second, the magnetic field and flow dynamics evident in Fig. 5.6 appear to almost always be associated with positive (duskward) enhancements in $(\mathbf{J} \times \mathbf{B})_y$, in contrast to the model dawnward sense of $(\mathbf{J} \times \mathbf{B})_y$. This is most noticeable for $(\mathbf{J} \times \mathbf{B}_{C1})_y$, but also apparent in the case of $(\mathbf{J} \times \mathbf{B}_{AVG})_y$. We therefore suggest that the dynamic behaviour of $(\mathbf{J} \times \mathbf{B})_y$ is simply consistent with the current sheet flapping and kinking in the magnetic field, which is associated with the transient changes in the dusk-dawn flow observed by C1.

5.4.4 Visualisation of the Observed Dynamics

In an attempt to visualise the above plasma sheet dynamics, in Figure 5.7 we show a series of schematics which aim to associate the observed magnetic field perturbations with the observed dusk-dawn convective flows. Each of the four panels correspond to the four time-windows indicated in Fig. 5.6 by the highlighted regions labelled a-d. In each panel, we indicate the approximate relative positions of the four Cluster spacecraft in GSM coordinates, as well as the appropriate sense of B_y measured by each spacecraft (purple arrows at each spacecraft location). We also superimpose nominal plasma sheet field lines (with exaggerated extent in Z_{GSM}) which display the sense of B_y implied by the TA15 data from Fig. 5.5 (long blue curved arrows). The dashed lines illustrate the location of the neutral sheet at the end of each time window. This is tilted slightly (appropriate for IMF $B_y > 0$), with the current state of any 'flap' implied by the sign of B_x measured by C1. Finally, shown in red is the perturbation to the field implied by the sign of B_y measured by C1.

In Fig. 5.7a C1 is located above the neutral sheet and observed negative B_y. At this time, a weakly duskward convective flow was observed (indicated by the thick grey arrow), consistent with the clear duskward sense of the $(\mathbf{J} \times \mathbf{B})_y$ force yet opposite to the dawnward sense of the model $(\mathbf{J} \times \mathbf{B})_y$ force associated with the background magnetic field curvature. In Fig. 5.7b, C1 is still above the neutral sheet but measured $B_y \approx 0$ and no dusk-dawn convective flow. In Fig. 5.7c, C1 is shown below the neutral sheet, where

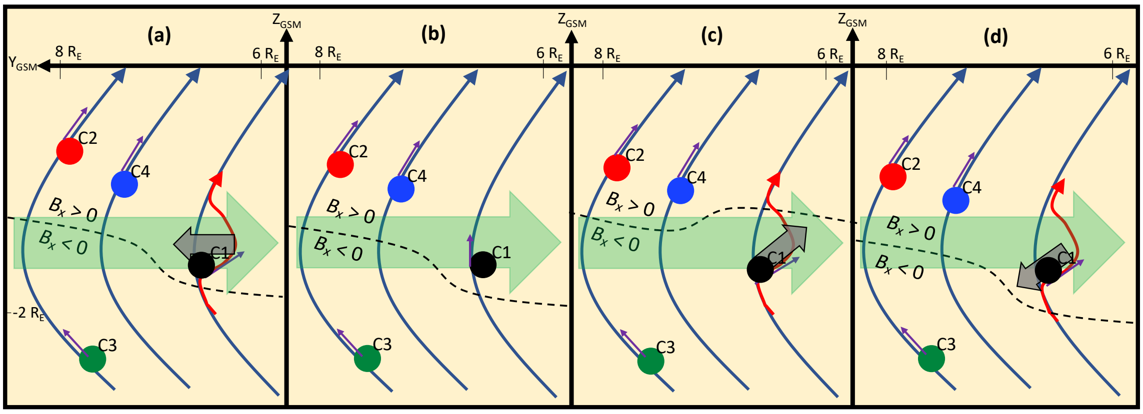

FIGURE 5.7: Schematic diagrams of the measured magnetic field perturbations and dusk-dawn convective flows during the time-windows indicated in Fig. 5.6 by the green highlighted regions (a)-(d). The approximate locations of the four Cluster spacecraft relative to one-another in the Y_{GSM}-Z_{GSM} plane are indicated (not to scale), by the coloured circles. The curved blue arrows represent magnetic field lines, with the short purple arrows indicating the local sense of B_y at the location of each spacecraft. The dashed black line indicates the neutral sheet. In panels (a), (c) and (d), the curved red arrow shows the 'kinked' magnetic field lines. The long thick green arrow shows the direction of the model $(\mathbf{J} \times \mathbf{B})_y$ force associated with the background curvature of the magnetic field, and the small thick grey arrows indicate the direction of the dusk-dawn convective flow observed by C1.

the background B_y would be positive based on the TA15 data (Fig. 5.5b). Instead, C1 observed an increasingly negative B_y, which we argue is associated with the presence of the kink in the field. Simultaneously, C1 observed a dawnward and slightly northward convective plasma flow. We suggest that this flow was associated with the dawnward or upward flap of the neutral sheet, and that the dawnward sense of the flow may have resulted in the increase in negative B_y seen during the time-window shown in Fig. 5.6c. The positive $(\mathbf{J} \times \mathbf{B}_{C1})_y$ at this time, despite being inconsistent with the dawnward sense of the flow, is still consistent with the magnetic field curvature associated with the kink. $(\mathbf{J} \times \mathbf{B}_{AVG})_y$, meanwhile, was negative, likely due to incorporating the larger-scale background curvature of the magnetic field observed by the other spacecraft. Finally, in Fig. 5.7d C1 is shown above the neutral sheet where it observed a weakly negative B_y. In this case, C1 now observed a flow with a duskward and slightly southward component. As in Fig. 5.7a, this flow occurred concurrent with a positive enhancement in $(\mathbf{J} \times \mathbf{B})_y$ relative to the model $(\mathbf{J} \times \mathbf{B})_y$. This implies that this flow may have been associated with the downward flap of the current sheet, and the duskward sense may indicate that it is acting to reduce the negative kink in B_y apparent over the time-window shown in Fig. 5.6d.

We do acknowledge a degree of uncertainty in the details of the interpretation presented above of the exact relationship between the flows and field. To our knowledge, we have applied the curlometer analysis for the first time at a *large* scale, and it is highly likely that on a smaller scale, the true sense and magnitude of $\mathbf{J} \times \mathbf{B}$ would be more accurately determined (i.e. at smaller spacecraft separation). Other forces, notably plasma pressure gradients (∇P), are also likely to be influencing the flow direction [e.g. *Li et al.* (2011)], but in practice are very difficult to calculate [*Hamrin et al.* (2013)]. Nevertheless, our analysis serves to illustrate three observations about this interval of which we can be very certain:

1. The IMF, ionospheric convection, and comparison of the plasma sheet magnetic field observations to the TA15 model field, all lead to the expectation of a large-scale IMF $B_y > 0$ asymmetry in the magnetosphere.
2. C1 observed convective flow with a dusk-dawn sense that was inconsistent with current theories of IMF B_y-induced dusk-dawn flows associated with magnetotail untwisting. Notably, the observed dawnward flow in the SH, whilst inconsistent with IMF $B_y > 0$, was also inconsistent with the expected (symmetric) duskward flow at this pre-midnight location even in the absence of IMF B_y-control.
3. Magnetic field perturbations that were indicative of a localised current sheet flapping and dusk-dawn kink in the magnetic field occurred coincident with the flows. It therefore seems likely that in this case the IMF B_y-driven asymmetry, or indeed the symmetric flow expected at the spacecraft location, was being overriden by the localised dynamics in governing the dusk-dawn component of the flow.

5.5 Summary

In this chapter, we have presented an event study from 12 October 2006 revealing a dynamic interval of plasma flows and current sheet flapping observed by Cluster. The key observations are summarised below:

- The OMNI data revealed that IMF B_y had been positive for several hours prior to our interval of Cluster data, with the exception of three short-lived negative excursions.

- The SuperDARN ionospheric convection observations revealed a large-scale asymmetry consistent with IMF $B_y > 0$, confirming the absence of a large-scale asymmetry in the flow pattern that might explain the dawnward flows observed by C1.

- C1 observed a changing B_x magnetic field component and associated duskward ($v_{\perp y} > 0$) flow when in the NH ($B_x > 0$) and dawnward ($v_{\perp y} < 0$) flow when in the SH ($B_x < 0$).

- The C2, C3 and C4 magnetic field observations suggested that the local B_y was being dominated by magnetotail flaring, as opposed to IMF B_y. C3 also observed duskward flow in the SH, consistent with the symmetric flow expected owing to the pre-midnight location of the spacecraft.

In contrast to the results of previous studies such as *Grocott et al.* (2007); *Pitkänen et al.* (2015), during this particular interval, the dusk-dawn sense of the convective magnetotail flows ($v_{\perp y}$); and notably, the dawnward flow observed by C1 in the SH, does not agree with expectations based on the theoretical understanding of global magnetotail untwisting and the prevailing positive IMF B_y conditions, nor to expectations based on the location of the spacecraft and associated magnetotail flaring. Instead, we attribute the flows to a localised magnetic field perturbation, or 'kink' in the magnetotail, which appears to have been independent of any large-scale dynamics and may have instead been related to the observed current sheet flapping. We suggested that the current sheet flapping may have been driven by localised reconnection, inferred as a result of the observation of continual bursty earthward flow. Analysis using the curlometer technique suggests that the $(\mathbf{J} \times \mathbf{B})_y$ force is consistent with the localised kinks and flapping in the magnetic field, that may be associated with the transient perturbations to the dusk-dawn flow observed by C1.

Although evidence for the large-scale penetration of IMF B_y is apparent, the IMF $B_y > 0$ penetration at the location of C1 appears to have been unable to override the variable dusk-dawn flow associated with the flapping. It is possible, therefore, that a fraction of the $\sim$30% of flows that do not exhibit the expected dusk-dawn direction could have been associated with intervals of current sheet flapping. In Chapter 7 we attempt to examine the extent to which this might be true by trying to identify in which of our fast flow intervals flapping may be occurring.

Chapter 6

The Influence of Localised Dynamics on Dusk-Dawn Convection in the Earth's Magnetotail

This chapter contains work from the article currently under review: *Lane, J. H., Grocott, A. and Case, N. A. (submitted). The Influence of Localized Dynamics on Dusk-Dawn Convection in the Earth's Magnetotail, J. Geophys. Res.*

6.1 Introduction

In this chapter we present Cluster spacecraft observations of an interval of active magnetotail behaviour during a substorm from 20 August 2003. During this interval, Cluster observed a series of fast convective earthward (BBF-like) flows, most of which also had a significant dawnward component. This flow was consistent with the symmetric flow that might be expected at the post-midnight NH location of the spacecraft, and also consistent with, although not evidence that, IMF $B_y > 0$ was governing the global magnetospheric dynamics. Despite this, the fastest flow measured during this interval had a significant duskward component, which could only be explained by the untwisting hypothesis in a negative IMF B_y situation. As with the previous chapter, this event therefore contributes to the ~30% of flows which do not appear to be IMF B_y-controlled and is thus not in agreement with the untwisting hypothesis. The duskward flow, unlike the prevalent dawnward flows, occurred in concert with a sudden reversal in the local B_y and a large-magnitude dipolarisation (20+ nT B_z increase) - a process expected to occur in association with the earthward propagation of bursty flows [e.g. *Sergeev et al.* (1996b); *Grocott et al.* (2004b); *Runov et al.* (2011)].

In this study, the B_y component of the concurrent upstream IMF had been consistently positive for around 1 hr 40 minutes prior to the interval of Cluster observations. Owing to strong evidence of a large-scale IMF $B_y > 0$ ionospheric convection pattern, the observed duskward flow burst was inconsistent with the expected IMF B_y-control. We also consider the relation of the duskward flow burst to changes in the large-scale convection associated with the coincident substorm activity. Overall, however, we attribute the duskward flow burst to localised dynamics accompanied by transient changes in the local B_y and B_z. These dynamics appeared to be able to temporarily override, or influence, the expected large-scale net dawnward convection at the location of Cluster.

These conclusions are discussed with respect to, and reinforced by, a statistical Superposed Epoch Analysis (SEA) of our asymmetric 'fast flow detections' (defined in Chapter 4). The SEA suggests that, on average, the expected sense of IMF B_y penetration is associated with the fast flows irrespective of whether they have a direction which agrees or disagrees with the untwisting hypothesis, although IMF B_y and the penetrated B_y ($B_{y,pen}$) tend to be stronger for 'agree' flows. Detections which agree (disagree) tend to be accompanied by a transient perturbation to the B_y component of the magnetotail magnetic field in the same sign as (opposite to) the prevailing IMF B_y conditions, which temporarily enhances (overrides) the penetrated field. We also find that agree (disagree) flows appear to be observed further away from (closer to) the neutral sheet, and are associated with weaker (stronger) magnetic field dipolarisation, as implied from Fig. 4.9. Finally, we find that the slower 'background' convective flow has an average direction which is consistent

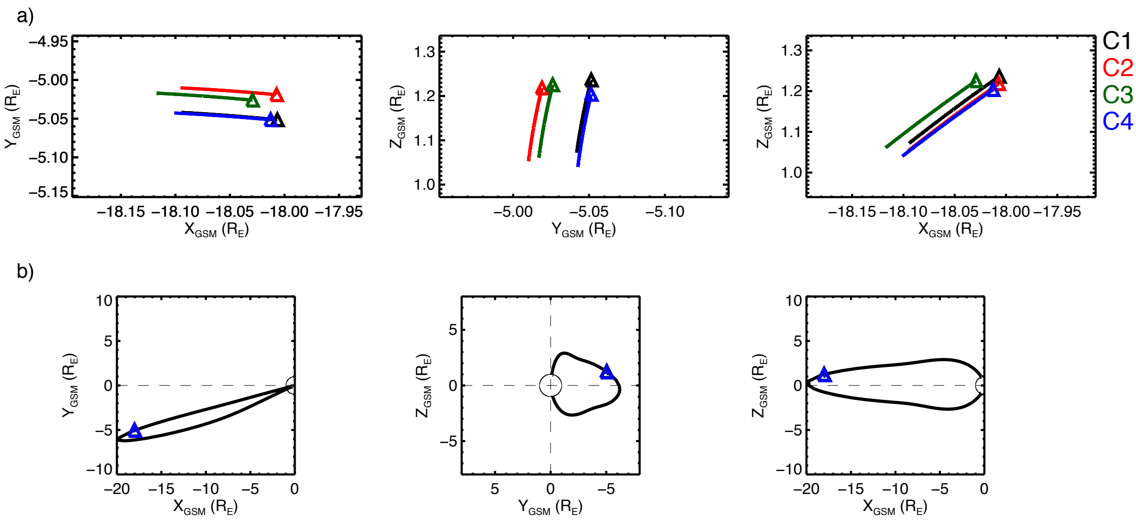

FIGURE 6.1: As in Fig. 5.1, but at 05:05 UT on 20 Aug 2003.

with penetration of the expected IMF B_y, regardless of whether the fast flow itself agrees or disagrees.

6.2 Instrumentation and Data Sets

The magnetospheric observations presented in this case study were made by Cluster, using the same instruments and data processing as in Section 5.2. The interval of study discussed here occurred between 05:05 - 05:30 UT on 20 Aug 2003. Unlike the study in Chapter 5, all four Cluster spacecraft here were located very close to one-another in the near-Earth magnetotail plasma sheet in the post-midnight sector at ($X_{GSM} \approx -18.0$, $Y_{GSM} \approx -5.0$, $Z_{GSM} \approx 1.2$) R_E. In Fig. 6.1a we show the respective spacecraft locations and trajectories, as well as a zoomed-out view with a TA15 modelled field line in Fig. 6.1b, where the C1-C3 markers are largely hidden due to the close proximity of the spacecraft. TA15 was parameterised with 1-hour mean-averaged P_{dyn}, IMF B_y, IMF B_z prior to 05:05 UT; these values were $P_{dyn} = 2.5$ nPa, IMF $B_y = +4.5$ nT and IMF $B_z = -3.2$ nT. The calculated N-index was $\sim$0.7, and there was a sunward dipole tilt of $\sim 2°$.

The SuperDARN data shown in Section 6.3.2 were processed in an identical manner to as described in Section 5.2. Additionally, in this chapter we use auroral indices data, accessed through the OMNI dataset.

The Superposed Epoch Analysis presented in Section 6.5 uses the same dataset of asymmetric fast flow detections derived in Chapter 4.

6.3 Observations

6.3.1 IMF and Cluster Observations

In Figure 6.2, we show an overview of the spacecraft observations in an identical format to Fig. 5.2. In Fig. 6.2a, we show IMF B_y and IMF B_z data from 01:00 - 06:30 UT on 20 Aug 2003. These data reveal that from 01:00 - 03:25 UT, IMF B_y was generally negative, and IMF B_z positive. After ~03:25 UT, both IMF B_y and IMF B_z changed sign, where they remained up until ~06:30 UT, with the exception of three extremely small, short-lived (few-min) IMF B_z sign changes.

In Fig. 6.2b, we show the Cluster magnetic field and plasma observations from 05:05 - 05:30 UT. At 05:05 UT, all four Cluster spacecraft were located well above the neutral sheet ($B_x \approx 15$ nT, Fig. 6.2b(i)), but still in the inner plasma sheet, evidenced by $\beta \approx 1$ (Fig. 6.2b(viii)). Between 05:05 - 05:08 UT, C1-C4 measured relatively steady B_x, B_y and B_z magnetic field components (Fig. 6.2b(i - iii)). Up until ~05:08 UT, the convective earthward flow, $v_{\perp x}$ (Fig. 6.2b(iv)), remained close to 0, and the dusk-dawn convective flow, $v_{\perp y}$ (Fig. 6.2b(v)), was dawnward (~ -200 km s^{-1}). However, at ~05:08 UT, all four spacecraft simultaneously detected a sudden drop in the B_z component of the magnetic field, followed by a large increase from ~2 to 22 nT in the space of around 30 seconds (vertical dashed line in Fig. 6.2b); a typical signature of dipolarisation [e.g. *Ohtani et al.* (2004); *Schmid et al.* (2011)]. As B_z peaked, B_y began to exhibit significant variations of several nT, even briefly turning negative. Concurrent with these magnetic field variations, $v_{\perp x}$ quickly increased and $v_{\perp y}$ turned strongly duskward, peaking just prior ~05:09 UT with $v_{\perp x} \approx 600$ km s^{-1} and $v_{\perp y} \approx 400$ km s^{-1} with a southward convective component of $v_{\perp z} \approx -400$ km s^{-1} (Fig. 6.2b(vi)). All the while, Cluster was in the NH ($B_x > 0$).

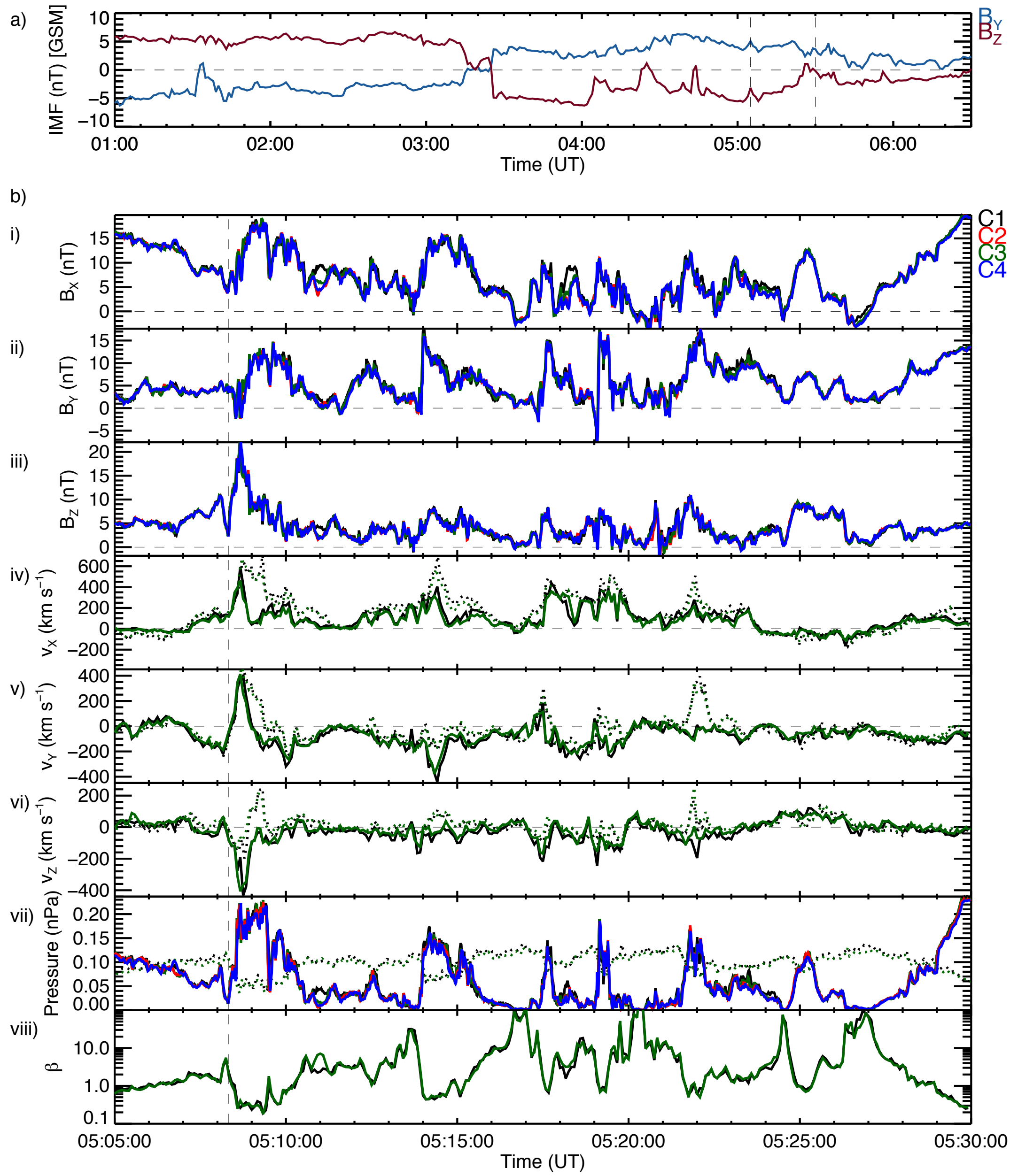

FIGURE 6.2: a) As in Fig. 5.2a but from 01:00 - 06:30 UT on 20 Aug 2003. The vertical dashed lines mark the start (05:05 UT) and end (05:30 UT) of the interval of Cluster data, below. b) As in Fig. 5.2b, but from 05:05 - 05:30 UT, also on 20 Aug 2003. The vertical dashed line marks the beginning of a large dipolarisation (discussed in-text).

By 05:09 UT, $v_{\perp x}$ had subsided almost completely ($v_{\perp x}$ $\leq$100 km s^{-1}), and $v_{\perp y}$ had turned dawnward, peaking at -300 km s^{-1} by ~05:10 UT. After 05:10 UT, $v_{\perp y}$ was mostly dawnward for the remainder of the interval. Further earthward flow bursts were detected between 05:14 - 05:15 UT, as well as between 05:17 - 05:20 UT; in both cases, peaking at around $v_{\perp x} \approx 400$ km s^{-1}. In these instances, there were no large-magnitude

B_z transitions coincident with the enhanced flow, and B_y was generally positive. In all cases, the flow bursts occurred in concert with increases in the magnetic pressure, and decreases in the ion thermal pressure (Fig. 6.2b(vii)); signatures typical of BBF passage over an observing spacecraft [e.g. *Walsh et al.* (2009)]. By 05:30 UT, any transient dynamics in the magnetic field and flow appeared to have subsided.

6.3.2 Ionospheric Convection Observations

As with our study in Chapter 5, in Figure 6.3 we provide the large-scale context which allows us to interpret the more localised observations from Cluster, by showing SuperDARN observations of the ionospheric convection. We present a selection of six 2-minute integration SuperDARN maps of the NH ionospheric convection pattern, beginning at 04:16 UT and ending at 05:18 UT on 20 Aug 2003. In all maps, plasma is generally flowing anti-sunward across the polar cap at high latitudes with a strong duskward sense. With the exception of maps Fig. 6.3c and e, the direction of the convection clearly reverses in the pre-midnight sector before returning sunward at lower latitudes. The convection pattern has also been rotated slightly clockwise, with the dawn cell extending into the pre-midnight sector. Such observations are consistent with the large-scale convection being influenced by a positive IMF B_y component [e.g. *Cowley and Lockwood* (1992)], and in particular, with that influence extending into the nightside [e.g. *Grocott et al.* (2007, 2008)].

In Fig. 6.3c, the dusk cell reverses much closer to midnight, and equatorward of the extended dawn cell. In Fig. 6.3e, the dusk cell is even more extended, almost touching the midnight boundary. In this case there are some duskward fitted vectors equatorward of the group of dawnward fitted vectors around 00 MLT, lending weight to the significance of this morphology. We discuss the potential implications of these observations in Section 6.4.

6.3.3 Auroral Indices Observations

In Figure 6.4 we show a time-series of the AU and AL indices from 01:00 - 06:30 UT on 20 Aug 2003. From 01:00 - 03:40 UT, AU and |AL| remained steady with magnitudes of

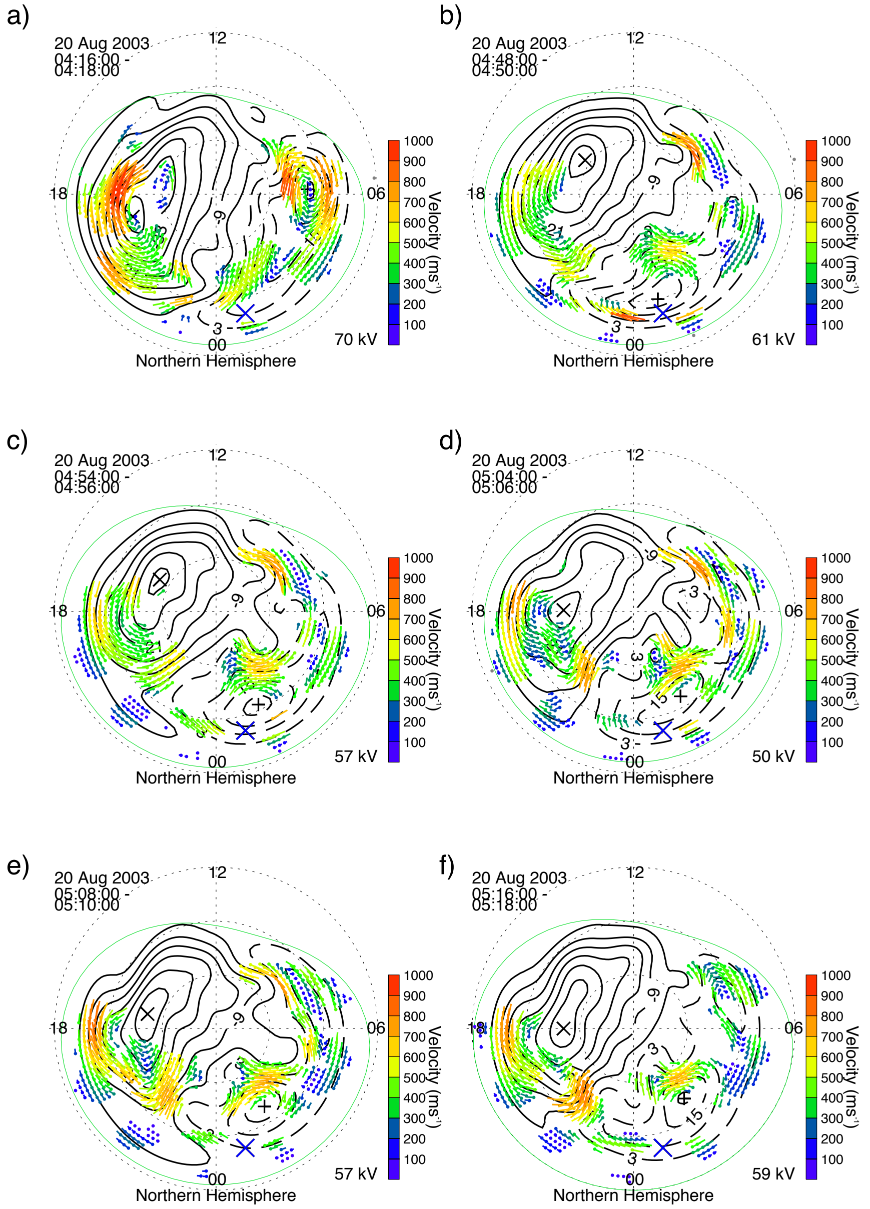

FIGURE 6.3: As in Fig. 5.4, but from 20 Aug 2003. Shown are six 2-minute NH maps from 04:16 - 04:18, 04:48 - 04:50, 04:54 - 04:56, 05:04 - 05:06, 05:08 - 05:10 and 05:16 - 05:18 UT. The blue X indicates the TA15 mapped footpoint of Cluster.

around 30 nT. However, at ~03:40 UT, around 15 minutes after the southward turning of the IMF B_z, AU began to increase, peaking at around 250 nT by 04:10 UT. AL had slowly decreased until ~04:35 UT, when it abruptly dropped by over 100 nT. At 05:00 UT, the difference between AU and AL was almost 500 nT. This difference remained large, but had decreased slightly to ~300 nT by 06:30 UT. Thus, our interval of fast flows, delineated by the vertical dashed lines in Fig. 6.4, occurred during a large (~300 nT) excursion of AL,

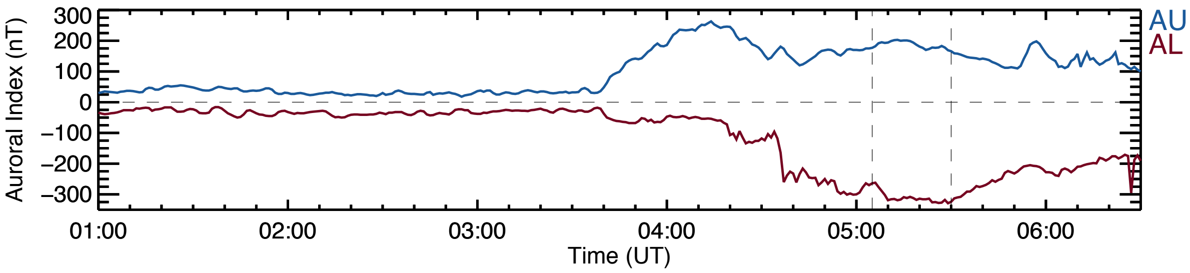

FIGURE 6.4: The AU (blue) and AL (red) indices from 01:00 - 06:30 UT on 20 Aug 2003. The vertical dashed lines mark the start (05:05 UT) and end (05:30 UT) of our interval of Cluster data.

when |AL| > AU (|AL| - AU ≈ 100 nT), indicative of a substorm expansion phase [e.g. *Hsu and McPherron* (2012); *Walach and Milan* (2015)].

6.4 Analysis and Discussion

We have presented observations of a dynamic interval of plasma flows and magnetic field in the Earth's magnetotail. In this section we will discuss our reasoning for interpreting the duskward flow burst as being inconsistent with the large-scale convection expected based on the spacecraft location and magnetotail untwisting considerations, and our alternative interpretation of its relationship to transient, localised dynamics.

6.4.1 Evidence for an Inconsistency with Large-Scale Magnetotail Untwisting

During the 25-minute interval studied (05:05 - 05:30 UT), Cluster measured predominant $B_x > 0$ (Fig. 6.2(i)), indicating that the spacecraft were located in the NH. Cluster also observed a series of BBF-like earthward flows, most of which had significant dawnward components (Fig. 6.2(iv) and (v)). The clear exception to this, however, was the large (∼400 km s^{-1}) duskward convective flow burst observed by Cluster just prior to 05:09 UT, which lasted for around 40 seconds. This flow also had an enhanced earthward component ($v_{\perp x} \approx 600$ km s^{-1}) and was observed in concert with a substantial, transient increase in B_z (20+ nT), and a sudden reversal in B_y from positive to negative. The observed duskward flow is inconsistent with the expected symmetric dawnward flow at the post-midnight location of Cluster, implying, as in Chapter 5, that the typical 'symmetrical' Dungey Cycle return flow [e.g. *Kissinger et al.* (2012)] cannot provide an explanation for its occurrence. We thus examine other possible explanations below.

A duskward flow burst in the NH would, according to *Pitkänen et al.* (2013), be consistent with magnetotail untwisting in the case of a negative IMF B_y penetration. For $\sim$1 hr 40 minutes prior to 05:05 UT, the IMF B_y had been steadily positive; prior to which, however, it had been steadily negative for almost 2 hours. If the longer 'Dungey Cycle' timescales supported by e.g. *Browett et al.* (2017) discussed in Section 2.3 and 5.4 were applicable, then it would be reasonable to expect that IMF $B_y < 0$ could be governing the large-scale sense of the magnetospheric convection; in which case, the duskward flow burst observed by Cluster would be consistent with being IMF B_y-controlled. Due to the post-midnight location of Cluster, and apparent dawn cell footpoint mapping (Fig. 6.3), this would also render the observed predominantly dawnward flow as not being inconsistent with an IMF $B_y < 0$ morphology if it was part of the 'symmetric' flow (see Fig. 4.7b). As with our study in Chapter 5, it is therefore important to determine which sense of IMF B_y is governing the global magnetospheric dynamics in order to determine if the duskward flow burst was indeed IMF B_y-controlled.

The possibility that the observed duskward flow burst was related to IMF $B_y < 0$ driving can, however, be effectively dismissed through inspection of the SuperDARN data. The maps presented here all point to evidence of a large-scale IMF $B_y > 0$ asymmetry, even as early as 04:16 UT (Fig. 6.3a), around 50 minutes after IMF B_y turned positive where the dawn cell was taking on a crescent shape and the direction of the convection reverses in the pre-midnight sector [e.g. *Reistad et al.* (2016); *Grocott* (2017)]. The IMF $B_y > 0$ morphology is then reinforced by the maps in e.g. Fig. 6.3d at 05:04 UT, where the clear extension of the dawn cell into the pre-midnight centre and clockwise rotation of the ionospheric convection was apparent. On this particular map, there were 11 fitted vectors close to midnight at 70° MLAT, suggesting that this pattern was indeed data-driven; supported by the fact that we again parameterised RG96 with IMF $B_y = 0$. Thus, the ionospheric convection data, combined with the prolonged (1 hr 40 min) IMF $B_y > 0$ conditions point to significant evidence of a large-scale positive IMF B_y asymmetry, implying that the duskward flow burst could not have been related to any possible IMF B_y-control, as this would have required IMF $B_y < 0$. Despite this, we noted in Section 6.3.2 that in Fig. 6.3c and Fig. 6.3e an extension of the dusk cell towards midnight was apparent. We do not suggest that this is related to any IMF $B_y < 0$ effect, however, but instead related to the apparent substorm activity, discussed in the following section.

6.4.2 Evidence for Magnetospheric Dynamics Overriding the IMF B_y Asymmetry

Magnetospheric dynamics are known to be more complicated during substorm activity, where IMF B_y-driven dusk-dawn asymmetry can be suppressed [e.g. *Reistad et al.* (2018)], or even reversed [e.g. *Grocott* (2017)]. The auroral indices data (Fig. 6.4) provide strong evidence that our interval of Cluster observations occurred during a substorm onset (expansion) phase, during which the plasma sheet is expected to expand [e.g. *Baumjohann et al.* (1992)]; AU and AL were separated by ~500 nT during the interval of Cluster data, with |AL| - AU ≈ 100 nT. Furthermore, around 30 minutes prior to our interval (~04:35 UT), a clear drop of over 100 nT in AL was observed, implicit of the presence of the substorm electrojet [e.g. *Milan et al.* (2017)].

Generally, if substorm dynamics are dominant (over IMF B_y), then they should be present on a global scale and their effect on the dusk-dawn asymmetry should be clear [*Grocott* (2017)]. In Fig. 6.3 the large-scale IMF B_y asymmetry is clear at high-latitudes, but becomes juxtaposed with the substorm asymmetries in the auroral zone in Figs. 6.3c and e. These asymmetries take the form of a well-known signature of enhanced magnetospheric convection during substorms known as the Harang reversal [e.g. *Grocott et al.* (2010)]. This is particularly easy to identify during IMF $B_y > 0$ conditions, due to its opposite sense compared to the concurrent $B_y > 0$ pattern, i.e. the extension of the dusk cell into the post-midnight sector, in a manner not dissimilar to convection driven by a negative IMF B_y [see Fig. 1 of *Kissinger et al.* (2013); Fig. 5d of *Grocott et al.* (2010)]. Indeed, the presence of the Harang reversal is apparent in Fig. 6.3c, but perhaps more prominently in Fig. 6.3e, where the dusk cell touches the midnight boundary, relatively close to the Cluster footpoint. This is identifiable from the fact that, beginning at the pole and moving equatorward along 00 MLT, the convection has a duskward sense, before reversing to a dawnward sense at $\sim 70°$ MLAT, again reversing to duskward at $\sim 62°$ MLAT; a situation resulting from the eastward electrojet being displaced equatorward of the westward electrojet [*Erickson et al.* (1991)]. The Harang reversal also appears to be persistent but variable in latitude, owing to the prolonged substorm activity and the fact that the relatively constant latitude of the radar coverage reveals the Harang continually 'appearing' and 'disappearing' across maps (c) - (f) in Fig. 6.3. The variable latitude of the Harang may be related to the substorm activity and the variation in the density of plasma sheet particles [*Gkioulidou et al.* (2009)] in association with the BBF-activity.

The clearest extension of the Harang reversal towards the footpoint of Cluster appeared between 05:08 - 05:10 UT (Fig. 6.3e); encompassing the time of the observed duskward flow burst. One possibility, therefore, is that Cluster (briefly) encountered a region in the plasma sheet which geomagnetically mapped to the duskward convection associated with the Harang reversal. This may have occurred as a result of the large scale equatorward-poleward (earthward-tailward) motion of the Harang reversal region, or as a consequence of a brief plasma sheet expansion or contraction [e.g. *Fairfield et al.* (1998); *Forsyth et al.* (2008)]. We state this only as a possibility, and cannot substantially reinforce this claim other than to note the coincidental nature of the concurrent Cluster and SuperDARN observations. We also proceed with caution in attempting to make detailed inferences owing to the fact that the SuperDARN maps are 2-min integrations, whereas the duskward flow burst observed by Cluster only lasted for ~ 40 seconds. It must also be acknowledged that even in the 05:08 UT map, the Cluster footpoint does appear to still be convincingly located on the dawn convection cell.

Irrespective of the large-scale picture, it is apparent that at the time of the duskward flow there were some localised transient dynamics in the fields and flows at the Cluster location. Whilst the M-I system is known to be a coupled regime [e.g. *Cowley and Lockwood* (1992); *Cowley* (2000)], it is also well known that transient, localised dynamics (in both time and space) can distort this coupling [e.g. *Hesse et al.* (1997); *Parker* (1996)]. This was demonstrated in Chapter 5, whereby despite substantial evidence for the large-scale penetration of IMF $B_y > 0$, the flows observed by C1, and notably the dawnward flow in the SH, appeared to override the expected net duskward convection at the spacecraft location. We instead suggested that the variable dusk-dawn flows were related to a flapping motion of the neutral sheet. Previous studies, such as *Keiling et al.* (2009) and *Pitkänen et al.* (2011) have illustrated that other localised phenomena such as flow vortices, which often form in conjunction with earthward BBF-propagation [*Birn et al.* (2004)], can dominate over the sense of the expected large-scale convection.

In the study presented in this chapter, there was no evidence to suggest that current sheet flapping or flow vortices were present; Cluster remained mostly in the NH, and observed earthward and predominantly dawnward convection, consistent with the large-scale picture illustrated by the SuperDARN data. There was, however, significant dipolarisation (increase in B_z of $\sim$20 nT) and a transient reversal in the local B_y at the time of the duskward flow burst (05:09 UT). Unlike in Chapter 5, owing to the lack of spatial coverage from the Cluster spacecraft, in this instance, we are unable to quantify the localised extent of these observations, other than to note the disagreement with the expected large-scale dawnward flow. It must be acknowledged, however, that even the earthward and dawnward flow (i.e. flow consistent with the large-scale convection) at e.g. 05:14 - 05:15 UT was observed shortly after a sudden $\sim$15 nT increase in B_y, and a small increase in B_z. Such transient variability in B_y cannot be attributed to IMF B_y penetration, which is expected to be a much subtler, gradual effect [*Tenfjord et al.* (2015); *Browett et al.* (2017)]. Also unclear is the extent to which dipolarisation could have an effect on dusk-dawn flow; indeed, bursty flows associated with dipolarisation have previously been shown to exhibit variable dusk-dawn components [e.g. *Sergeev et al.* (1996b); *Panov et al.* (2010)].

To better understand the features presented in the above event study, in Section 6.5 we use our dataset of asymmetric fast flow detections in a superposed epoch analysis to examine statistically the extent to which the transient behaviour of B_y and B_z, for example, might differ between flows that appear to be IMF B_y-controlled, and those that are not. Given the predominant level of dawnward flow observed during our case study, we also test the hypothesis that bursty flows are in-fact IMF B_y-independent, but superposed onto a background of 'slower' flow which is consistent with IMF B_y, resulting in bursty flows being IMF B_y-controlled $\sim$70% of the time.

6.5 Superposed Epoch Analysis

6.5.1 Results

In this section, we apply a technique known as Superposed Epoch Analysis (SEA) to our asymmetric fast flow detections. SEA allows us to examine how the mean-averaged (superposed) time series of parameters related to our fast flow detections vary relative to some reference point ('Epoch 0'), defined here as being the fast flow detection time. SEA has been used previously in studies of magnetotail flows by e.g. *Frühauff and Glassmeier* (2016) and *Case et al.* (2020). Here we examine the time frame of ± 20 minutes about each flow detection, with the aim of understanding whether there are distinct differences (on average) around the time of fast flows when comparing 'Agree' (AG) and 'Disagree' (DAG) flows (Section 4.3.3). Rather than just split by AG and DAG, however, here we also consider the sign of IMF B_y, resulting in four categories. We note that these categories are defined based on the flow at, and 130-min averaged IMF B_y relative to, Epoch 0 of each flow detection. In total, for IMF $B_y > 0$, there were 561 AG and 223 DAG flows, and for IMF $B_y < 0$ there were 596 AG and 259 DAG flows, and thus 71.6% and 69.7% exhibit the expected dusk-dawn direction, respectively (in agreement with Fig. 4.8). We then perform SEA on the following parameters related to our flows:

a. IMF B_y.

b. $B_{y,pen}$, as an inference for the 'penetrated B_y'. This is calculated for each flow in an identical manner to that described in Chapter 4.

c. $|B_x|$, to provide a proxy for how close to the neutral sheet ($B_x = 0$) the flows occur.

d. B_z, to provide an indication of magnetic field dipolarisations accompanying the fast flows.

e. $v_{\perp y}$, the convective dusk-dawn flow velocity. As a simplification, we 'map' our SH ($B_x < 0$) flows into the NH by multiplying any SH $v_{\perp y}$ values by a factor of -1, allowing us to discuss our results from the perspective of the NH.

As additional considerations before performing SEA of $v_{\perp y}$, we only included flow data from the respective time series of a flow detection where the observing spacecraft was located in the same magnetic hemisphere as it was at Epoch 0. This is done to avoid any difficulties in interpretation where a spacecraft has switched hemispheres during a single 'event' ($\pm$ 20 min. period). We also only included $v_{\perp y}$ flow data in the superposed average if the concurrent $v_{\perp x}$ was positive (earthward). This is due to expecting the dusk-dawn sense of the flow to reverse if the earthward-tailward sense does too [see Fig. 2 and Fig. 3 of *Pitkänen et al.* (2019)]. The results of this analysis are shown in Figure 6.5.

In each panel of Fig. 6.5, four curves are shown, one for each of the four flow and IMF B_y categories. In Fig. 6.5a the superposed (mean) IMF B_y values for each category are shown. It is noticeable that |IMF B_y| is ~1 nT larger for AG flows than DAG flows, and that there is only subtle variation in each curve. In Fig. 6.5b we show the superposed time series of $B_{y,pen}$. In all categories, at times well away from Epoch 0, the sign of $B_{y,pen}$ is clearly in agreement with the prevailing IMF B_y conditions. We note that $|B_{y,pen}|$ is larger for AG than DAG flows, which may be a consequence of the greater |IMF B_y| (i.e. indicating more substantial penetration on average). At Epoch 0, on the other hand, there is a clear difference between AG and DAG flows. For the AG flows, $|B_{y,pen}|$ increases by the order of 1 nT, in the same sign as the prevailing IMF B_y conditions. The DAG flows, however, show a change of the order of 1 nT opposite to that of the prevailing IMF B_y conditions, such that the average $|B_{y,pen}|$ is close to 0 in these cases.

In Fig. 6.5c, we show the superposed epoch of $|B_x|$. In all categories, $|B_x|$ begins at larger values and slowly decreases, minimising at Epoch 0 before steadily increasing again. It is noticeable, however, that $|B_x|$ reaches lower values of ~3 nT for DAG flows, compared with 5 to 6 nT for the AG flows.

In Fig. 6.5d, we show the superposed epoch of B_z. In each category, B_z begins between 2 and 3 nT and generally increases, peaking at the time of the fast flow detection (Epoch 0), before decreasing slightly and levelling off at values larger than they were prior to Epoch 0. For the AG flows, the increase in B_z prior to Epoch 0 is steadier than the DAG flows, and B_z peaks at just over 3 nT. Conversely, for the DAG flows, the superposed B_z is more

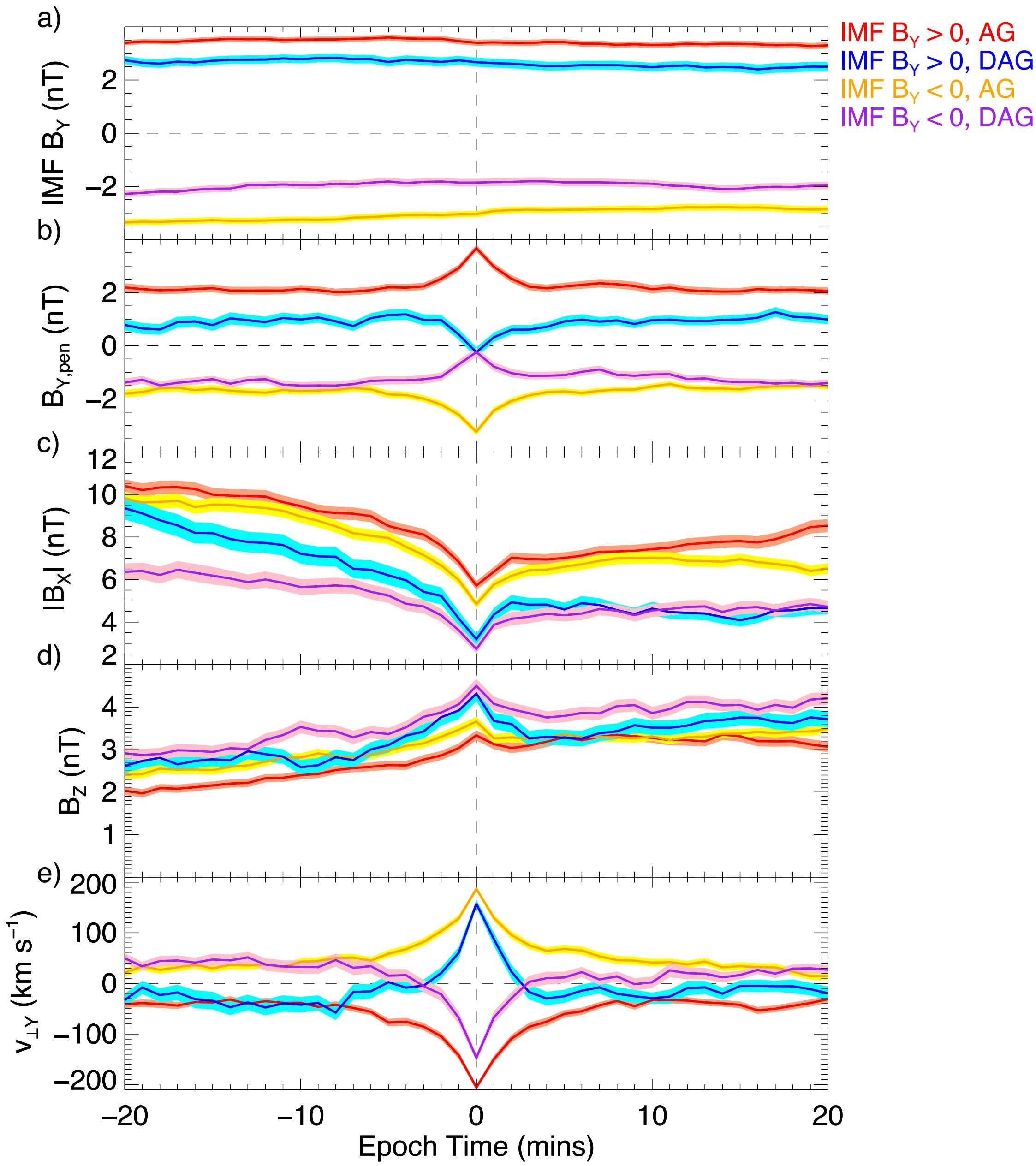

FIGURE 6.5: Superposed epoch of a) IMF B_y, b) $B_{y,pen}$, c) $|B_x|$, d) B_z, and e) $v_{\perp y}$ for IMF $B_y > 0$, AG (red), IMF $B_y > 0$, DAG (blue), IMF $B_y < 0$, AG (yellow), and IMF $B_y < 0$, DAG (purple) categories (defined relative to Epoch 0). The shaded region around each curve corresponds to the standard error of the mean ($\pm\sigma/\sqrt{N}$), where σ is the standard deviation and N is the number of flow detections at each epoch time.

variable, and has larger peaks of over 4 nT.

Finally, in Fig. 6.5e we show a superposed epoch of $v_{\perp y}$ (mapped into the NH). In all categories, it can be seen that at Epoch -20 mins, $v_{\perp y}$ has a magnitude of < 50 km s^{-1}, in all cases in the 'agree' direction, and remains at similar levels until ~ -6 mins. For the AG flows, $v_{\perp y}$ then increases in magnitude, peaking at Epoch 0 before decreasing towards $\sim +6$ mins, then levelling off towards Epoch +20 mins; the direction of the average $v_{\perp y}$ never changes sign. Conversely, for the DAG flows, at Epoch -6 mins, $v_{\perp y}$ decreases in magnitude, with $v_{\perp y}$ changing sign at Epoch ~ -3 mins, peaking at Epoch 0. $v_{\perp y}$ then decreases in magnitude, changing sign again at Epoch $\sim +3$ mins, and again levelling off towards Epoch +20 mins. Therefore, for the DAG flows, and contrary to the AG flows, the average direction of $v_{\perp y}$ at times away from Epoch 0 (beyond Epoch $\pm$ 3 mins) is in the opposite direction to the flow at Epoch 0.

Overall, the results presented in Fig. 6.5 reveal clear differences (on average) between convective fast flows which do and do not exhibit the expected dusk-dawn asymmetry when examined on a temporal scale of $\pm$ 20 minutes. We discuss the implications of this in the following section.

6.5.2 Analysis and Discussion

The idea that the dusk-dawn direction of magnetotail convection should be controlled by the penetration of IMF B_y is a well-established idea [*Grocott et al.* (2007); *Pitkänen et al.* (2015)]. Despite this, the event study presented earlier in this chapter illustrated observation of a duskward flow burst in the NH where IMF $B_y > 0$ which, based on the categorisations for our SEA, would be classified as an 'IMF $B_y > 0$, DAG' flow. Indeed, the features observed in that event are somewhat manifested in the statistical results presented in Fig. 6.5; the isolated duskward flow burst in a period of mostly dawnward 'background' flow, significant dipolarisation, and a sharp reversal in B_y (opposite to the prevailing IMF $B_y > 0$) at the time of the duskward flow. This suggests that the observed duskward flow burst was associated with transient dynamics that were potentially overriding the expected IMF B_y control. We consider this in the discussion below.

Pitkänen et al. (2013) suggested that fast flows with an unexpected dusk-dawn sense could be attributed to a misidentification of the sense of IMF B_y penetration. As discussed in Chapter 4, there exists some ambiguity regarding the time taken for IMF B_y

to penetrate into the magnetotail, and so they attempted to remove this ambiguity by demanding that the local B_y have the same sense as IMF B_y, which inadvertently introduced a locational bias. To avoid the possibility of including such bias in our analysis, we have not filtered by local B_y, but instead examined $B_{y,pen}$, attempting to exclude sources of B_y not related to IMF B_y penetration, as well as only including 'asymmetric' flows. Our results appear to refute the idea that an unexpected sense of IMF B_y penetration could result in the unexpected dusk-dawn sense of the fast flows. The data presented in Fig. 6.5a and Fig. 6.5b clearly indicate that, in-fact, the expected IMF B_y component had (on average) penetrated into the magnetotail, and remained steady at times surrounding the flow detections, with $B_{y,pen}$ exhibiting the expected dusk-dawn sense almost exclusively throughout the 40 mins, regardless of whether the flow burst at Epoch 0 had the expected dusk-dawn direction (AG) or not (DAG). This suggests that it is not necessarily appropriate to attribute a transient flow with the unexpected sense of $v_{\perp y}$ to a 'lack' of IMF B_y penetration. It may be the case, however, that insignificant (i.e. weak) IMF B_y penetration may be insufficient to direct such dusk-dawn flows. This was suggested by *Pitkänen et al.* (2013), and we provide supporting evidence for this, as |IMF B_y| was at least 1 nT larger for AG flows than DAG flows, reflected in the stronger (weaker) $|B_{y,pen}|$ values for AG (DAG) flows seen in Fig. 6.5.

As a further matter, only close to Epoch 0 did $B_{y,pen}$ exhibit any significant change, strengthening in the AG categories whilst becoming notably weaker in the DAG categories. This change was therefore in the same sign as the prevailing IMF B_y conditions for AG flows, but opposite to the prevailing IMF B_y conditions for the DAG flows. We note that due to the stability of the model B_y values with minute-scale changes in spacecraft position and our 130-min averaged model parameterisations, that the transient changes in $B_{y,pen}$ at Epoch 0 can only be explained by transient dynamics (i.e. sudden changes in the local B_y), and are thus not a true reflection of the 'penetrated' B_y at the fast flow time. The argument that this could be an effect of 'sudden' IMF B_y penetration, rather than a transient change, can be refuted on the basis that $B_{y,pen}$ returns to similar levels a few minutes after Epoch 0. Of course, the role of IMF B_y is to introduce a B_y perturbation into the magnetotail (in the same sense as the IMF B_y) - the size of which depends on the IMF B_y magnitude [e.g. *Petrukovich* (2011)]. The subsequent Dungey Cycle convective return flows are expected to respond to this, inheriting the dusk-dawn asymmetry of the closed plasma sheet field lines and enabling the untwisting process to occur. This portrays the notion that the flows are indeed IMF B_y-controlled [e.g. *Grocott et al.* (2007); *Pitkänen et al.* (2013, 2015)]. However, our analysis implies that even if there was clear IMF $B_y > 0$, for example, but at Epoch 0 a transient change in the local B_y component (unrelated to any IMF B_y effect), then this may be what the coincident convective flow would respond to; that is, localised transient dynamics potentially 'overriding' (or preventing) the expected IMF B_y-control. Determining such origins of the perturbations in B_y is beyond the scope of this work, but previous studies have shown that transitory B_y (and concurrent dusk-dawn flow) dynamics could be related to activity associated with current sheet flapping [*Volwerk et al.* (2008); *Lane et al.* (2021)], flow vortices [*Keika et al.* (2009); *Pitkänen et al.* (2011)], or bursty bulk flows and associated magnetic field dipolarisations [e.g. *Walsh et al.* (2009)]. We attempt to examine the transient variability in $B_{y,pen}$ further in Chapter 7.

The argument that localised dynamics may override or prevent any IMF B_y-control is reinforced further by considering the data presented in Fig. 6.5c and Fig. 6.5d. As alluded to in Chapter 4 in reference to Fig. 4.9, it is perhaps unsurprising that $|B_x|$ reaches a minimum in all categories at Epoch 0, as this is where $v_{\perp x}$ and β (which part-define our fast flows) will be larger [*Baumjohann et al.* (1989)]. In agreement with Fig. 4.9, SEA revealed that, irrespective of the sense of IMF B_y, DAG flows have a tendency to be observed at smaller $|B_x|$ than AG flows, implicit of observation closer to the neutral sheet ($B_x \approx 0$). As discussed in Chapter 5, the neutral sheet is a highly dynamic region, where dynamic phenomena such as 'flapping' may be able to influence dusk-dawn flow. Perhaps, therefore, a number of DAG flows are being observed during such intervals where the observing spacecraft may be close to and/or crossing the neutral sheet. We attempt to investigate this in Chapter 7.

SEA also showed that in all cases, B_z appeared to remain at higher levels following Epoch 0 than before, likely indicating a local dipolarisation of the magnetic field, occurring as the magnetic field turns from being strongly parallel, to perpendicular to the neutral sheet [*Schmid et al.* (2011)]. These peaks in B_z are therefore consistent with the minima in

$|B_x|$ [see Fig. 3 of *Ohtani et al.* (2004)]. However, DAG flows have a $\sim$1 nT larger superposed B_z than AG flows. We suggest that this is related to the high proportion of low B_z detections in the AG categories (Fig. 4.9f). This result therefore indicates that weaker dipolarisation may be more commonly associated with the AG flows, and stronger dipolarisation more closely associated with DAG flows. Of course, it is well known that dipolarisations are expected to occur in conjunction with episodes of transient magnetotail dynamics, and the earthward propagation of bursty flows, which themselves may exhibit variable dusk-dawn components [e.g. *Sergeev et al.* (1996b); *Nakamura et al.* (2005)], generate flow vortices [e.g. *Birn et al.* (2004)] and have a dusk-dawn influence on the ambient plasma [e.g. *Liu et al.* (2013)]. One possibility, therefore, is that DAG flows are in some way more likely to be associated with more enhanced transitory dynamics, where any expected IMF B_y-control is suppressed [*Reistad et al.* (2018)], occurring within a background of the larger-scale Dungey Cycle convection. As we also noted in reference to Fig. 4.9f, however, there are also a noticeable proportion of AG flows with large B_z, and thus it may therefore be a relatively naive conclusion to simply assume that flows associated with stronger dipolarisation are independent of any IMF B_y-control. This is a possibility that we aim to explore further in Chapter 7.

It is also apparent from the SEA in Fig. 6.5e that the direction of the 'background' flow (away from Epoch 0) appears to be, on average, consistent with the expected IMF B_y penetration in all flow categories. This is in agreement with the results of *Pitkänen et al.* (2019), whose study of 'slower' flows ($v_{\perp xy} < 200$ km s^{-1}) suggested that flows exhibited a dominant dusk-dawn direction which was in accordance with IMF B_y. We show that this trend holds, irrespective of whether the fast flow at Epoch 0 has the expected dusk-dawn direction or not. For example, if one considers the blue curve (IMF $B_y > 0$, DAG) in Fig. 6.5e, then at Epoch 0, the flow is duskward (by definition). However, once beyond $\pm$ 3 mins, this flow has reversed to be weakly dawnward, such that this 'background' flow now seems to agree with the expected dusk-dawn direction. A similar effect is observed in the case of IMF $B_y < 0$, DAG flows.

We note that the constraint on the flow at Epoch 0 being asymmetric does limit the extent to which we can make inferences about asymmetry in the DAG background flows.

In the case of any AG background flows, these are, on average, in the same sense as the fast flow at Epoch 0. This implies that there is strong evidence for the expected IMF B_y-driven asymmetry being present in the 'background' flow pattern. The DAG background flows on the other hand are, on average, in the opposite direction to the fast flow at Epoch 0. The asymmetry constraint thus implies that the average DAG background flow must be 'symmetric' (such as the dawnward flow observed in the post-midnight sector in the event study presented in this chapter). In other words, such a flow observation from a single point does not explicitly demonstrate the presence of the expected IMF B_y-asymmetry, even though it is consistent with it. What we can be certain of, however, is that there is less disagreement than at Epoch 0, i.e. if an asymmetry inconsistent with IMF B_y was present in the large-scale convection, then its presence must be reduced in the background flow; otherwise we would not see the average dusk-dawn sense of the flow reverse. Thus, there is a measurable transient effect on the flow at the time of the DAG fast flows that is distinct from the AG case.

6.6 Summary

In this chapter, we have presented Cluster spacecraft observations of period of bursty magnetotail flows, the fastest flow of which had a significant duskward component. This observation could only be explained by the untwisting hypothesis in the case of a negative IMF B_y scenario. The IMF and ionospheric convection data, on the other hand, suggested evidence of a large-scale asymmetry consistent with IMF $B_y > 0$, meaning that the observed flow could not be IMF B_y-controlled. Instead, we attributed the duskward flow burst to being associated with localised, transient dynamics related to changes in the local B_y and B_z which appeared to be able, temporarily, to override the expected large-scale net dawnward convection at the location of Cluster. This conclusion was discussed within the context of, and reinforced by, a statistical Superposed Epoch Analysis, where we investigated our separate populations of 'agree' and 'disagree' asymmetric fast flows (first introduced in Chapter 4), noting that the presented event study was a typical example of a 'disagree' flow. We summarise our key findings as follows:

- The expected sense of IMF B_y penetration is associated with both agree and disagree flows, although IMF B_y, and the penetrated B_y field tend to be stronger for agree flows.

- Agree (disagree) flows tend to be accompanied by a localised perturbation to the B_y component of the magnetotail magnetic field in the same sign as (opposite) to the prevailing IMF B_y conditions, which temporarily enhances (overrides) the penetrated field.

- In agreement with Fig. 4.9, agree (disagree) flows tend to be observed on average at larger (smaller) values of $|B_x|$, suggesting that they occur further away from (closer to) the neutral sheet ($B_x = 0$). They also occur in association with weaker (stronger) magnetic field dipolarisation (B_z enhancement).

- The average dusk-dawn direction of slower 'background' convection is consistent with the expected IMF B_y penetration, irrespective of whether the fast flow itself is agree or disagree.

Our results overall suggest that a likely explanation for the $\sim$30% disagreement may be in relation to transient, localised dynamics overriding or preventing IMF B_y-control of fast flows, particularly when |IMF B_y| is weaker. This is reinforced by the fact that the average dusk-dawn sense of the slower 'background' flow, occurring when conditions in the magnetotail are less likely to be perturbed, does not exhibit the same disagreement with IMF B_y. These transient dynamics may be associated with phenomena such as current sheet flapping, dipolarisation, and transitory changes in the local B_y component. We attempt to further identify the extent to which these phenomena might influence dusk-dawn convection and suppress IMF B_y-control of the flows in Chapter 7.

Chapter 7

A Statistical Identification of Possible Drivers of Dusk-Dawn Convective Flow in the Earth's Magnetotail

7.1 Introduction

As discussed in Chapter 4, using our database of asymmetric fast flow detections, we obtained a similar relationship to *Pitkänen et al.* (2013, 2017), whereby ∼70% (∼30%) of flows did (did not) exhibit the expected dusk-dawn sense based on the preceding IMF B_y conditions and hemisphere (Fig. 4.8). We termed such flows as being 'Agree' (AG) and 'Disagree' (DAG), respectively. In Chapters 5 and 6, we presented detailed case studies with the aim of investigating instances where the expected dusk-dawn flow direction was not always observed, despite evidence for the influence of the expected IMF B_y sense on the large-scale convection. In Chapter 5, we attributed the variable dusk-dawn magnetotail flow to being associated with localised flapping motions of the magnetotail current sheet. In Chapter 6, we identified an isolated duskward (unexpected) flow burst in a period of predominantly dawnward flow and suggested that its occurrence may have been related to the nature of a sudden reversal in the local B_y and the observed large (20+ nT) dipolarisation. In both cases, we argued that localised or transient dynamics were 'overriding' or 'preventing' the expected IMF B_y-control of the flow. In order to more closely examine the time-variable nature of these dynamics, we also performed a statistical SEA of our fast flow detections. This, along with our statistical overview (Fig. 4.9), provided stronger evidence for transitory dynamics overriding or preventing IMF B_y-control, notably in cases where |IMF B_y| was weaker. This is consistent with the finding of *Pitkänen et al.* (2013) that the magnitude (and not just the direction) of IMF B_y is likely to be a key factor in controlling the dusk-dawn sense of the flow.

In this final chapter, we subject our dataset to some further statistical analyses in order to explore the extent to which dynamic phenomena, such as those noted in the previous chapters (e.g. current sheet flapping, transient changes in B_y, dipolarisation, and flow vortices) are prevalent within our dataset of asymmetric fast flow detections, and hence may be influencing the observed dusk-dawn flow and suppressing any IMF B_y-control. We do this by considering not instantaneous parameters as was done in Chapter 4, but by defining new parameters that encompass a 10 minute time window around the fast flow event and attempt to capture the dynamic processes listed above. We discover that, generally, a higher percentage of flows exhibiting the expected dusk-dawn direction is observed when 1) the spacecraft is steadily in one magnetic hemisphere (implying no current sheet flapping), 2) transient changes in local B_y are in the same sign as the prevailing IMF B_y, 3) changes in B_z are smaller (less significant dipolarisation), and 4) evidence for any vortical flow is weak. Finally, we perform a threshold analysis to demonstrate how $> 90\%$ of flows exhibit the expected dusk-dawn asymmetry when attempting to exclude such phenomena from our dataset.

7.2 Instrumentation and Data Sets

The dataset used in this study is identical to the fast flow dataset derived in Chapter 4. As noted, we only consider 'asymmetric' flow in the following sections. The total number of flow detections in our dataset is therefore 1639.

7.3 Observations and Results

7.3.1 Current Sheet Flapping

In this section, we attempt to define a simple parameter that can be used as a proxy to identify the phenomenon of current sheet flapping in our fast flow dataset. This has been shown to influence dusk-dawn flow to the extent that any expected IMF B_y-control of the flow may be overridden or prevented [see Chapter 5, *Lane et al.* (2021) and references therin]. To attempt to identify current sheet flapping statistically, we look for crossings of the current sheet, with a single 'crossing' corresponding to a change in sign of B_x [*Rong et al.* (2011)]. Given the ∼minute-scale average duration of current sheet flapping [Table 2 of *Wei et al.* (2019)], it is important to examine the time-series of B_x for each flow detection, as a single B_x value in itself does not reveal any useful information about the phenomenon. Therefore, for each flow detection at time t, we simply count the number of crossings in an arbitrary timeframe of $t \pm 5$ minutes (11 data points in total, thus a maximum of 10 crossings), beginning at $t - 5$. We argue that it is more likely that a given flow was observed during an interval of current sheet flapping if more crossings were observed.

Firstly, we split our flow detections into the two 'Agree' (AG) and 'Disagree' (DAG) categories as defined previously in Chapter 4, for simplicity. Due to the discrete nature of the 'crossings' parameter, in Fig. 7.1a we show a bar chart of the number of crossings per 10 minutes. In Fig. 7.1b, we then show the overall percentage of flows exhibiting the expected dusk-dawn asymmetry at each crossings value; that is, the ratio of the number of AG to total (AG + DAG) flows in each 'bin'. In order to provide a simple estimate for uncertainty on each percentage, we chose to model this situation using a binomial distribution; namely, each flow detection is either a 'success' (AG), or 'failure' (DAG). We then calculate the 95% confidence interval from the normal (Wald) approximation interval, given as:

$$\hat{p} \pm z\sqrt{\frac{\hat{p}(1-\hat{p})}{N}} \tag{7.1}$$

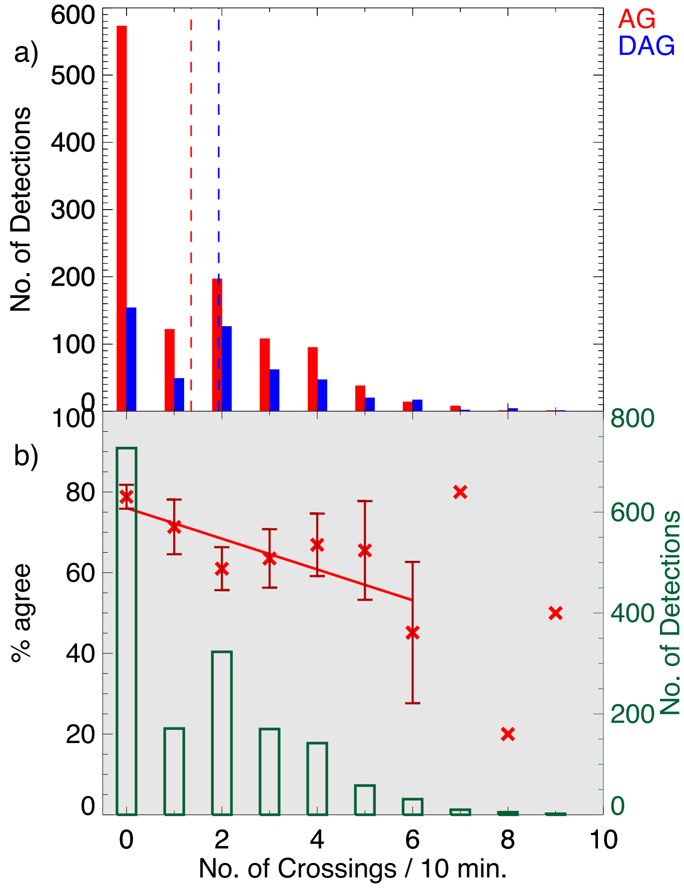

FIGURE 7.1: a) A bar chart of the number of current sheet crossings in a ± 5 minute time frame about each fast flow detection (defined in-text) for AG (red) and DAG (blue) flows. The vertical dashed lines indicate the mean number of crossings per 10 minutes. b) *Left-y-axis*: The percentage of flows exhibiting the expected dusk-dawn asymmetry at each crossing value, shown by the red Xs, with the associated Wald confidence intervals represented by the error bars. The solid red line indicates a linear least-squares regression, fitted only to those data points which have a confidence interval indicated. *Right-y-axis*: A bar chart of the total number of detections at each crossing value, shown in green.

where $\hat{p}$ is the ratio of the number of successes to total number (N) of flow detections in each bin (i.e. the percentage in the expected region), and $z = 1.96$ (for a 95% confidence interval). This tells us that we can be 95% confident that the 'true' probability of a given flow being in the expected region lies within this range of percentages. We choose to indicate this only where $N\hat{p}$, $N(1-\hat{p}) > 10$ due to the approximation being inappropriate at small N and $\hat{p} \approx 0\%$, 100% [see *Brown et al.* (2001)].

Fig. 7.1a reveals that the most common number of observed current sheet crossings across the ± 5 minute window centred on each detection is 0, and this is true in both the case of AG and DAG flows. This is observed in ~570 AG and ~150 DAG flow detections, respectively. These numbers drop off significantly at 1 crossing, before increasing slightly again at 2 crossings. In both categories, the number of flows then steadily decreases at larger numbers of crossings, before almost disappearing entirely at 9 crossings, where there is 1 AG and 1 DAG flow. The percentage of flows exhibiting the expected dusk-dawn asymmetry, reflected by the respective number of AG and DAG flows at each crossing value, is indicated in Fig. 7.1b. This shows that the strongest and most statistically significant agreement was at 0 crossings, where ~80% of flows exhibit the expected dusk-dawn asymmetry. This percentage slowly decreases to ~60% at 2 crossings, before slightly increasing to ~65% at 4 crossings. There is also ~80% agreement at 7 crossings, but there are only 10 detections (8 AG, 2 DAG) where 7 crossings were measured. The overall trend, modelled using a simple linear least squares fitting to the data points which have a confidence interval indicated, and shown by the red line, suggests that the percentage of flows exhibiting the expected dusk-dawn sense decreases as the number of crossings increases.

7.3.2 Changes in Penetrated B_y

In this section, we attempt to identify which of our fast flows may have occurred in association with transient changes in the local B_y. In Chapter 6, SEA showed that AG (DAG) flows tended to be accompanied, on average, by a transient perturbation to the B_y component of the magnetotail magnetic field in the same sign as (opposite to) the prevailing IMF B_y conditions, which temporarily enhanced (overrode) the penetrated field, $B_{y,pen}$. Therefore, here we investigate the possibility that a proportion of the ~30% is related to the sign of transient changes in the local B_y. In order to examine this, we define a 'perturbed' $B_{y,pen}$:

$$\Delta B_{y,pen} = B_{y,pen} - < B_{y,pen} > \tag{7.2}$$

where $B_{y,pen}$ is the 'penetrated B_y' at the fast flow time, and $< B_{y,pen} >$ is the mean $B_{y,pen}$ in the $\pm$ 5 minute timeframe about each flow detection. $\Delta B_{y,pen}$ is therefore not a measure of any instantaneous IMF B_y penetration, but is instead a measure of the extent to which the local B_y changes about the time of each fast flow detection as a consequence

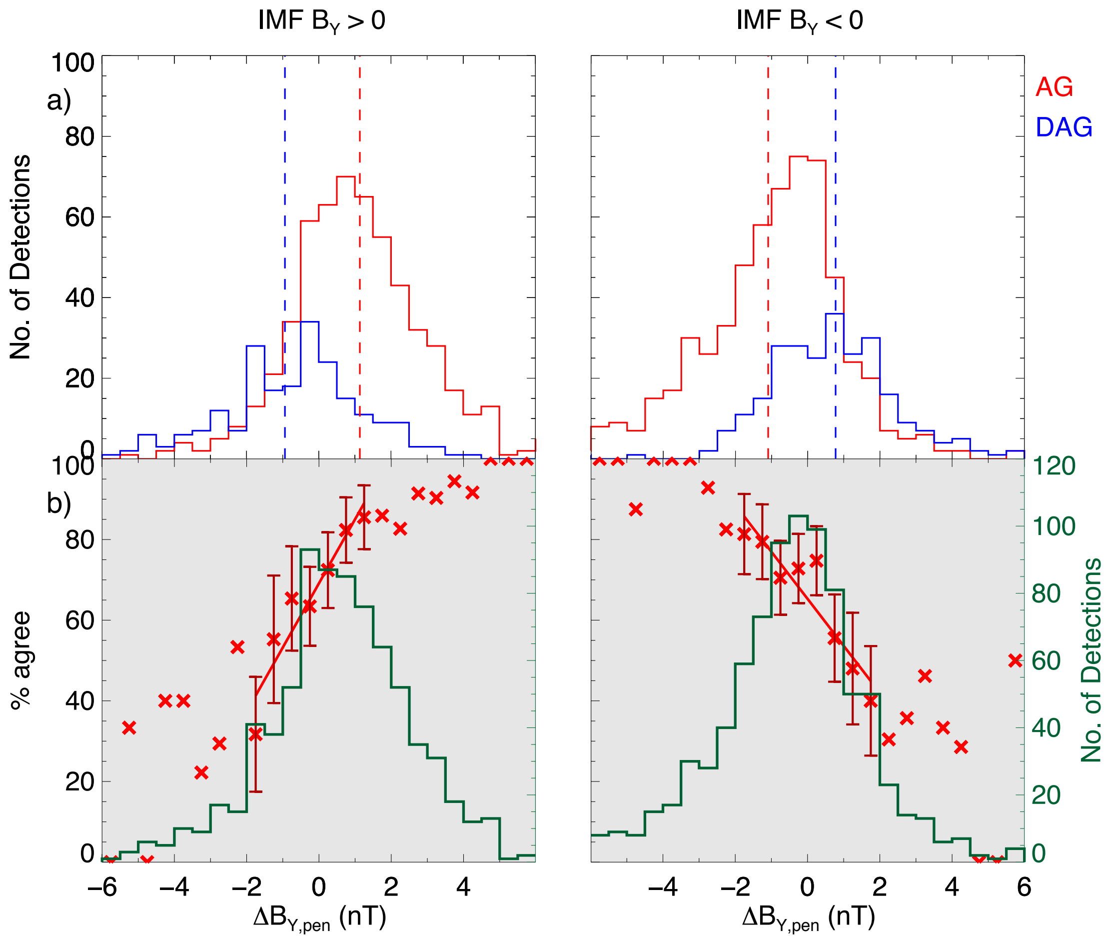

FIGURE 7.2: a) Histograms of $\Delta B_{y,pen}$ (defined in-text), split by sign of IMF B_y, for AG (red) and DAG (blue) flows. The vertical dashed lines indicate the mean values of $\Delta B_{y,pen}$. b) *Left-y-axis*: The percentage of flows exhibiting the expected dusk-dawn asymmetry at each range of $\Delta B_{y,pen}$, shown by the red X's, with the associated Wald confidence intervals represented by the error bars. Each data point lines up with the middle of the corresponding histogram bin. The solid red line indicates a linear least-squares regression, fitted only to those data points which have a confidence interval indicated. *Right-y-axis*: A histogram of the total number of detections in each $\Delta B_{y,pen}$ bin, shown in green.

of non-IMF B_y-dependent transient dynamics. Owing to the need to look at the sign of $\Delta B_{y,pen}$, we separately examine our AG and DAG flows split by positive and negative IMF B_y. In Fig. 7.2a, we then show a histogram of the distribution of $\Delta B_{y,pen}$ for our flows, before calculating the percentage with the expected dusk-dawn flow direction in Fig. 7.2b.

Fig. 7.2a shows that there are distinct differences between the populations of AG and DAG flows when examining $\Delta B_{y,pen}$, both in the case of IMF $B_y > 0$ and IMF $B_y < 0$. For IMF $B_y > 0$ (LHS), the AG flows are clearly centred on positive $\Delta B_{y,pen}$, with a mean $\Delta B_{y,pen}$ of just above 1 nT. By contrast, the DAG flows are centred on weakly negative $\Delta B_{y,pen}$, with a mean $\Delta B_{y,pen}$ of approximately -1 nT. Consequently, at negative values of $\Delta B_{y,pen}$, the percentage of flows exhibiting the expected dusk-dawn asymmetry, shown in Fig. 7.2b, is low ($\leq$ 50%). At positive values of $\Delta B_{y,pen}$, the percentage of flows exhibiting the expected dusk-dawn asymmetry rises to $\geq$ 80%, increasing up to 100% at $\Delta B_{y,pen} \geq 4.5$ nT. The linear trend (red line) suggests that the percentage of flows exhibiting the expected dusk-dawn sense clearly increases as $\Delta B_{y,pen}$ increases. The IMF $B_y < 0$ flows (RHS), by contrast, are effectively a mirror image of the IMF $B_y > 0$ flows; that is, the AG flows are clearly centred on negative $\Delta B_{y,pen}$, with the DAG flows centred on weakly positive $\Delta B_{y,pen}$, and a greater percentage of flows exhibit the expected dusk-dawn asymmetry at more negative values of $\Delta B_{y,pen}$. As a result, the linear trend (red line) suggests that the percentage of flows exhibiting the expected dusk-dawn sense clearly increases as $\Delta B_{y,pen}$ decreases.

7.3.3 Increases in B_z as a Proxy for Field Dipolarisations

In this section, we attempt to identify which of our flows may have occurred in association with large magnitude dipolarisations, which we investigate using as a proxy the observed increase in B_z. It was noted in Chapter 6 that DAG flows were, on average, associated with more variable B_z and larger peaks, perhaps indicating more significant dipolarisation, which may have been influencing the expected IMF B_y-control of the flows. AG flows, meanwhile, were more commonly observed in association with smaller B_z, and thus less significant dipolarisation. A possibility that we investigate here, therefore, is that a proportion of the ~30% disagreement is related to the magnitude of any changes in B_z, in association with the fast flows. Statistically, dipolarisations have been identified by looking for sharp increases in B_z of at least 4 nT across a given time-window [e.g. *Schmid et al.* (2011); *Fu et al.* (2012)]. In the following analysis, we use a similar proxy, in that we attempt to identify the maximum increase in B_z across the same ± 5 minute time frame examined previously. Across this time frame, we identify the peak B_z value, $B_{z,max}$. We then identify the minimum B_z value prior to this time, $B_{z,min}$, and calculate:

$$\Delta B_z = B_{z,max} - B_{z,min} \tag{7.3}$$

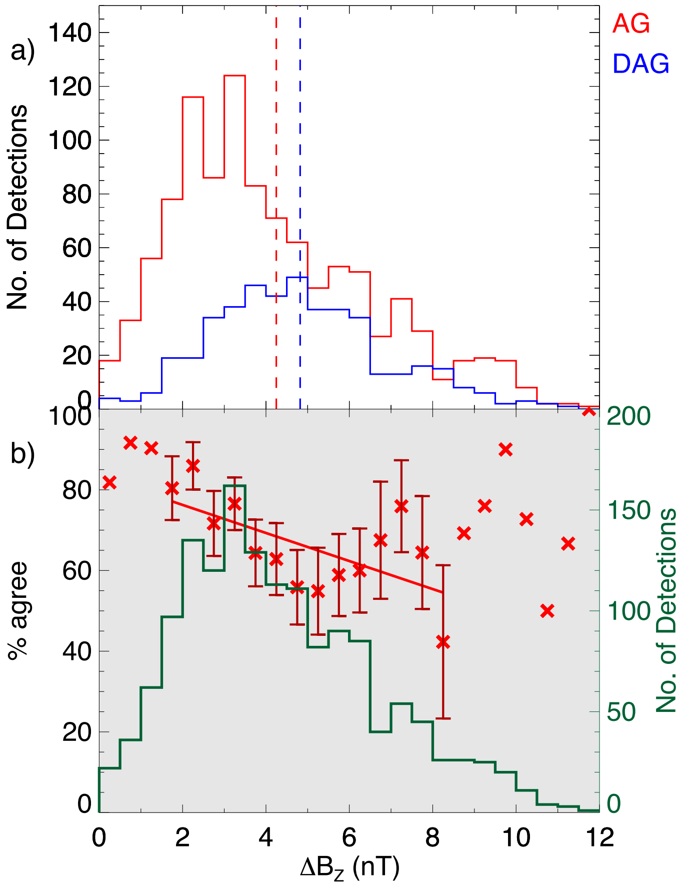

FIGURE 7.3: As in Fig. 7.2, but now for ΔB_z (defined in-text) and not split by sign of IMF B_y.

In Fig. 7.3a, we then show a histogram of the distribution of ΔB_z for our flows, before then again calculating the percentage with the expected dusk-dawn flow direction in Fig. 7.3b.

Fig. 7.3a suggests that the distribution of ΔB_z for both the AG and DAG flows exhibits similar characteristics to the histogram of B_z presented in Fig. 4.9f. Notably, the peak ΔB_z for the AG flows occurs at around 3-3.5 nT, whereas the peak ΔB_z for the DAG flows occurs at slightly greater values of 4.5-5.0 nT. Consequently, the mean ΔB_z is around 0.6 nT larger for the DAG flows. There are, however, a number of AG flows where large (8.5+ nT) ΔB_z was measured. Fig. 7.3b shows that when ΔB_z is small (< 2.5 nT), over 80% of flows exhibit the expected dusk-dawn direction. This percentage then begins to decrease to $< 60\%$ at $\sim$5-5.5 nT, before increasing again to $\sim$75% at 7-7.5 nT.

ΔB_z then minimises at ∼40% in the 8-8.5 nT range, before then increasing back towards and above 70% at larger values of ΔB_z. The overall trend (red line) suggests a gradual decrease in the percentage of flows exhibiting the expected dusk-dawn asymmetry as ΔB_z increases, although it should be emphasised that this trend is weak and should not be over-interpreted.

7.3.4 Flow Vortices

Flow vortices are a phenomenon which can have a significant effect on the large-scale convection, and exist over several Earth radii [e.g. *Hones Jr et al.* (1978)]. Typically, flow vortices, produced as a consequence of BBF-propagation and braking [e.g. *Birn et al.* (2004)], are identified as a consequence of variable earthward-tailward and duskward-dawnward flow and have been observed previously in a number of studies [e.g. *Keika et al.* (2009); *Keiling et al.* (2009)]. Almost by definition, therefore, a flow vortex must include an element of disagree flow if it is comprised of both a duskward and a dawnward component. In order to be able to examine the extent to which any vortical flow might be obscuring any IMF B_y-control of the dusk-dawn flow, and therefore explain a proportion of the ∼30% disagreement, we must attempt to identify which of our fast flow detections might have been detected simply as a consequence of an observed flow vortex meeting the fast flow criteria at a given detection time.

To attempt to identify vortices statistically, we calculated the angle, θ, between the earthward-tailward sense of the convective flow, $v_{\perp x}$, and the dusk-dawn convective flow, $v_{\perp y}$, for each of the 11 data points in the ± 5 minute time frame about each fast flow detection. Such a timeframe should be appropriate to capture any potential vortices [see e.g. *Hones Jr et al.* (1978); *Keiling et al.* (2009); *Pitkänen et al.* (2011)]. Thus, we calculated:

$$\theta = \tan^{-1}(v_{\perp y}, v_{\perp x}) \tag{7.4}$$

with an angle of 0° corresponding to earthward flow, +90° for duskward flow, −90° for dawnward flow, and ± 180° for tailward flow. We then calculate the standard deviation, σ_θ, of the angles calculated across the 10 minute window associated with each fast flow detection from:

$$\sigma_\theta = \sqrt{\frac{\sum_{i=1}^{N}(\theta_i - \bar{\theta})^2}{N-1}} \tag{7.5}$$

where θ_i is each individual angle, $\bar{\theta}$ is the mean of the angles, and N is the number of angles (data points). A smaller value of σ_θ implies that any flow has had a steadier direction; by contrast, a larger value of σ_θ implies that the flow direction has been highly variable, and possibly vortical. We additionally only include θ data in the calculation of σ_θ for each detection where the observing spacecraft was located in same magnetic hemisphere as it was at the fast flow time. This is, again, to avoid any difficulties in interpretation where a spacecraft has switched hemispheres, which may result in a change in sign of $v_{\perp y}$, especially close to midnight [*Grocott et al.* (2007)]. A change in sign of $v_{\perp y}$ would likely increase the value of σ_θ, which could result in potential misidentification of vortices; as implied above, σ_θ is effectively a measure of the variability of the direction of the convective flow in the X_{GSM}-Y_{GSM} plane. In Fig. 7.4a, we then show a histogram of the distribution of σ_θ for our flows, split by AG and DAG, before then again calculating the percentage with the expected dusk-dawn flow direction in Fig. 7.4b. To ensure that this analysis was robust, we only show σ_θ values which had at least 6 (out of a possible 11) θ values with which to calculate σ_θ.

Fig. 7.4a shows that the distributions of AG and DAG flows are overall relatively similar when examining σ_θ. The AG flows have a mean σ_θ of ∼53°, whereas the DAG flows have a slightly larger mean of ∼58°. Interestingly, however, the number of AG flows peaks in the 60-70° range, whereas the number of DAG flows peaks in the 50-60° range. We suggest that this may be related to the seemingly large number of low σ_θ AG flows influencing the mean; in the 0-10° range, there are 57 AG flows, but only 4 DAG flows. Accordingly, in Fig. 7.4b, 93.4% of the flows exhibit the expected dusk-dawn direction at this range of σ_θ. Fig. 7.4b shows that as σ_θ increases to 40°, the percentage of flows exhibiting the expected dusk-dawn sense consistently decreases to a minimum of ∼55% at the 30-40° range. This percentage then increases, remaining relatively steady at values close to 70% for the remaining ranges of σ_θ, with the exception of the final bin (100-110°) where the agreement is ∼45%. The linear trend (red line) suggests that the percentage of flows exhibiting the expected dusk-dawn sense very slightly decreases as σ_θ increases.

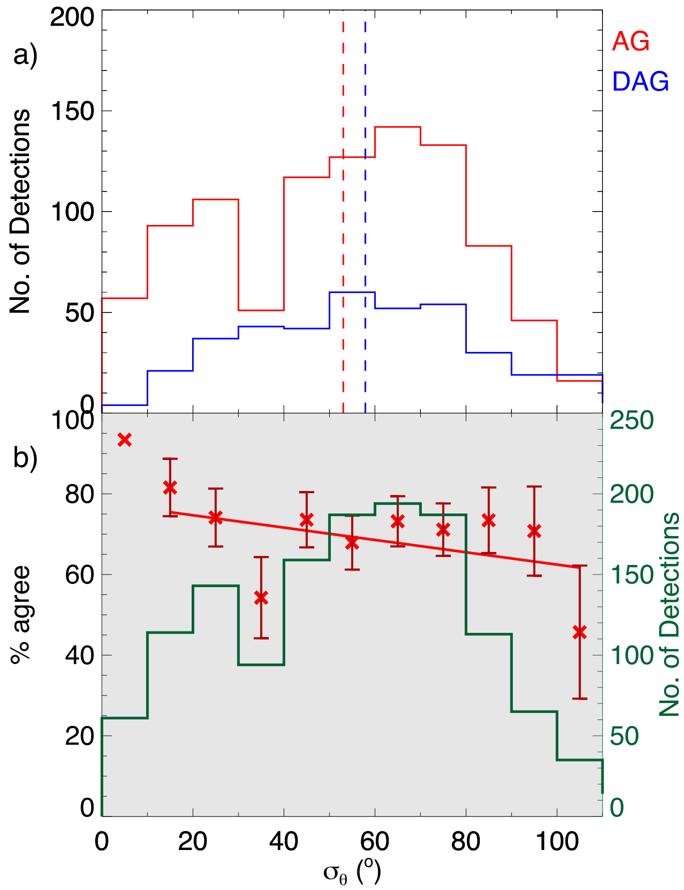

FIGURE 7.4: As in Fig. 7.3, but now for σ_θ (defined in-text).

7.4 Discussion

It is relatively well known that dusk-dawn convection in the Earth's magnetotail is heavily influenced by the sense of IMF B_y [e.g. *Grocott et al.* (2007); *Pitkänen et al.* (2013)]. As well as the sense of IMF B_y, however, the strength of the preceding IMF B_y has also been shown to be an important factor [*Pitkänen et al.* (2013)]. Previously, it has been shown that the stronger the magnitude of IMF B_y, the greater the penetrated B_y and thus the more significant twist which is put into the magnetotail [e.g. *Kaymaz et al.* (1994); *Petrukovich* (2011); *Cao et al.* (2014)]. *Pitkänen et al.* (2013) argued that 'weaker' IMF B_y penetration may be unable to sufficiently twist the magnetotail and subsequently direct the flows in a direction with agrees with the untwisting hypothesis. The results presented in Fig. 4.9 provided support for this argument, by revealing that a greater proportion of flows generally had the expected dusk-dawn direction when their preceding 130-min averaged IMF B_y was larger in magnitude. This was reinforced by a superposed epoch analysis (Fig. 6.5), which showed that the average IMF B_y of AG flows was stronger than for DAG flows. To investigate the above suggestion made by *Pitkänen et al.* (2013) in more detail, we manually inspected the number of flows in the AG and DAG categories in Fig. 4.9 for $|\text{IMF } B_y| < 1$ nT. We find that there are 45 AG flows, and 36 DAG flows, meaning 55.6% of flows had the expected direction, even at this relatively 'weak' IMF B_y threshold. This implies that even weak IMF B_y penetration can twist the tail sufficiently to produce a measurable but small bias towards the expected sense of $v_{\perp y}$, but that evidently, this agreement is much stronger at larger magnitudes of IMF B_y. Whilst this is perhaps an unsurprising result, it indicates that there must be other factors, that we suggest are related to localised and/or transient dynamics, which appear to influence whether flows exhibit the expected dusk-dawn asymmetry, in-effect overriding or suppressing the expected IMF B_y control of the flows, particularly when IMF B_y is weaker in magnitude. In this chapter, we have attempted to identify these 'non-IMF B_y-dependent dynamics' (discussed below) statistically, and investigate their effect on the percentage of flows exhibiting the expected dusk-dawn asymmetry to examine whether they may be related to the ~30% disagreement with IMF B_y.

The first phenomenon which we attempted to identify was current sheet flapping. This was explored in detail in the case study presented in Chapter 5 [*Lane et al.* (2021)], whereby despite evidence of a large-scale IMF $B_y > 0$ asymmetry, the localised flows; and notably, the observed dawnward flow in the southern hemisphere, was inconsistent with the expected duskward convection based on the location of the spacecraft and magnetotail untwisting. The variable flows were, instead, attributed to being associated with a flapping of the current sheet. Inherently, questions arise from such a discovery: is this a frequent occurrence, and can it be identified statistically?

In this work, we have used sign changes in the earthward-tailward (B_x) component of the magnetic field as a proxy for 'crossings' of the current sheet. A valid question then arises as to how many 'crossings' might constitute 'flapping' behaviour. Typically, flapping has a timescale of around a minute [*Wei et al.* (2019)], and several crossings are generally observed during a single flapping 'episode' [e.g. *Runov et al.* (2003, 2009); *Wu et al.* (2016); *Lane et al.* (2021)]. Given these expected properties, we can be relatively confident that 0 or 1 crossings per 10 minutes is not strong evidence of flapping; 0 crossings implies that the spacecraft has remained in the same hemisphere, whereas 1 crossing implies a single change of hemisphere of the spacecraft, which could simply be due to the motion of the spacecraft. The spacecraft trajectories do not abruptly change, however (see e.g. Fig. 5.1a), and thus an additional crossing (i.e. a change back into the original hemisphere, meaning a single 'flap') could not be explained by the spacecraft motion, but instead only by motion of the current sheet itself. This implies that at least 2 crossings must be measured across our $\pm$ 5 minute timeframe for there to be a possibility that flapping is being observed. The fact that there were more flows observed at 2 crossings than 1 crossing in Fig. 7.1 suggests that observing a flap of the current sheet is more common than a single change in hemisphere of a spacecraft. Fig. 7.1 indicated that the strongest, and most statistically significant agreement of $\sim$80% was observed at 0 crossings. This implies that the apparent IMF B_y-control of the dusk-dawn flow is approximately 10% stronger than the overall 70% average when we can be more confident that flapping is not occurring, and certain that the spacecraft has not been crossing the current sheet on a 1 minute timescale. Meanwhile, agreement for between 2 and 6 crossings was close to 60%, which is 10% less than on average, and only 10% greater than the result we would expect for no IMF B_y-control. The linear trend shown in Fig. 7.1b therefore provides support for the study of *Lane et al.* (2021), in that it appears in general that dusk-dawn flow may show weaker IMF B_y-control if the spacecraft is crossing the current sheet more frequently - which we argue is implicit of an increased probability that flapping is occurring. Despite this, there are still $\sim$20% of flows which do not exhibit the expected dusk-dawn direction, even when the spacecraft remains in a single hemisphere. The lack of complete (100%) agreement may be in relation to other phenomena, discussed below.

The second phenomenon that we investigated was the possible association of transient changes in B_y on the dusk-dawn flow at the times of our fast flows. It was noted in Chapter 6 that AG (DAG) flows were accompanied, on average, by a transient perturbation to the B_y component of the magnetotail magnetic field in the same sign as (opposite to) the prevailing IMF B_y conditions, which temporarily enhanced (overrode) the penetrated field, $B_{y,pen}$. In our analysis shown in Fig. 7.2, we calculated a perturbed $B_{y,pen}$ for each flow, $\Delta B_{y,pen}$, an inference for how $B_{y,pen}$ at the flow detection time changed relative to the mean $B_{y,pen}$ surrounding ($\pm$ 5 min.) the fast flow time. For the AG flows, the mean $\Delta B_{y,pen}$ was convincingly in the same sign as the prevailing IMF B_y conditions, with agreement up to 100% occurring at greater magnitudes of $\Delta B_{y,pen}$ ($|\Delta B_{y,pen}| \geq \sim$4 nT). By contrast, for the DAG flows, the mean $\Delta B_{y,pen}$ was in the opposite sign to the prevailing IMF B_y conditions. As noted previously, these sudden changes in $B_{y,pen}$ ($\Delta B_{y,pen}$) cannot be attributed to IMF B_y penetration, which is known to be a more gradual effect [e.g. *Tenfjord et al.* (2015); *Browett et al.* (2017)]. We suggest that they must instead be associated with transient changes in the local B_y. As discussed in Chapter 6, it is unclear how these perturbations arise and what may control their sign. It is convincing, however, that if these perturbations happen to be in a direction which agrees with the prevailing IMF B_y, that there is a much greater likelihood that the associated dusk-dawn flow will agree with IMF B_y, implying, as hinted at by *Pitkänen et al.* (2019), that the sense of dusk-dawn convection is perhaps more closely associated with the local B_y sign, as opposed to IMF B_y. That is not to say that these changes in B_y are causing the flows, but that they are influenced or driven in association with the flows as a direct consequence of the frozen-in-theorem [e.g. *Pitkänen et al.* (2021)].

The third phenomenon that we examined was the possible influence on dusk-dawn flow of enhancements in B_z (ΔB_z) across the $\pm$ 5 minute time frame of our detections, in association with dipolarisation, occurring as the magnetic field is convected earthward by bursty flows [e.g. *Ohtani et al.* (2004); *Walsh et al.* (2009); *Schmid et al.* (2011)]. The histograms of ΔB_z shown in Fig. 7.3a illustrated a similar result to simply examining the distribution of B_z (Fig. 4.9), in that AG (DAG) flows tended to have a lower (greater) mean ΔB_z. As referenced in Chapter 6, a rather naive conclusion would be that DAG flows are more likely to be associated with 'stronger' dipolarisation than AG flows, and thus more transient or bursty dynamics where IMF B_y-control may be less apparent [e.g. *Reistad et al.* (2018)]. A counter point to this, however, is there were still a number of AG flows observed when ΔB_z was substantially (notably at 8.5+ nT) large. Indeed, Fig. 7.3b shows that whilst $\sim$80% of flow detections exhibit the expected dusk-dawn direction at the 1.5-2.0 nT range, a similar agreement ($\sim$76%) is observed at the 9.0-9.5 nT range.

This ~76% agreement is greater than the ~50% we might expect if larger ΔB_z flows were associated with a lack of IMF B_y-control. To investigate whether this could therefore be related to the 'strength' of the IMF B_y-control, we manually inspected the AG flows at the 1.5-2.0 nT and 9.0-9.5 nT ΔB_z ranges. We find that the mean |IMF B_y| of the flows at the 1.5-2.0 nT range was 3.52 nT, compared with 4.94 nT for the 9.0-9.5 nT range. By contrast, the mean |IMF B_y| for the DAG flows at the 9.0-9.5 nT range was 3.30 nT. This suggests, tentatively, that if large ΔB_z flows are indeed associated with a lack of IMF B_y-control, as alluded to in Chapter 6, this may only be true when |IMF B_y| is sufficiently weak, such that the transient dynamics associated with that dipolarisation can 'override' or out-compete IMF B_y. This suggestion does, however, require more extensive investigation to confirm (alluded to further, below).

Finally, we attempted to identify highly variable flow phenomena, such as 'flow vortices', in our fast flow dataset, to examine the extent to which they might be contributing to the 30% disagreement. Due to their variable earthward-tailward and duskward-dawnward nature [e.g. *Hones Jr et al.* (1978); *Keika et al.* (2009); *Keiling et al.* (2009); *Pitkänen et al.* (2011)], we chose to examine the standard deviation of the angles between the earthward-tailward ($v_{\perp x}$) and duskward-dawnward ($v_{\perp y}$) sense of the flow, again across the familiar ± 5 minute time frame for each detection. The results shown in Fig. 7.4b revealed that the strongest agreement of 93.4% was observed when σ_θ was small (0-10°). A smaller value of σ_θ implies that the angle between $v_{\perp x}$ and $v_{\perp y}$ has been more steadily and consistently in a particular direction, which one would definitely expect not to occur if flow vortices were present. The modelled linear trend shown suggests that the percentage of flows with the expected dusk-dawn direction slowly decreases at larger values of σ_θ, implying that periods of more variable flow could be associated with a lack of IMF B_y-control. We noted in Section 7.3.4, however, that at σ_θ values from 40-100°, the percentage of flows with the expected dusk-dawn sense in-fact remained relatively steady at ~70%, with a minimum of ~55% agreement occurring at the 30-40° range. This is despite the flows in this category exhibiting less variability in their direction than flows at larger values of σ_θ. Rather than investigate whether this is could be related to the 'strength' of the IMF B_y-control, as examined above for ΔB_z, we instead performed an alternative speculative analysis involving examining the mean number of current sheet crossings at each σ_θ range.

This analysis suggests that the flows in the 30-40° range have a larger mean number of crossings (∼1.62) than the surrounding σ_θ values, such as at 70-80° range (∼0.87). Thus, one possibility is that the weaker (∼55%) agreement at the 30-40° range is related to a number of those flows being observed during periods of current sheet flapping, where the expected IMF B_y-control is being suppressed. We suggest this only as a possibility based on a rather simple analysis, and indeed the possible 'competition' between the IMF B_y strength and all of the transient phenomena explored in this section (such as flapping) must be investigated more thoroughly in a future study. Overall, however, we argue that these results suggest that unless the flow direction in the X_{GSM}-Y_{GSM} plane is extremely ($\sigma_\theta < 10°$) steady, then we should still expect it to have a dusk-dawn sense which disagrees with IMF B_y ∼30% of the time.

7.4.1 Closing The Loop

The overall purpose of this thesis was to investigate the ∼30% of flows, first identified in *Pitkänen et al.* (2013, 2017), which demonstrate a lack of the expected IMF B_y-control and attempt to explain why. Here, we use the results from the current chapter to illustrate how a number of flows may be 'filtered' out from our population of asymmetric fast flows to improve on the original ∼70% agreement. Unlike *Pitkänen et al.* (2013, 2017), who also filtered by sign of the local B_y component and introduced a location bias, our filters do not incorporate such a bias. In the following example, we perform a simple threshold analysis to examine how the percentage of flows with the expected dusk-dawn sense improves from the previously found 70% agreement with IMF B_y when we additionally impose a number of arbitrarily chosen thresholds:

1. No. of Crossings / 10 min. ≤ 1
2. $\Delta B_z \leq 5$ nT
3. $\sigma_\theta \leq 60°$

We further required that the sign of $\Delta B_{y,pen}$ was in agreement with the prevailing IMF B_y sign. We then recreated the plot shown in Fig. 4.8, again split by IMF $B_y > 0$ and IMF

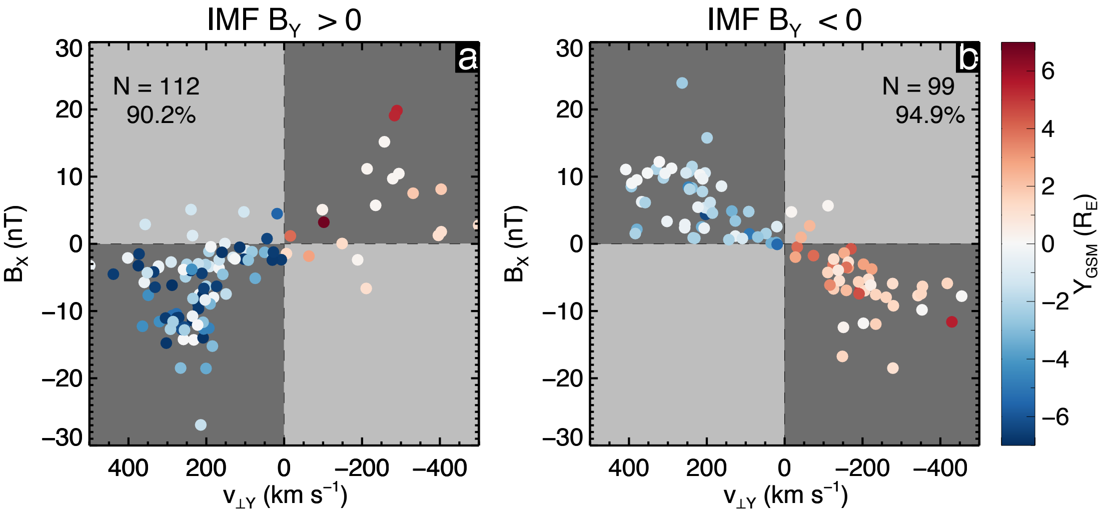

FIGURE 7.5: As in Fig. 4.8, but with additional criteria imposed (see text).

$B_y < 0$, with these additional criteria imposed. The results of this analysis are shown in Fig. 7.5.

As can be seen from Fig. 7.5, more than 90% of the remaining fast flows now exhibit the expected dusk-dawn asymmetry. This is an improved result even to that obtained by *Pitkänen et al.* (2013) when they imposed their additional (but location-biased) B_y criteria. Inherently, there are now several hundred less flows than previously, and there are still a few flows which do not appear to be IMF B_y-controlled. This example highlights that it is not a trivial exercise to define and derive a set of criteria which can only exclude all DAG flows, whilst keeping all AG ones. This is especially true given the amount of overlap between the AG and DAG distributions, in the case of each parameter.

To attempt to quantify the differences between the AG and DAG populations of flows for each parameter, we performed a simple Welch's t-test [see Chapter 14 of *Press et al.* (1992)]. This involves calculating:

$$t = \frac{\bar{X}_{AG} - \bar{X}_{DAG}}{\sqrt{s^2_{\bar{X}_{AG}} + s^2_{\bar{X}_{DAG}}}} \tag{7.6}$$

Parameter	*t-statistic*
No. of Crossings / 10 min.	-5.98
$\Delta B_{y,pen}$	IMF $B_y > 0$: 11.32, IMF $B_y < 0$: -12.45
ΔB_z	-4.54
σ_θ	-3.13

TABLE 7.1: *t-statistics* for comparison of the AG and DAG flow populations for each parameter.

where $\bar{X}_{AG}$ ($\bar{X}_{DAG}$) is the mean value of a given parameter for the AG (DAG) flow populations, and $s_{\bar{X}_{AG}}$ ($s_{\bar{X}_{DAG}}$) is the standard error, i.e.:

$$s_{\bar{X}_{AG}} = \frac{\sigma_{AG}}{\sqrt{N_{AG}}} \tag{7.7}$$

$$s_{\bar{X}_{DAG}} = \frac{\sigma_{DAG}}{\sqrt{N_{DAG}}} \tag{7.8}$$

where σ_{AG} (σ_{DAG}) is the standard deviation and N_{AG} (N_{DAG}) is the number of AG (DAG) flows. The results of this are shown in Table 7.1. Table 7.1 shows that the respective *t-statistics* are all large in magnitude ($|t| \geq 3$). The corresponding significance levels (p-values) are extremely small $<< 0.05$. This implies that, for each parameter, despite the amount of overlap between the AG and DAG populations, their means are significantly different, and there is almost a zero probability that such a result could have occurred by chance if there were truly no differences between the AG and DAG flow populations.

7.5 For Further Consideration

A final point for discussion, first introduced in Chapter 4, is in relation to how we have treated each individual 1 minute flow detection as being 'unique'. It is not uncommon for 1-min timescale flows to be observed successively, which may be a part of a longer period of BBF-like activity [*Angelopoulos et al.* (1992, 1994)]. A relevant question concerns the treatment of such intervals: should each 'flow' be considered separately (as we have done), or used in a more temporally considerate manner when performing statistical analyses? The exact answer to this question is perhaps an issue for a separate study but will be explored here briefly.

One of the main difficulties in answering such a question is that many studies of magnetotail flows have separate definitions of what constitutes a flow 'event', or 'detection'. For example, *McPherron et al.* (2011) identified their fast flow duration as being the time period where $v_{\perp x} > 150$ km s^{-1}. *Kissinger et al.* (2012) applied similar criteria to *McPherron et al.* (2011), with a threshold of 200 km s^{-1}. By contrast, *Frühauff and Glassmeier* (2016), whilst also using a threshold of 200 km s^{-1}, adopted a similar approach to us, in that they had a minimum flow 'event' separation of a minute apart. They also performed an additional analysis whereby they only looked as 'isolated' flow events, which did not occur within 10 minutes of a previous event. In the context of this work, we simply want to ensure that our choice to count each 1-min flow 'detection' as being unique did not have an impact on our results.

To test this, we performed a similar analysis to *Frühauff and Glassmeier* (2016), by grouping only 'isolated' flows. To do this, we ordered our fast flow detections chronologically, and only included flows which did not occur within ± 10 minutes of a previous flow. Using this technique, instead of the 1639 asymmetric flow detections, we now had only 165; approximately 1/10th of the original amount, suggesting that 'isolated' flow detections are relatively uncommon. In the case of IMF $B_y > 0$, there were now only 63 AG and 29 DAG flows, and for IMF $B_y < 0$ there were 55 AG and 18 DAG flows, and thus 68.4% and 75.3% exhibit the expected dusk-dawn direction, respectively. These percentages are similar to the ~70% agreement observed in the case of using every flow detection (Fig. 4.8). Provisionally, this implies that there is not a significant difference in agreement with IMF B_y when looking at 'successive' flows, or only 'isolated' flows, although this should be investigated more thoroughly in a future study.

7.6 Summary

In this chapter, we have analysed our dataset of 1639 asymmetric 'fast flow detections' and attempted to identify which of these detections may have occurred during periods of transient phenomena such as current sheet flapping, transient changes in B_y and B_z (dipolarisation) and flow vortices, which may have been overriding or preventing the expected IMF B_y-influence on the flows, and thus explain some of the ∼30% disagreement. Using a number of derived proxies based on the arbitrary time frame of ± 5 minutes about each flow detection to try and identify the above phenomena, we separately inspected how the percentage of flows exhibiting the expected dusk-dawn asymmetry varied relative to the baseline ∼70% agreement, in relation to each phenomenon. In summary, we find that the percentage of flows exhibiting the expected dusk-dawn asymmetry:

- Is largest (up to ∼80%) when the observing spacecraft does not cross the current sheet around the time of the flow detections. This percentage agreement tends to decrease at increased numbers of crossings. No or minimal crossings implies that current sheet flapping is unlikely to be occurring.
- Is largest (up to ∼100%) when perturbations in $B_{y,pen}$ ($\Delta B_{y,pen}$), indicative of transient changes in the local B_y around the time of the flow detections, are in the same sign as the preceding IMF B_y conditions. This percentage agreement decreases substantially when IMF B_y and $\Delta B_{y,pen}$ do not share the same sign.
- Is largest (up to ∼80%) when changes in B_z (ΔB_z), which we suggest are indicative of dipolarisations, are small (1.5-2 nT) around the time of the flow detections. This percentage agreement tends to decrease gradually at larger values of ΔB_z, although, similar (∼80%) agreement was also observed at the 9.0-9.5 nT range.
- Is largest (up to ∼93%) when the standard deviation of the angles between the earthward-tailward ($v_{\perp x}$) and dusk-dawn ($v_{\perp y}$) convective sense of the flow around the time of the flow detections, σ_θ, is small ($< 10°$). This we interpret as indicating that flow vortices are less likely to be prevalent, or, at least, that a relatively steady flow is being observed. This also implies that the 'background' flow (Chapter 6) has a consistent direction. This percentage agreement decreased slightly but remained relatively steady at ∼70% for $\sigma_\theta \geq 40°$.

Collectively, the results presented in this chapter suggest that the expected IMF B_y-control of the dusk-dawn flow is strongest (≥ 90%, Fig. 7.5) when phenomena such as current sheet flapping and flow vortices are less likely to be occurring, dipolarisation is weaker, and if any transient changes in the local B_y are in the same sign as the preceding IMF B_y. Further work is required to understand the full extent to which these phenomena 'compete' with IMF B_y, and specifically, the strength of the preceding IMF B_y, for governance of the dusk-dawn flow. Even when the possible effects of these phenomena are reduced (Fig. 7.5), disagreement is still observed a few percent of the time. The strong overlap between the parameter distributions for populations of flows which agree and disagree with the expected dusk-dawn sense implies that there may well be other dynamics which are still preventing the IMF B_y-control of dusk-dawn flow that is otherwise expected based on the untwisting hypothesis.

Chapter 8

Summary

8.1 Review

The purpose of the work undertaken in this thesis was to better understand the dependence, or lack thereof, earthward convective dusk-dawn flows in the Earth's magnetotail on the IMF B_y component. This dependence, explained in terms of the magnetotail 'untwisting hypothesis' [*Grocott et al.* (2007)], was only observed in around ∼70% of cases in the studies of *Pitkänen et al.* (2013, 2017). The aim of this work was to explore what might be responsible for the remaining ∼30% of flows which did not show this expected dependence. The main conclusions from this work are summarised chapter-by-chapter, below:

In Chapter 4, we used the TA15 magnetic field model to demonstrate the effect of magnetotail flaring on B_y in the Earth's magnetotail, and that using the local B_y as an inference for IMF B_y penetration is inappropriate due to flaring dominating away from midnight and from the neutral sheet. We demonstrated the locational bias introduced by using the local B_y sign as a filter, as applied to our dataset of magnetotail fast flow 'detections', and illustrated how this left ambiguity regarding the asymmetry of the observed flow. Subsequently, we argued that only flows which clearly demonstrated an asymmetry (i.e. flow toward the midnight boundary, and thus associated with the large-scale asymmetric 'extended' convection cells) were appropriate to include in a study of dusk-dawn asymmetry associated with magnetotail untwisting. A statistical overview of our 'asymmetric' flows suggested that there were clear differences between flows which agreed and disagreed with the expected dusk-dawn asymmetry. In particular, a greater proportion of agree flows tended to occur when |IMF B_y|, the magnitude of the 'penetrated' B_y ($|B_{y,pen}|$) and $|v_{\perp y}|$ were larger than for disagree flows. Disagree flows, meanwhile, tended to be observed when $|B_x|$ was smaller than it was for agree flows, implying greater proximity to the neutral sheet ($B_x = 0$), and when B_z was larger, which could be suggestive of more significant dipolarisation.

In Chapter 5 we inspected more closely an interval of disagree flow containing instances of very small $|B_x|$, observed by C1 as it repeatedly crossed the neutral sheet at $\mathrm{Y}_{GSM} \approx 6\ \mathrm{R}_E$. Observations of the upstream solar wind conditions from OMNI and ionospheric convection measurements from SuperDARN indicated a large-scale asymmetry consistent with positive IMF B_y penetration into the magnetotail. At the pre-midnight location of Cluster, however, the 'disagree' dawnward flow observed by C1 when below the neutral sheet could only be explained by the untwisting hypothesis in a negative IMF B_y scenario. The Cluster magnetic field data also revealed a flapping of the magnetotail current sheet, which has been known to influence dusk-dawn flow. A curlometer analysis suggested that the dusk-dawn sense of the $\mathbf{J} \times \mathbf{B}$ force was consistent with the localised kinks in the magnetic field associated with the transient perturbations to the dusk-dawn flow observed by C1. We thus concluded that the flapping overcame the dusk-dawn sense of the large-scale convection, which we would have expected to be duskward at the location of C1.

In Chapter 6, we presented Cluster observations of a strong dipolarisation (B_z increase) at $\mathrm{Y}_{GSM} \approx -5\ \mathrm{R}_E$ and found this to be associated with a 'disagree' duskward flow burst which appeared to be inconsistent with the large-scale IMF $B_y > 0$ asymmetry in the convection, indicated by observations from SuperDARN. We therefore attributed it to localised or transient dynamics accompanied by changes in the local B_y and B_z, possibly related to the concurrent substorm activity. These observations were then discussed in the context of a statistical superposed epoch analysis of our asymmetric fast flow detections. This revealed that flows with a dusk-dawn sense which appear to 'disagree' with IMF B_y, such as in the presented event study, occurred when |IMF B_y| and $|B_{y,pen}|$ were weaker on average than for flows which 'agree' with IMF B_y. This also showed, however, that disagree flows are not necessarily associated with a 'lack' of expected IMF B_y penetration. Moreover, agree (disagree) flows tended to be associated with transient changes in the local B_y component which temporarily enhanced (overrode) $B_{y,pen}$. As suggested in Chapter 4, the superposed epoch analysis also showed that disagree flows were observed, on average, in association with stronger dipolarisation (B_z increase) and measured closer to the neutral sheet (smaller $|B_x|$) than agree flows, and thus could be associated with more enhanced transitory dynamic phenomena. These results therefore suggested that a likely explanation for the ~30% disagreement may be in relation to transient, localised dynamics overriding or preventing IMF B_y-control of fast flows, particularly when the IMF B_y magnitude is weaker. This was reinforced by the fact that the average dusk-dawn sense of the slower 'background' flow, occurring when conditions in the magnetotail are less likely to be perturbed, did not exhibit the same disagreement with IMF B_y.

In Chapter 7, we attempted to identify dynamic phenomena in our dataset of fast flow detections, including current sheet flapping, transient changes in B_y, dipolarisation, and flow vortices, to understand the extent to which these may be related to the ~30% disagreement with IMF B_y. These results overall suggested that the expected IMF B_y-control of the dusk-dawn flow is strongest ($\geq 90\%$) when current sheet flapping and flow vortices are less likely to be occurring, dipolarisation is smaller, and if any transient changes in the local B_y are also in the same sign as the preceding IMF B_y.

The fundamental conclusion from our research is that transient dynamics appear to be able to override and/or prevent the expected IMF B_y-control of convective dusk-dawn magnetotail flows, which we believe explains at least two thirds (i.e. 20%) of the original ~30% disagreement (compare Fig. 4.8 to Fig. 7.5). This is evident on a localised scale, as even when the large-scale convection appears to be consistent with IMF B_y; as was shown in the event studies in Chapters 5 and 6, flow disagreement on the spatial and temporal scales of an observing spacecraft is measurable.

8.2 Possibilities for Future Work

This research has raised a number of questions and possibilities which still remain unanswered and should be strongly considered in future studies, which we now discuss. One possibility is to incorporate the use of the SuperDARN data into the superposed epoch analysis presented in Chapter 6. This would allow, for those flows which 'disagree' with IMF B_y, to observe what proportion of the 'symmetric' background flows are indeed associated with the expected large-scale IMF B_y asymmetry. Additionally, whilst we have utilised maps of the large-scale ionospheric convection, it could prove to be a useful investigation to more closely inspect the LOS data from the SuperDARN radars to examine whether any transient changes in the plasma sheet flow are observed on a smaller scale in the ionosphere (i.e. changes which don't significantly influence the global fits used here).

As mentioned in Chapter 7, it is also important to understand to a greater extent the 'competition' between IMF B_y strength and localised dynamics for influence on the dusk-dawn flow. For example, we suggested in Section 7.4 that the ∼55% agreement with IMF B_y at the 30-40° σ_θ range was as a result of a relatively large mean number of current sheet crossings in this bin compared to the other (larger) ranges of σ_θ, where ∼70% agreement was observed. It could prove a useful exercise to additionally inspect, for example, the average |IMF B_y|, $|\Delta B_{y,pen}|$ and ΔB_z values in each σ_θ bin to gain further insight into how these factors potentially compete or overlap with one-another and ultimately affect agreement with IMF B_y. This could be repeated for each parameter explored in Chapter 7.

Also, as discussed in Section 7.5, we have defined our flows in such a way that each flow 'detection' only had to have a minimum separation of 1 minute. Whilst we have briefly investigated the robustness of this choice, by e.g. examining our results only for 'isolated' flows (separated by a minimum of 10 min.) and ensuring that this did not have a significant impact on our results, we have not quantified any effects of flow burst timescale in detail. Indeed, the lack of unanimity amongst previous studies as to how a single flow 'burst', 'event', or 'detection' should be defined invites a conundrum for future work.

A further possibility for future work would be to incorporate data from the recent Magnetospheric Multiscale (MMS) mission into the studies presented in this thesis. MMS is analagous to Cluster, in that there are four identical spacecraft [*Burch et al.* (2016)], yet these spacecraft are able to make observations on a spatial ($\sim$10 km separation) and temporal ($<<$ 1 s) resolution not seen before. It would be fascinating to examine whether, on an even smaller scale than the observations presented in this thesis, similar issues arise in relation to the influence of localised, transient dynamics on dusk-dawn convection and how this affects agreement with IMF B_y (e.g. could agreement be $< 70\%$ on an even smaller scale?).

Another possibility concerns the potential to which machine learning techniques could be used within this area of research [e.g. *Bortnik et al.* (2016)]. Throughout this thesis, we have noted clear degrees of overlap between 'agree' and 'disagree' flows when examining a number of parameters (Fig. 4.9). Given the sense of IMF B_y, B_x and $v_{\perp y}$, it is a simple exercise to determine whether a flow agrees or disagrees with the expected dusk-dawn sense [*Pitkänen et al.* (2013)]. In this thesis, we have, however, examined other parameters that the untwisting hypothesis does not directly rely on (e.g. X_{GSM}, B_z, AL). It would be intriguing to test whether a machine learning technique such as a decision tree algorithm [see e.g. *Bentley et al.* (2020)], would be able to create a model which successfully predicts whether a flow would be more likely to be an 'agree', or 'disagree' flow, purely based on values of such parameters. Indeed, the increasing use of machine learning techniques may open up entirely new and exciting possibilities for the future of magnetospheric physics.

Bibliography

Acuña, M. H. (2002), Space-based magnetometers, *Rev. Sci. Instrum.*, *73*(11), 3717–3736, doi:10.1063/1.1510570.

Akasofu, S.-I. (1964), The development of the auroral substorm, *Planet. and Space Sci.*, *12*(4), 273–282, doi:10.1016/0032-0633(64)90151-5.

Alfvén, H. (1942), Existence of Electromagnetic-Hydrodynamic Waves, *Nature*, *150*, 405–406, doi:10.1038/150405d0.

Anderson, H. R., and R. R. Vondrak (1975), Observations of Birkeland Currents at Auroral Latitudes, *Rev. Geophys.*, *13*(1), 243–262, doi:10.1029/RG013i001p00243.

Angelopoulos, V. (2008), The THEMIS Mission, *Space Sci. Rev.*, *141*(5), 5–34, doi:10.1007/s11214-008-9336-1.

Angelopoulos, V., W. Baumjohann, C. F. Kennel, F. V. Coroniti, M. G. Kivelson, R. Pellat, et al. (1992), Bursty Bulk Flows in the Inner Central Plasma Sheet, *J. Geophys. Res.*, *97*(A4), 4027–4039, doi:10.1029/91JA02701.

Angelopoulos, V., C. F. Kennel, F. V. Coroniti, R. Pellat, M. G. Kivelson, R. J. Walker, et al. (1994), Statistical characteristics of bursty bulk flow events, *J. Geophys. Res.*, *99*(A11), 21,257–21,280, doi:10.1029/94JA01263.

Angelopoulos, V., J. P. McFadden, D. Larson, C. W. Carlson, S. B. Mende, H. Frey, et al. (2008), Tail Reconnection Triggering Substorm Onset, *SCIENCE*, *321*(5891), 931–935, doi:10.1126/science.1160495.

Artemyev, A., S. Lu, M. El-Alaoui, Y. Lin, V. Angelopoulos, X.-J. Zhang, et al. (2021), Configuration of the Earth's Magnetotail Current Sheet, *Geophys. Res. Lett.*, *48*(6), e2020GL092,153, doi:10.1029/2020GL092153.

Auster, H. U., K. H. Glassmeier, W. Magnes, O. Aydogar, W. Baumjohann, D. Constantinescu, et al. (2008), The THEMIS fluxgate magnetometer, *Space Sci. Rev.*, *141*, 235–264, doi:10.1007/s11214-008-9365-9.

Balogh, A., C. M. Carr, M. H. Acuña, M. W. Dunlop, T. J. Beek, P. Brown, et al. (2001), The Cluster Magnetic Field Investigation: Overview of in-flight performance and initial results, *Ann. Geophys.*, *19*, 1207–1217, doi:10.5194/angeo-19-1207-2001.

Bame, S. J., J. R. Asbridge, H. E. Felthauser, E. W. Hones, and I. B. Strong (1967), Characteristics of the plasma sheet in the Earth's magnetotail, *J. Geophys. Res.*, *72*(1), 113–129, doi:10.1029/JZ072i001p00113.

Baumjohann, W. (2002), Modes of convection in the magnetotail, *Physics of Plasmas*, *9*(9), 3665–3667, doi:10.1063/1.1499116.

Baumjohann, W., and R. Treumann (1997), *Basic Space Plasma Physics (Revised Edition)*, Imperial College Press.

Baumjohann, W., G. Paschmann, and C. A. Cattell (1989), Average Plasma Properties in the Central Plasma Sheet, *J. Geophys. Res.*, *94*(A6), 6597–6606, doi:10.1029/JA094iA06p06597.

Baumjohann, W., G. Paschmann, and H. Lühr (1990), Characteristics of High-Speed Ion Flows in the Plasma Sheet, *J. Geophys. Res.*, *95*(A4), 3801–3809, doi:10.1029/JA095iA04p03801.

Baumjohann, W., G. Paschmann, and T. Nagai (1992), Thinning and Expansion of the Substorm Plasma Sheet, *J. Geophys. Res.*, *97*(A11), 17,173–17,175, doi:10.1029/92JA01519.

Bentley, S. N., J. R. Stout, T. E. Bloch, and C. E. J. Watt (2020), Random Forest Model of Ultralow-Frequency Magnetospheric Wave Power, *Earth and Space Sci.*, *7*(10), e2020EA001,274, doi:10.1029/2020EA001274.

Berchem, J., and C. T. Russell (1982), The thickness of the magnetopause current layer: ISEE 1 and 2 observations, *J. Geophys. Res.*, *87*(A4), 2108–2114, doi:10.1029/JA087iA04p02108.

Birkeland, K. (1908), *The Norwegian Aurora Polaris Expedition 1902-1903, vol. 1*, H. Aschehoug & Co., New York and Christiania.

Birn, J., M. Hesse, G. Haerendel, W. Baumjohann, and K. Shiokawa (1999), Flow braking and the substorm current wedge, *J. Geophys. Res.*, *104*(A9), 19,895–19,903, doi:10.1029/1999JA900173.

Birn, J., J. Raeder, Y. L. Wang, R. A. Wolf, and M. Hesse (2004), On the propagation of bubbles in the geomagnetic tail, *Ann. Geophys.*, *22*(5), 1773–1786, doi:10.5194/angeo-22-1773-2004.

Boakes, P. D., R. Nakamura, M. Volwerk, and S. E. Milan (2014), ECLAT Cluster Spacecraft Magnetotail Plasma Region Identifications (2001-2009), *Dataset Papers in Science, vol. 2014*(684305), 1–13, doi:10.1155/2014/684305.

Borovsky, J. E., M. F. Thomsen, and D. J. McComas (1997), The superdense plasma sheet: Plasmaspheric origin, solar wind origin, or ionospheric origin?, *J. Geophys. Res.*, *102*(A10), 22,089–22,097, doi:10.1029/96JA02469.

Bortnik, J., W. Li, R. M. Thorne, and V. Angelopoulos (2016), A unified approach to inner magnetospheric state prediction, *J. Geophys. Res.*, *121*(3), 2423–2430, doi:10.1002/2015JA021733.

Browett, S. D., R. C. Fear, A. Grocott, and S. E. Milan (2017), Timescales for the penetration of IMF B_y into the Earth's magnetotail, *J. Geophys. Res.: Space Physics*, *122*(1), 579–593, doi:10.1002/2016JA023198.

Brown, L. D., T. T. Cai, and A. DasGupta (2001), Interval Estimation for a Binomial Proportion, *Statist. Sci.*, *16*(2), 101–133, doi:10.1214/ss/1009213286.

Burch, J. L., T. E. Moore, R. B. Torbert, and B. L. Giles (2016), Magnetospheric Multiscale Overview and Science Objectives, *Space Sci. Rev.*, *199*, 5–21, doi:10.1007/s11214-015-0164-9.

Cao, J. B., Y. D. Ma, G. Parks, H. Réme, I. Dandouras, R. Nakamura, et al. (2006), Joint observations by Cluster satellites of bursty bulk flows in the magnetotail, *J. Geophys. Res.*, *111*(A4), A04,206, doi:10.1029/2005JA011322.

Cao, J. B., A. Duan, M. Dunlop, X. Wei, and C. Cai (2014), Dependence of IMF B_y penetration into the neutral sheet on IMF B_z and geomagnetic activity, *J. Geophys. Res.*, *119*(7), 5279–5285, doi:10.1002/2014JA019827.

Carrington, R. C. (1859), Description of a Singular Appereance seen in the Sun on September 1, 1859, *Monthly Notices of the Royal Astronomical Society*, *20*(1), 13–15, doi:10.1093/mnras/20.1.13.

Case, N. A., and J. A. Wild (2012), A statistical comparison of solar wind propagation delays derived from multispacecraft techniques, *J. Geophys. Res.*, *117*(A2), A02,101, doi:10.1029/2011JA016946.

Case, N. A., A. Grocott, S. Haaland, C. J. Martin, and T. Nagai (2018), Response of Earth's neutral sheet to reversals in the IMF B_y component, *J. Geophys. Res.: Space Physics*, *123*(10), 8206–8218, doi:10.1029/2018JA025712.

Case, N. A., A. Grocott, R. C. Fear, S. Haaland, and J. H. Lane (2020), Convection in the Magnetosphere-Ionosphere System: a Multi-Mission Survey of Its Response to IMF B_y Reversals, *J. Geophys. Res.*, *125*(10), e2019JA027,541, doi:10.1029/2019JA027541.

Case, N. A. C. (2014), *Solar Wind-Magnetosphere Interactions: A Statistical Analysis of Spacecraft Measurements*, Lancaster University, Doctoral Thesis.

Chapman, S., and V. C. A. Ferraro (1931), A new theory of magnetic storms, *Terr. Magn. Atmos. Electr.*, *36*(2), 77–97, doi:10.1029/TE036i002p00077.

Chapman, S., and V. C. A. Ferraro (1941), The Geomagnetic Ring-Current: 1 - Its Radial Stability, *Terr. Magn. Atmos. Electr.*, *46*(1), 1–6, doi:10.1029/TE046i001p00001.

Chaston, C. C., T. D. Phan, J. W. Bonnell, F. S. Mozer, M. Acuña, M. L. Goldstein, et al. (2005), Drift-Kinetic Alfvén Waves Observed near a Reconnection X Line in the Earth's Magnetopause, *Phys. Rev. Lett.*, *95*(6), 065,002, doi:10.1103/PhysRevLett.95.065002.

Chen, C. X., and R. A. Wolf (1993), Interpretation of high-speed flows in the plasma sheet, *J. Geophys. Res.*, *98*(A12), 21,409–21,419, doi:10.1029/93JA02080.

Chisham, G., M. Lester, S. E. Milan, M. P. Freeman, W. A. Bristow, A. Grocott, et al. (2007), A decade of the Super Dual Auroral Radar Network (SuperDARN): scientific achievements, new techniques and future directions, *Surveys in Geophysics*, *28*, 33–109, doi:10.1007/s10712-007-9017-8.

Chisham, G., M. P. Freeman, G. A. Abel, M. M. Lam, M. Pinnock, I. J. Coleman, et al. (2008a), Remote sensing of the spatial and temporal structure of magnetopause and magnetotail reconnection from the ionosphere, *Rev. Geophys.*, *46*(1), RG1004, doi:10.1029/2007RG000223.

Chisham, G., T. K. Yeoman, and G. J. Sofko (2008b), Mapping ionospheric backscatter measured by the SuperDARN HF radars - Part 1: A new empirical virtual height model, *Ann. Geophys.*, *26*(4), 823–841, doi:10.5194/angeo-26-823-2008.

Chiu, M. C., U. I. Von-Mehlem, C. E. Willey, T. M. Betenbaugh, J. J. Maynard, J. A. Krein, et al. (1998), ACE SPACECRAFT, *Space Sci. Rev.*, *86*, 257–284, doi:10.1023/A:1005002013459.

Cnossen, I., M. Wiltberger, and J. E. Ouellette (2012), The effects of seasonal and diurnal variations in the Earth's magnetic dipole orientation on solar wind-magnetosphere-ionosphere coupling, *J. Geophys. Res.*, *117*, A11,211, doi:10.1029/2012JA017825.

Cowley, S. W. H. (1981), Magnetospheric asymmetries associated with the y-component of the IMF, *Planet. Space Sci.*, *29*(1), 79–96, doi:10.1016/0032-0633(81)90141-0.

Cowley, S. W. H. (1982), The causes of convection in the Earth's magnetosphere: A review of developments during the IMS, *Rev. Geophys.*, *20*(3), 531–565, doi:10.1029/RG020i003p00531.

Cowley, S. W. H. (2000), Magnetosphere-Ionosphere Interactions: A Tutorial Review, *Magnetospheric Current Systems, Geophys. Monogr. Ser.*, *118*, 91–106, doi:10.1029/GM118p0091.

Cowley, S. W. H., and M. Lockwood (1992), Excitation and decay of solar wind-driven flows in the magnetosphere-ionosphere system, *Ann. Geophys.*, *10*, 103–115.

Cowley, S. W. H., J. P. Morelli, and M. Lockwood (1991), Dependence of convective flows and particle precipitation in the high-latitude dayside ionosphere on the X and Y components of the interplanetary magnetic field, *J. Geophys. Res.*, *96*(A4), 5557–5564, doi:10.1029/90JA02063.

Crooker, N. U. (1979), Dayside merging and cusp geometry, *J. Geophys. Res.*, *84*(A3), 951–959, doi:10.1029/JA084iA03p00951.

Davis, T. N., and M. Sugiura (1966), Auroral electrojet activity index AE and its universal time variations, *J. Geophys. Res.*, *71*(3), 785–801, doi:10.1029/JZ071i003p00785.

Domingo, V., and D. Wyn-Roberts (1984), The L1-lagrangian point orbit as a suitable site for helioseismologic measurements, *Mem. Soc. Astron. Ital*, *55*(1-2), 375–381.

Dungey, J. W. (1961), Interplanetary Magnetic Field and the Auroral Zones, *Phys. Rev. Lett.*, *6*(2), 47–48, doi:10.1103/PhysRevLett.6.47.

Dungey, J. W. (1965), The length of the magnetospheric tail, *J. Geophys. Res.*, *70*(7), 1753, doi:10.1029/JZ070i007p01753.

Dunlop, M. W., D. J. Southwood, K.-H. Glassmeier, and F. M. Neubauer (1988), Analysis of multipoint magnetometer data, *Adv. in Space Res.*, *8*(9-10), 273–277, doi:10.1016/0273-1177(88)90141-X.

Dunlop, M. W., T. I. Woodward, and C. J. Farrugia (1995), Minimum Variance Analysis: Cluster Themes, *Proceedings of the Cluster Workshops on Data Analysis Tools, Braunschweig, Germany, 28-30 September 1994*, *ESA SP-371*.

Dunlop, M. W., A. Balogh, K.-H. Glassmeier, and P. Robert (2002), Four-point Cluster application of magnetic field analysis tools: The Curlometer, *J. Geophys. Res.*, *107*(A11), SMP 23–1–SMP 23–14, doi:10.1029/2001JA005088.

Dunlop, M. W., X.-C. Dong, T.-Y. Wang, J. P. Eastwood, P. Robert, S. Haaland, et al. (2021), Curlometer Technique and Applications, *J. Geophys. Res.*, *126*(11), e2021JA029,538, doi:10.1029/2021JA029538.

Erickson, G. M., R. W. Spiro, and R. A. Wolf (1991), The physics of the Harang discontinuity, *J. Geophys. Res.*, *96*(A2), 1633–1645, doi:10.1029/90JA02344.

Eriksson, S. (2001), *Global Magnetospheric Plasma Convection*, Alfvén Laboratory, Division of Plasma Physics, KTH, Stockholm, Sweden, Doctoral Thesis.

Eriksson, S., M. Maimaiti, J. B. H. Baker, K. J. Trattner, D. J. Knipp, and F. D. Wilder (2017), Dual E x B flow responses in the dayside ionosphere to a sudden IMF By rotation, *Geophys. Res. Lett*, *44*(13), 6525–6533, doi:10.1002/2017GL073374.

Escoubet, C. P., M. Fehringer, and M. Goldstein (2001), The Cluster mission, *Ann. Geophys.*, *19*(10-12), 1197–1200, doi:10.5194/angeo-19-1197-2001.

Fairfield, D. H. (1967), Polar magnetic disturbances and the interplanetary magnetic field, *Space Res.*, *VIII*, 107–119.

Fairfield, D. H. (1979), On the average configuration of the geomagnetic tail, *J. Geophys. Res.*, *84*(A5), 1950–1958, doi:10.1029/JA084iA05p01950.

Fairfield, D. H., T. Mukai, A. T. Y. Lui, C. A. Cattell, G. D. Reeves, T. Nagai, et al. (1998), Geotail observations of substorm onset in the inner magnetotail, *J. Geophys. Res.*, *103*(A1), 103–117, doi:10.1029/97JA02043.

Fazakerley, A. N., S. J. Schwartz, and G. Paschmann (1998), *Measurement of Plasma Velocity Distributions, in: Analysis Methods for Multi-Spacecraft Data, edited by: Paschmann, G. and Daly, W.*, ESA Publications Division., 91-124.

Fear, R. C., and S. E. Milan (2012), The IMF dependence of the local time of transpolar arcs: Implications for formation mechanism, *J. Geophys. Res.*, *117*(A3), A03,213, doi:10.1029/2011JA017209.

Fedder, J. A., C. M. Mobarry, and J. G. Lyon (1991), Reconnection voltage as a function of IMF clock angle, *Geophys. Res. Lett*, *18*(6), 1047–1050, doi:10.1029/90GL02722.

Forsyth, C., M. Lester, S. W. H. Cowley, I. Dandouras, A. N. Fazakerley, R. C. Fear, et al. (2008), Observed tail current systems associated with bursty bulk flows and auroral streamers during a period of multiple substorms, *Ann. Geophys.*, *26*(1), 167–184, doi:10.5194/angeo-26-167-2008.

Freidberg, J. P. (2014), *Ideal MHD*, Cambridge University Press.

Frey, H. U., T. D. Phan, S. A. Fuselier, and S. B. Mende (2003), Continuous magnetic reconnection at Earth's magnetopause, *Lett. to Nature*, *426*, 533–537, doi:10.1038/nature02084.

Frey, S., V. Angelopoulos, M. Bester, J. Bonnell, T. Phan, and D. Rummel (2008), Orbit Design for the THEMIS Mission, *Space Sci. Rev.*, *141*, 61–89, doi:10.1007/s11214-008-9441-1.

Friis-Christensen, E., Y. Kamide, A. D. Richmond, and S. Matsushita (1985), Interplanetary magnetic field control of highlatitude electric fields and currents determined from Greenland Magnetometer Data, *J. Geophys. Res.*, *90*(A2), 1325–1338, doi:10.1029/JA090iA02p01325.

Frühauff, D., and K.-H. Glassmeier (2016), Statistical analysis of magnetotail fast flows and related magnetic disturbances, *Ann. Geophys.*, *34*(4), 399–409, doi:10.5194/angeo-34-399-2016.

Fu, H. S., Y. V. Khotyaintsev, A. Vaivads, M. André, and S. Y. Huang (2012), Occurrence rate of earthward-propagating dipolarization fronts, *Geophys. Res. Lett.*, *39*(10), L10,101, doi:10.1029/2012GL051784.

Fukunishi, H. (1975), Dynamic relationship between proton and electron auroral Substorms, *J. Geophys. Res.*, *80*(4), 553–574, doi:10.1029/JA080i004p00553.

Ganushkina, N. Y., M. W. Liemohn, and S. Dubyagin (2018), Current systems in the Earth's magnetosphere, *Rev. of Geophys.*, *56*(2), 309–332, doi:10.1002/2017RG000590.

Gkioulidou, M., C.-P. Wang, L. R. Lyons, and R. A. Wolf (2009), Formation of the Harang reversal and its dependence on plasma sheet conditions: Rice convection model simulations, *J. Geophys. Res.*, *114*(A7), A07,204, doi:10.1029/2008JA013955.

Gold, T. (1959), Motions in the magnetosphere of the Earth, *J. Geophys. Res.*, *64*(9), 1219–1224, doi:10.1029/JZ064i009p01219.

Gonzalez, W. D., J. A. Joselyn, Y. Kamide, H. W. Kroehl, G. Rostoker, B. T. Tsurutani, and V. M. Vasyliūnas (1994), What is a geomagnetic storm?, *J. Geophys. Res.*, *99*(A4), 5771–5792, doi:10.1029/93JA02867.

Grimald, S., I. Dandouras, P. Robert, and E. Lucek (2012), Study of the applicability of the curlometer technique with the four Cluster spacecraft in regions close to Earth, *Ann. Geophys.*, *30*(3), 597–611, doi:10.5194/angeo-30-597-2012.

Grocott, A. (2017), *Time Dependence of Dawn-Dusk Asymmetries in the Terrestrial Ionospheric Convection Pattern, in: Dawn-Dusk Asymmetries in Planetary Plasma Environments, edited by: Haaland, S., Runov, A. and Forsyth, C.*, the American Geophysical Union, and John Wiley and Sons, Inc., 107-123.

Grocott, A., and S. E. Milan (2014), The influence of IMF clock angle timescales on the morphology of ionospheric convection, *J. Geophys. Res.*, *119*(7), 5861–5876, doi: 10.1002/2014JA020136.

Grocott, A., S. V. Badman, S. W. H. Cowley, T. K. Yeoman, and P. J. Cripps (2004a), The influence of IMF By on the nature of the nightside high-latitude ionospheric flow during intervals of positive IMF Bz, *Ann. Geophys.*, *22*(5), 1755–1764, doi:10.5194/angeo-22-1755-2004.

Grocott, A., T. K. Yeoman, R. Nakamura, S. W. H. Cowley, H. U. Frey, H. Réme, and B. Klecker (2004b), Multi-instrument observations of the ionospheric counterpart of a bursty bulk flow in the near-Earth plasma sheet, *Ann. Geophys.*, *22*(4), 1061–1075, doi:10.5194/angeo-22-1061-2004.

Grocott, A., T. K. Yeoman, S. E. Milan, and S. W. H. Cowley (2005), Interhemispheric observations of the ionospheric signature of tail reconnection during IMF-northward non-substorm intervals, *Ann. Geophys.*, *23*(5), 1763–1770, doi:10.5194/angeo-23-1763-2005.

Grocott, A., T. K. Yeoman, S. E. Milan, O. Amm, H. U. Frey, L. Juusola, et al. (2007), Multi-scale observations of magnetotail flux transport during IMF-northward non-substorm intervals, *Ann. Geophys.*, *25*(7), 1709–1720, doi:10.5194/angeo-25-1709-2007.

Grocott, A., S. E. Milan, and T. K. Yeoman (2008), Interplanetary magnetic field control of fast azimuthal flows in the nightside high-latitude ionosphere, *Geophys. Res. Lett.*, *35*(8), L08,102, doi:10.1029/2008GL033545.

Grocott, A., S. E. Milan, T. K. Yeoman, N. Sato, A. S. Yukimatu, and J. A. Wild (2010), Superposed epoch analysis of the ionospheric convection evolution during substorms: IMF B_y dependence, *J. Geophys. Res.*, *115*, A00I06, doi:10.1029/2010JA015728.

Grocott, A., S. E. Milan, S. M. Imber, M. Lester, and T. K. Yeoman (2012), A quantitative deconstruction of the morphology of high-latitude ionospheric convection, *J. Geophys. Res.*, *117*(A5), A05,317, doi:10.1029/2012JA017580.

Grocott, A., et al. (2004c), Multi-instrument observations of bursty bulk flows and their ionospheric counterparts, *Proc. Seventh Internat. Conf. on Substorms, UDK-52-854, FMI, Helsinki, Finland*, pp. 107–110.

Hamrin, M., P. Norqvist, T. Karlsson, H. Nilsson, H. S. Fu, S. Buchert, et al. (2013), The evolution of flux pileup regions in the plasma sheet: Cluster observations, *J. Geophys. Res.*, *118*(10), 6279–6290, doi:10.1002/jgra.50603.

Hapgood, M. A. (1992), Space Physics Coordinate Transformations: A user guide, *Planet. Space Sci.*, *40*(5), 711–717, doi:10.1016/0032-0633(92)90012-D.

Hargreaves, J. K. (1979), *The upper atmosphere and solar-terrestrial relations*, Van Nostrand Reinhold Co. Ltd, New York.

Harvey, C. C., and S. J. Schwartz (1998), *Time Series Resampling Methods, in: Analysis Methods for Multi-Spacecraft Data, edited by: Paschmann, G. and Daly, W.*, ESA Publications Division.

Heppner, J. P., and N. C. Maynard (1987), Empirical high-latitude electric field models, *J. Geophys. Res.*, *92*(A5), 4467–4489, doi:10.1029/JA092iA05p04467.

Hesse, M., and J. Birn (1991), On dipolarization and its relation to the substorm current wedge, *J. Geophys. Res.*, *96*(A11), 19,417–19,426, doi:10.1029/91JA01953.

Hesse, M., J. Birn, and R. A. Hoffman (1997), On the mapping of ionospheric convection into the magnetosphere, *J. Geophys. Res.*, *102*(A5), 9543–9551, doi:10.1029/96JA03999.

Hill, T. W. (1974), Origin of the plasma sheet, *Rev. Geophys.*, *12*(3), 379–388, doi:10.1029/RG012i003p00379.

Hones Jr, E. W., G. Paschmann, S. J. Bame, J. R. Asbridge, N. Sckopke, and K. Schindler (1978), Vortices in magnetospheric plasma flow, *Geophys. Res. Lett.*, *5*(12), 1059–1062, doi:10.1029/GL005i012p01059.

Hones Jr, E. W., R. D. Zwickl, T. A. Fritz, and S. J. Bame (1986), Structural and dynamical aspects of the distance magnetotail determined from ISEE-3 plasma measurements, *Planet. Space. Sci.*, *34*(10), 889–901, doi:10.1016/0032-0633(86)90001-2.

Hori, T., K. Maezawa, Y. Saito, and T. Mukai (2000), Average profile of ion flow and convection electric field in the near-Earth plasma sheet, *Geophys. Res. Lett.*, *27*(11), 1623–1626, doi:10.1029/1999GL003737.

Hsu, T.-S., and R. L. McPherron (2012), A statistial analysis of substorm associated tail activity, *Adv. Space Res.*, *50*(10), 1317–1343, doi:10.1016/j.asr.2012.06.034.

Iijima, T., and T. A. Potemra (1976), The amplitude distribution of field-aligned currents at northern high latitudes observed by Triad, *J. Geophys. Res.*, *81*(13), 2165–2174, doi:10.1029/JA081i013p02165.

Juusola, L., N. Østgaard, and E. Tanskanen (2011), Statistics of plasma sheet convection, *J. Geophys. Res.*, *116*(A8), A08,201, doi:10.1029/2011JA016479.

Kan, J., and L. Lee (1979), Energy coupling function and solar wind-magnetosphere dynamo, *Geophys. Res. Lett*, *6*(7), 577–580, doi:10.1029/GL006i007p00577.

Karlsson, T., M. Hamrin, H. Nilsson, A. Kullen, and T. Pitkänen (2015), Magnetic forces associated with bursty bulk flows in the Earth's magnetotail, *Geophys. Res. Lett*, *42*(9), 3122–3128, doi:10.1002/2015GL063999.

Kaymaz, Z., G. L. Siscoe, J. G. Luhmann, R. P. Lepping, and C. T. Russell (1994), Interplanetary magnetic field control of magnetotail magnetic field geometry: IMP 8 observations, *J. Geophys. Res.*, *99*(A6), 11,113–11,126, doi:10.1029/94JA00300.

Keika, K., R. Nakamura, M. Volwerk, V. Angelopoulos, W. Baumjohann, A. Retinò, et al. (2009), Observations of plasma vortices in the vicinity of flow-braking: a case study, *Ann. Geophys.*, *27*(8), 3009–3017, doi:10.5194/angeo-27-3009-2009.

Keiling, A. (2009), Alfvén Waves and Their Roles in the Dynamics of the Earths Magnetotail: A Review, *Space Sci. Rev.*, *142*, 73–156, doi:10.1007/s11214-008-9463-8.

Keiling, A., V. Angelopoulos, A. Runov, J. Weygand, S. V. Apatenkov, S. Mende, et al. (2009), Substorm current wedge driven by plasma flow vortices: Themis observations, *Geophys. Res. Lett.*, *114*(A1), A00C22, doi:10.1029/2009JA014114.

Khurana, K. K., R. J. Walker, and T. Ogino (1996), Magnetospheric convection in the presence of interplanetary magnetic field B_y: A conceptual model and simulations, *J. Geophys. Res.*, *101*(A3), 4907–4916, doi:10.1029/95JA03673.

Kiehas, S. A., A. Runov, V. Angelopoulos, H. Hietala, and D. Korovinksiy (2018), Magnetotail Fast Flow Occurrence Rate and Dawn-Dusk Asymmetry at $X_{GSM} \sim -60\ R_E$, *J. Geophys. Res.*, *123*(3), 1767–1778, doi:10.1002/2017JA024776.

King, J. H., and N. E. Papitashvili (2005), Solar wind spatial scales in and comparisons of hourly Wind and ACE plasma and magnetic field data, *J. Geophys. Res.*, *110*(A2), A02,104, doi:10.1029/2004JA010649.

Kissinger, J., R. L. McPherron, T.-S. Hsu, and V. Angelopoulos (2012), Diversion of plasma due to high pressure in the inner magnetosphere during steady magnetospheric convection, *J. Geophys. Res.*, *117*(A5), A05,206, doi:10.1029/2012JA017579.

Kissinger, J., F. D. Wilder, R. L. McPherron, T.-S. Hsu, J. B. H. Baker, and L. Kepko (2013), Statistical occurrence and dynamics of the Harang discontinuity during steady magnetospheric convection, *J. Geophys. Res.*, *118*(8), 5127–5135, doi:10.1002/jgra.50503.

Kistler, L. M., C. Mouikis, E. Möbius, B. Klecker, J. A. Sauvaud, H. Réme, et al. (2005), Contribution of nonadiabatic ions to the cross-tail current in an O^+ dominated thin current sheet, *J. Geophys. Res.*, *110*(A6), A06,213, doi:10.1029/2004JA010653.

Kivelson, M. T., and C. Russell (1995), *Introduction to Space Physics*, Cambridge University Press.

Kletzing, C. A., J. D. Scudder, E. E. Dors, and C. Curto (2003), Auroral source region: Plasma properties of the high-latitude plasma sheet, *J. Geophys. Res.*, *108*(A10), 1,360, doi:10.1029/2002JA009678.

Kokubun, S., T. Yamamoto, M. H. Acuña, K. Hayashi, K. Shiokawa, and H. Kawano (1994), The Geotail Magnetic Field Experiment, *J. Geomag. Geoelec.*, *46*(1), 7–21, doi:10.5636/jgg.46.7.

Kubyshkina, D. I., D. A. Sormakov, V. A. Sergeev, V. S. Semenov, N. V. Erkaev, I. V. Kubyshkin, et al. (2014), How to distinguish between kink and sausage modes in flapping oscillations?, *J. Geophys. Res.*, *119*(4), 3002–3015, doi:10.1002/2013JA019477.

Laakso, H., C. Perry, S. McCaffrey, D. Herment, A. J. Allen, C. C. Harvey, et al. (2010), Cluster Active Archive: Overview, *Astrophysics and Space Science Proceedings, edited by: Laakso, H., Taylor, M. and Escoubet, C. P., Springer*, pp. 3–37, doi:10.1007/978-90-481-3499-1_1.

Lane, J. H., A. Grocott, N. A. Case, and M.-T. Walach (2021), Dynamics of variable dusk-dawn flow associated with magnetotail current sheet flapping, *Ann. Geophys.*, *39*(6), 1037–1053, doi:10.5194/angeo-39-1037-2021.

Larson, D., R. Lin, and V. Angelopoulos (2009), The solid state telescope for THEMIS, *Space Sci. Rev.*, *in-preparation.*

Laundal, K. M., and A. D. Richmond (2017), Magnetic Coordinate Systems, *Space Sci. Rev.*, *206*, 27–59, doi:10.1007/s11214-016-0275-y.

Lavraud, B., and D. E. Larson (2016), Correcting moments of in situ particle distribution functions for spacecraft electrostatic charging, *J. Geophys. Res.*, *121*(9), 8462–8474, doi:10.1002/2016JA022591.

Levy, E. H. (1976), The physical basis of geomagnetism and geomagnetic reversals, *AIP Conference Proceedings*, *29*(1), 10–15, doi:10.1063/1.30540.

Li, S.-S., V. Angelopoulos, A. Runov, X.-Z. Zhou, J. McFadden, and D. Larson (2011), On the force balance around dipolarization fronts within bursty bulk flows, *J. Geophys. Res.*, *116*(A5), A00I35, doi:10.1029/2010JA015884.

Liou, K., and E. Mitchell (2019), Effects of the interplanetary magnetic field y component on the dayside aurora, *Geosci. Lett.*, *6*(11), 1–10, doi:10.1186/s40562-019-0141-3.

Liou, K., and P. T. Newell (2010), On the azimuthal location of auroral breakup: Hemispheric asymmetry, *Geophys. Res. Lett.*, *37*(23), L23,103, doi:10.1029/2010GL045537.

Liu, J., V. Angelopoulos, A. Runov, and X. Z. Zhou (2013), On the current sheets surrounding dipolarizing flux bundles in the magnetotail: The case for wedgelets, *J. Geophys. Res.*, *118*(5), 2000–2020, doi:10.1002/jgra.50092.

Lockwood, M. (1991), Modelling the high-latitude ionosphere, *IEE Colloqium on National Radio Propagation Programme'*, *10*, 1–6.

Lockwood, M. (1993), Modelling high-latitude ionosphere for time-varying plasma convection, *IEE Proceedings-H*, *140*(2), 91–100, doi:10.1049/ip-h-2.1993.0015.

Lockwood, M., S. W. H. Cowley, and M. P. Freeman (1990), The excitation of plasma convection in the high-latitude ionosphere, *J. Geophys. Res.*, *95*(A6), 7961–7972, doi: 10.1029/JA095iA06p07961.

McFadden, J. P., C. W. Carlson, D. Larson, R. Ludlam, M. Abiad, B. Elliott, et al. (2008), The THEMIS ESA Plasma Instrument and In-flight Calibration, *Space Sci. Rev.*, *141*, 277–302, doi:10.1007/s11214-008-9440-2.

McPherron, R. L. (1979), Magnetospheric substorms, *Rev. Geophys.*, *17*(4), 657–681, doi: 10.1029/RG017i004p00657.

McPherron, R. L., C. T. Russell, and M. P. Aubry (1973), Satellite studies of magnetospheric substorms on August 15, 1968: 9. Phenomenological model for substorms, *J. Geophys. Res.*, *78*(16), 3131–3149, doi:10.1029/JA078i016p03131.

McPherron, R. L., J. M. Weygand, and T.-S. Hsu (2008), Response of the Earth's magnetosphere to changes in the solar wind, *J. Atmos. Solar-Terr. Phys.*, *70*(2-4), 303–315, doi:10.1016/j.jastp.2007.08.040.

McPherron, R. L., T.-S. Hsu, J. Kissinger, X. Chu, and V. Angelopoulos (2011), Characteristics of plasma flows at the inner edge of the plasma sheet, *J. Geophys. Res.*, *116*(A5), A00I33, doi:10.1029/2010JA015923.

Milan, S. E., M. Lester, S. W. H. Cowley, K. Oksavik, M. Brittnacher, R. A. Greenwald, et al. (2003), Variations in the polar cap area during two substorm cycles, *Ann. Geophys.*, *21*(5), 1121–1140, doi:10.5194/angeo-21-1121-2003.

Milan, S. E., G. Provan, and B. Hubert (2007), Magnetic flux transport in the Dungey cycle: A survey of dayside and nightside reconnection rates, *J. Geophys. Res.*, *112*(A1), A01,209, doi:10.1029/2006JA011642.

Milan, S. E., J. S. Gosling, and B. Hubert (2012), Relationship between interplanetary parameters and the magnetopause reconnection rate quantified from observations of the expanding polar cap, *J. Geophys. Res.*, *117*(A3), A03,226, doi:10.1029/2011JA017082.

Milan, S. E., L. B. N. Clausen, J. C. Coxon, J. A. Carter, M.-T. Walach, K. Laundal, et al. (2017), Overview of Solar Wind-Magnetosphere-Ionosphere-Atmosphere Coupling and the Generation of Magnetospheric Currents, *Space Sci. Rev.*, *206*, 547–573, doi: 10.1007/s11214-017-0333-0.

Miyashita, Y., S. Machida, Y. Kamide, D. Nagata, K. Liou, M. Fujimoto, et al. (2009), A state-of-the-art picture of substorm-associated evolution of the near-earth magnetotail obtained from superposed epoch analysis, *J. Geophys. Res.*, *114*(A1), A01,211, doi: 10.1029/2008JA013225.

Mukai, T., S. Machida, Y. Saito, M. Hirahara, T. Terasawa, N. Kaya, et al. (1994), The Low Energy Particle (LEP) Experiment onboard the Geotail Satellite, *Journal of Geomagnetism and Geoelectricity*, *46*(8), 669–692, doi:10.5636/jgg.46.669.

Musmann, G., and Y. Afanassiev (2010), *Fluxgate Magnetometers for Space Research*, Books on Demand, GmbH, Norderstedt.

Nagai, T., M. Fujimoto, Y. Saito, S. Machida, T. Terasawa, R. Nakamura, et al. (1998), Structure and dynamics of magnetotail reconnection for substorm onsets with Geotail observations, *J. Geophys. Res.*, *103*(A3), 4419–4440, doi:10.1029/97JA02190.

Nakamura, R., W. Baumjohann, C. Mouikis, L. M. Kistler, A. Runov, M. Volwerk, et al. (2004), Spatial scale of high speed flows in the plasma sheet observed by Cluster, *Geophys. Res. Lett.*, *31*(9), L09,804, doi:10.1029/2004GL019558.

Nakamura, R., O. Amm, H. Laasko, N. C. Draper, M. Lester, A. Grocott, et al. (2005), Localized fast flow disturbance observed in the plasma sheet and in the ionosphere, *Ann. Geophys.*, *23*(2), 553–566, doi:10.5194/angeo-23-553-2005.

Ness, N. F. (1965), The Earth's Magnetic Tail, *J. Geophys. Res.*, *70*(13), 2989–3005, doi:10.1029/JZ070i013p02989.

Newell, P. T., T. Sotirelis, K. Liou, C. I. Meng, and F. J. Rich (2007), A nearly universal solar wind-magnetosphere coupling function inferred from 10 magnetospheric state variables, *J. Geophys. Res.*, *112*(A1), A01,206, doi:10.1029/2006JA012015.

Nishida, A. (1994), The Geotail Mission, *Geophys. Res. Lett*, *21*(25), 2871–2873, doi: 10.1029/94GL01223.

Nishida, A., and C. T. Russell (1978), On the expected signatures of reconnection in the magnetotail, *J. Geophys. Res.*, *83*(A8), 3890–3892, doi:10.1029/JA083iA08p03890.

Nishitani, N., J. M. Ruohoniemi, M. Lester, J. B. H. Baker, A. V. Koustov, S. G. Shepherd, et al. (2019), Review of the accomplishments of mid-latitude Super Dual Auroral Radar Network (SuperDARN) HF radars, *Prog. Earth. Planet. Sci.*, *6*(27), 1–57, doi:10.1186/s40645-019-0270-5.

Ogilvie, K. W., D. J. Chornay, R. J. Fritzenreiter, F. Hunsaker, J. Keller, J. Lobell, et al. (1995), SWE, a comprehensive plasma instrument for the WIND spacecraft, *Space Sci. Rev.*, *71*, 55–77, doi:10.1007/BF00751326.

Ohma, A., N. Østgaard, J. P. Reistad, P. Tenfjord, K. M. Laundal, K. Snekvik, et al. (2018), Evolution of Asymmetrically Displaced Footprints During Substorms, *J. Geophys. Res.*, *123*(12), 10,030–10,063, doi:10.1029/2018JA025869.

Ohma, A., N. Østgaard, J. P. Reistad, P. Tenfjord, K. M. Laundal, T. Moretto Jørgensen, et al. (2019), Observations of Asymmetric Lobe Convection for Weak and Strong Tail Activity, *J. Geophys. Res.*, *124*(12), 9999–10,017, doi:10.1029/2019JA026773.

Ohtani, S.-I., M. A. Shay, and T. Mukai (2004), Temporal structure of the fast convective flow in the plasma sheet: Comparison between observations and twofluid simulations, *J. Geophys. Res.*, *109*(A3), A03,210, doi:10.1029/2003JA010002.

Østgaard, N., S. B. Mende, H. U. Frey, T. J. Immel, L. A. Frank, J. B. Sigwarth, and T. J. Stubbs (2004), Interplanetary magnetic field control of the location of substorm onset and auroral features in the conjugate hemispheres, *J. Geophys. Res.*, *109*(A7), A07,204, doi:10.1029/2003JA010370.

Østgaard, N., B. K. Humberset, and K. M. Laundal (2011), Evolution of auroral asymmetries in the conjugate hemispheres during two substorms, *Geophys. Res. Lett.*, *38*(3), L03,101, doi:10.1029/2010GL046057.

Pallé, E. (2010), *The Earth as a Distant Planet: A Rosetta Stone for the Search of Earth-Like Worlds (Astronomy and Astrophysics Library)*, Berlin: Springer.

Panov, E. V., R. Nakamura, W. Baumjohann, V. Angelopoulos, A. A. Petrukovich, A. Retinò, et al. (2010), Multiple overshoot and rebound of a bursty bulk flow, *Geophys. Res. Lett.*, *37*(8), L08,103, doi:10.1029/2009GL041971.

Park, K. S., T. Ogino, and R. J. Walker (2006), On the importance of antiparallel reconnection when the dipole tilt and IMF B_y are nonzero, *J. Geophys. Res.*, *111*(A5), A05,202, doi:10.1029/2004JA010972.

Parker, E. N. (1957), Sweet's mechanism for merging magnetic fields in conducting fluids, *J. Geophys. Res.*, *62*(4), 509–520, doi:10.1029/JZ062i004p00509.

Parker, E. N. (1958), Dynamics of the interplanetary gas and magnetic fields, *Astrophys. J.*, *128*, 664–676, doi:10.1086/146579.

Parker, E. N. (1965), Dynamical theory of the solar wind, *Space Sci. Rev.*, *4*, 666–708, doi:10.1007/BF00216273.

Parker, E. N. (1996), The alternative paradigm for magnetospheric physics, *J. Geophys. Res.*, *101*(A5), 10,587–10,625, doi:10.1029/95JA02866.

Paschmann, G., and P. W. Daly (1998), *Analysis Methods for Multi-Spacecraft Data, ESA Publications Division.*

Paschmann, G., A. N. Fazakerley, and S. J. Schwartz (1998), *Moments of Plasma Velocity Distributions, in: Analysis Methods for Multi-Spacecraft Data, edited by: Paschmann, G. and Daly, W.*, ESA Publications Division., 125-158.

Paularena, K. I., and J. H. King (1999), *NASAs IMP 8 Spacecraft, in: Interball in the ISTP Program, edited by: D. G. Sibeck and K. Kudela, pp. 145*, Springer.

Petrukovich, A. A. (2011), Origins of plasma sheet B_y, *J. Geophys. Res.*, *116*(A7), A07,217, doi:10.1029/2010JA016386.

Petrukovich, A. A., W. Baumjohann, R. Nakamura, R. Schödel, and T. Mukai (2001), Are earthward bursty bulk flows convective or field-aligned?, *J. Geophys. Res.*, *106*(A10), 21,211–21,215, doi:10.1029/2001JA900019.

Petrukovich, A. A., W. Baumjohann, R. Nakamura, A. Runov, and A. Balogh (2005), Cluster vision of the magnetotail current sheet on a macroscale, *J. Geophys. Res.*, *110*(A6), A06,204, doi:10.1029/2004JA010825.

Pettigrew, E. D., S. G. Shepherd, and J. M. Ruohoniemi (2010), Climatological patterns of high-latitude convection in the Northern and Southern hemispheres: Dipole tilt dependencies and interhemispheric comparisons, *J. Geophys. Res.*, *115*(A7), A07,305, doi:10.1029/2009JA014956.

Pitkänen, T., A. T. Aikio, O. Amm, K. Kauristie, H. Nilsson, and K. U. Kaila (2011), EISCAT-Cluster observations of quiet-time near-Earth magnetotail fast flows and their signatures in the ionosphere, *Ann. Geophys.*, *29*(2), 299–319, doi:10.5194/angeo-29-299-2011.

Pitkänen, T., M. Hamrin, P. Norqvist, T. Karlsson, and H. Nilsson (2013), IMF dependence of the azimuthal direction of earthward magnetotail fast flows, *Geophysical Research Letters*, *40*(21), 5598–5604, doi:10.1002/2013GL058136.

Pitkänen, T., M. Hamrin, P. Norqvist, T. Karlsson, H. Nilsson, A. Kullen, et al. (2015), Azimuthal velocity shear within an Earthward fast flow - further evidence for magnetotail untwisting?, *Ann. Geophys.*, *33*(3), 245–255, doi:10.5194/angeo-33-245-2015.

Pitkänen, T., M. Hamrin, A. Kullen, R. Maggiolo, T. Karlsson, H. Nilsson, and P. Norqvist (2016), Response of magnetotail twisting to variations in IMF B_y: A THEMIS case study 1-2 January 2009, *Geophys. Res. Lett*, *43*(15), 7822–7830, doi:10.1002/2016GL070068.

Pitkänen, T., M. Hamrin, T. Karlsson, H. Nilsson, and A. Kullen (2017), *On IMF B_y-Induced Dawn-Dusk Asymmetries in Earthward Convective Fast Flows, in: Dawn-Dusk Asymmetries in Planetary Plasma Environments, edited by: Haaland, S., Runov, A. and Forsyth, C.*, the American Geophysical Union, and John Wiley and Sons, Inc., 95-106.

Pitkänen, T., A. Kullen, K. M. Laundal, P. Tenfjord, Q. Q. Shi, P. J. S., et al. (2019), IMF B_y Influence on Magnetospheric Convection in Earth's Magnetotail Plasma Sheet, *Geophys. Res. Lett.*, *46*(21), 11,698–11,708, doi:10.1029/2019GL084190.

Pitkänen, T., M. Hamrin, G. S. Chong, and A. Kullen (2021), Relevance of the North-South Electric Field Component in the Propagation of Fast Convective Earthward Flows in the Magnetotail: An Event Study, *J. Geophys. Res.*, *126*(7), e2021JA029,233, doi: 10.1029/2021JA029233.

Pizzo, V. (1978), A three-dimensional model of corotating streams in the solar wind, 1. Theoretical foundation, *J. Geophys. Res.*, *83*(A12), 5563–5572, doi:10.1029/JA083iA12p05563.

Press, W. H., S. A. Teukolsky, W. T. Vetterling, and B. P. Flannery (1992), *Numerical Recipes in C: Second Edition*, Cambridge University Press.

Priest, E. R. (2012), *Solar Magnetohydrodynamics*, Kluwer Academic Publishers.

Primdahl, F. (1979), The fluxgate magnetometer, *J. Phys. E: Sci. Instrum.*, *12*(4), 241–253, doi:10.1088/0022-3735/12/4/001.

Pulkkinen, T. (2007), Space Weather: Terrestrial Perspective, *Living Rev. Sol. Phys*, *4*(1), doi:10.12942/lrsp-2007-1.

Raj, A., T. Phan, R. P. Lin, and V. Angelopoulos (2002), Wind survey of high-speed bulk flows and field-aligned beams in the near-Earth plasma sheet, *J. Geophys. Res*, *107*(A12), SMP 3–1–SMP 3–17, doi:10.1029/2001JA007547.

Reid, G. C. (1968), The formation of small-scale irregularities in the ionosphere, *J. Geophys. Res.*, *73*(5), 1627–1640, doi:10.1029/JA073i005p01627.

Reistad, J. P., N. Østgaard, P. Tenfjord, K. M. Laundal, K. Snekvik, S. Haaland, et al. (2016), Dynamic effects of restoring footpoint symmetry on closed magnetic field lines, *J. Geophys. Res.*, *121*(5), 3963–3977, doi:10.1002/2015JA022058.

Reistad, J. P., N. Østgaard, K. M. Laundal, A. Ohma, K. Snekvik, P. Tenfjord, et al. (2018), Observations of Asymmetries in Ionospheric Return Flow During Different Levels of Geomagnetic Activity, *J. Geophys. Res.*, *123*(6), 4638–4651, doi:10.1029/2017JA025051.

Rème, H., J. M. Bosqued, J. A. Sauvaud, A. Cros, I. Dandouras, C. Aoustin, et al. (1997), The Cluster Ion Spectrometry (CIS) Experiment, *Space Sci. Rev.*, *79*, 303–350, doi:10.1023/A:1004929816409.

Rème, H., C. Aoustin, J. M. Bosqued, I. Dandouras, B. Lavraud, J. A. Sauvaud, et al. (2001), First multispacecraft ion measurements in and near the Earth's magnetosphere with the identical Cluster ion spectrometry (CIS) experiment, *Ann. Geophys.*, *19*(10/12), 1303–1354, doi:10.5194/angeo-19-1303-2001.

Ridley, A. J., T. I. Gombosi, and D. L. DeZeeuw (2004), Ionospheric control of the magnetosphere: conductance, *Ann. Geophys.*, *22*(2), 567–584, doi:hal-00317238.

Ridley, A. J., Y. Deng, and G. Tóth (2006), The global ionosphere-thermosphere model, *J. Atmos. Solar-Terr. Phys.*, *68*(8), 839–864, doi:10.1016/j.jastp.2006.01.008.

Robert, P., M. W. Dunlop, A. Roux, and G. Chanteur (1998), *Accuracy of Current Density Determination, in: Analysis Methods for Multi-Spacecraft Data, edited by: Paschmann, G. and Daly, W.*, ESA Publications Division., 395-418.

Rong, Z. J., W. X. Wan, C. Shen, X. Li, M. W. Dunlop, A. A. Petrukovich, et al. (2011), Statistical survey on the magnetic structure in magnetotail current sheets, *J. Geophys. Res.*, *116*(A9), A09,218, doi:10.1029/2011JA016489.

Rong, Z. J., S. Barabash, G. Stenberg, Y. Futaana, T. L. Zhang, W. X. Wan, et al. (2015), Technique for diagnosing the flapping motion of magnetotail current sheets based on single-point magnetic field analysis, *J. Geophys. Res.*, *120*(5), 3462–3474, doi:10.1002/2014JA020973.

Runov, A., R. Nakamura, W. Baumjohann, T. L. Zhang, M. Volwerk, H.-U. Eichcelberger, and A. Balogh (2003), Cluster observation of a bifurcated current sheet, *Geophys. Res. Lett.*, *30*(2), 1036, doi:10.1029/2002GL016136.

Runov, A., V. Angelopoulos, V. A. Sergeev, K.-H. Glassmeier, U. Auster, J. McFadden, et al. (2009), Global properties of magnetotail current sheet flapping: THEMIS perspectives, *Ann. Geophys.*, *27*(1), 319–328, doi:10.5194/angeo-27-319-2009.

Runov, A., V. Angelopoulos, X.-Z. Zhou, X.-J. Zhang, S. Li, F. Plaschke, and J. Bonnell (2011), A THEMIS multicase study of dipolarization fronts in the magnetotail plasma sheet, *J. Geophys. Res.*, *116*(A5), A05,216, doi:10.1029/2010JA016316.

Ruohoniemi, J. M., and K. B. Baker (1998), Large-scale imaging of high-latitude convection with Super Dual Auroral Radar Network HF radar observations, *J. Geophys. Res.*, *103*(A9), 20,797–20,811, doi:10.1029/98JA01288.

Ruohoniemi, J. M., and R. A. Greenwald (1996), Statistical patterns of high-latitude convection obtained from Goose Bay HF radar observations, *J. Geophys. Res.*, *101*(A10), 21,743–21,763, doi:10.1029/96JA01584.

Ruohoniemi, J. M., and R. A. Greenwald (2005), Dependencies of high-latitude plasma convection: Consideration of interplanetary magnetic field, seasonal, and universal time factors instatistical patterns, *J. Geophys. Res.*, *110*(A9), A09,204, doi:10.1029/2004JA010815.

Russell, C., et al. (2016), *Space Physics: An Introduction*, Cambridge University Press.

Russell, C. T. (1972), The Configuration of the Magnetosphere, *Critical Problems of Magnetospheric Physics, IUCSTP Secreteriat, National Academy of Sciences, Washington D.C.*

Russell, C. T., and K. I. Brody (1967), Some remarks on the position and shape of the neutral sheet, *J. Geophys. Res.*, *72*(23), 6104–6106, doi:10.1029/JZ072i023p06104.

Schmid, D., M. Volwerk, R. Nakamura, W. Baumjohann, and M. Heyn (2011), A statistical and event study of magnetotail dipolarization fronts, *Ann. Geophys.*, *29*(9), 1537–1547, doi:10.5194/angeo-29-1537-2011.

Schödel, R., W. Baumjohann, R. Nakamura, V. A. Sergeev, and T. Mukai (2001), Rapid flux transport in the central plasma sheet, *J. Geophys. Res.*, *106*(A1), 301–313, doi:10.1029/2000JA900139.

Sergeev, V. A., R. C. Elphic, F. S. Mozer, A. Saint-Marc, and J. A. Sauvard (1992), A two-satellite study of nightside flux transfer events in the plasma sheet, *Planet. Space Sci.*, *40*(11), 1551–1572, doi:10.1016/0032-0633(92)90052-P.

Sergeev, V. A., R. J. Pellinen, and T. I. Pulkkinen (1996a), Steady magnetospheric convection: A review of recent results, *Space Sci. Rev.*, *75*, 551–604, doi:10.1007/BF00833344.

Sergeev, V. A., V. Angelopoulos, J. T. Gosling, C. A. Cattell, and C. T. Russell (1996b), Detection of localized, plasma-depleted flux tubes or bubbles in the midtail plasma sheet, *J. Geophys. Res.*, *101*(A5), 10,817–10,826, doi:10.1029/96JA00460.

Sergeev, V. A., D. A. Sormakov, S. V. Apatenkov, W. Baumjohann, R. Nakamura, A. V. Runov, et al. (2006), Survey of large-amplitude flapping motions in the midtail current sheet, *Ann. Geophys.*, *24*(7), 2015–2024, doi:10.5194/angeo-24-2015-2006.

Shepherd, S. G., and J. M. Ruohoniemi (2000), Electrostatic potential patterns in the high-latitude ionosphere constrained by SuperDARN measurements, *J. Geophys. Res.*, *105*(A10), 23,005–23,014, doi:10.1029/2000JA000171.

Shiokawa, K., W. Baumjohann, and G. Haerendel (1997), Braking of high-speed flows in the near-Earth tail, *Geophys. Res. Lett*, *24*(10), 1179–1182, doi:10.1029/97GL01062.

Siscoe, G. L., and T. S. Huang (1985), Polar cap inflation and deflation, *J. Geophys. Res.*, *90*(A1), 543–547, doi:10.1029/JA090iA01p00543.

Snekvik, K., S. Haaland, N. Østgaard, H. Hasegawa, R. Nakamura, T. Takada, et al. (2007), Cluster observations of a field aligned current at the dawn flank of a bursty bulk flow, *Ann. Geophys*, *25*(6), 1405–1415, doi:10.5194/angeo-25-1405-2007.

Song, P., T. I. Gombosi, and A. J. Ridley (2001), Three-fluid Ohm's law, *J. Geophys. Res.*, *106*(A5), 8149–8156, doi:10.1029/2000JA000423.

Sonnerup, B. U. Ö., and L. J. Cahill Jr. (1967), Magnetopause structure and attitude from Explorer 12 observations, *J. Geophys. Res.*, *72*(1), 171–183, doi:10.1029/JZ072i001p00171.

Sonnerup, B. U. Ö., and B. G. Ledley (1979), Ogo 5 magnetopause structure and classical reconnection, *J. Geophys. Res.*, *84*(A2), 399–405, doi:10.1029/JA084iA02p00399.

Sonnerup, B. U. Ö., and M. Scheible (1998), *Minimum and Maximum Variance Analysis, in: Analysis Methods for Multi-Spacecraft Data, edited by: Paschmann, G. and Daly, W.*, ESA Publications Division.

Speiser, T. W. (1965), Particle trajectories in model current sheets. 1. Analytical solutions, *J. Geophys. Res.*, *70*(17), 4219–4226, doi:10.1029/JZ070i017p04219.

Stawarz, J. E., L. Matteini, T. N. Parashar, L. Franci, J. P. Eastwood, C. A. Gonzalez, et al. (2021), Comparative Analysis of the Various Generalized Ohm's Law Terms in Magnetosheath Turbulence as Observed by Magnetospheric Multiscale, *J. Geophys. Res.*, *126*(1), e2020JA028,447, doi:10.1029/2020JA028447.

Stern, D. P. (1977), Large-scale electric fields in the Earth's magnetosphere, *Rev. Geophys.*, *15*(2), 156–194, doi:10.1029/RG015i002p00156.

Stern, D. P. (1983), The origins of the Birkeland currents, *Rev. Geophys.*, *21*(1), 125–138, doi:10.1029/RG021i001p00125.

Stern, D. P. (1994), The art of mapping the magnetosphere, *J. Geophys. Res.*, *99*(A9), 17,169–17,198, doi:10.1029/94JA01239.

Strangeway, R. J., C. T. Russell, C. W. Carlson, J. P. McFadden, R. E. Ergun, M. Temerin, et al. (2000), Cusp field-aligned currents and ion outflows, *J. Geophys. Res*, *105*(A9), 21,129–21,142, doi:10.1029/2000JA900032.

Tenfjord, P., N. Østgaard, K. Snekvik, K. M. Laundal, J. P. Reistad, S. Haaland, and S. E. Milan (2015), How the IMF B_y induces a B_y component in the closed magnetosphere and how it leads to asymmetric currents and convection patterns in the two hemispheres, *J. Geophys. Res.*, *120*(11), 9368–9384, doi:10.1002/2015JA021579.

Tenfjord, P., N. Østgaard, R. Strangeway, S. Haaland, K. Snekvik, K. M. Laundal, et al. (2017), Magnetospheric response and reconfiguration times following IMF B_y reversals, *J. Geophys. Res.*, *122*(1), 417–431, doi:10.1002/2016JA023018.

Tenfjord, P., N. Østgaard, S. Haaland, K. Snekvik, K. M. Laundal, J. P. Reistad, et al. (2018), How the IMF B_y Induces a Local B_y Component During Northward IMF B_z and Characteristic Timescales, *J. Geophys. Res.*, *123*, 3333–3348, doi:10.1002/2018JA025186.

Thébault, E., C. C. Finlay, C. D. Beggan, P. Alken, J. Aubert, O. Barrois, et al. (2015), International Geomagnetic Reference Field: the 12th generation, *Earth, Planet. Sp.*, *67*(79), 1–19, doi:10.1186/s40623-015-0228-9.

Thomas, B. T., and E. J. Smith (1981), The structure and dynamics of the heliospheric current sheet, *J. Geophys. Res.*, *86*(A13), 11,105–11,110, doi:10.1029/JA086iA13p11105.

Thomas, E. G., and S. G. Shepherd (2018), Statistical Patterns of Ionospheric Convection Derived From Mid-Latitude, High-Latitude and Polar SuperDARN HF Observations, *J. Geophys. Res.*, *123*(4), 3196–3216, doi:10.1002/2018JA025280.

Thomas, E. G., P. V. Ponomarenko, D. D. Billett, E. C. Bland, A. G. Burrell, K. Kotyk, A. S. Reimer, et al. (2018), SuperDARN Radar Software Toolkit (RST) 4.2, *Zenodo*, doi:10.5281/zenodo.1403226.

Tsyganenko, N. A. (1996), Effects of the solar wind conditions in the global magnetospheric configurations as deduced from data-based field models, *Third International Conference on Substorms, ESA Special Publication*, *389*, 181–185.

Tsyganenko, N. A., and V. A. Andreeva (2015), A forecasting model of the magnetosphere driven by an optimal solar wind coupling function, *J. Geophys. Res.*, *120*(10), 8401–8425, doi:10.1002/2015JA021641.

Volwerk, M., T. L. Zhang, K.-H. Glassmeier, A. Runov, W. Baumjohann, A. Balogh, et al. (2008), Study of waves in the magnetotail region with Cluster and DSP, *Adv. Space Res.*, *41*(10), 4731–4735, doi:10.1016/j.asr.2007.04.005.

Walach, M.-T., and S. E. Milan (2015), Are steady magnetospheric convection events prolonged substorms?, *J. Geophys. Res.*, *120*(3), 1751–1758, doi:10.1002/2014JA020631.

Walsh, A. P., A. N. Fazakerley, A. D. Lahiff, M. Volwerk, A. Grocott, M. W. Dunlop, et al. (2009), Cluster and Double Star multipoint observations of a plasma bubble, *Ann. Geophys.*, *27*(2), 725–743, doi:10.5194/angeo-27-725-2009.

Walsh, A. P., S. Haaland, C. Forsyth, A. M. Keesee, J. Kissinger, and K. Li (2014), Dawn-dusk asymmetries in the coupled solar-wind-magnetosphere-ionosphere system: a review, *Ann. Geophys.*, *32*(7), 705–737, doi:10.5194/angeo-32-705-2014.

Wardinski, I., D. Saturnino, H. Amit, A. Chambodut, B. Langlais, M. Mandea, and E. Thébault (2020), Geomagnetic core field models and secular variation forecasts for the 13th International Geomagnetic Reference Field (IGRF-13), *Earth, Planet. Sp.*, *72*(155), 1–22, doi:10.1186/s40623-020-01254-7.

Watanbe, M., T. Iijima, M. Nakagawa, T. A. Potemra, L. J. Zanetti, S.-I. Ohtani, and P. T. Newell (1998), Field-aligned current systems in the magnetospheric ground state, *J. Geophys. Res.*, *103*(A4), 6853–6869, doi:10.1029/97JA03086.

Wei, Y. Y., S. Y. Huang, Z. J. Rong, Z. G. Yuan, K. Jiang, X. H. Deng, et al. (2019), Observations of Short-period Current Sheet Flapping Events in the Earth's Magnetotail, *The Astrophysical Journal Letters*, *874*(2), L18, doi:10.3847/2041-8213/ab0f28.

Weimer, D. R. (1995), Models of high-latitude electric potentials derived with a least error fit of spherical harmonic coefficients, *J. Geophys. Res.*, *100*(A10), 19,595–19,607, doi:10.1029/95JA01755.

Weygand, J. M., E. Zesta, and O. Troshichev (2014), Auroral electrojet indices in the Northern and Southern Hemispheres: A statistical comparison, *J. Geophys. Res.*, *119*(6), 4819–4840, doi:10.1002/2013JA019377.

Wild, J. A. (2000), *Electrodynamics of the auroral ionosphere during magnetospheric substorms*, University of Leicester, Doctoral Thesis.

Wilmot-Smith, A. L., E. R. Priest, and G. Hornig (2005), Magnetic diffusion and the motion of field lines, *Geophys. Astrophys. Fluid Dyn.*, *99*(2), 177–197, doi:10.1080/03091920500044808.

Wolf, R. A., V. Kumar, F. R. Toffoletto, G. M. Erickson, A. M. Savoie, C. X. Chen, and C. L. Lemon (2006), Estimating local plasma sheet $PV^{5/3}$ from single-spacecraft measurements, *J. Geophys. Res.*, *111*(A12), A12,218, doi:10.1029/2006JA012010.

Wu, M., Q. Lu, M. Volwerk, Z. Vörös, X. Ma, and S. Wang (2016), Current sheet flapping motions in the tailward flow of magnetic reconnection, *J. Geophys. Res.*, *121*(8), 7817–7827, doi:10.1002/2016JA022819.

Xiao, S., T. Zhang, Y. Ge, G. Wang, W. Baumjohann, and R. Nakamura (2016), A statistical study on the shape and position of the magnetotail neutral sheet, *Ann. Geophys.*, *34*(2), 303–311, doi:10.5194/angeo-34-303-2016.

Zhang, L. Q., W. Baumjohann, C. Wang, L. Dai, and B. B. Tang (2016), Bursty bulk flows at different magnetospheric activity levels: Dependence on IMF conditions, *J. Geophys. Res.*, *121*(9), 8773–8789, doi:10.1002/2016JA022397.